

Machine Design and Electron Beam Control of a Single-Pass Linac for Free Electron Laser: the FERMI@Elettra Case Study

Simone Di Mitri



University of Groningen
Zernike Institute
for Advanced Materials

Zernike Institute PhD thesis series 2011–22

ISSN 1570–1530

ISBN printed version: 978-90-367-5175-9

ISBN electronic version: 978-90-367-5176-6

This work has been performed as part of the research program "FERMI@Elettra Free Electron Laser" at the Elettra Laboratory of Sincrotrone Trieste (Italy).

RIJKSUNIVERSITEIT GRONINGEN

**Machine Design and Electron Beam Control
of a Single-Pass Linac for Free Electron
Laser: the FERMI@Elettra Case Study**

Proefschrift

ter verkrijging van het doctoraat in de
Wiskunde en Natuurwetenschappen
aan de Rijksuniversiteit Groningen
op gezag van de
Rector Magnificus, dr. E. Sterken,
in het openbaar te verdedigen op
vrijdag 28 oktober 2011
om 11:00 uur

door

Simone Di Mitri

geboren op 9 oktober 1976
te Terni, Italië

Promotores: Prof. dr. P. H. M. van Loosdrecht
Prof. dr. S. Brandenburg
Prof. dr. F. Parmigiani

Beoordelingscommissie: Prof. dr. R. Hoekstra
Prof. dr. M. J. van der Wiel
Prof. dr. M. Eriksson

*To my wife
Valentina*

Contents

1	Introduction	10
2	The FERMI@Elettra Linac-based FEL	15
2.1	Overview	15
2.2	Accelerating Structures	18
2.3	Magnetic Lattice	19
2.4	High Gain Harmonic Generation Free Electron Laser	22
2.5	Electron Beam Requirements	25
2.6	Conclusions	28
3	Theoretical Tools for Machine Design	29
3.1	Particle Motion in the Phase Space	30
3.1.1	Liouville’s Theorem: Limit of Applicability	30
3.1.2	Beam Emittance	34
3.2	Single Particle Dynamics	41
3.2.1	Optics Mismatch, Field Errors and Filamentation	41
3.2.2	Magnetic Bunch Length Compression	47
3.3	Collective Effects of the Electron Beam	53
3.3.1	Short-Range Space Charge Forces	53
3.3.2	Short-Range Structural Wake Fields	54
3.3.3	Microbunching Instability	57
3.3.4	Free Electron Laser	61
3.4	Conclusions	64
4	Machine Design and Single-Particle Dynamics	67
4.1	Magnet Specifications	68
4.1.1	Magnetic Field Tolerances	68
4.1.2	Magnet Alignment Tolerances	70
4.2	Beam Transport and Diagnostics	71
4.2.1	Design of a Dispersion-Free Diagnostic Line	71

4.2.2	Design of a Dispersive Diagnostic Line	75
4.2.3	Screen Resolution	83
4.2.4	Geometric Collimation	84
4.3	Conclusions	95
5	Machine Design and Electron Beam Collective Effects	96
5.1	Short-Range Space Charge Forces	97
5.2	Longitudinal Structural Wake Field	98
5.2.1	Energy Loss	98
5.2.2	Cubic Energy Chirp	99
5.2.3	Current Shaping	103
5.3	Transverse Structural Wake Field	110
5.3.1	Emittance Growth	110
5.3.2	Single-Bunch Transverse Wake Field Instability	111
5.3.3	Slice Centroid Courant-Snyder Amplitude	119
5.4	Coherent Synchrotron Radiation Instability	128
5.4.1	Energy Loss	128
5.4.2	Emittance Growth	131
5.4.3	Optics Design to Suppress CSR Instability	133
5.4.4	Numerical Methods	135
5.5	Microbunching Instability	136
5.5.1	Energy Spread	136
5.5.2	Landau Damping	140
5.5.3	Numerical Methods	144
5.6	Conclusions	146
6	Schemes of Magnetic Bunch Length Compression	147
6.1	Working Point	147
6.2	Two-Stage Compression	152
6.3	One-Stage Compression	154
6.4	Enhanced Phase Mixing	160
6.5	Conclusions	165
7	Electron Beam Control	167
7.1	Longitudinal Phase Space	167
7.2	Trajectory Control	169
7.3	Residual Dispersion	177
7.4	Optics Matching	179
7.5	Emittance Studies	182
7.6	Microbunching Instability	185
7.7	Conclusions	188

8 Concluding Remarks and Outlook	190
8.1 General Remarks for Seeded FELs	190
8.2 Machine Design	192
8.3 Electron Beam Quality and Control	195
8.4 Outlook	199
Bibliography	201
Summary	209
Samenvatting	217
Acknowledgments	226
Curriculum Vitae	228
List of Publications	229

Chapter 1

Introduction

In classical electromagnetism, a charged particle radiates energy in the form of electromagnetic radiation when it is subject to a force. This effect is the principle behind many useful sources of radiation across a wide range of the electromagnetic spectrum. Synchrotron radiation is one such source. In the last 60 years it has emerged as a fundamental and indispensable tool for the study of materials which encompasses a wide spectrum of sciences, technologies and applications, from life sciences to nanotechnologies, from environmental sciences and geochemistry to archeology. The main figures of merit of synchrotron radiation sources are (narrow) spectral bandwidth, photon wavelength tunability and brilliance, which defines the intensity of radiation, within a given bandwidth around the desired wavelength, that can be focused unto a sample of given area. Typical brilliance values for the highest performance “third generation” light sources are around 10^{19} to 10^{21} photons/s/mm²/mrad²/0.1% bandwidth.

In addition to the synchrotron radiation, a strong need has emerged over the last few years for a source of radiation with extremely high brilliance, close to full spatial and temporal coherence, a bandwidth approaching the Fourier limit and a stable and well characterized temporal structure in the femtosecond time domain. This new type of light source enables the study of not only the static structure of materials but also the dynamics of processes in complex materials and molecules. Such a source is the single-pass Free Electron Laser (FEL) that, due to a Doppler frequency up-shifting of radiation emitted by relativistic electrons, is particularly well-suited to generating short wavelength X-ray pulses with peak brilliance many orders of magnitude higher than that generated in present third generation sources and with sub-picosecond pulse lengths. There are currently no alternative sources that have such high pulse energies and short durations. The investigation domain opened by the new sources covers essen-

tially all basic science fields giving access to explorations of matter in practically unexplored regimes. The scientific opportunities will in fact impact studies of a large number of disciplines ranging from materials and biomaterials sciences, nanosciences, plasma physics, molecular and cluster femto- and nano- physics and chemistry, as well as having various connections to life, environmental, astrophysical and earth sciences.

The generation of FEL radiation relies on the extraction of electromagnetic energy from kinetic energy of a relativistic electron beam by propagating it along the axis of a periodic lattice of alternating magnetic dipolar fields, known as undulator. This forces the beam to undulate transversally, thus causing the electrons to emit electromagnetic radiation. The fundamental wavelength emitted is proportional to λ_u/γ^2 , where λ_u is the undulator period, typically a few centimeters long, and γ is the relativistic Lorentz factor of the electrons, which typically reaches several thousand for X-ray emission. The first theoretical works describing such undulator radiation were reported in [1] and [2] in the late 1940s to early 1950s. Experiments at Stanford in 1953 generated the first incoherent undulator radiation at visible and millimeter wavelengths [3]. A few years later, Phillips conducted research on an undulator microwave source called the ubitron. This was characterized by $\gamma \geq 1$ and minimal Doppler up-shifting of the radiation wavelength from that of one undulator period. Two main qualitative features common with a FEL interaction were already present in the Phillips' experiment: a density modulation (bunching) of the electron beam along its direction of propagation, and radiation energy extraction from the kinetic energy of the beam. It was not until 1971 that Madey [4] published a seminal theory of the FEL that described a small gain process in a relativistic electron beam/undulator system. The first amplification and lasing from a FEL was demonstrated in a small gain infrared FEL oscillator system at Stanford a few years later. The FEL oscillator is a multi-pass electron beam/undulator system in which the undulator radiation is collected in the optical cavity of two mirrors with high reflectivity. The high FEL intensity is obtained by summing up the single-pass undulator emission over many turns of the electron beam in the optical cavity. From the late 1970s a body of work was developed that described classically what is now termed the high gain regime of FEL operation [5–9]. In this high gain regime, the radiation power increases exponentially as the electron beam and radiation co-propagate along the undulator. Thus, an initial small source, which may originate as noise, can be amplified by many orders of magnitude until the process saturates. In the X-ray FEL there is therefore no need for potentially troublesome mirrors to form an oscillator cavity. Most of the present X-ray FEL facilities and designs are based on this type of interaction, which has been made possible by many advances in electron beam generation and acceleration over the past few decades.

The remarkable step in performance of X-ray FELs – as compared with third generation light sources, ten orders of magnitude increase in peak photon brightness and two orders of magnitude reduction of pulse length – has been made possible, in part, by the advent of the photocathode RF electron gun [10] and recent progress in beam brightness preservation for linear colliders [11, 12]. Of critical importance is the normalized transverse beam emittance, $\epsilon_n = \gamma\epsilon$, where the geometric transverse emittance ϵ is a measure of the transverse phase space domain occupied by the beam. A limit on the geometric beam emittance for ensuring good spatial (transverse) coherence from sources of spontaneous undulator radiation was derived in [13], giving $\epsilon \leq \lambda/(4\pi)$, where $\lambda/(4\pi)$ is the minimum phase space area for a diffraction limited photon beam. Although this expression was derived for systems without gain, it turns out that it is also a requirement for the successful operation of a high-gain amplifier FEL. This relation gives a rough rule-of-thumb estimate of the electron energy/wavelength possibilities and shows, for example, that the minimum wavelength achievable decreases with the normalized emittance, for a given beam energy. Note that the local emittance (referred to as “slice emittance”) can vary significantly along the bunch to give hot-spots where lasing can occur. In fact, in contrast to linear colliders, where particle collisions effectively integrate over the entire bunch length, the X-ray FELs usually concern only very short fractions of the electron bunch length. The integration length is given by the “FEL slippage length” that is the electron-to-photon longitudinal slippage over the length of undulator, prior to FEL power saturation. The slippage length is typically in the range 1–30 μm , a small fraction of the total bunch length. Thus, the electron bunch slice duration can reasonably be defined of the order (or a fraction) of the FEL slippage length. The self-consistently coupled equations that describe a FEL reveal an exponential instability in both the field amplitude and the fundamental electron bunching. So, the radiation power exponentially grows until the electron/photon interaction saturates. At saturation, $P \approx \rho P_e$ where P_e is the electron beam power and ρ [14] is seen to be a measure of the efficiency of the interaction, with typical values in the X-ray regime of $10^{-4} \leq \rho \leq 10^{-3}$. The relative energy spread of the electron beam at saturation is $\sigma_\delta \approx \rho$. Hence, it becomes clear that the quality of the electron beam is of critical importance. If there is an initial electron energy spread approaching the maximum, which occurs at a FEL saturation of $\sigma_\delta \geq \rho$, then the FEL interaction is greatly reduced. Typical electron beam parameters of the fourth generation – very high brightness – linac-based FELs (from infrared to X-rays spectral range) are: 0.2–1 nC bunch charge, 1–3 mm mrad normalized emittance, 0.5–3 kA peak current, 0.05–0.1 % relative energy spread and 1–50 GeV final electron energy.

Delivering such high machine flexibility to serve a broad range of potential applications imposes severe requirements on the quality of the electron beam.

To meet these requirements, the need of a linac design based on extensive studies of possible perturbations that may affect the electron beam dynamics, of means to correct them and of parameter optimization has emerged. The realization of a valid machine design is therefore a fundamental and critical step for the success of a FEL project. Because of the special sensitivity of the FEL generation to the electron beam emittance, relative energy spread and trajectory control [15, 16], this thesis focuses on the design strategies to control these parameters and on how the design challenges translate into modeling and simulation challenges. Some methods and results have acquired a general validity within the field of accelerator physics and have been translated into publications in refereed journals [17–21]. Some other aspects of our machine study have been developed for the specific FEL scheme known as harmonic generation. In fact, we can identify two general ways to generate X-ray FEL. The Self Amplified Spontaneous Emission (SASE) [14, 22–25] relies on the interaction of the electrons with photons that are emitted by the electron beam itself. Since the electron bunching starts to grow from the natural noise of the initial electron distribution, the SASE output radiation is relatively poor in longitudinal coherence. In the High Gain Harmonic Generation (HG HG) scheme [5–9, 26, 27], instead, the initial energy modulation is driven by an external seed laser. It is then transformed into density bunching in a dispersive section inserted in the undulator chain. In this case, the output FEL properties reflect the high longitudinal coherence of the seeding laser.

Starting from very general principles of machine design and electron beam control, the quantitative analysis reported in this thesis focuses on the FERMI@Elettra FEL case study employing the HG HG scheme. The FERMI@Elettra single-pass linac-based FEL at the Elettra Laboratory of Sincrotrone Trieste [28, 29] is one of the FEL based European projects, designed to become the international user facility in Italy for scientific investigations of ultra-fast and ultra-high resolution processes in material science and physical biosciences with ultra high brilliance X-ray pulses. With a peak brightness of about 6 orders of magnitude higher than third generation sources, full transverse coherence, (close to) transform limited bandwidth, pulse lengths of the order of a picosecond or less, variable polarization and energy tunability, the FERMI source is a powerful tool for scientific exploration in a wide spectrum of disciplines. The coherence properties will open up new perspectives for single shot imaging, allowing to study the dynamics of chemical reactions and other phenomena through single pulse coherent diffraction imaging with a spatial resolution in the nm domain and matter under extreme thermodynamic conditions (warm and dense matter phases). The high peak power will allow studying nonlinear multi-photon processes in a regime never explored before, in dilute samples that are of paramount importance in atmospheric, astrophysical and environmental physics as well as in the

characterization of nano-size materials. The short pulse duration will open the door to visualizing ultra-fast intra-atomic and electronic dynamics. So, the ultra-bright, ultra-short pulses will allow single photon pulse experiments to collect images at time scales faster than radiation damage. This in turn will open the possibility of studying the morphology and the structure of bio-systems unstable under X-ray radiation exposure. As the seed laser determines the duration, bandwidth, and wavelength of the output radiation, all are tunable and controllable, covering a wide spectral range. The seed laser furthermore provides a reference signal throughout the FERMI facility (including the experimental beam-lines) to facilitate the femtosecond level precision timing and synchronization of all systems. The seeded FEL driven by an external laser is therefore particularly suitable for pump-probe synchronization at time scales well below 1 ps. Pump-probe experiments are usually carried out as follows. An ultra-short light pulse (pump) excites an atom, a molecule or a condensed system, while a second pulse (probe), properly delayed in time, probes the excited sample, allowing to follow the system evolution back to the non-excited state. By using fs long pulses at VUV or soft X-ray wavelengths, it will be possible to observe the atomic motion in real time. In conclusion, applications of FERMI@Elettra FEL extend from chemical reaction dynamics to biological systems, materials and surfaces, nano-structures and superconductors. The choice of design parameters allows FERMI to generate FEL radiation with a wide range of characteristics tailored to match a diversity of experimental requirements, ranging from single shot, short (≤ 50 fs), high brilliance, time-resolved experiments to ultra-fast pump-probe experiments, to high resolution experiments with close to transform-limited radiation on the 10's of fs time scale.

The original contributions of this thesis are structured as follows. Chapter 2 is an introduction to the FERMI@Elettra layout based on the FERMI Technical Design Study [30]. Chapter 3 introduces for the Reader's convenience well-established theoretical tools which are used in the the following chapters to describe the electron beam dynamics and the 6-D emittance degradation. The validity of the theoretical models for the FERMI case study is discussed. Chapter 4 deals with the machine design from the point of view of the single particle dynamics, including the specification of the magnetic field tolerances and alignment, the optics design of diagnostic and production lattice and geometric collimation. Chapter 5 describes the impact of collective effects such as wake fields, space charge forces and emission of coherent synchrotron radiation on the electron beam dynamics. Chapter 6 is focused on the determination of the machine working point in terms of bunch length compression factor and final electron beam parameters. Finally, Chapter 7 reports about the FERMI@Elettra commissioning results that are relevant for a comparison with the theoretical and simulation studies carried out in the previous Chapters.

Chapter 2

The FERMI@Elettra Linac-based FEL

2.1 Overview

The FERMI single-pass FEL facility¹ is driven by the Elettra 3 GHz S-band linac upgraded with seven structures from CERN, following the completion of the construction of a new injector booster complex for the storage ring [31]. The accelerator and FEL complex comprises the following parts: a photo-injector generating a bright electron beam, the main linear accelerator in which the beam is time-compressed and accelerated up to 1.5 GeV, the system to transport the beam to the undulators, the undulator complex generating the FEL radiation, the photon beamlines taking the radiation from the undulator to the experimental area and the experimental area itself. After leaving the undulators, while the FEL radiation is transported to the experimental area, the electron beam is brought to a beam dump by a sequence of bending magnets. The whole infrastructure is installed about 5 m below ground level. Figure 2.1 shows a schematic plan (on scale) of the Elettra Laboratory. The circular building containing the Elettra synchrotron is visible at center. Below, the FERMI@Elettra linac, undulator hall and experimental hall infrastructure is shown (the electron beam goes from right to left). Figure 2.2 shows a sketch (not to scale) of the FERMI@Elettra accelerator, FEL and experimental beamlines complex.

The new RF photo-injector, low emittance electron source is based on the

¹This Chapter is based on the following technical note, later included in the FERMI@Elettra Conceptual Design Report: *FERMI@Elettra Accelerator technical Optimization Final Report*, ST/F-TN-06/15 (2006), by M. Cornacchia, P. Craievich, S. Di Mitri, I. Pogorelov, J. Qiang, M. Venturini, A. A. Zholents, D. Wang and R. Warnock.

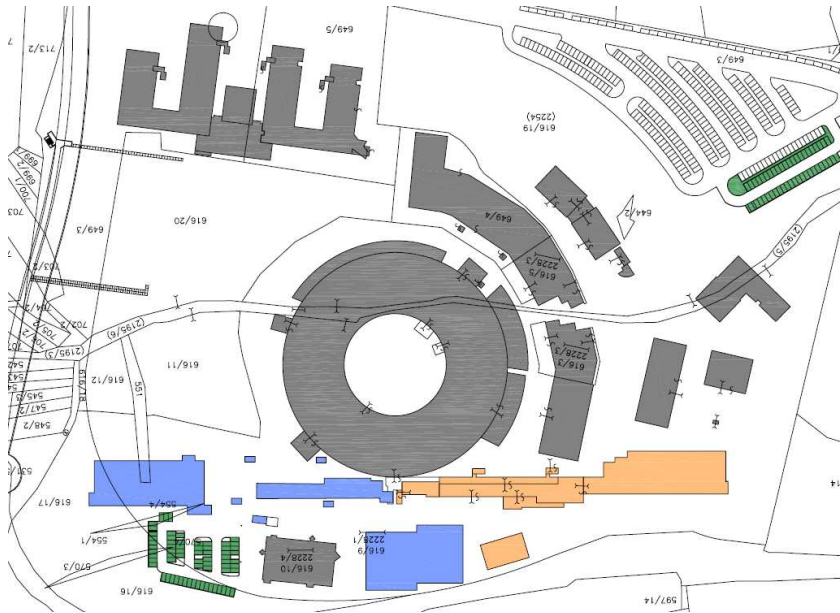


Figure 2.1: Plan of the Elettra Laboratory.

proven 1.6 cell electron gun developed at BNL/SLAC/UCLA [32]. Given the similarities between the LCLS FEL at SLAC [33] and the FERMI photo-injector requirements, this design draws heavily on the LCLS concept to produce a 5 to 10 ps long pulse with ≤ 1 nC charge and an rms normalized transverse emittance ≤ 1.0 mm mrad. The present repetition rate is 10 Hz, but the design allows for upgrading the photo-injector to 50 Hz, the maximum repetition rate of the RF systems at FERMI. Following standard layout schemes, the design includes a solenoid for emittance compensation [34, 35] and acceleration to 100 MeV with two S-band RF sections. A laser pulse provides temporal and spatial bunch shaping. The FERMI design calls for a novel temporal bunch profile in which the bunch current increases linearly with time (linear ramp) [17]. Such profile at the start of acceleration produces a more uniform energy and current profile at the entrance of the undulator. Two magnetic bunch compressors, BC1 and BC2, are at the energy of ~ 350 MeV and at ~ 600 MeV, respectively. They allow continuously tunable compression of the bunch length by a factor from 1 to ~ 50 . The nominal compression factor of 10 can be implemented with a two-stage compression or with BC1 only. The two schemes imply a different balance of the parameters characterizing the final electron beam quality, such as cur-

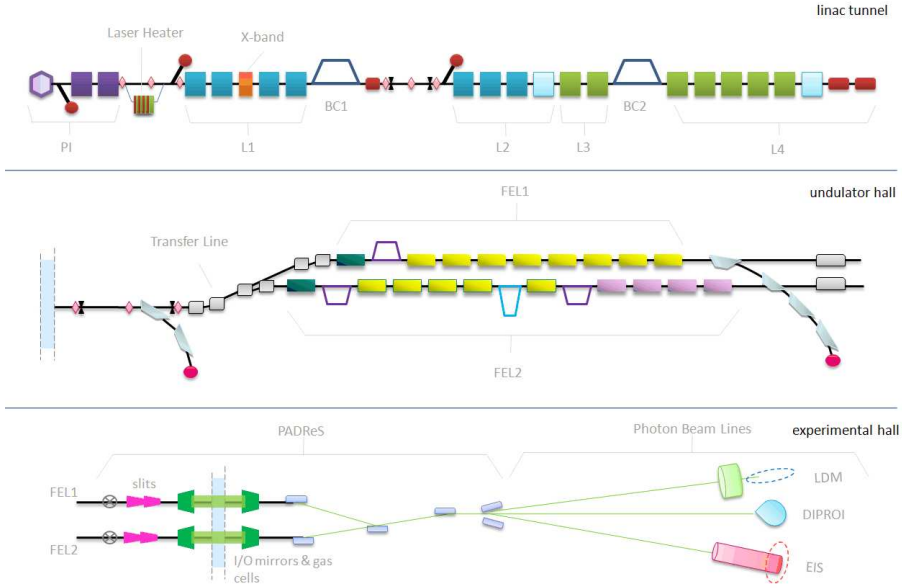


Figure 2.2: FERMI@Elettra electron and photon beam delivery system (conceptual).

rent and energy flatness, emittance and slice energy spread. Hence, they can be tuned differently, according to specific FEL requirements. The top 1.5 GeV beam energy is determined by the maximum gradient of the accelerating structures, available RF power including overhead and de-rating for reliable operations and off-crest operation for control of the energy chirp. Specific RF phase settings of the linac allow, at the same time, the correct setting of the energy chirp required for compression, the achievement of the design energy for each FEL line and the minimization of the final energy spread. Moreover, an energy range of operation is foreseen for both FEL1 and FEL2 in order to provide a wavelength tunability wider than that achieved with the undulator movable gap only. For the FEL1 Commissioning phase, only 3 accelerating structures have been installed in L2 and only 5 sections in L4 (see Figure 2.2). In spite of this, the present linac configuration ensures the nominal beam energy of 1.2 GeV at the undulator. In the near future a 4th harmonic X-band cavity is planned to be placed in the middle of L1 (see Figure 2.2) to linearize the longitudinal phase space and make the bunch compression process more efficient [36, 37]. Since the whole beam delivery system acts like a huge amplifier of energy and density modulations,

a laser heater [38] is installed at 100 MeV just after the photo-injector to provide control of the uncorrelated energy spread in the beam and minimize the potential impact of the so-called microbunching instability on the current and particle energy distribution. The uncorrelated energy spread induced by the laser heater is able to suppress the modulation in the energy and density distributions at a scale small with respect to the bunch length. A timing system [39] based on the transmission of optical signals over a highly stabilized fiber optic system will distribute timing signals throughout the facility. This provides synchronization of the photo-cathode laser to the RF gun phase, stabilized drive signals to RF systems in the facility and synchronization of the FEL seed laser with the arrival time of the electron beam. The upgraded linac plus the complex of state-of-the-art undulators allow FERMI to cover the 100-20 nm wavelength region in the first FEL1 phase and to reach down to 4 nm in a later FEL2 phase. Wavelength tunability, variable polarization and higher electron beam energies to reach even shorter output wavelengths are also in the machine delivery plan. The seeded FEL process occurs in the standard HGHG scheme for FEL1 and in a two-stage cascade for FEL2. The X-ray pulse duration is essentially determined by the seed laser duration. The photon beams from the FELs are transported in beamlines to hutches and the adjoining downstream experimental hall. Laser systems in the experimental area are synchronized to the FEL output using the stabilized optical timing system distributed around the facility.

2.2 Accelerating Structures

The accelerator uses three types of structures. Two SLAC-type structures in L0 follow the electron gun and are used for the initial acceleration and the emittance compensation scheme. A detailed description of the injector and its parameters can be found in [29]. Seven CERN-type structures (C1-C7) are divided between L1 (4 structures) and L2 (3 structures), located upstream and downstream of BC1, respectively. All these are traveling wave (TW) structures operating in the $2\pi/3$ mode. Seven Elettra-type structures (S1-S7) make up L3 (2 structures) and L4 (5 structures), located upstream and downstream of BC2, respectively. They are backward traveling wave (BTW) structures operating in the $3\pi/4$ mode. The inner geometries of the accelerating structures are different for each type of the afore-mentioned elements: the SLAC-type and the CERN-type structures are configured in TW forward wave mode with on-axis coupling and operated a relatively modest gradient of 15 MV/m. The geometry of the Elettra-type structures corresponds to a nose-cone type structure with magnetic coupling; these operate in BTW mode and at high gradient, up to 25 MV/m. The magnetic coupling in the BTW structures allows them to provide a higher

accelerating gradient than the others. Unfortunately, the smaller iris radius of 5 mm, instead of that of 9 mm in the TW structures, leads to a higher impedance that induces a bigger electron beam energy loss and emittance dilution. The BTW structures are powered by an RF pulse compression system of the SLED type. The same type of klystron, without SLED configuration, simultaneously supplies two structures of the others. Table 2.1 summarizes the operational parameters of the linac structures. The first value of two in the same cell refers to the nominal operation for both FEL1 and FEL2; the second value in parenthesis refers to the configuration for FEL1 commissioning. In this case, the additional X-band structure is not taken into account. Notice that the final energy computed in the Table overestimates the real one by approximately 10 MeV because of the energy loss induced by the linac geometric impedance.

Table 2.1: Linac energy budget for on-crest and off-crest acceleration.

Type of structure	Max. gain per structure [MeV]	Qt.	Place	Tot. energy on-crest [MeV]	RF phase off-crest [deg, S-band]	Tot. energy off-crest [MeV]
Gun		1	Gun	5	0	5
Injector (TW)	47.5	2	L0	95	0	95
CERN (TW)	60	7	L1, L2	420	-27.5 (-25), -20 (0)	387 (399)
Elettra (BTW)	140 (102)	7	L3, L4	980 (714)	0, 0	980 (716)
X-band	24 (0)	1	L1	24 (0)	180	-20 (0)
<i>Total w/o X-band</i>		17		1500 (1234)		1467 (1213)
<i>Total with X-band</i>		18		1524 (1234)		1447 (1213)

2.3 Magnetic Lattice

The magnetic lattice of the FERMI@Elettra beam delivery system has been designed in a way that it minimizes the emittance degradation and, at the same time, allows relaxed magnetic specifications. The values of the Twiss parameters at specific locations of the lattice are constrained by the optimization of diagnostics performance, the efficiency of the collimation process and the beam matching to the downstream lattice. In particular, the FERMI linac focusing system is designed to minimize the transverse emittance dilution due to transverse wake fields, momentum dispersion and coherent emission of synchrotron radiation in bends. Figure 2.3 shows the optics of the FERMI@Elettra electron beam delivery system for FEL1 (neither X-band cavity, nor BC2 are included).

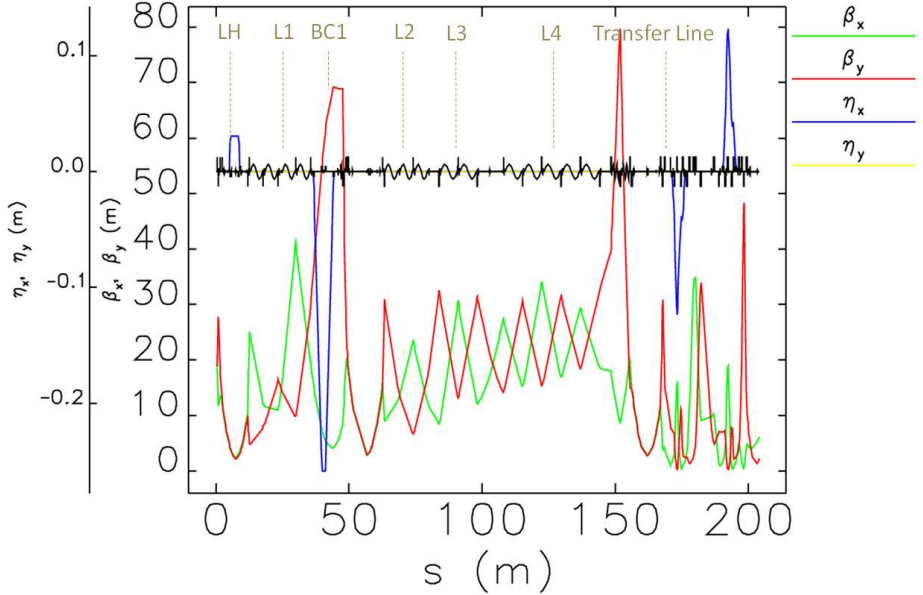


Figure 2.3: Optics of the FERMI@Elettra electron beam delivery system for FEL1. The black line sketches the machine layout. Labels for different machine areas are on the top.

A 0.8 m long drift section is foreseen after each accelerating structure to provide focusing and trajectory control. It includes one quadrupole magnet with bipolar power supply with normalized integrated gradient $kl \leq 0.14 \text{ m}^{-1}$ and one combined corrector magnet with maximum kick angle of $\sim 1.0 \text{ mrad}$ for trajectory correction in the horizontal and vertical plane. The average betatron function along the main linac is approximately 20 m. The positioning of correctors and Beam Position Monitors (BPMs) was chosen to optimize the trajectory steering for one-to-one (any corrector forces the trajectory to zero at the succeeding BPM) as well as global correction (based on inversion of the trajectory response matrix). A sole chicane design, mechanical and magnetic, for BC1 and BC2 has been developed in house at the Elettra Laboratory, inspired by the LCLS [33] and LEUTL [40] movable chicane design. The 8.0 m long symmetric chicane of FERMI is shown in Figure 2.4. It includes 4 identical bending magnets all powered by one power supply, 2 identical quadrupole magnets in the lateral arms and 4 independently powered trim coils, each of them associated with one bending magnet. These are intended for a fine tuning of the disper-

sion bump by compensating the field-to-current calibration errors in the dipole fields. The trim coils act in the horizontal plane only and can be used as weak trajectory correctors as well. Some electron beam diagnostics is in between the two inner bending magnets: one horizontal scraper, one BPM and one screen. As in the LCLS design, during the set up of the required bending angle, the outer dipoles stay fixed, the lateral arms rotate and the central drift and dipole magnets translate in the horizontal plane to allow a continuously tunable bending angle. Accordingly, the beam is always at the center of the vacuum chamber, for the nominal energy and any angle in the range 0–0.122 rad. Some important upgrades were carried out to the original LCLS design to improve the magnetic field quality of the dipole magnets and to ensure a very precise and reliable mechanical movement of the chicane in the bending plane. The dipole field homogeneity has been measured to the 10^{-5} level (limited by the measurement resolution). The mechanical movement is directed by a linear encoder with 50 μm relative accuracy and sub-micron reproducibility.

Two transfer lines, one assigned to FEL1 and the other to FEL2, transport the electron beam from the linac end to the undulator. This system, called “Spreader”, starts with an achromat that is common to the two lines; it is made of two 3 degree dipole magnets that deflect the beam away from the linac axis (see Figure 2.2). In the line that leads to the FEL2 undulator, an identical achromat with dipoles of opposite polarity brings the beam back parallel to the linac at a distance from it of 1 m. When operating the FEL1 line, one of the aforementioned dipoles is switched off and the beam proceeds to another achromat that again bends the beam parallel to the linac and displaced from it by 3 m. The two undulator lines are thus parallel and separated by 2 m. In this way, all beam lines in the Experimental Hall have the possibility of receiving the output light from FEL1 and FEL2, also thanks to a proper layout of switching mirrors located at the end of the Undulator Hall. The compactness of the Spreader line, only 20 m long for FEL2 and 30 m long for FEL1, forces to adopt relatively strong quadrupole focusing with integrated strength $kl \leq 1.52 \text{ m}^{-1}$. The optics was designed to cancel any emittance blow up due to the emission of coherent synchrotron radiation in the bends by a suitable choice of the small bending angles and 180° betatron phase advance between the dipoles. Four quadrupoles at the end of each Spreader branch line ensure the optics matching to the downstream undulator lattice.

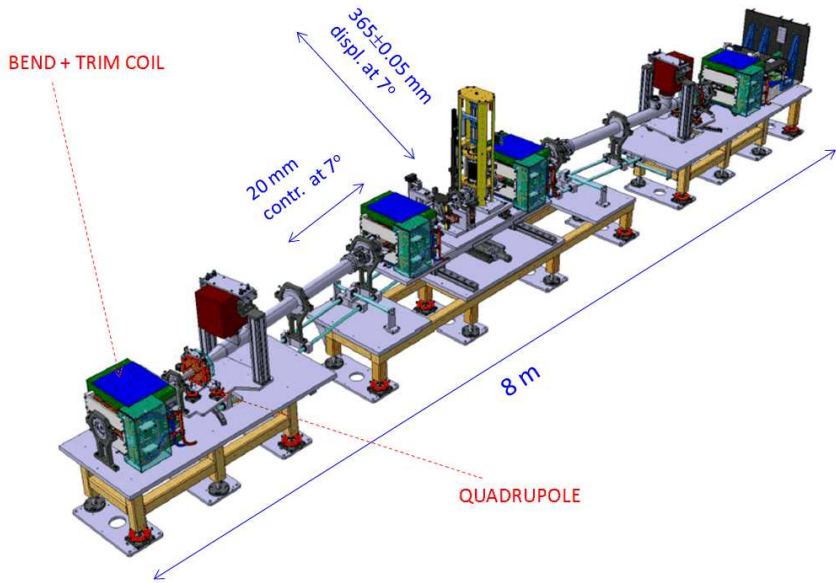


Figure 2.4: FERMI@Elettra movable magnetic chicane for bunch length compression. Drawing courtesy of D. La Civita.

2.4 High Gain Harmonic Generation Free Electron Laser

FERMI@Elettra FEL is based on the harmonic up-shifting of an initial seed signal in a single-pass FEL amplifier employing multiple undulators. The basic principles which underlie this approach are: the energy modulation of the electron beam via the resonant interaction with an external seed laser in a first undulator, called “modulator”; the use of a dispersive section to then develop a strong density modulation with large harmonic overtones and the production of coherent radiation by the microbunched beam in a downstream undulator, called “radiator”. The radiator is tuned at a harmonic of the seed laser wavelength.

The first stage of the project, FEL1, generates coherent output radiation in the 20-100 nm spectral range. For these wavelengths, users require short (<100 fs) pulses with adjustable polarization and high temporal and spatial reproducibility. FEL1 relies upon a single-stage, HGHG scheme (i.e., modulator-dispersive

section-radiator). The second stage, FEL2, extends the spectral range to 4 nm. For FEL2, a two-stage harmonic cascade is needed to reach short wavelengths. The selected configuration is based on the so-called “fresh bunch” approach [41], in which the output from the first radiator modulates the energy (in a subsequent modulator) of a part of the electron beam that did not interact with the external seed. Both the FEL1 and FEL2 undulator layout is shown in Figure 2.2. If a seed laser source using harmonic generation in gas would become available at ~ 20 nm, FEL2 could be operated with a single up-shift in frequency as FEL1 thus eliminating the double harmonic cascade. Design choices for FEL2 do not preclude this attractive possibility. In the following, each element of the FEL1 and FEL2 scheme are discussed in turn.

An external laser provides an initial, wavelength-tunable seed signal. This signal, in conjunction with the magnetic field generated by the modulator, produces a relatively strong energy modulation $\Delta\delta$ (δ is here the relative energy deviation) of the beam electrons at the seed wavelength via resonant interaction. Figure 2.5 shows the energy modulation induced in the modulator. Following

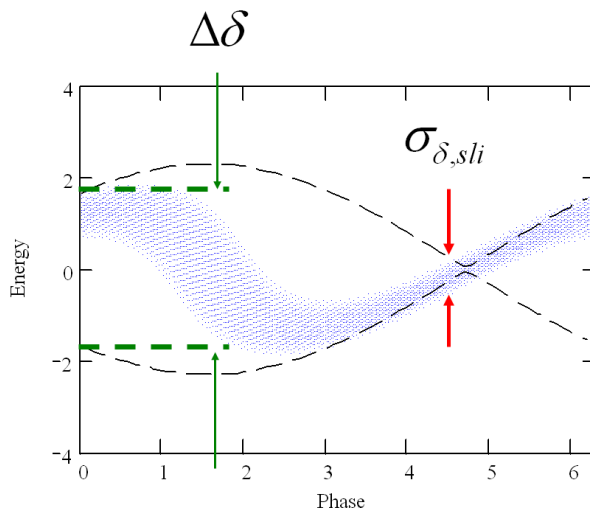


Figure 2.5: Energy modulation induced by the external seeding laser in the modulator of FEL1. The energy modulation amplitude $\Delta\delta$ induced by the seeding laser and the slice energy spread $\sigma_{\delta,slī}$ are indicated by arrows. The dotted lines enclosing the electron bunch are the separatrices that define the region of stable, periodic particle motion in the longitudinal phase space. Figure courtesy of G. De Ninno.

its exit from the modulator, the electron beam then passes through a dispersive section in which a density modulation develops from path length differences associated with the energy modulation. As long as $\Delta\delta \gg \sigma_{\delta,s}$, where $\sigma_{\delta,s}$ is the relative initial slice energy spread, a strong periodic density modulation is created at the wavelength λ_0 of the seed laser, containing large higher harmonic components, up to the harmonic number $m \sim \Delta\delta/\sigma_{\delta,s}$. At this point the electron beam enters the radiator, whose wavelength and magnetic strength are tuned such that the FEL resonance occurs at an integer harmonic m of the original seed laser wavelength. For FERMI, m varies between 3 and 6 for the first radiator. If, as in FEL1, this radiator is the final undulator, it generally is made sufficiently long for the FEL radiation to grow to saturation (or even longer via tapering if greater output power is sought).

In the FEL2 fresh bunch approach, the duration of the electron bunch is at least two times longer than the duration of the seed laser pulse. In this case radiation from the first radiator is used to energy-modulate part of the electron beam in a subsequent modulator; the first radiator is made only long enough that the radiation is sufficient to produce adequate downstream energy modulation. The emitted radiation is effectively coherent spontaneous emission, whose power scales as the square of the product of the current and the longitudinal distance inside the undulator (ignoring diffraction and debunching effects). Following the first radiator is a section (essentially a chicane) that temporally delays the electron beam in order to make the output radiation temporally coincident with a “fresh” section of the electron beam closer to the beam head. This fresh section of the bunch has not had its slice energy spread increased via FEL interaction in the first stage. Thus, it can be far more easily energy- and density-modulated in the second stage undulator than the “used” electron beam section that interacted with the seed laser pulse in the first modulator and radiator. The second stage for the fresh bunch approach consists of a modulator, a final radiator, and, in general, an intervening dispersive section. The modulator uses the radiation from the first stage radiator as its seed radiation; it must therefore have its undulator period and magnetic strength tuned to be resonant at that same wavelength. The harmonic up-shift factor between the second stage modulator and radiator is 4 or less for the FERMI case. The second stage radiator is usually much longer than that of the first stage both because the initial bunching is normally smaller and because the FEL is normally run to saturation. The process of light emission in the final radiator includes at first a quadratic (as in the first stage) and then an exponential growth regime.

For the first modulator in FEL1 and FEL2, which must satisfy FEL resonance over a nominal wavelength range of 240 to 360 nm, the undulator wavelength selected, λ_u , is 100 mm for 30 periods. For the second stage modulator of FEL2, the adopted wavelength is 55 mm for 42 periods, matching that of the first stage

radiator. The choice of λ_u for the radiators is driven by two principal requirements: 1) the FEL resonance be physically possible at the longest wavelength (i.e., 100 nm for FEL1 and 20 nm for FEL2) for beam energies of 1.2 GeV; 2) there be sufficient gain (i.e., $K \geq 1$, K being the normalized rms undulator magnetic strength) at the shortest desired output wavelength. FEL1 and FEL2 are required to provide, at all wavelengths, continuously tunable beam polarization ranging from linear-horizontal via circular to linear-vertical. The FEL1 radiator and the final radiator in FEL2 have therefore been chosen to be of the APPLE-II [42], pure permanent magnets type. For the modulator a simple, linearly-polarized configuration is best, due to both its simplicity and because the input radiation seed can be linearly polarized. Wavelength tuning will be done by changing the undulator gap (and thus K) rather than by changing the electron beam energy. As the coupling between the radiation and the electron beam can depend strongly on the beam radius, the FERMI design includes external quadrupole focusing to produce an average value of 10 m for the betatron function in each plane. The FEL1 and FEL2 radiators consist of 6 and 8 undulator magnets. The magnetic length of the individual magnets is 2.3 m. The number of periods is 42 in the FEL1 and first four FEL2 radiator segments ($\lambda_u = 55$ mm) and 66 in the last four FEL2 radiator segments ($\lambda_u = 35$ mm). Electromagnetic quadrupoles, high resolution beam position monitors, and quadrupole movers are installed in between two consecutive undulator segments.

After leaving the undulators, the electron beam, carrying an average power of 75 W at 50 Hz, is dumped into a shielding block by a sequence of bending magnets, while the FEL radiation is transported to the experimental areas. Pulse length preservation, monochromatization, energy resolution, source shift compensation, focusing into the experimental chamber and beam splitting are all included in the design of the FEL radiation transport system. It is designed to handle the high power of up to 10 GW in a sub-ps long pulse. Its differentially pumped vacuum system is windowless, the low-Z material beam line components operate at grazing incidence angles and the radiation intensity is controlled by a gas absorption cell.

2.5 Electron Beam Requirements

FEL1 and FEL2 output performance require a high electron beam quality at the entrance of the undulator and also set tight tolerances on the shot-to-shot reproducibility of the beam delivery system. The baseline FEL output specifications for FEL1 and FEL2 and the corresponding main electron beam parameters are listed in Table 2.2. Present scientific proposals involve time-domain experiments such as pump-probe interactions, nonlinear phenomena, elastic and inelastic

scattering. Consequently, the requirements are related to the total photon number per pulse (i.e., $0.42 \cdot 10^{14}$), pulse duration (20–100 fs) and spectral bandwidth.

Depending on the experiments, an electron bunch final peak current of 500 A or higher shall be provided. Including the inevitable inefficiency of the compression system, the maximum obtainable peak current is 800 A with 0.8 nC of charge from the photo-injector. Because in multi-stage operation the first stage radiation output power scales quadratically with the bunch current, the final output power also drops sharply as the bunch current is lowered below design. Should one rely upon strong exponential gain in the final radiator, the output power would also be very sensitive to the beam current. A critical parameter affecting the required electron beam duration is the arrival time jitter of the beam relative to that of the seed laser. The expected rms arrival time jitter from the accelerator with respect to the seeding laser is 150 fs [29]. In order to ensure sufficient overlap between the seed and the electrons, the duration of the electron bunch must be at least as long as 600 fs for 100 fs long seed pulses. The correlations of the energy and charge distributions with the distance along the electron bunch should be as small as possible in order not to broaden the FEL bandwidth. The design values of energy and peak current variations along the usable part of the bunch are specified to be less than $2 \cdot 10^{-4}$ and 100 A respectively. A multi-stage harmonic cascade is very sensitive to slice energy spread because of the very nonlinear process leading to harmonic micro-bunching at the seed frequency. A very sharp limit in fact exists on the tolerable electron beam slice energy spread that aims a value of $\sigma_{E,s} \leq 200$ keV for FEL1 and ≤ 150 keV for FEL2.

The electron beam optics and the photon beam brightness are affected by the electron beam projected emittance, that therefore should be made as small as possible. However, even in the case of a factor of 2 worse emittance, the optics along the undulator is generally recoverable since the beam size would only be increased by a factor $\sqrt{2}$ for the same average betatron function. Moreover, as the seeding laser pulse is much shorter than the bunch length, the output photon brightness depends on the slice emittance. In fact, the FEL saturation length is only affected by the slice emittance, which is the high priority parameter to be minimized. The horizontal and vertical, normalized slice emittances at the end of the FERMI linac should not exceed 1.5 mm mrad for FEL1 and 1.0 mm mrad for FEL2 to meet the desired photon output. This value, at least $\sim 20\%$ higher than predicted by photo-injector simulations, includes a safety margin against emittance dilution effects. As an emittance of 1.0 mm mrad is demanded at the shortest output wavelength, the accelerator performance is designed to satisfy this most stringent requirement. The specification could be relaxed during longer wavelength operation.

Albeit a complete jitter study is not in the outline of this thesis, we want to

point out that shot-to-shot repeatability is an important parameter associated with time domain experiments. Ideally, for nonlinear phenomena experiments, the shot-to-shot rms jitter in normalized photon number should be 5% or less. Such a low value seems unlikely with the presently expected accelerator and injector parameters. A large class of FEL1 experiments can tolerate values as high as 25% by recording the shot-by-shot photon number for post-processing. Although the total photon jitter is not critical for most experiments in the frequency domain, shot-to-shot central wavelength jitter during narrow bandwidth operation may be of concern unless the bandwidth can be maintained at or below the required spectral resolution. So, in the operation the wavelength jitter should be less than the individual shot bandwidth in order to not increase the effective time-averaged, output bandwidth as seen by the user. For both FEL1 and FEL2, calculations based on time-steady input parameters and full start-to-end time-dependent simulations were performed using the 3-D numerical codes Genesis [43] and Ginger [44]. They predict a satisfactory shot-to-shot output stability for most of the planned experiments on both FEL1 and FEL2 if the following specifications for the electron beam stability are ensured at the entrance of the undulator: emittance jitter $\Delta\epsilon/\epsilon \leq 10\%$, peak current jitter $\Delta I/I \leq 8\%$, slice energy spread jitter $\Delta\sigma_{\delta,s}/\sigma_{\delta,s} \leq 10\%$, mean energy jitter $\Delta E/E \leq 0.1\%$.

Table 2.2: Main electron and photon beam parameters of FERMI FEL1 and FEL2.

	FEL1 Commissioning	FEL1 Operation	FEL2 Operation	Units
Electron Beam Parameters				
Energy	1.2	0.9–1.2	1.2–1.5	GeV
Charge	0.35	≤ 0.80	0.80	nC
Slice Norm. Emittance (rms)	≤ 1.5	1.5	1.0	mm mrad
Slice Energy Spread (rms)	≤ 0.10	≤ 0.20	≤ 0.15	MeV
Total Energy Spread (rms)	≤ 0.1	≤ 0.1	≤ 0.1	%
Peak Current (flat region)	200–400	≥ 500	800	A
Bunch Duration (fwhm)	0.7–1.3	0.7	0.7	ps
Energy Jitter (rms)	≤ 0.1	≤ 0.1	≤ 0.1	%
Arrival time jitter (rms)	≤ 200	≤ 150	≤ 150	fs
Photon Beam Parameters				
Output Wavelength Range	40–60	20–100	4–20	nm
Output Pulse Duration (rms)	≤ 150	≤ 50	≤ 50	fs
Bandwidth (rms)	20–40	17 (at 40nm)	5 (at 10nm)	meV
Polarization	Variable	Variable	Variable	
Peak Power	≥ 0.1	1–5	≥ 0.3	GW
Photons per Pulse	$\geq 10^{12}$	$\geq 10^{13}$	$\geq 10^{12}$	in 1meV bw
Peak Power Stability	≤ 50	≤ 30	≤ 50	%
Transverse Stability (rms)	≤ 50	≤ 50	≤ 50	μm
Repetition Rate	10	50	50	Hz

2.6 Conclusions

The main parameters and layout of the FERMI@Elettra single-pass FEL have been introduced. The first stage of the project, FEL1, is based on the one-stage High Gain Harmonic Generation (HG) scheme that allows the 1.2 GeV electron beam to emit at the FEL fundamental wavelength of 20 nm. FEL1 is presently being commissioned and is nearly fully realized. The second stage of the project, FEL2, implements the two-stage HG scheme in the version of the so-called fresh bunch technique. In this way, the 1.5 GeV electron beam could emit at the fundamental wavelength of 4 nm. Commissioning of FEL2 is going to start at the end of 2011. Due to the relatively low energy of the electron beam, the harmonic up-shifting of an initial seed signal is an obliged choice for FERMI in order to reach the FEL fundamental emission at such short wavelengths. At the same time, the seeding interaction puts a tight constraint on the maximum slice energy spread of the electron beam at the undulator entrance that is approximately 150 keV (rms value), only a factor of 5 bigger than the minimum theoretical uncorrelated energy spread expected after bunch length compression. Peak power saturation at the fundamental wavelength is ensured by the several hundred's Ampere electron beam with a normalized slice emittance equal or smaller than 1 mm mrad. To provide such high brightness electron beam, the S-band, normal conducting Elettra linac has been upgraded with other 7 accelerating structures from CERN. Only the Elettra structures should be able to provide the remarkable accelerating gradient of 25 MV/m, instead of 15 MV/m in the others, by virtue of the SLED system for RF pulse length compression. Unfortunately, the BTW structures have irises with inner radius of only 5 mm, instead of the 9 mm in the TW structures. Such a small radius excite strong longitudinal and transverse wake fields that have to be carefully considered in the machine design and study of the electron beam dynamics. A movable, achromatic, four dipole magnetic chicane has been designed to manage the magnetic bunch length compression. Two of these chicanes, BC1 and BC2, are integrated in the linac magnetic lattice. A 30 m long transfer line brings the high energy electron beam to the parallel undulator lines of FEL1 and FEL2. The electron beam is finally dumped in the horizontal plane, while the emitted photons are transmitted to the downstream photon beam lines for experiments.

Chapter 3

Theoretical Tools for Machine Design

This Chapter¹ contains the theoretical basis used to describe the single particle and electron beam collective dynamics in a single-pass linac. In spite of the general validity of the theoretical models, their applicability to the FERMI case study is discussed. First, Liouville's theorem of phase space volume conservation is recalled to illustrate the goal of an ideal machine design that is the full preservation of the electron beam 6-D emittance. Then, perturbations of the beam dynamics that invalidate the theorem are considered. The single particle transverse dynamics includes the issue of optics matching, magnetic field errors and chromatic aberrations. The principle of linear and nonlinear bunch length compression is discussed for the longitudinal dynamics. The collective effects refer to the short-range space charge forces, short-range structural (also called geometric) wake fields in the linac and microbunching instability developing first in the linac – as the resultant perturbative interaction of coherent synchrotron radiation emission in bends, longitudinal space charge force in the linac and dispersive motion in the magnetic compressor – and then in the FEL.

¹This Chapter recalls well known theory of accelerator physics. The references are highlighted in the text.

3.1 Particle Motion in the Phase Space

3.1.1 Liouville's Theorem: Limit of Applicability

Particle motion in an optoelectronic transport system is called laminar if it assumes a point emitter and optics elements free of aberrations, which implies the system is perfectly linear and non-dispersive. Since these conditions cannot be satisfied in reality (a particle beam has finite extensions and velocity spread, the optical line has some residual aberrations), the concepts of beam emittance and brightness have been introduced. The former describes the spread in the configuration (x, y, z) and velocity (v_x, v_y, v_z) space of the beam population with respect to an arbitrary defined reference particle (usually this is the beam center of mass or center of charge); the latter defines the time averaged or peak transverse particle density. Formally, the definitions of emittance and brightness imply physical quantities that are related to the single-particle motion satisfying the linear approximation of the second-order paraxial ray equation [45]. This describes the particle trajectory in the configuration space for small deviations from the optical axis and only linear variations of electric and magnetic fields around it. This formalism is the basis for the corpuscular optics and very suitable for studying laminar beams. Since beam emittance and brightness involve by definition a whole ensemble of particles, a paraxial envelope equation has also been associated with the single-particle ray equation: provided that the emittance is invariant (a constant of the motion), the envelope equation describes the behaviour of a "perfect", nonlaminar beam.

The paraxial formalism becomes inadequate when we try to follow the evolution of an intense beam with appreciable spatial dimensions in a complicated transport system. In this case, the optical line design and optimization study has to prevent deterioration of the injected beam quality. This problem is considerably simplified by the use of the Hamiltonian formalism, which governs the trajectories of points representing particles in phase space. The concepts of emittance and brightness were then introduced in terms of invariants that result from Liouville's theorem [46]. Complementary definitions of rms, projection and section emittance were firstly given by Lapostolle [47], the latter ones being recently translated into the more common notations of projected and slice emittance, respectively.

The Hamiltonian – or canonical – equations of motion of a N -particle ensemble with k degrees of freedom consist of a set of $2k$ first-order differential equations:

$$\begin{aligned}dq_i/dt &= \partial H/\partial p_i \\ dp_i/dt &= -\partial H/\partial q_i\end{aligned}\tag{3.1}$$

that involves a set of $2k$ generalized coordinates defining the phase space (q_i, p_i) ,

with $i = 1, \dots, N$, and the total energy Hamiltonian function H . The more probable configurations of the ensemble of particles are represented by higher values of a probability function also known as the phase space density function, f_{6N} . For N identical and non-interacting particles in the 3-D configuration space and with 6 degrees of freedom, the single-particle Hamiltonian depends only on the 6 pseudo-canonical coordinates $(x, x', y, y', z, \delta)$. Here the angular divergences x', y' are defined as the ratio of the transverse over the longitudinal momentum, $x' = p_x/p_z$, $y' = p_y/p_z$. The relative energy or momentum deviation $\delta = \Delta p_z/p_z$ is also introduced.

We summarize without proof [45] the main properties of the trajectories associated with the coordinates (q_1, p_1) and independent of the 4 others.

- The trajectories in the 2-D phase space (q_1, p_1) , Γ_2 , depend uniquely on the initial values (q_0, p_0) and the time. Thus, at a given instant of time the trajectories corresponding to different initial pairs nowhere intersect. As a consequence, if H is explicitly independent of time – it is an invariant of the motion – the trajectories in Γ_2 are independent of time and cannot intersect. In the case of an oscillatory system, the curves of constant H are closed and do not intersect.
- A boundary that encloses a group of particles at time t_1 will transform into another boundary at time t_2 enclosing the same group of particles.
- Under linear transformation of the particle coordinates – linear transfer map describing the optical system – the topology of the curves in phase space is preserved. For Hamiltonian systems, the area of an ellipse is conserved, although the eccentricity changes with time, since the determinant of the transfer matrix is equal to unity for non-dissipative equations of motion.

The last statement is, in fact, a special case of Liouville's theorem that corresponds to the continuity equation for the phase space density function f :

$$\frac{df}{dt} = \frac{\partial f}{\partial t} + \sum_i^k \left(\frac{\partial f}{\partial q_i} \dot{q}_i + \frac{\partial f}{\partial p_i} \dot{p}_i \right) = 0 \quad (3.2)$$

Eq.3.2 states that for Hamiltonian systems, the density of the representative points – or particles – in the appropriate phase space is invariant along the trajectory at any given point. The theorem can also be expressed in terms of the invariance of the phase space hypervolume enclosing a chosen group of particles as they move in phase space, if the number of particles in the volume does not change with time: the fictitious gas of points thus behaves as an incompressible fluid. So, if we define $\vec{w} = (\dot{q}, \dot{p})$ and $d\vec{f}$ is the vector of the surface element

enclosing the hypervolume $V(t)$, then at the time $t + \Delta t$ the particles will be occupying another volume $V(t + \Delta t)$, as shown in Figure 3.1. Following [48], we show that the initial and the last volumes are the same that is the volume is preserved by the Hamiltonian flow:

$$\frac{dV(t)}{dt} = \int \vec{w} \cdot d\vec{f} = \int \nabla \cdot \vec{w} dv = \int \left(\frac{\partial \dot{q}}{\partial q} + \frac{\partial \dot{p}}{\partial p} \right) dv = \int \left(\frac{\partial^2 H}{\partial q \partial p} + \frac{\partial^2 H}{\partial p \partial q} \right) dv = 0 \quad (3.3)$$

The shape of the domain boundary in phase space may be considerably deformed, for example, under the effect of nonlinear forces, but the volume enclosed remains constant. This volume is the emittance of the particle ensemble.

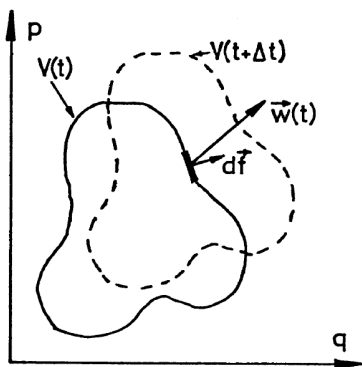


Figure 3.1: Area-preserving map in the canonical phase space [48].

In its more general sense, Liouville's theorem applies to Hamiltonian systems in which the forces can be derived from a potential $\phi(\vec{q}, t)$ that may be time dependent, but must not depend on the particles' momentum. This is shown by assuming non-Hamiltonian forces denoted by Q_i , so that in the associated generalized phase space the Liouville invariance condition, eq.3.2, becomes:

$$\frac{df}{dt} = -f \sum_1^k \frac{\partial Q_i}{\partial p_i} \quad (3.4)$$

Eq.3.4 gives the rate of change of phase space density under the action of non-Hamiltonian forces. The phase space density may be preserved, provided that the non-Hamiltonian forces are not dependent on the momenta. Thus, the following phenomena limit the applicability of the Liouville's theorem to particles motion in an accelerator: collisions, wave mechanical effects, space charge forces

– intended as short-range inter-particle Coulomb interactions –, wake fields, electromagnetic radiation emission and absorption. One of the main purposes of the machine design and optimization study carried out for FERMI@Elettra was that of preserving the initial 6-D volume – or density, for a constant number of particles – along the entire electron beam delivery system. Almost all the afore-mentioned effects have been analytically evaluated and simulated in order to predict not only the volume distortion, but also its blow up due to frictional forces, as depicted in the following.

- ii) Dipole and quadrupole magnets field errors, misalignment and vibration leads to specifications for the machine static alignment and stability, as discussed in Section 4.1.
- i) The effect of the geometric collimation on the transverse particle distribution is evaluated and discussed in Section 4.2.
- iii) The particle motion in the presence of short-range space charge (SC) forces² along the FERMI linac is investigated in Section 5.1.
- iv) The geometric longitudinal wake field in the accelerating structures dilutes the longitudinal phase space of the beam by introducing linear and nonlinear correlations. The wake field induced energy chirp requires a suitable arrangement of the linac RF phases in order to minimize the final energy spread, to recover the nominal energy and to ensure an efficient bunch length compression. The electron beam dynamics in the presence of longitudinal wake field in the FERMI@Elettra linac is discussed in Section 5.2.
- v) The geometric transverse wake field in the accelerating structures dilutes the transverse phase space of the beam by introducing linear and nonlinear correlations between the longitudinal coordinate z inside the bunch and the transverse phase space. The wake field induced transverse emittance dilution can be compensated by canceling the transverse wake field kick with a proper trajectory correction along the entire linac, as shown in Section 5.3.

²In general, Liouville's theorem still applies in the 6-D phase space in the limit of very small correlations established by the space charge forces between particles, so that each particle moves in the same way than all the others, in the collective (also named "mean") field generated by all the others. Quantitatively, this situation is satisfied if the number of particles in the Debye sphere surrounding any particle is large, that is $\lambda_D \gg n^{-1/3}$, where n is the density of charged particles in the configuration space and λ_D is the Debye length that is the ratio of the thermal velocity, $(KT/m)^{1/2}$, to the plasma frequency $\omega_p = (q^2 n / m \epsilon_0)^{1/2}$, q and m being the particle charge and mass. Then, a smoothed out potential due to all particles may be calculated from the density distribution in the configuration space and its contribution included in the Hamiltonian system of forces appearing in Liouville's equation 3.2. This procedure leads to the derivation of the Maxwell-Vlasov equation, which self-consistently describes the behaviour of an assembly of charged particles.

- vi) Coherent Synchrotron Radiation (CSR) emission implies a careful design of the dispersive systems used for magnetic bunch length compression and beam transport. A detailed study of the CSR instability for FERMI@Elettra is carried out in Section 5.4.
- vi) Longitudinal Space Charge (LSC) field inside a high charge density beam induces broad bandwidth energy modulations that corrupt the flatness of the beam longitudinal phase space. Moreover, energy modulations are converted into density modulations when the beam passes through dispersive sections of the lattice. The amplification of such conversion along the accelerator is called microbunching instability and its development in FERMI@Elettra is discussed in Section 5.5.
- vii) Alternative schemes of magnetic compression that suppress the microbunching instability and improve the electron beam quality are discussed in Chapter 6.

3.1.2 Beam Emittance

The FEL demands full preservation of the 6-D electron beam emittance as at the injector level. The emittance conservation law is stated in Liouville's theorem. Provided that the Liouville's theorem is (approximately) valid for the case of interest, it can be applied considering any special features of the system such as symmetry and possible interdependence between the degrees of freedom. For each 4-D phase space, Γ_4 , one may, for example, consider the motion of the N particles of the whole system whatever the coordinates associated with the two other components. Hence, the domain in Γ_2 appears as the "projection" of the hypervolume occupied in Γ_6 onto the particular 2-D plane:

$$f_2(q_1, p_1) = \int \int \int \int f_6(q_1, p_1, q_2, p_2, q_3, p_3) dq_2 - dq_3 dp_2 - dp_3 \quad (3.5)$$

$$Area(\Gamma_2) = \int \int_{all\ N\ points} dq_1 dp_1$$

Alternatively, one may consider the behaviour of a limited fraction of the particles cloud – for example, particles satisfying conditions imposed on the coordinates of the other two degrees of freedom. Particular "sections" through Γ_6 are then obtained. If the degrees of freedom are not coupled, Liouville invariance applies both to projection and section phase space domains. These domains do not, however, refer to the same number of particles and, in general, their extent and density in phase space are different.

Figure 3.2, left plot, conceptually illustrates eqs.3.5 applied to the 3-D real space, in which for simplicity of representation a spherical volume is initially

considered. A particle density function f_3 is defined in the volume. By integrating f_3 along the z -coordinate, the projected area in the (x, y) plane is obtained, characterized by the 2-D density function f_2 . A further integration along the y -coordinate projects the initial f_3 onto the f_1 density function, which describes the particle distribution along the segment extending in the x -direction, irrespective of the other two coordinates y and z . We now assume that each particle contained in the initial volume has an additional velocity vector (v_x, v_y, v_z) . The definition of the initial density function f_3 is therefore extended to the 6-D f_6 . The integration of f_6 over all coordinates behaves exactly in the same way than f_3 . So, f_2 is obtained that describes the distribution of particle position and velocity along the horizontal segment shown in Figure 3.2, left plot. The 2-D area occupied by the ensemble of particles in the phase space (x, v_x) is called horizontal projected emittance. Identical definitions apply to the other planes, by integrating f_6 along different axes.

The same procedure can be repeated but now restricted to a small longitudinal portion of the volume, for example denoted by the longitudinal coordinates z and $z + \Delta z$, as sketched in Figure 3.2, right plot. Typically, Δz is chosen to be much smaller than total length of the volume. The horizontal emittance can still be computed as a projection of the initial 6-D emittance onto the plane (x, v_x) . But, since only the particles inside the small portion of the volume of length Δz are considered, the projected area is now called horizontal slice emittance. Identical definition applies to the other planes, by projecting the 6-D emittance onto different axes and selecting portions of the volume along different directions.

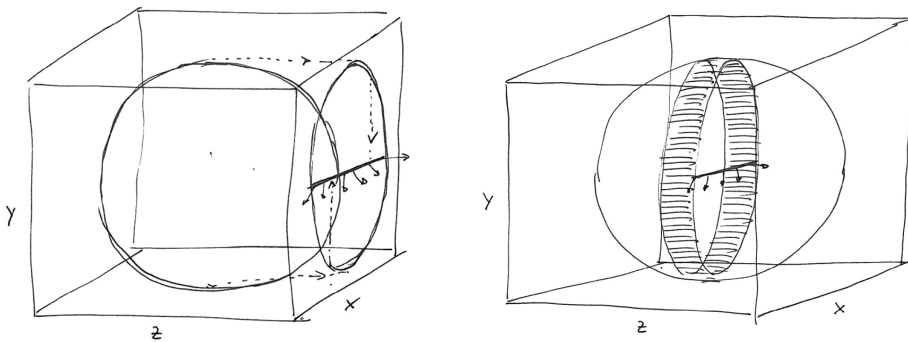


Figure 3.2: Conceptual illustration of projected (left) and slice (right) phase space area in 3-D.

In the case the electron beam dynamics in a linac for a FEL, the slice notation usually refers to the longitudinal coordinate (time duration or bunch length) in-

side the particle cloud. For this reason, the transverse slice emittance could be preserved along the transport system, for each bunch slice, but the slices misalignment or mismatch in the transverse phase space – each slice centroid is following a different trajectory or each slice has a different emittance from another – can effectively lead to a projected emittance growth. On one hand, the preservation of the slice emittance as the injector level is important because it ensures an efficient FEL power amplification. On the other hand, time arrival jitter between the electron beam and the external seed laser for HGHG FELs focuses the attention on a portion of the bunch much longer than the FEL cooperation length, so that the preservation of the projected emittance (either defined over the whole bunch length or a considerable part of it) is important as well.

Real measurements of the transverse emittance usually involve particle coordinates in the so called pseudo-canonical transverse phase space (x, x', y, y') , instead of the afore-mentioned canonically conjugate coordinates $(x, p_x; y, p_y)$. The exact relation between the canonical momentum and the angular divergence of a relativistic particle is:

$$p_x = m_{rel}v_x + qA_x = mc\beta\gamma x' + qA_x \quad (3.6)$$

where we have used the usual relativistic parameters $\beta = v_z/c$, $\gamma = 1/(1 - \beta^2)^{1/2}$ and the magnetic field potential A_x . The same formalism applies to the vertical plane. If we restrict the magnetic field to the transverse plane ($A_x = A_y = 0$), such as in the hard-edge field approximation, the Liouville invariant can be written as follows:

$$\begin{aligned} Y_4 &= \int \int \int \int_{allNpoints} dx dp_x dy dp_y = \\ &= (mc\beta\gamma)^2 \int \int \int \int_{allNpoints} dx dx' dy dy' = (mc\beta\gamma)^2 V_4 \end{aligned} \quad (3.7)$$

As a consequence, the hypervolume of the pseudo-canonical phase space, V_4 , is preserved only if the particles longitudinal momentum is a constant of the motion. The hypervolume is called “geometric” hyperemittance, $\epsilon_4 = V_4$ in units of $m^2 rad^2$ and the brightness, B_4 , which is the average value of the particle density in the pseudo-canonical phase space is also given: $B_4 = I/\epsilon_4$, in units of $Am^{-2} rad^{-2}$. According to eq.3.7, the “normalized” hyperemittance, $\epsilon_{N,4} = Y_4/(m^2 c^2) = \beta^2 \gamma^2 \epsilon_4$, is preserved even during acceleration, as well as the normalized brightness $B_{N,4} = I/\epsilon_{N,4}$.

It is straightforward to restrict the same analysis to the 2-D phase spaces representing the particle motion in the horizontal or in the vertical plane. Assuming the motion in the two planes is uncoupled, we can write for each plane:

$$\epsilon = \int \int dx dx' = \frac{\epsilon_N}{\beta\gamma} \quad (3.8)$$

in units of $m\text{ rad}$. The energy dependence of the geometric emittance, eq. 3.8, is called “adiabatic damping”.

Under special conditions, the relation between the 4-D hypervolume V_4 and the 2-D phase space areas described by eq.3.8 assumes a general form:

$$V_4 = A_{2,x}A_{2,y}/\chi \longrightarrow \epsilon_4 = \epsilon_x\epsilon_y/\chi \longrightarrow B = \chi I/(A_{2,x}A_{2,y}) \quad (3.9)$$

in which χ is a form factor, approximately equal to 2. This value corresponds to a hyperellipsoid in Γ_4 , the projections of which have elliptical boundaries [74]. The trajectory of harmonic oscillator is an ellipse in Γ_2 and elliptic domains will therefore occur if: i) the particles move in a field that attracts them linearly towards the axis (linear paraxial approximation); ii) the motion is unbounded in configuration space (no collimation). The special volume in Γ_4 in fact corresponds to a surface density uniformly distributed over a hyperellipsoid and is known as the *Kapchinsky-Vladimirsky distribution* or the *microcanonical distribution*. It gives rise to linear SC fields so that the propagation of such beams can be studied analytically, even when the current is high.

Unlike the microncanonical distribution, if the beam has boundary contours in phase space very different from ellipses, then the alternative definition of statistical emittance may be used that relies on the idea that it is always possible to define a perfect beam – corresponding to a uniformly filled ellipse –, the behaviour of which indicates that of the real beam. This idea proved to be invaluable as a measure of the order or disorder in the domain occupied by the beam in the configuration space. In order to explain this, we consider a real beam, with density $f_2(x, x')$. The second moments of this distribution, $\langle x^2 \rangle$, $\langle x'^2 \rangle$ and $\langle xx' \rangle$ are related to the beam width, transverse velocity spread and position-to-angular divergence correlations, respectively. The “equivalent” perfect beam is then defined to be the perfect beam having the same intensity and the same second moments of the real projected transverse distribution. Notice that for a perfect beam, by definition, the half-width, a , in the x -direction is the maximum value of x : $a = x_{max} = \sqrt{\langle x^2 \rangle}$. The half-angular velocity spread, a' , defined to be x'_{max} , is then: $a' = x'_{max} = \sqrt{\langle x'^2 \rangle}$. The geometric root mean square or rms emittance, in units of $m\text{rad}$, is therefore given by [49]:

$$\epsilon = pq = \sqrt{\langle x^2 \rangle \langle x'^2 \rangle - (\langle xx' \rangle)^2} \quad (3.10)$$

irrespective of the orientation of the ellipse relative to the axis. For an upright ellipse, $\langle xx' \rangle = 0$. The expression in the square root is also the determinant of the so called *beam matrix*:

$$\epsilon = \sqrt{\det \begin{pmatrix} \langle x^2 \rangle & \langle xx' \rangle \\ \langle xx' \rangle & \langle x'^2 \rangle \end{pmatrix}} \quad (3.11)$$

With the use of the standard deviations σ_x , $\sigma_{x'}$ and the correlation coefficient $r = \frac{\langle xx' \rangle}{\sqrt{\langle x^2 \rangle \langle x'^2 \rangle}} \leq 1$, the expression of the rms emittance can also be written as:

$$\epsilon = \sigma_x \sigma_{x'} \sqrt{1 - r^2} \quad (3.12)$$

Unlike eq.3.10 and 3.11, this expression is still valid when the mean values $\langle x \rangle$ and $\langle x' \rangle$ do not vanish. For simplicity of notation, in the following we will always assume $\langle x \rangle = 0$ and $\langle x' \rangle = 0$ (same in the other two phase spaces) unless differently specified, so that the rms definition coincides with that of standard deviation.

A further mathematical manipulation of eq.3.10 allows one to write the statistical emittance also in this form [50]:

$$\epsilon = \frac{1}{N} \sqrt{2 \sum_{i=0}^N \sum_{j=0}^N A_{ij}^2} \quad (3.13)$$

that is the (square root of) the sum of the squared areas A_{ij}^2 of all the $N(N-1)$ triangles formed by any couple of representative points $M_i = (q_i, p_i)$, $M_j = (q_j, p_j)$ in Γ_2 and the origin of coordinates O. Thus, the emittance can be considered as a statistical mean area: the rms area of the triangles OM_iM_j as sketched in Figure 3.3. This statistical mean area is not the area of a limiting contour, such as in the case of the Liouville emittance, but the measure of the spread of the points around their barycentre. When their spread increases, the rms triangle area increases. For the same reason, points at very large distance from the barycentre give large contribution to the statistical emittance. If there is a long but small tail, the statistical emittance overestimates the spread of the distribution.

The mean-square values are bounded for all distributions of practical interest and the rms emittance is a highly indicative measure of the fraction of interest for the most real beams. Thus, we can define the statistical emittance as function of the betatron function β_x and the standard deviation of the beam size $\sigma_x = (\langle x^2 \rangle)^{1/2}$ at a certain position along the transport system, for any desired percentage of particles (P) contained in the ellipsoidal boundary (of the equivalent perfect beam) defined in the 2-D pseudo-canonical phase space:

$$\epsilon_x(P) = \frac{A(\sigma_x^2)}{\beta_x} = \frac{k^2 \sigma_x^2}{\beta_x} \quad (3.14)$$

where k is the effective fraction of beam size that corresponds to the betatron amplitude $A(\sigma_x)$. In the special case of a Gaussian 2-D distribution function,

$$f_2(x, x') = \frac{1}{2\pi\sigma_x\sigma_{x'}} e^{-\frac{x^2}{2\sigma_x^2} - \frac{x'^2}{2\sigma_{x'}^2}} \quad (3.15)$$

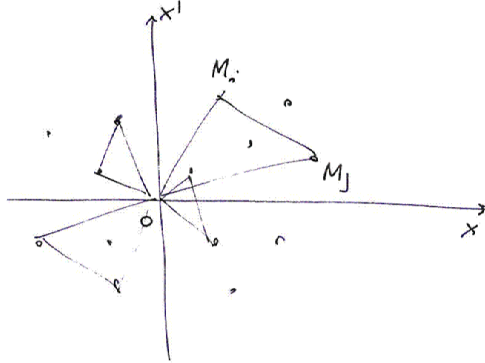


Figure 3.3: Emittance as a statistical mean area.

k is related to the percentage P of beam particles to which the statistical emittance refers by $k = \sqrt{-2\ln(1-P)}$. Thus, the percentage of particles enclosed by the ellipsoidal contour in Γ_2 can be computed for any k value, as shown in Table 3.1. The probability that a particle is inside the phase space contour corresponding to the specified statistical emittance is $1 - e^{-c/2}$, where c is the constant term in the equation describing the ellipsoidal contour in Γ_2 :

$$\frac{x^2}{2\sigma_x^2} + \frac{x'^2}{2\sigma_{x'}^2} = c \quad (3.16)$$

Table 3.1: Fraction of particles in the 2-D phase space vs. number of standard deviations of the beam transverse size.

k	1.0	1.2	1.5	1.8	2.0	2.15	2.45	3.0	4.0
P [%]	39	51	67.5	80	86.5	90	95	98.9	99.97

The beam statistical emittance is an invariant of the motion if and only if the focusing effect of the transport system is linear [49]. In fact, its invariance is a consequence of the transformation imposed on an ellipse by a linear system and not of Liouville's theorem, which is only applicable to a surface enclosing an ensemble of effective representative points. We stress that the area within an isodensity curve in phase space is conserved as the particles move through an even nonlinear but Hamiltonian system; on the other hand, the statistical emittance will increase as a result of distortion or even filamentation of the oc-

cupied area in Γ_2 . In other words, in the presence of a nonlinear transfer map the straight line joining a couple of points M_i, M_j is not mapped onto a straight line and the triangle OM_iM_j mentioned above is not mapped into another triangle. As a matter of fact, the majority of the experimental set ups deal with the statistical emittance, not with the Liouville one, because the particles' coordinates can be measured and the emittance easily computed with eqs.3.10–3.12. In practical applications, the statistical emittance is a good measure of the beam line acceptance needed to transport the beam without losses. Consistently with the experiments, most of the particle tracking codes used in this Thesis compute the rms emittance starting from the particle distribution. The rms emittance coincides with the Liouville emittance as long as the transport system is linear. So, the rms emittance is a convenient parameter for matching a beam to a linear transport system and, at the same time, it might be used for describing the degree of nonlinearity of the real system and the consequent mismatch of the beam to the magnetic lattice.

We now move to the longitudinal particle motion. We consider a 6-D particle density $f_6(x, x', y, y', t, \delta)$. The time coordinate, $t = cz$, depicts the longitudinal position along the bunch of an ultra-relativistic particle ($\beta \approx 1$). The origin of coordinates is that of a reference particle whose vector of coordinates is zero. By integrating f_6 over the four transverse coordinates and then again along t , we obtain the 1-D distribution of the particle energy relative deviation. We define the rms of such a distribution as the *total* relative energy spread of the particle beam that is occupying the hypervolume of interest. The total energy spread includes, in general, two contributions: the correlation term between the longitudinal coordinates (t, δ) and the uncorrelated term that is only given by δ . We want to give their mathematical definition by introducing first the longitudinal emittance of a particle beam. Since we are mainly interested in sources of nonlinear motion in the longitudinal phase space, we will consider the statistical emittance, which is affected by such a nonlinear dynamics, instead of the Liouville emittance. By replicating for the pseudo-canonical longitudinal phase space the definition of rms emittance as in eq.3.10, we find:

$$\epsilon_t = \sqrt{\langle t^2 \rangle \langle \delta^2 \rangle - (\langle t\delta \rangle)^2} = \sigma_t \sigma_\delta \sqrt{1 - r^2} \quad (3.17)$$

For an upright ellipse, $r = 0$ and its projection on the energy axis (integration of the 2-D density function over t) defines the *uncorrelated* relative energy spread of the particle beam. On the contrary, as r approaches 1, the phase space topology is dominated by the (t, δ) correlation and the corresponding projection on the energy axis is called *correlated* relative energy spread. In reality, a particle beam always has an uncorrelated energy spread that originates, for example, by the thermal motion during beam generation at very low energies. In a typical RF photoinjector (employing low quantum efficiency cathodes) for normal

conducting linac-based FELs, this is expected to be in the range 1–3 keV rms, but most of the times it can be neglected with respect to the correlated energy spread that runs in the range 0.1–10 MeV. So as for the transverse emittance, the *slice* energy spread is defined as the total energy spread of a longitudinal portion of the beam that is the projection of f_6 restricted to those particles lying in a temporal range Δt . In general, the slice energy spread still contains a correlated and an uncorrelated contribution, but as $\Delta t \rightarrow 0$ (the slice is much shorter than the bunch), $\langle t\delta \rangle \rightarrow 0$ and the slice energy spread approaches the uncorrelated one.

3.2 Single Particle Dynamics

3.2.1 Optics Mismatch, Field Errors and Filamentation

The problem of beam line design is usually that of guiding a given beam, of known current and emittance, in such a way that the loss of particles and deterioration of the original optical properties are kept as low as possible. The solution requires an analysis of the beam dynamics and is considerably facilitated by the use of the phase space representation. For any given optical element or for an ensemble of them, we define the acceptance of the beam transport system as the region of phase space within which the motion of all particles will be stable through the whole system. The acceptance domain is equivalent to the maximum hyperemittance domain that a beam may occupy if it is to pass through the system without loss of particles. As far as the transverse motion is concerned, the injected beam will be completely transmitted if the shape of the geometric emittance contour will lie within the acceptance contour of the system corresponding to the same location along the line. Provided that the statistical emittance is less than the acceptance of the system, optical elements such as quadrupole magnets can be inserted into the system with the main purpose of transforming the beam Twiss parameters, which govern the spatial and angular particle distribution in the transverse planes, in such a way that the emittance remains constant during the transport and the beam Twiss parameters coincide with their design value at any point of the lattice. In this case the beam is said to be “matched” to the optical element (or system).

Particle propagation through the lattice corresponds to a rotation of the emittance domain in Γ_2 . If the matching is not performed correctly, the emittance domain will sample larger amplitudes (in both configuration and angular coordinate) of the phase space. Let us assume an optics mismatch of the electron beam. We postpone the discussion of mismatch sources to a few paragraphs below. Now, if the forces are not linear – this is the case of high order multipole components of the external magnetic field – or even linearly dependent from the

particle energy – such as in the presence of large energy spread beam traveling in a linear focusing lattice –, the angular velocities of rotation of the representative points in Γ_2 vary with their radial distance, with the result that the emittance diagram becomes deformed and filamentation occurs. Filamentation is here meant to be the distortion of the beam emittance contour in phase space due to the difference in the phase advance of the particles within the bunch. Even though the Liouville invariance in Γ_2 is unaffected by the filamentation, the representative points become scattered over a much larger region of phase space: the Liouville emittance is still conserved while the rms emittance increases. There are several sources of filamentation. The most common and, as we will see, the most relevant for the dynamics in the FERMI linac, is the linear chromaticity, $\xi = \Delta\tilde{\mu}/(\mu\delta)$, which characterizes the energy dependence of the betatron phase advance. Here $\Delta\tilde{\mu}$ is the phase advance difference of a particle from the mean phase advance of the bunch. In the presence of chromatic filamentation, the particle phase space ellipse assumes a contour larger than the initial one, thus effectively increasing the beam emittance. If $\xi\delta$, the lattice chromaticity times the relative energy spread, is smaller than 1, the filamentation is contained [51]. This is the case of FERMI where $|\xi_x|\delta \leq 5.1 \cdot 10^{-3}$ and $|\xi_y|\delta \leq 0.7 \cdot 10^{-3}$. On the contrary, if $|\xi|\delta > 1$, the filamentation is complete.

It is possible to formally recognize two main processes leading to a beam optics mismatch. The *betatron mismatch* affects the superposition of the Γ_2 beam emittance contour onto the lattice acceptance, i.e. the beam Twiss parameters $\tilde{\beta}_{x,y}(s), \tilde{\alpha}_{x,y}(s)$ do not match the lattice design parameters $\beta_{x,y}(s), \alpha_{x,y}(s)$. In this case, both the beam size and divergence are affected and will diverge from the expected behaviour. The deviation of the beam Twiss parameters from those defined by the lattice is usually characterized in terms of the mismatch parameter, B_{mag} [52]:

$$B_{mag} = \frac{1}{2}(\tilde{\beta}\gamma - 2\tilde{\alpha}\alpha + \tilde{\gamma}\beta) \quad (3.18)$$

By definition, the mismatch parameter is always equal or larger than 1 and it has an important physical meaning. If a beam is injected into a ring or a linac with an optics mismatch, the beam will filament until its distribution approaches a shape that is matched to the lattice. However, the filamentation causes the beam emittance to increase, such that it is finally related to the initial (at injection) emittance by $\tilde{\epsilon} = B_{mag}\epsilon$. So, in the case of β -mismatch, the emittance growth is a multiplicative effect. In the FERMI linac, three main areas are devoted to betatron optics matching with quadrupole focusing: in the laser heater area, at the end of the injector (100 MeV); in the BC1 diagnostic area, downstream of the magnetic chicane (350 MeV) and at the linac end, before entering into the Spreader (1.2 GeV). Six, five and four quadrupoles are used, respectively, in each of the mentioned area to match the 4 independent Twiss parameters, $\alpha_{x,y}$

and $\beta_{x,y}$, of the incoming beam to the downstream lattice. The beam optics is expected to become closer and closer to the model as the beam is matched and travels along the linac. If the machine is reasonably well tuned, a mismatch parameter smaller than 5% in both planes is expected, so keeping the final projected emittance within the FEL specification.

The *dispersive mismatch* is a mismatch of the dispersion function and of its derivative, usually designed to be zero at the injection point. A residual $\Delta\eta$ and $\Delta\eta'$ distorts the beam trajectory in the presence of mean energy deviation and increases the rms emittance because the particles start coherent β -oscillations around the matched phase space. A typical source of residual (mismatched) dispersion is given by a particle that traverses a misaligned quadrupole. The particle is subject to a dipole-like kick $\Delta u' = kl_q \Delta q$, which is proportional to the integrated normalized quadrupole strength kl_q and to the quadrupole-to-beam lateral displacement Δq . The beam offset after a drift of length l is therefore $\Delta u = \Delta u' \cdot l$ or, for a more general path of the particle through active optics elements [53]:

$$\Delta u = kl\Delta q \sqrt{\beta_q \beta_l} \sin \Delta\mu_{ql} \quad (3.19)$$

Eq.3.19 introduces the betatron function at the quadrupole location, β_q , and at the observation point downstream of it, β_l . $\Delta\mu_{ql} = \frac{1}{2\pi} \int_{s=q}^{s=l} \frac{1}{\beta(s)} ds$ is the betatron phase advance between the quadrupole and the observation point. So, a strong focusing translates into a strong kick and this in turn excites a large trajectory distortion. The dipole-like kick from a misaligned quadrupole excites a residual momentum dispersion η (simply dispersion, in the following) of the order of $\Delta u' l_q / 2$ and a momentum dependent kick $\eta' = d\eta / ds$ of the order of $\Delta u' / 2$, just out of the magnet. We recall that, in general, the standard deviation of the beam size is governed by the following relation:

$$\sigma = \sqrt{\epsilon\beta + (\eta\delta)^2} \quad (3.20)$$

where β is the betatron function and η is the dispersion function that runs over the lattice. So, in the presence of a relatively high energy spread δ , such as in the bunch length compression area, the dispersion would contribute to enlarge the beam size because of the chromatic particle motion or, equivalently, to increase the effective transverse emittance according to:

$$\frac{\Delta\epsilon}{\epsilon} \simeq \frac{(\eta\delta)^2}{\beta\epsilon} \quad (3.21)$$

or, for the exact expression in the presence of a non-zero α parameter:

$$\frac{\tilde{\epsilon}}{\epsilon} = \sqrt{1 + \sigma_\delta^2 \frac{\Delta\eta^2 + (\beta\eta' + \alpha\Delta\eta)^2}{\epsilon\beta}} \Rightarrow \frac{\Delta\epsilon}{\epsilon} \simeq \frac{1}{2} \sigma_\delta^2 \frac{\tilde{H}}{\epsilon} \quad (3.22)$$

where we have defined the following quantities:

$$\Delta\eta = \eta - \frac{\langle x\delta \rangle}{\sigma_\delta^2}, \quad \Delta\eta' = \eta' - \frac{\langle x'\delta \rangle}{\sigma_\delta^2}, \quad H = \frac{\eta^2 + (\beta\eta' + \alpha\eta)^2}{\beta} \quad (3.23)$$

H should be made as small as possible by manipulating the two orthogonal vectors η and $(\beta\eta' + \alpha\eta)$ in order to minimize the emittance dilution. Unlike the β -mismatch, the emittance dilution induced by η -mismatch is an additive effect. It can therefore be compensated by removing the residual dispersion with a suitable trajectory manipulation [54]. By keeping the indicative threshold of 1% emittance growth, residual values of $\Delta\eta \leq 1$ mm and $\Delta\eta' \leq 1$ mrad can be tolerated locally in the presence of total energy spread $\leq 0.1\%$. Across the compressor areas where the energy spread rises up to 2%, we obtain the tighter tolerances $\Delta\eta \leq 1$ mm and $\Delta\eta' \leq 0.1$ mrad.

Even in the case of a perfectly matched beam at the injection point, the distortion of the phase space contour in Γ_2 can still arise due to imperfections of the successive magnetic field pattern. The analytical evaluation of a magnet field and alignment error depends on the magnet multipolar components (i.e. dipole, quadrupole, sextupole field, etc.) and on the type of effects (i.e. chromatic or geometric aberration, misalignment, etc.) one is investigating. Geometric aberrations, generated by terms proportional to the betatron amplitude, are responsible for the betatron motion distortion (dependence of the betatron motion on the betatron amplitude). Chromatic aberrations, generated by terms that depend on the particle energy deviation, are responsible for the linear and nonlinear chromaticity, as well as for the distortion of the betatron motion with an energy deviation. Owing to the fact that the particle motion in the FERMI linac is characterized by a relatively high energy spread over most of the entire lattice (between 0.1% and 2%) and that, due to the small emittance, the betatron oscillation amplitudes never exceed a few hundred microns, the specification for the field quality of the magnets in the FERMI linac is based on a model of the single particle motion in the presence of chromatic aberrations (up to the 2nd order in δ) and nonlinear magnetic field components (up to the 2nd order in x and y). An “ideal” magnet is here defined as one without magnetic or mechanical imperfections and perfectly aligned on the machine reference trajectory. This is the line on which, by design, all magnetic and electric axis of the machine components should lie. The “ideal” betatron motion around the reference trajectory is purely linear, without chromatic dependences and described by the well known Twiss functions. In reality, a linear magnetic lattice made of dipole and quadrupole magnets provide also a nonlinear field pattern because of magnetic field imperfections. These can be grouped into systematic errors, due to the finite extension of the magnet, and random errors, due to constructional imperfections. Both types of error induce multipolar field components. For example, the magnetic symmetry in a dipole allows a systematic sextupole and decapole

field component; a quadrupole includes a systematic 12- and 20-pole field component, etc. In general, all real magnets include random field components of any order. Notice that the expression “higher order”, when applied to the magnetic field expansion and to the particle equation of motion, should always be intended “in the particle coordinates”, which are defined over the 6-D phase space $(x, x', y, y', z, \delta)$. The magnetic field expansion in Cartesian coordinates to the n -th order can be expressed through the function of a complex variable [55]:

$$B_y + iB_x = \sum_{n=1}^{+\infty} (b_n - ia_n) (x - iy)^{n-1} \quad (3.24)$$

According to eq.3.24, b_n are called normal coefficients, a_n are called skew coefficients. They are the field gradient at the n -th order:

$$b_n = \frac{1}{(n-1)!} \frac{\partial^{n-1} B_y}{\partial x^{n-1}} \quad a_n = \frac{1}{(n-1)!} \frac{\partial^{n-1} B_x}{\partial y^{n-1}} \quad (3.25)$$

Alternatively, one can normalize the Taylor expansion as follows:

$$B_y \simeq b_0 + b_1 \left(\frac{x}{R}\right)_{y=0} + b_2 \left(\frac{x}{R}\right)_{y=0}^2 + b_3 \left(\frac{x}{R}\right)_{y=0}^3 + O(x^4) = \sum_0^n b_n \left(\frac{x}{R}\right)_{y=0}^n \quad (3.26)$$

with R an arbitrary distance in the transverse plane from the magnetic axis. The multipolar normal field coefficients become:

$$b_0 = B_0; b_1 = \left(\frac{\partial B_y}{\partial x}\right)_{y=0} R; b_2 = \frac{1}{2} \left(\frac{\partial^2 B_y}{\partial x^2}\right)_{y=0} R^2; \dots b_n = \frac{1}{n!} \left(\frac{\partial^n B_y}{\partial x^n}\right)_{y=0} R^n; \quad (3.27)$$

In the following we adopt the definition given in eq.3.27. All formulas refer to the horizontal plane but are equally valid in the vertical plane when neither bending nor dispersion is involved. Only the normal field components are considered because neither skew magnets nor big skew field error components are usually present in the linac lattice for FELs. A general treatment of the magnetic field with normal and skew components can be found in [56] and [57].

Once the error kick due to a perturbation is known – optics mismatch, chromaticity, magnet field error or misalignment –, the beam matrix formalism allows the calculation of the perturbed geometric emittance as a function of the perturbation action. By setting a threshold on the maximum tolerable emittance growth, one obtains the tolerance on the perturbation strength. To illustrate

this formalism, we initially define $\vec{X} = \begin{pmatrix} x \\ x' \end{pmatrix}$ as the vector of the particle coordinates and $A = \begin{bmatrix} \gamma_x & \alpha_x \\ \alpha_x & \beta_x \end{bmatrix}$ the matrix of the Twiss parameters (same for

the vertical plane). The particle geometric emittance ϵ_x is defined by $\vec{X}^t A \vec{X} = \sum_{ij} A_{ij} x_i x_j = \epsilon_x$. The beam matrix is defined as $\sigma_b = A^{-1} = \epsilon_x \begin{bmatrix} \beta_x & -\alpha_x \\ -\alpha_x & \gamma_x \end{bmatrix}$. Let us consider an angular kick error $\Delta x'$ induced by the magnetic field error or, equivalently, by the energy dependence of the magnetic force on the particle motion. The initial beam divergence is modified as follows:

$$\langle x'^2 \rangle = \langle x_0'^2 \rangle + \langle \Delta x'^2 \rangle \quad (3.28)$$

and the perturbed beam matrix becomes:

$$\tilde{\sigma}_b = \epsilon_x \begin{bmatrix} \beta_x & -\alpha_x \\ -\alpha_x & \gamma_x + \frac{\langle \Delta x'^2 \rangle}{\epsilon_x} \end{bmatrix} \quad (3.29)$$

Now the perturbed emittance $\tilde{\epsilon}_x$ can be calculated as the determinant of the perturbed beam matrix:

$$\tilde{\epsilon}_x = \sqrt{\det[\tilde{\sigma}_b]} = \sqrt{\epsilon_x^2 \left(1 + \frac{\langle \Delta x'^2 \rangle \beta_x}{\epsilon_x} \right)} \quad (3.30)$$

In the approximation of a small emittance growth, that is $\Delta\epsilon_x \ll \epsilon_x$, we find:

$$\frac{\Delta\epsilon_x}{\epsilon_x} \simeq \frac{1}{2} \frac{\beta_x}{\epsilon_x} \langle \Delta x'^2 \rangle \quad (3.31)$$

This formalism has been implicitly applied to derive eq.3.22. In this case, the perturbed emittance is computed by modifying the beam matrix as follows: $\beta \rightarrow \beta + (\eta\delta)^2/\epsilon$ and $\gamma \rightarrow \gamma + (\eta'\delta)^2/\epsilon$ and then computing the square root of the perturbed beam matrix determinant. Another important application of eq.3.31 concerns the chromatic aberration induced by the quadrupole focusing in the presence of high energy spread. It depends on the integrated quadrupole strength, kl , on the β -function at the quadrupole and on the relative energy spread, σ_δ :

$$\frac{\Delta\epsilon}{\epsilon} \simeq \frac{1}{2} \beta^2 \sigma_\delta^2 (kl)^2 \quad (3.32)$$

The point of the FERMI lattice most sensitive to chromatic aberrations is expected to be in proximity of BC1, where the rms energy spread may reach a maximum value of about 2% and a vertical betatron function of 68 m is designed for diagnostic purposes. Thus, eq.3.32 predicts $\sim 10\%$ vertical emittance dilution in this region. Once the whole magnetic lattice is known, it is straight forward to evaluate that the total contribution from all other quadrupoles in the FERMI linac, in both planes, is smaller than 5%. The Spreader focusing brings less than 1% emittance growth by virtue of the relatively smaller energy spread ($\sigma_\delta = 0.1\%$).

3.2.2 Magnetic Bunch Length Compression

Magnetic bunch length compression is carried out via ballistic contraction or elongation of the particles path length in a magnetic chicane. The linac located upstream of the magnetic chicane is run off-crest to establish a correlation between the particle longitudinal momentum, or equivalently its energy deviation δ (usually of the order of 1%) with respect to the reference particle and the z -coordinate along the bunch, i.e. the bunch head has a lower energy than the tail. In the magnetic chicane, due to their lower (higher) rigidity, leading (trailing) particles travel on a shorter (longer) path than trailing (leading) particles. The reference trajectory is conventionally defined by the motion of the bunch centroid. Since all particles of the ultra-relativistic beam travel in practice at the speed of light, the bunch edges approach the centroid position and the total bunch length is finally reduced. Notice that, since the chicane is made of four identical dipole magnets and is therefore totally symmetric, it is a perfect achromat to every order in δ . In the bending plane, horizontal here, the beam size reaches its maximum extension ($\Delta x \sim 10$'s mm full width) between the two inner dipole magnets, where the dispersion is maximum ($\Delta x/\delta \sim 0.1$ m). At the chicane end the beam size is restored to a much smaller value determined by pure geometric optics ($\eta_x = 0$).

The integral of the dispersion along the chicane, taken with the signed curvature of each dipole, is proportional to the transport matrix element R_{56} that governs the linear path-length dependence from the particle energy:

$$z = z_0 + R_{56}\delta \quad (3.33)$$

R_{56} is therefore the momentum compaction of the dispersive line times the on-energy path length. In the following, we choose a longitudinal coordinate system such that the head of the bunch is at $z < 0$. A chicane has $R_{56} < 0$ with this convention. The exact and the approximated ($\theta \ll 1$) expressions for the R_{56} and the maximum dispersion $R_{16} = \eta_x$ of a four dipole magnet symmetric chicane is:

$$R_{56}(\theta) = - \left[4 \frac{l_{eff}}{\sin \theta} (\tan \theta - \theta) + 2 - d \frac{\tan^2 \theta}{\cos \theta} \right] \approx 2\theta^2 \left(d + \frac{2}{3} l_{eff} \right) \quad (3.34)$$

$$\eta(\theta) = - \left[2 \frac{l_{eff}}{\sin \theta} \left(\frac{1}{\cos \theta} - 1 \right) + d \frac{\tan \theta}{\cos^2 \theta} \right] \approx (d + l_{eff})\theta \quad (3.35)$$

Here θ is the bending angle, l_{eff} is the dipole magnet rectilinear length over which the integrated field is computed and that relates to the bending radius ρ as $l_{eff} = \rho \sin \theta$; d is the distance between the first (third) and second (fourth) bend magnet calculated along the straight line. For $\theta \ll 1$, η_x is very close to

the trajectory offset with respect to the straight line ($\theta = 0$). In FERMI, R_{56} is never bigger than 50 mm (absolute value), while the maximum horizontal displacement of the magnetic chicanes from the straight line is 300 mm for a bending angle of 7 deg.

A linac with energy gain $eV \sin \phi$ (V and ϕ are the RF accelerating peak voltage and phase, respectively) imparts to the beam the following linear energy chirp:

$$h = \frac{1}{E_{BC}} \frac{dE}{dz} = \frac{2\pi}{\lambda_{RF}} \frac{eV \cos \phi}{E_0 + eV \sin \phi} \approx \frac{\sigma_\delta}{\sigma_z} \quad (3.36)$$

where E_0 and E_{BC} are the beam mean energy at the entrance and at the exit of the linac, respectively. The rms bunch length after compression is obtained in the “linear approximation” by substituting eq.3.36 into eq.3.33:

$$\sigma_z = \langle z^2 - \langle z \rangle^2 \rangle = \sqrt{(R_{56} \sigma_{\delta 0, \mu})^2 + (1 + hR_{56})^2 \sigma_{z0}^2} \approx (1 + hR_{56}) \sigma_{z0} \quad (3.37)$$

where σ_{z0} and $\sigma_{\delta 0, \mu}$ are the rms bunch length and the uncorrelated energy spread before compression. The “linear compression factor” is therefore:

$$C = \frac{\sigma_{z0}}{\sigma_z} \approx \frac{1}{1 + hR_{56}} \quad (3.38)$$

Figures 3.4, 3.5 and 3.6 plot the linear compression factor in BC1, eq. 3.38, as function of the RF phase of the upstream linac, L1 (accelerating crest is at 90 deg S-band). Each curve is for a different bending angle of the magnetic chicane dipole magnets. We point out that the linear term $(1 + hR_{56})$ in eq.3.38 can be forced to zero by setting $R_{56} = -1/h < 0$ that defines the point of “full-compression”. This is shown by the asymptotic behaviour to $+\infty$ in Figures 3.5 and 3.6. In reality, at the point of full-compression, the minimum bunch length is determined by nonlinear terms in the particle motion and by the uncorrelated energy spread. It is desirable that the compression process remains linear in z and δ in order to avoid bifurcations in longitudinal phase space and high peak current spikes at the edges of the electron bunch. The mechanisms leading to this kind of degradation of the current profile will be discussed later. At the moment, we can rely on the fact that a distribution as uniform as possible is aimed for, as it provides the maximum peak current in the main body of the bunch and narrows the bandwidth of the FEL output.

In practice, compressions by a factor bigger than ~ 3 are dominated by nonlinear effects such as sinusoidal RF time-curvature (mostly giving a quadratic energy chirp) in the upstream linac and the chicane 2^{nd} order path-length dependence from the particle energy. For simple magnetic chicanes with no strong focusing inside, the RF and path-length effects always conspire with the same signed 2^{nd} order terms to make the problem worse. The 2^{nd} order term T_{566} ,

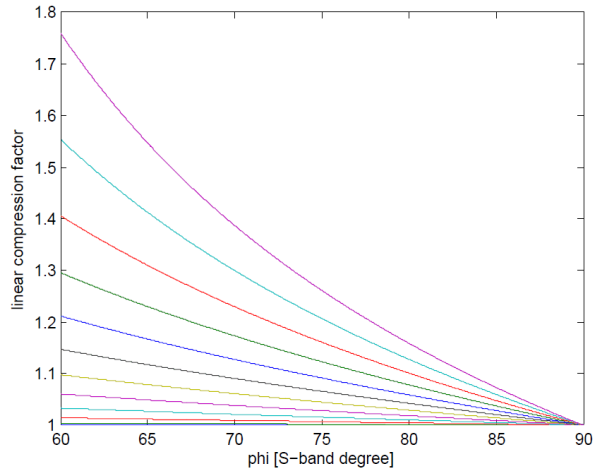


Figure 3.4: Linear compression factor as given by the FERMI@Elettra magnetic chicane, BC1, vs. L1 RF phase, for bending angle in the range 0–0.055 rad.

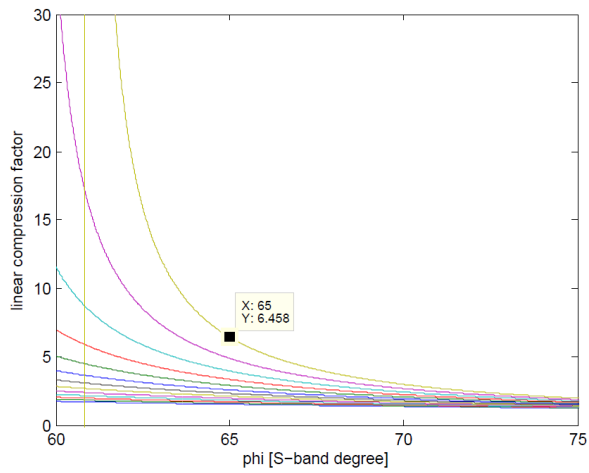


Figure 3.5: Linear compression factor as given by the FERMI@Elettra magnetic chicane, BC1, vs. L1 RF phase, for bending angle in the range 0.055–0.085 rad. The working point for the one-stage compression is also shown by labels.

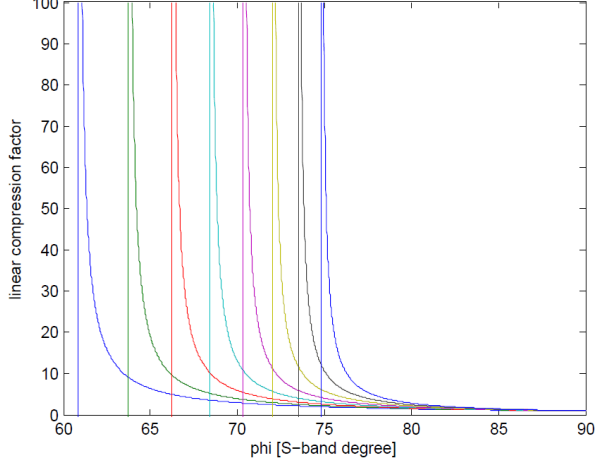


Figure 3.6: Linear compression factor as given by the FERMI@Elettra magnetic chicane, BC1, vs. L1 RF phase, for bending angle in the range 0.085–0.120 rad.

describing the path-length energy dependence of the chicane transport matrix, is approximately equal to $-3R_{56}/2$ for a simple symmetric chicane. The bunch length transformation through magnetic compression at 2^{nd} order is:

$$z = z_0 + R_{56}\delta + T_{566}\delta^2 \quad (3.39)$$

Also δ can be expanded up to the 2^{nd} order energy chirp h' :

$$\delta = \frac{\Delta E}{E_{BC1}} \approx \delta_{0,\mu} + hz_0 + h'z_0^2 \quad (3.40)$$

With the afore-mentioned convention for the accelerating field, the 2^{nd} order energy chirp is given by:

$$h' = \frac{1}{2} \frac{dh}{dz} = - \left(\frac{2\pi}{\lambda_{RF}} \right)^2 \frac{eV \sin \phi}{E_0 + eV \sin \phi} \quad (3.41)$$

As already done for the linear case, by inserting eq.3.41 and eq.3.40 into eq.3.39, the bunch length transformation is now obtained at 2^{nd} order:

$$\begin{aligned} \sigma_z^2 &= (R_{56}\sigma_{\delta 0,\mu})^2 + (1 + hR_{56})^2 \sigma_{z0}^2 + (T_{566}\sigma_{\delta 0,\mu}^2)^2 + \\ &(h^2T_{566} + h'R_{56})^2 \sigma_{z0}^4 + (2hT_{566}\sigma_{z0}\sigma_{\delta 0,\mu})^2 \end{aligned} \quad (3.42)$$

The higher order beam dynamics makes the compression factor always finite and a finite minimum bunch length is also determined. The minimum bunch length can be evaluated starting from the statistical definition of the longitudinal emittance, eq.3.17. The correlation term $\langle \delta z \rangle$ is dominated by the 2^{nd} order optics and energy chirp, so that eq.3.17 can be rewritten as:

$$\epsilon_z = \sqrt{\sigma_z^2 \sigma_\delta^2 + (h' \sigma_z^2)^2 + (T_{566} \sigma_\delta^3)^2} \quad (3.43)$$

At the end, the minimum bunch length is determined by imposing the condition of no correlation in the longitudinal phase space. So, given the emittance in eq.3.43, the minimum bunch length achievable with magnetic compression is:

$$\sigma_{z,min} \approx \frac{\epsilon_z}{\sigma_{\delta0,u}} \approx \sqrt{\frac{\sigma_{z0}^4 + \sigma_{\delta0,u}^4 \left(\frac{T_{566} \sigma_{\delta0,u}}{h' \sigma_{z0}} \right)^2}{\sigma_{z0}^2 + (2/\pi) \lambda_{RF} \tan^2 \phi}} \quad (3.44)$$

In order to linearize the 2^{nd} order bunch length transformation, the use of a short section of RF accelerating field at a higher harmonic of the linac RF frequency [36, 37] is usually adopted, thereby maintaining the initial temporal bunch profile and avoiding unnecessary amplification of undesired collective effects. Following [37] and without loss of generality, we consider the beam is 1) near-crest accelerated in the injector with energy gain $eV_0 \sin(\phi_0 + k_s z_0)$, 2) far-crest accelerated in the linac upstream of the magnetic chicane with energy gain $eV_1 \sin(\phi_1 + k_s z_0)$ and 3) in the X-band section with energy gain $eV_x \sin(\phi_x + k_x z_0)$. Here k_s, k_x is S-band and X-band RF wavenumber and z_0 is the electron longitudinal position with respect to the reference particle (bunch centroid); the bunch head is at $z < 0$. The RF phase ϕ_0, ϕ_1, ϕ_x is defined to be $\pi/2$ at accelerating crest and a phase in the interval $0 < \phi < \pi/2$ will accelerate the bunch head less than it will the bunch tail. Finally, the particle energy at the magnetic chicane is:

$$E_{BC1} = E_0 + eV_0 \sin(\phi_0 + k_s z_0) + eV_1 \sin(\phi_1 + k_s z_0) + eV_x \sin(\phi_x + k_x z_0) \quad (3.45)$$

For 2^{nd} order harmonic compensation, the X-band RF phase is set to $-\pi/2$ ($eV_x \geq 0$) at decelerating crest. The relative energy deviation with respect to the reference particle to 2^{nd} order in z_0 is then given by [57]:

$$\begin{aligned} \frac{\Delta E}{E_{BC1}} &\approx \left(\frac{eV_0 k_s \cos \phi_0 + eV_1 k_s \cos \phi_1}{E_{BC1}} \right) z_0 - \left(\frac{eV_0 k_s^2 \sin \phi_0 + eV_1 k_s^2 \sin \phi_1 - eV_x k_x^2}{2E_{BC1}} \right) z_0^2 \\ &\equiv az_0 + bz_0^2 \end{aligned} \quad (3.46)$$

where, by definition, $a > 0$ for $eV_0 > 0, eV_1 > 0$ and $0 \leq \phi_0, \phi_1 \leq \pi/2$. Similarly,

$b < 0$ with the harmonic RF switched off ($eV_x = 0$). The incoming uncorrelated energy spread is ignored for simplicity; it is usually of the order of 0.01% at ~ 100 MeV and therefore negligible with respect to the correlated one, which is at the level of 1%. Inserting eq.3.46 into eq.3.39, we obtain:

$$z = (1 + aR_{56})z_0 + (bR_{56} + a^2T_{566})z_0^2 \quad (3.47)$$

To linearize the transformation, the 2^{nd} order term must be set to zero:

$$b = -\frac{T_{566}}{R_{56}}a^2 \approx \frac{3}{2}a^2 \quad (3.48)$$

As anticipated above, eq.3.48 asks for the RF phase of the harmonic section to be chosen at decelerating crest. Since the harmonic voltage is lowering the nominal beam energy, the linac voltage has to be increased accordingly to keep the chicane energy constant:

$$eV_1 \sin \phi_1 = E_{BC1} - E_0 - eV_0 \sin \phi_0 + eV_x \quad (3.49)$$

Similarly, the compression factor is also dependent on main RF voltage settings, so a second requirement is to hold the linear chirp, h , constant:

$$-eV_1 \cos \phi_1 = eV_0 \cos \phi_0 - \frac{aE_{BC1}}{k_s} \quad (3.50)$$

The two constraints of constant energy at the chicane, eq.3.49, and of constant linear chirp, eq.3.50, are used to calculate the harmonic voltage needed to completely cancel 2^{nd} order compression terms by eliminating the eV_1 terms from eq.3.48. The linear compression relation $-aR_{56} \approx (1 - \sigma_z/\sigma_{z0})$ is also applied, which ignores the typically negligible uncorrelated energy spread. The necessary harmonic voltage is finally calculated:

$$eV_x = \frac{E_{BC1} \left[1 + \frac{\lambda_s^2}{2\pi^2} \frac{T_{566}}{|R_{56}|^3} \left(1 - \frac{\sigma_z}{\sigma_{z0}} \right)^2 \right] - E_0}{\left(\frac{\lambda_s}{\lambda_x} \right)^2 - 1} \quad (3.51)$$

The square of the harmonic ratio $n^2 = (\lambda_s/\lambda_x)^2$ in the denominator suggests that higher harmonics are more efficient for 2^{nd} order compensation, decelerating the beam less.

3.3 Collective Effects of the Electron Beam

3.3.1 Short-Range Space Charge Forces

The present study concerns the machine design and electron beam dynamics in the main linac of a FEL facility. This implies that we are not going to deal with the electron beam generation and transport at energies lower than 50 MeV. Thus, we will consider SC forces, that scale as $\sim E^{-2}$ in the laboratory frame, only in two cases. In the first case, the longitudinal electric field generated by clusters of charges or density modulation along the bunch can still be sufficiently high to induce an energy modulation as the beam travels along the accelerator. Such an energy modulation translates into density modulation when the beam passes through a dispersive region (in FERMI, this happens in BC1, BC2 and in the Spreader), with a consequent degradation of the energy and the current flatness. This dynamics is assumed to be purely longitudinal and it is discussed in detail in Section 5.5.

In the second case, SC forces might be enhanced because of the very high charge density achieved with the bunch length compression. Although 3-D tracking codes can be used to simulate the compression – such simulations are actually recommended to investigate detailed aspects of the beam dynamics in the presence of SC forces –, an analytical estimation of the impact of these forces on the transverse dynamics is still possible. Following [58] we find that the rms transverse envelope equation for a bunched beam in a linac is:

$$\sigma'' + \frac{\gamma'}{\gamma}\sigma' + K\sigma = \frac{k_s}{\gamma^3\sigma} + \frac{\epsilon_{th}}{\gamma^2\sigma^3} \quad (3.52)$$

Here, the standard deviation of the beam transverse size σ is assumed to be a function of the axial position s along the linac, $\gamma' = d\gamma/ds$ is the accelerating gradient, $K = (eB_0)^2/(2mc\gamma)^2$ is the focusing gradient of a solenoid of central field B_0 , $k_s = I/(2I_A)$, $I_A = 17kA$ being the Alfven current, and ϵ_{th} is the thermal emittance, which is mainly due to the photoemission process at the cathode surface: it is a Liouville invariant throughout acceleration. We now consider the following invariant envelope solution for the beam size:

$$\bar{\sigma} = \frac{1}{\gamma'} \sqrt{\frac{k_s}{\gamma(1/4 + \Omega^2)}} \quad (3.53)$$

where $\Omega = \sqrt{K}\gamma/\gamma'$. The laminarity parameter, ρ_L , is defined as the ratio of the “space charge term” driven by k_s and the “emittance term” driven by ϵ_{th} in

eq.3.52, computed with the substitution $\sigma = \bar{\sigma}$:

$$\rho_L = \left(\frac{k_s}{\epsilon_{th} \gamma \gamma' \sqrt{1/4 + \Omega^2}} \right)^2 \quad (3.54)$$

If $\rho_L \gg 1$, the particles motion is dominated by SC forces with negligible contribution from the betatron motion. By computing the laminarity parameter as function of the beam parameters along the transport system, we can identify machine areas where $\rho_L \gg 1$, which should be investigated more carefully with 3-D codes. As an example, for an electron linac driven by a standing wave photoinjector with no external focusing, $\Omega^2 = 1/8$, the energy at which the transition occurs, $\rho_L = 1$, can be quite high:

$$\gamma_{tr} = \sqrt{\frac{2}{3}} \frac{2k_s}{\epsilon_{th} \gamma'} \quad (3.55)$$

often corresponding to several hundreds of MeV. Unfortunately, the transition from SC-dominated ($\rho_L \gg 1$) to quasi-laminar ($\rho_L \ll 1$) motion cannot be described accurately by this model because, by definition, $\bar{\sigma}$ is a valid solution of eq.3.52 only for $\rho_L \gg 1$.

3.3.2 Short-Range Structural Wake Fields

For a longitudinal charge distribution λ_z , the energy loss of a test electron due to the electromagnetic wake of leading electrons is given by the geometric wake potential [59, 60]:

$$W(z) = - \int_z^\infty w(z-z') \lambda_z(z') dz' \quad (3.56)$$

where $w(z-z')$ is the Green's function, also called "wake function", that emulates the effect of the wake fields as generated by a single particle. Because of the principle of causality, the wake is zero if the test electron is in front of the wake source. If the relaxation time of the wake field is shorter than the repetition time of the accelerator, then the e.m. field associated with two succeeding bunches do not interfere and the single bunch wake field is said to be in the *short range* regime. This is the case of the FERMI linac, as opposite to the *long range* wake field usually present in rings, recirculating linacs and single-pass linacs dealing with a bunch train. In addition to this, if the beam is much shorter than the characteristic wake field length s_0 [61] and if the structure length L is much longer than the catch-up distance $a^2/(2\sigma_z)$, where a is the cell iris radius and σ_z is the rms bunch length, then the wake field is said to be, respectively, in the *periodic structure* and in the *steady state* regime:

$$\frac{a^2}{2L} \ll \sigma_z \ll s_0 \quad (3.57)$$

The characteristic length $s_0 = (0.41a^{1.8}g^{1.6}/L_c^{2.4})$ [61] is function of the cell iris radius a , of the cell inner width g and of the iris-to-iris distance L_c . In the very special case of periodic structure, steady state regime and very short electron bunches, the wake function assumes a simple form. For the longitudinal and transverse field component we have:

$$w_L(0^+) = \frac{Z_0 c}{\pi a^2} \quad w_T(0^+) = \frac{Z_0 c s_1}{\pi a^4} \quad (3.58)$$

Here $Z_0=377 \Omega$ is the free vacuum impedance. For FERMI, typical values are $s_0=1.5$ mm, $s_1=0.5$ mm, $\sigma_z=40-100 \mu\text{m}$ and $a^2/(2L_c)=2-20 \mu\text{m}$. So, while the steady state approximation is always satisfied, the periodic structure approximation is not. Nevertheless, it was found that by computing the short-range wake numerically and fitting it with a simple function, one can obtain a result that is valid over a large range of z (position along the bunch) and over a useful range of parameters [62]. For the longitudinal wake function we have:

$$w(z) = \frac{Z_0 c}{\pi a^2} \cdot e^{(-\sqrt{z/s_0})} \left[\frac{V}{C \cdot m} \right] \quad (3.59)$$

So, for the FERMI L0 accelerating structures one obtains [61]:

$$w(z) = 380 \cdot e^{(-\sqrt{z[mm]/1.28})} \left[\frac{V}{pC \cdot mm} \right] \quad (3.60)$$

For the FERMI CERN-type accelerating structures in L1 and L2 [61]:

$$w(z) = 311 \cdot e^{(-\sqrt{z[mm]/1.38})} \left[\frac{V}{pC \cdot mm} \right] \quad (3.61)$$

For the Elettra-type BTW accelerating structures in L3 and L4, the computed wake function integrated over the whole structure length and for $z \leq 5$ mm is [63]:

$$w(z) = 7450 \cdot e^{(-\sqrt{z[mm]/0.3})} + \frac{3}{\sqrt{z[mm]}} + 3000\sqrt{z[mm]} \left[\frac{V}{pC} \right] \quad (3.62)$$

The main difference between the wake function of the BTW and those of the other structures is due to the very different internal shaping and smaller average iris radius (5 mm instead of 9 mm) of the BTW single cell.

Similarly to the longitudinal case, the transverse wake function of the FERMI linac structures can be approximated with analytical expression, as suggested in [64]:

$$w^1(z) = \frac{4s_1 Z_0 c}{\pi a^4} \left[1 - \left(1 + \sqrt{\frac{z}{s_1}} \right) e^{-\sqrt{z/s_1}} \right] \left[\frac{V}{C \cdot m^2} \right] \quad (3.63)$$

For the L0 accelerating structures and $z \leq 5\text{mm}$, one obtains [29]:

$$w^1(z) = 9623 \cdot \left[1 - \left(1 + \sqrt{\frac{z[\text{mm}]}{0.6}} \right) \cdot e^{-\sqrt{z[\text{mm}]/0.6}} \right] \left[\frac{V}{pC \cdot m^2} \right] \quad (3.64)$$

For the CERN-type accelerating structures in L1 and L2 [29]:

$$w^1(z) = 7524 \cdot \left[1 - \left(1 + \sqrt{\frac{z[\text{mm}]}{0.7}} \right) \cdot e^{-\sqrt{z[\text{mm}]/0.7}} \right] \left[\frac{V}{pC \cdot m^2} \right] \quad (3.65)$$

For the Elettra-type BTW accelerating structures in L3 and L4 an analytical model was chosen that is a combination of periodic and one-cell structure solutions. The transverse wake function integrated over the structure length, for a maximum bunch length of 2 mm is [63]:

$$w^1(z) = 1.7 \cdot 10^5 \cdot \left[1 - \left(1 + \sqrt{\frac{z[\text{mm}]}{0.12}} \right) \cdot e^{-\sqrt{z[\text{mm}]/0.12}} \right] + \\ + 8.5 \cdot 10^4 \cdot \sqrt{z[\text{mm}]/10^{-3}} \left[\frac{V}{pC \cdot m} \right] \quad (3.66)$$

Again, the main difference between the wake function of the BTW and of the other structures is due to the different internal shaping and iris radius. Figure 3.7 shows the longitudinal (left plot) and transverse (right plot) geometric wake functions of the FERMI accelerating structures (here S0A and S0B refer to the structures in L0).

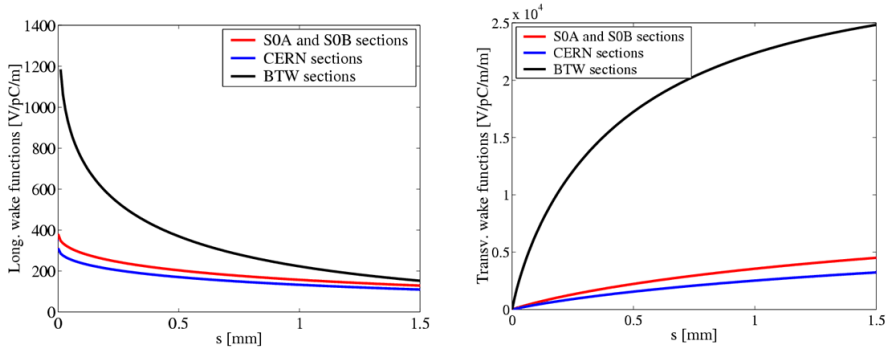


Figure 3.7: Longitudinal (left) and transverse (right) geometric wake functions per unit length of the FERMI linac.

The excitation of the longitudinal wake potential induces energy loss and, in particular, increases the correlated energy spread of the electron bunch. Depending on the bunch length and wake function strength, such correlation with the longitudinal particle coordinate inside the bunch can be linear or nonlinear. Unlike the monopole nature of the longitudinal wake field pattern, the short-range geometric transverse wake field is excited by electrons traveling off-axis. When the electron bunch travels near the axis of the accelerating structures, the transverse wake field is dominated by the dipole field component. As a result, the bunch tail oscillates with respect to the head forming in the (z, x) and in the (z, y) plane a characteristic “banana shape” [65]. Persistence of the slice oscillations along the linac and their amplification may cause the conversion of the bunch length into the transverse dimension (beam break up). So, the displaced bunch tail adds a contribution to the projection of the beam size on the transverse plane, actually increasing the projected emittance.

3.3.3 Microbunching Instability

Coherent Synchrotron Radiation (CSR) [66–70] in the bending magnets of the two bunch compressors plays a major role in the micro-fragmentation of the electron bunch. This effect will be considered later. In this paragraph the effect of synchrotron radiation is analyzed for a smooth electron density function, when the emission is at wavelengths of the order of the bunch length and much longer than the typical wavelength of incoherent emission: $\lambda_{CSR} \geq l_b \gg \lambda_{incoh}$, where $\lambda_{incoh} = (4\pi R/3\gamma^3)$, γ is the relativistic Lorentz factor and R is the bending radius. The coherent emission is characterized by an intensity spectrum that is proportional to the square of the number of particles N times the single particle intensity, unlike the incoherent emission that is simply linear with the number of particles:

$$\left(\frac{dI}{d\omega}\right)_{tot} = N(N+1)|F(\omega)| \left(\frac{dI}{d\omega}\right)_e \quad (3.67)$$

where $|F(\omega)|$ is the Fourier transform of the longitudinal particle distribution (form factor); it is of the order of 1 for very short bunches. When $\lambda_{CSR} \approx l_b$, a cooperative scale length of the process can be defined that describes the interaction of electrons and photons during the emission. This is the “slippage length” [70], $s_L = \frac{R\theta}{2\gamma^2} + \frac{R\theta^3}{24}$, where θ is the bending angle. In this case, the CSR emission depends on the details of the charge distribution, of the geometry of the electrons path and it causes a variation of the electron energy along the bunch (energy chirp). Owing to the fact that the energy variation happens in a dispersive region and that different slices of the bunch are subject to a different

energy variation, they start betatron oscillating around new, different dispersive orbits during the emission, thus increasing the projection of beam size on the transverse plane. At the end of compression, the bunch will be suffering of an additional (nonlinear) energy chirp and of a projected emittance growth in the bending plane.

The energy variation along the the electron bunch can be evaluated by means of the CSR wake potential. In the "steady state" approximation $R/\gamma^3 \ll l_b \leq s_L$, it can be expressed as follows [70]:

$$W_{CSR}^{SS}(z) = -\frac{1}{4\pi\epsilon_0} \frac{2e}{3^{1/3}R^{2/3}} \int_{-\infty}^z \frac{1}{(z-z')^{1/3}} \frac{d\lambda_z(z')}{dz'} dz' \quad (3.68)$$

The energy loss per unit length of the reference particle due to the radiation emission of the entire bunch is then $dE/dz = NeW_{CSR}^{SS}(z)$. In [70] the authors distinguish different regimes of CSR emission, depending on the relation between bunch length, bending magnet length and slippage length. So, using eq.3.68 in the *short bunch* ($l_b \leq s_L$), *long magnet* ($\gamma\theta \gg 1$) approximation, the energy loss per unit length of the reference particle due to the emission of a Gaussian line-charge distribution is [70]:

$$\frac{dE}{dz} = -\frac{1}{4\pi\epsilon_0} \frac{2e^2N}{3^{1/3}R^{2/3}\sigma_z^{4/3}} \frac{I_0(z/\sigma_z)}{\sqrt{(2\pi)}} \quad (3.69)$$

where $I_0(z/\sigma_z)$ is the CSR wake potential that has an oscillating behaviour along the Gaussian bunch. While leading particles gain energy, tailing particles loose it. Averaged over the entire bunch, the particles loose energy. The induced rms relative energy spread [72] and the total emitted peak power [70] are:

$$P_{coh} \approx \frac{0.352}{4\pi} \frac{c}{\epsilon_0} \frac{e^2N}{R^{2/3}\sigma_z^{4/3}} \quad (3.70)$$

$$\sigma_{\delta,CSR} = 0.2459r_e \frac{N}{R^{2/3}\sigma_z^{4/3}} \frac{R\theta}{\gamma} \quad (3.71)$$

Eq.3.68 points out that the energy loss is proportional to the first derivative of the longitudinal charge distribution. So, a stronger CSR induced energy loss is expected, for example, from a Gaussian line-charge than from a uniform one with smooth edges. Also, a current spike in the bunch tail could drive a damaging CSR emission. As an example, we report in the following the analytical expression for the CSR induced energy loss and coherently emitted power for a uniform charge distribution. The total energy loss, which is N -times the single particle loss, and the emitted power in the *short bunch, long magnet* regime are [70]:

$$\Delta E_{CSR,tot} = N\Delta E_{CSR,e} \simeq \frac{3^{2/3}}{4\pi\epsilon_0} \frac{N^2 e^2}{R^{2/3} l_b^{4/3}} R\theta \quad (3.72)$$

$$P_{coh} \simeq \frac{3^{2/3}}{4\pi\epsilon_0} \frac{ce^2 N}{R^{2/3} l_b^{4/3}} \quad (3.73)$$

When the bunch is much longer than the slippage length, the afore-mentioned steady state regime provides incorrect results. Transient effects when the bunch enters and leaves the magnet have to be taken into account. So, in the *long bunch* ($s_L \ll l_b$), *long magnet* ($\gamma\theta \gg 1$), the total energy loss is [70]:

$$\Delta E_{CSR,tot} = N\Delta E_{CSR,e} \simeq \frac{1}{4\pi\epsilon_0} \frac{N^2 e^2}{l_b} [4\ln(\gamma\theta) - 2] \quad (3.74)$$

while for the *long bunch* ($s_L \ll l_b$), *short magnet* ($\gamma\theta \ll 1$) regime we have [70]:

$$\Delta E_{CSR,tot} = N\Delta E_{CSR,e} \simeq \frac{1}{6\pi\epsilon_0} \frac{N^2 e^2}{l_b} (\gamma\theta)^2 \quad (3.75)$$

CSR emission is only one aspect of a more complex dynamics called microbunching instability. In fact, the instability is driven by the interaction and reciprocal amplification of the CSR and the LSC field. The latter is meant to be the short-range inter-particle Coulomb interaction that determines the variation of particles' longitudinal momentum. When the beam exits the photoinjector, the space-charge oscillation period is typically of the order of meters and any beam density modulation is practically frozen. Thus, without loss of generality, the microbunching instability is assumed to start at the photoinjector exit from a pure density modulation caused by shot noise or unwanted modulation in the photoinjector laser temporal profile. Several studies [74–76] indicate that such density modulation amplitudes are of the order of 0.01% in the sub-micron range and reach $\sim 1\%$ at longer wavelengths. As the beam travels along the linac to reach BC1, the density modulation leads to an energy modulation via the LSC wake. This is equal to the free space-charge wake for the wavelength of interest:

$$\lambda_m \ll \frac{2\pi d}{\gamma} \quad (3.76)$$

d being the transverse size of the vacuum chamber and γ the Lorentz factor. The expression for the LSC impedance is [71]:

$$Z(k) = \frac{iZ_0}{\pi k r_b^2} \left[1 - \frac{k r_b}{\gamma} K_1 \left(\frac{k r_b}{\gamma} \right) \right] \quad (3.77)$$

where $Z_0 = 377\Omega$ is the free space impedance, r_b is the radius of the transverse cross section for a uniform distribution and K_1 is the modified Bessel function of the second kind.

According to the theory developed in [77], the current spectrum is characterized by a bunching factor:

$$b(k) = \frac{1}{Nec} \int I(z)e^{-ikz} dz \quad (3.78)$$

where N is the total number of electrons. $b(k)$ couples with the LSC impedance along a path L to produce energy modulation of amplitude [77]:

$$\Delta\gamma(k) \approx -\frac{I_0 b(k)}{I_A} \int_0^L \frac{4\pi Z(k, s)}{Z_0} ds \quad (3.79)$$

where $I_A = 17$ kA is the Alfvén current.

We now consider that the bunch length is compressed in an achromatic magnetic chicane such as BC1 characterized by a momentum compaction $R_{56,1}$ (we now adopt this notation to differentiate the first magnetic chicane from a second one). For a generic initial energy distribution $V_0(\delta\gamma/\gamma)$ at the entrance of BC1, the resultant density modulation can be expressed through the bunching factor at the compressed wavelength [78]:

$$b_1(k_1) = \left[b_0(k_0) - ik_1 R_{56,1} \frac{\Delta\gamma(k_0)}{\gamma} \right] \int d\left(\frac{\delta\gamma}{\gamma}\right) V_0\left(\frac{\delta\gamma}{\gamma}\right) e^{(-ik_1 R_{56,1} \frac{\delta\gamma}{\gamma})} \quad (3.80)$$

where $k_1 = 2\pi/\lambda_1 = k_0/(1 + hR_{56,1})$ is the wave number of the modulation after compression; it is equal to the initial wave number k_0 times the linear compression factor $C = 1/(1 + hR_{56,1})$, h being the linear energy chirp. The bunching evolution in a two-stage compression is obtained by iterating the previous expression:

$$\begin{aligned} b_2(k_2) = & \left\{ \left[b_0(k_0) - ik_1 R_{56,1} \frac{\Delta\gamma(k_0)}{\gamma} \right] \int d\left(\frac{\delta\gamma}{\gamma}\right) V_0\left(\frac{\delta\gamma}{\gamma}\right) e^{(-ik_1 R_{56,1} \frac{\delta\gamma}{\gamma})} - ik_2 R_{56,2} \frac{\Delta\gamma(k_1)}{\gamma} \right\} \times \\ & \times \int d\left(\frac{\delta\gamma}{\gamma}\right) V_1\left(\frac{\delta\gamma}{\gamma}\right) \exp\left(-ik_2 R_{56,2} \frac{\delta\gamma}{\gamma}\right) \end{aligned} \quad (3.81)$$

where the suffix ₂ refers to the BC2 element. So, according to eq.3.79 the energy modulation amplitude in front of BC1 is:

$$\Delta\gamma(k_0) = \frac{I_0 b_0(k_0)}{I_A} \int_0^{BC1} \frac{4\pi Z(k_0, s)}{Z_0} ds \quad (3.82)$$

while that in front of BC2 is:

$$\Delta\gamma(k_1) = \frac{I_0 b_1(k_1)}{I_A} \int_{BC1}^{BC2} \frac{4\pi Z(k_1, s)}{Z_0} ds \quad (3.83)$$

The bunching described by eq.3.80 assumes a very simple form for an initial Gaussian energy distribution:

$$b_1(k_1) = \left[b_0(k_0) - ik_1 R_{56,1} \frac{\Delta\gamma(k_0)}{\gamma} \right] \exp \left[-\frac{1}{2} \left(k_1 R_{56,1} \frac{\sigma_\gamma}{\gamma} \right)^2 \right] \quad (3.84)$$

The exponential term shows that the particle longitudinal phase mixing contributes to the suppression of the instability if the initial uncorrelated energy spread σ_γ/γ is sufficiently larger than the energy modulation amplitude $\Delta\gamma/\gamma$. In case of non-reversible particle mixing in the longitudinal phase space (total suppression of the instability), this damping mechanism is called energy Landau damping. We stress that the present analysis is in the linear approximation because it assumes that the microbunching instability starts from a small energy or density modulation, $|CkR_{56}\Delta\gamma/\gamma| \ll 1$.

The spectral dependence of the microbunching instability gain in the density modulation can be expressed as the ratio of the final over the initial bunching. In the case of magnetic compression, if the initial bunching term can be neglected with respect to the chicane contribution, the instability is said to be in the "high gain regime", $G(k) \gg 1$. So, the gain in the density modulation after linear compression, due to an upstream energy modulation and for a Gaussian energy distribution, is given by:

$$G(\lambda) = \left| \frac{b_f(\lambda_f)}{b_i(\lambda_i)} \right| = k_f R_{56} \frac{\Delta\gamma}{\gamma} \exp \left(-\frac{1}{2} k_f R_{56} \frac{\sigma_{\gamma,i}}{\gamma} \right) \quad (3.85)$$

3.3.4 Free Electron Laser

The emission of a FEL in an undulator chain relies on an instability mechanism very similar to that of the afore-mentioned microbunching instability in a linac. As the electron beam passes through the undulator, the initial spontaneous or externally seeded radiation induces a longitudinal density modulation at the radiation wavelength scale. As a result, the radiation becomes amplified in intensity and enhanced in coherent characteristics, finally leading to an exponential instability. As the optical power builds up, electrons become trapped and rotate in the longitudinal phase space bucket. Eventually, the beam-wave interaction becomes nonlinear, putting the exponential power growth into saturation. According to the steady-state model that describes a FEL in the 1-D, plane-wave

limit and driven by an electron beam of infinite duration and uniform density, the FEL power initial growth and saturation can be described simply by [79]:

$$P = \alpha P_n e^{s/L_g} < P_{sat} \quad (3.86)$$

where P_n is the effective input power, α is the coupling coefficient representing the fraction of the power P_n coupled into the dominant mode exponentially growing in s (the distance along the undulator) with a power gain length L_g and P_{sat} is the saturation power. The input power is the frequency integrated synchrotron radiation power in an FEL gain bandwidth generated in the first gain length [80]. As for the saturation power, one may define a saturation length given by:

$$L_{sat} = L_g \ln \left(\frac{P_{sat}}{\alpha P} \right) \quad (3.87)$$

that is the length of the undulator required to reach the maximum output power. The quantities L_g , L_{sat} and P_{sat} are the major performance parameters for the FEL process. In this model the quantities in eq.3.86 are given by:

$$\alpha = 1/9, \quad P_n \approx \rho^2 c E / \lambda_r, \quad L_g = \frac{\lambda_u}{4\pi\sqrt{3}\rho}, \quad P_{sat} \approx \rho P_{beam} \quad (3.88)$$

where E is the mean beam energy, λ_u is the undulator magnetic period, λ_r is the FEL output wavelength at the fundamental emission, $P_{beam}[GW] = I[A]E[GeV]$ is the total peak power of the electron beam and ρ is a dimensionless parameter known as the Pierce parameter [14]. This is defined by:

$$\rho = \left[\left(\frac{I}{I_A} \right) \left(\frac{\lambda_u A_u}{2\pi\sigma} \right)^2 \left(\frac{1}{2\gamma_0} \right)^3 \right]^{1/3} \quad (3.89)$$

where $I_A = 17.045$ kA is the Alfvén current, σ is the standard deviation of the electron beam transverse size and A_u is a parameter related to the configuration of the undulator phase that is helical or planar. If we define the dimensionless undulator parameter $K = e\lambda_u B_0 / 2\pi m_0 c^2 = 0.934\lambda_u[cm]B_0[T]$, where B_0 is the peak undulator magnetic field, then we also define $a_u = K$ for the helical undulator and $a_u = K/\sqrt{2}$ for planar undulator. Finally, $A_u = a_u$ for a helical undulator and $A_u = a_u [J_0(\xi) - J_1(\xi)]$ for a planar undulator, where $\xi = \frac{a_u^2}{2(1+a_u^2)}$ and J 's are Bessel functions. Here it is sufficient to mention that the 1-D gain length is predicted to be increased by some parameters that measure the deviation of the electron beam from the 1-D case (transverse emittance, energy spread). Specifically, the increase is given by the diffraction process of the FEL radiation (spatial 3-D effect), the electron's longitudinal velocity spread caused

by finite transverse emittance and energy spread. Given some goal FEL performance, the criteria for the optimization of the undulator parameters is to have the shortest possible saturation length in order to minimize the size and hence the cost of the project.

The study of the electron beam dynamics in the accelerator is the *conditio sine qua non* for the validation of the FEL performance. In general, the FEL process asks for high charge density in the 3-D configuration and velocity space. The repulsive SC forces tend to dilute the charge density. They scale in all directions as γ^{-2} in the laboratory frame, so that a high accelerating gradient, usually bigger than 100 MV/m in the electron gun and 20 MV/m in the succeeding booster linac, is required. The transverse emittance is the electron beam quality factor used to evaluate the particle spatial and velocity spread as a resultant of the balance between (high) charge density, (strong) accelerating field and space charge forces. The emittance has to be minimized at the injector end and preserved up to the undulator.

The close interaction of the electron beam with first the seeding laser and then the self-emitted photons, to build up the FEL amplification implies a correct superposition of the two beams along the FEL line. The electron/photon transverse coupling is ensured by the following condition on the 2-D normalized emittance, $\gamma\epsilon$ [13]:

$$\gamma\epsilon \leq \frac{\gamma\lambda_r}{4\pi} \quad (3.90)$$

This equation says the electron beam has never to exceed the photon beam size defined by the radiation diffraction limit. So, for example, a normalized emittance smaller than 2 mm mrad has to be ensured at the FERMI undulator for 10 nm output wavelength at fundamental emission.

The on-axis fundamental radiation wavelength can be related to the undulator/electron beam system by considering a simple time-of-flight argument. By considering simple wave interference, only those wavelengths that propagate ahead of the electron (in vacuum, a co-propagating radiation wavefront will always move ahead of an electron) by an integer number of wavelengths in one undulator period will constructively interfere after many such periods. The time taken for an electron propagating along the undulator axis with mean speed \bar{v}_z to travel one undulator period, $t_e = \lambda_u / \bar{v}_z$, is the same time a resonant wavefront takes to travel the distance $\lambda_u + n\lambda_n$. By equating these expressions, the following relation for the resonant wavelength is obtained:

$$\lambda_{r,n} = \frac{\lambda_u}{n} \left(\frac{1 - \bar{v}_z/c}{\bar{v}_z/c} \right) \approx \frac{\lambda_u}{2n\gamma^2} (1 + K^2) \quad (3.91)$$

where $n = 1, 2, 3, \dots$, the undulator magnetic period, λ_u is usually a few mm long and K is the undulator strength parameter, usually of the order unity. According

to eq.3.91, the 1.5 GeV electron beam energy and an undulator period 35 mm long ensure a fundamental FEL radiation output wavelength in the range 5–15 nm for $K=1-2$.

Eq.3.91 also implies that a spread of the electron energy potentially enlarges the output radiation bandwidth and/or shifts the central radiation wavelength. The electron beam total energy spread, $\sigma_{E,tot}$, is approximately given by the quadratic sum of the uncorrelated term, $\sigma_{E,u}$, the rms energy modulation amplitude induced by the seeding laser, ΔE_s , and the term of correlation between the particle energy and the z-coordinate inside the bunch (energy chirp), $\sigma_{E,c}$:

$$\sigma_{E,tot} = \sqrt{\sigma_{E,u}^2 + \sigma_{E,c}^2 + \Delta E_s^2} \quad (3.92)$$

The maximum acceptable deviation of the longitudinal phase space (relative energy deviation $\Delta E/E_0$ vs. z) from the desired *flatness* is determined by the Pierce parameter ρ that is the FEL gain bandwidth expressed in terms of normalized energy. The flatness defines the value of the nonlinear component of the energy variation along the bunch for which the increase in bandwidth of the X-ray signal due to this variation becomes equal to the Fourier transform limited bandwidth defined by the bunch length.

The electron/photon interaction in the FEL undulator is actually a local interaction that happens over a cooperation length, $L_c = \lambda_r/4\pi\rho$, usually much shorter than the electron bunch, i.e. on a fs scale compared to 100s of fs bunch duration. The 10s of fs long seed laser pulse activates the FEL amplification process over several cooperation lengths, so underlining the importance of correlations of the electron beam parameters with the longitudinal coordinate along the bunch. The linac design has to ensure the preservation of the electron beam quality on the slice scale. In practice, this scale will be determined by the resolution of the electron bunch length measurement. Owing to a shot-to-shot arrival time jitter of the order of 100 fs between the seed laser and the electron beam at the entrance of the undulator, different bunch portions participate to the FEL interaction at different shots. So, a bunch portion longer than the seed laser should be suitably prepared for the FEL interaction. For this reason, the longitudinal correlation of the slice beam parameters is usually studied over the whole bunch length.

3.4 Conclusions

The theoretical tools for describing the single particle and electron beam collective motion in a single-pass linac have been recalled and their applicability to the FERMI case study has been discussed. Liouville's theorem illustrates the primary goal of 6-D electron beam emittance preservation as at the injector level.

The high beam quality that is required for the FEL process is expressed in terms of the Liouville transverse emittance and energy spread. In reality, the applicability of Liouville's theorem to the beam transport and bunch length compression in a linac-based FEL is invalidated by several single particle and collective frictional forces. These degrade time-projected or local (in the z -coordinate) beam parameters. To investigate such different effects, the concept of projected and slice emittance has been introduced for the transverse motion. The definition of correlated, uncorrelated and slice energy spread has been given for the longitudinal motion. The rms emittance has also been introduced as a statistical measure of the particle spread in the phase space. In fact, most of the measurements of the electron beam parameters deal with that, rather than with the Liouville one. Unfortunately, unlike the latter, the former is diluted by chromatic filamentation. Because of the relatively high energy spread required from the magnetic bunch length compression, the chromatic filamentation may develop in the presence of beam optics mismatch or magnetic field errors. Nevertheless, the beam matrix formalism allows one to determine the design tolerances in terms of mismatch parameter, magnet alignment and field quality to avoid an emittance dilution beyond the specifications. As for the longitudinal dynamics, the theory of magnetic bunch length compression has been expanded up to the second order in the particle coordinates. It has been shown how the second order energy chirp and path-length-to-energy correlation term limit the compression efficiency and, therefore, the minimum bunch length achievable with a magnetic chicane. The effect of a higher harmonic RF cavity in the longitudinal particle motion has been introduced in order to cancel the second order terms.

The analytical treatment of the most important collective effects has also been given. The interaction of the electron beam with the image charge field in the accelerating structures has been described in terms of longitudinal and transverse wake potential. The beam dynamics in the presence of the electromagnetic self-field has been investigated through the laminarity parameter. This could be used to identify the linac regions in which short range space charge forces corrupt the quasi-laminar particle motion by virtue of the very high charge density. This is expected to happen, for example, during the bunch length compression, even at high energy. The space charge forces are then modeled with a longitudinal wake function that induces an energy modulation at wavelengths much shorter than the bunch length. It is transformed into a density modulation in the chicanes' dispersive region, therefore enhancing the emission of coherent synchrotron radiation that, in turn, amplifies the initial energy modulation. This self-amplifying process is called microbunching instability and degrades both the energy and the particle density distribution. Formulas for the computation of the linear gain, in the one- and two-stage compression scheme have been given. A very similar process is at the basis of the FEL instability. The 1-D

modeling of the FEL generation has been sketched and the requirements on the electron beam quality have been deduced from some basic formulas; the beam quality is essentially characterized in terms of peak current, transverse emittance and relative energy spread.

Chapter 4

Machine Design and Single-Particle Dynamics

This Chapter¹ contains the analytical evaluations of the effect of the magnetic field errors, magnet misalignments and chromatic aberrations on the transverse beam dynamics in the presence of linear and nonlinear fields. Using the beam matrix formalism and theory of field expansion introduced in Section 3.2, it produces the tolerances on the magnets field quality and alignment in the FERMI linac and predicts the emittance growth in the presence of chromatic filamentation of the particle transverse phase space. After that, under the assumption of linear optics transport, the design of a dispersion-free, straight diagnostic line and of a dispersive diagnostic line is presented. In fact, these studies have been implemented in the FERMI lattice. The constraints imposed by the beam diagnostic performance on the optics design are considered. The measurement of several beam parameters is simulated with particle tracking. Finally, a two-stage station for geometric beam collimation, integrated into the diagnostic line, is discussed; the collimation efficiency is analytically evaluated and the prediction is compared with the result of particle tracking.

¹This Chapter is based on the following works: *Analytical evaluation of chromatic aberrations and alignment tolerances in single-pass linacs*, ST/F-TN-09/01 (2009) by S. Di Mitri and M. Cornacchia. *Compact multi-purpose optics insertion in the FERMI@Elettra linac bunch compressor area*, WEPB42 in Proc. of Free Electron Laser Conf. 2010, Malmo, Sweden, by S. Di Mitri and M. Cornacchia. *Geometric efficiency of a two-stage fully absorbing collimation system in single-pass linacs*, Phys. Rev. Special Topics – Accel. and Beams, **13**, 052801 (2010), by S. Di Mitri.

4.1 Magnet Specifications

4.1.1 Magnetic Field Tolerances

Let us first consider a real dipole magnet. A quadrupole field component (random error) causes emittance blow up by excitation of chromatic aberration through the following kick: $\Delta x' = k_{1,dip} l x = k_{1,dip} l \eta \delta$. The quadrupole normalized strength $k_{1,dip}$ can be defined in terms of the quadrupole coefficient normalized to the dipole coefficient:

$$k_{1,dip} = \frac{e \mathcal{G}_{dip}}{p} = \frac{\theta}{Rl} \left| \frac{b_1}{b_0} \right| \quad (4.1)$$

The notation is that adopted in Section 3.2. The kick error becomes:

$$\Delta x' = \frac{\theta}{R} \eta \delta \left| \frac{b_1}{b_0} \right| \quad (4.2)$$

According to 3.31, the corresponding emittance growth is:

$$\frac{\Delta \epsilon}{\epsilon} \simeq \frac{\beta}{2\epsilon} \left(\frac{\theta}{R} \right)^2 (\eta \sigma_\delta)^2 \left| \frac{b_1}{b_0} \right|^2 \quad (4.3)$$

So, the following expression can be used to obtain the tolerance on the relative quadrupole field component in a dipole magnet corresponding to a maximum emittance growth $\frac{\Delta \epsilon}{\epsilon}$:

$$\left| \frac{b_1}{b_0} \right| \leq \frac{1}{\theta} \frac{R}{\eta \sigma_\delta} \sqrt{\frac{\Delta \epsilon}{\epsilon} \frac{2\epsilon}{\beta}} \quad (4.4)$$

The sextupole-like kick of a dipole magnet for an off-momentum particle is primarily related to the 2nd order chromatic aberration in a dispersive path: $\Delta x' = k_{2,dip} l x^2 = k_{2,dip} l (\eta \delta)^2$. The sextupole normalized strength $k_{2,dip}$ can be defined in terms of the sextupole coefficient normalized to the dipole coefficient:

$$k_{2,dip} = \frac{e m_{dip}}{p} = \frac{2\theta}{R^2 l} \left| \frac{b_2}{b_0} \right| \quad (4.5)$$

so that the kick becomes:

$$\Delta x' = \frac{2\theta}{R^2} (\eta \delta)^2 \left| \frac{b_2}{b_0} \right| \quad (4.6)$$

According to 3.31, the corresponding emittance growth is:

$$\frac{\Delta \epsilon}{\epsilon} \simeq \frac{\beta}{2\epsilon} \left(\frac{2\theta}{R} \right)^2 (\eta \sigma_\delta)^4 \left| \frac{b_2}{b_0} \right|^2 \quad (4.7)$$

and the tolerance on the relative sextupole field component in a dipole magnet corresponding to a maximum emittance growth $\frac{\Delta\epsilon}{\epsilon}$ will be:

$$\left| \frac{b_2}{b_0} \right| \leq \frac{1}{\theta} \left(\frac{R}{\eta\sigma_\delta} \right)^2 \sqrt{\frac{\Delta\epsilon}{\epsilon} \frac{\epsilon}{2\beta}} \quad (4.8)$$

Table 4.1 lists the magnetic specifications for the quadrupole and sextupole field components of the dipole magnets in the FERMI electron beam delivery system in order to ensure an emittance growth equal to or less than 1% from each individual contribution. The multipolar components are computed for $R=20$ mm. The specifications for the Spreader dipole magnets are much more relaxed than in BC1 and BC2 because of the very small energy spread, $\sigma_\delta < 0.1\%$, expected in that region.

Table 4.1: Magnetic field quality specifications for the FERMI dipole magnets.

	$ b_1/b_0 $	$ b_2/b_0 $
BC1	$\leq 0.6 \cdot 10^{-4}$	$\leq 1.5 \cdot 10^{-4}$
BC2	$\leq 1.2 \cdot 10^{-4}$	$\leq 1 \cdot 10^{-3}$
Spreader	$\leq 1 \cdot 10^{-3}$	$\leq 5 \cdot 10^{-3}$

Similarly to the dipole magnet case, a real quadrupole magnet might be affected by a sextupole field component (random error) that causes emittance blow up by excitation of chromatic aberration in a dispersive path or by geometric aberration. The sextupole-like kick is: $\Delta x' = k_{2,q} l x^2$, where x might be dominated by the particle dispersive motion, $x = \eta\delta$, or by the pure betatron motion, $x = \sqrt{\epsilon\beta}$. The sextupole normalized strength $k_{2,q}$ can be defined in terms of the sextupole coefficient normalized to the quadrupole coefficient:

$$k_{2,q,quad} = \frac{em_q}{p} = \frac{2k_1}{R} \left| \frac{b_2}{b_1} \right| \quad (4.9)$$

so that the kick is:

$$\Delta x' = \frac{2k_1 l}{R} x^2 \left| \frac{b_2}{b_1} \right| \quad (4.10)$$

The tolerance on the relative sextupole field component in a quadrupole magnet is therefore:

$$\left| \frac{b_2}{b_1} \right| \leq \frac{1}{k_1 l} \frac{R}{(\eta\sigma_\delta)^2} \sqrt{\frac{\Delta\epsilon}{\epsilon} \frac{\epsilon}{2\beta}} \quad (4.11)$$

or

$$\left| \frac{b_2}{b_1} \right| \leq \frac{1}{k_1 l} \frac{R}{\epsilon\beta} \sqrt{\frac{\Delta\epsilon}{\epsilon} \frac{\epsilon}{2\beta}}$$

In FERMI, both these formulas provide a specification for the quadrupole magnet field at least one order of magnitude larger than that for the dipoles, already shown in Table 4.1.

4.1.2 Magnet Alignment Tolerances

A dipole magnet roll angle ϕ_d may generate residual dispersion in the non-bending plan, vertical here, that in turn may lead to vertical emittance dilution. The vertical kick given by the dipole field with a roll angle to the beam with finite energy spread is: $\Delta y' = \frac{\int B dl}{B\rho} \phi_d \sigma_\delta$. A constraint on the vertical emittance growth leads to the tolerance on the maximum acceptable roll angle:

$$|\phi_d| \leq \frac{1}{\theta \sigma_\delta} \sqrt{\frac{\Delta \epsilon_y}{\epsilon_y} \frac{2\epsilon_y}{\beta_y}} \quad (4.12)$$

For the constraint of 1% emittance blow up, the tighter specification on the dipole magnets alignment over the whole FERMI beam delivery system is set by the maximum bending angle in BC1 ($\theta = 0.122$ rad) in the presence of the maximum relative energy spread ($\sigma_\delta = 2\%$): $\phi_d \leq 500 \mu\text{rad}$ (rms value).

A quadrupole magnet roll angle ϕ_q in a dispersion free region may induce geometric coupling. The kick given by the quadrupole gradient projected on the vertical plane is: $\Delta y' = k_1 l x_\beta \phi_q$. A constraint on the vertical emittance growth leads to the tolerance on the (maximum) roll angle:

$$|\phi_q| \leq \frac{1}{|k_1 l| \sigma_{\beta,x}} \sqrt{\frac{\Delta \epsilon_y}{\epsilon_y} \frac{2\epsilon_y}{\beta_y}} \quad (4.13)$$

For the constraint of 1% emittance blow up, one has to satisfy $\phi_q \leq 20$ mrad (rms value) for the average focusing length $f = 1/k_1 l = 5$ m and average β -function of 20 m, which are typical values in the FERMI linac.

If the quadrupole is in a dispersive region, instead, the roll angle excites residual vertical dispersion that, in turn, will cause vertical emittance dilution. The kick given by the quadrupole gradient projected on the vertical plane is then: $\Delta y' = k_1 l x_\eta \delta \phi_q$. A constraint on the vertical emittance growth leads to the tolerance on the maximum roll angle:

$$|\phi_q| \leq \frac{1}{|k_1 l| \eta_x \sigma_\delta} \sqrt{\frac{\Delta \epsilon_y}{\epsilon_y} \frac{2\epsilon_y}{\beta_y}} \quad (4.14)$$

Then, the 1% emittance blow up requests the tighter alignment of $\phi_q \leq 10$ mrad (rms value) respect to the case of non-dispersive motion. An uncorrected dispersion of 10 mm and an rms relative energy spread of 2% are here assumed.

Finally, a quadrupole magnet lateral displacement causes a dipole kick that generates residual dispersion. The dipole-like kick for the vertical plane is: $(\Delta y') = k_1 l (\Delta y)$. A constraint on the vertical emittance growth leads to the tolerance on the maximum lateral displacement of the quadrupole magnetic axis from the beam path:

$$|\Delta y| \leq \frac{1}{|k_1 l| \sigma_\delta} \sqrt{\frac{\Delta \epsilon_y}{\epsilon_y} \frac{2\epsilon_y}{\beta_y}} \quad (4.15)$$

Due to the bunch length compression, the BC1 area sees the maximum energy spread of $\sigma_\delta = 2\%$ of the whole line. The energy spread couples to $kl \leq 0.26 m^{-1}$ and $\beta_y \leq 68 m$, so that an emittance blow up smaller than 1% is ensured by $\Delta x, \Delta y \leq 100 \mu m$ (rms value). The same area includes a RF vertical deflector for beam diagnostics, as shown in the next Section. During the vertical deflection of a 1 ps long beam, the particle maximum vertical displacement at the quadrupoles is $\Delta y \leq 500 \mu m$ (this really applies only to the deflected bunch edges). With the upper limit of $kl \leq 0.14 m^{-1}$ and $\beta_y \leq 68 m$ as defined by the optics design in this region, we obtain $\Delta \epsilon / \epsilon \leq 1\%$. More details about the optics design and the magnetic lattice of this area are given in the next Section.

4.2 Beam Transport and Diagnostics

4.2.1 Design of a Dispersion-Free Diagnostic Line

A low- β symmetric optics insertion covering $2\pi/3$ betatron phase advance, devoted to beam diagnostics and beam transport, is in the laser heater area (100 MeV), in the BC1 area (~ 350 MeV) and at the end of the linac (≤ 1.5 GeV), as shown in Figures 2.2 and 2.3. Each optics insertion includes quadrupole magnets ($kl \leq 0.26 m^{-1}$) for beam optics matching to the downstream lattice and a spectrometer line for energy measurement. The optics or, equivalently, the quadrupole normalized strengths are made the same in all the aforementioned areas by scaling the quadrupole magnet gradient with the beam energy, $g[T/m] = E[GeV] \cdot k[m^{-2}]/0.2998$. Differently from the other locations, a larger energy spread is used in the BC1 area for bunch length compression. For this reason, the chromatic aberration sets a tighter constraint on the maximum quadrupole integrated strengths, as mentioned in the previous Section. The presence of a vertically deflecting RF cavity used for diagnostic purposes requires an even more accurate optics design. The lattice of the FERMI@Elettra BC1 area is shown in Figure 4.1. The arrangement of magnetic and diagnostic elements is mainly determined by the constraint of having a single optics for beam diagnostics and transport. The compactness of the insertion has been achieved to save space for acceleration in the linac tunnel. The constraints on the Twiss

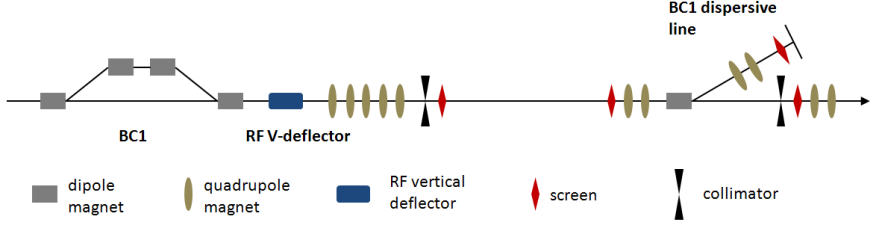


Figure 4.1: Schematic layout of the FERMI@Elettra BC1 area.

parameters in the BC1 area are listed below, in the order of importance:

- 1) The horizontal betatron function β_x has to be shrunk to the 1 m level in the second half of the magnetic chicane to minimize the projected emittance growth induced by CSR emission.
- 2) The effective strength of the vertical RF deflector is proportional to the transport matrix element from the deflector to the screen on which the beam is projected [81], $S_y = \sqrt{\beta_{y,1}\beta_{y,2}} \sin \Delta\mu_{y,12}$. The expression contains 3 independent optics parameters and it must be maximized by a suitable optics.
- 3) The choice of a single optics for diagnostic and transport suggests to adopt a periodic phase advance $\Delta\mu_{x,y}$ pattern, so that the horizontal and vertical emittance measurement can also be done with the multi-screen technique, alternative to the usual quadrupole scan.
- 4) A small β_x and a high horizontal dispersion η_x are required at the screen in the spectrometer line to characterize the particle energy distribution.
- 5) The 4 independent Twiss parameters $\beta_{x,y}$ and $\alpha_{x,y}$ have to be matched in the area to keep the optics under control (i.e., sufficiently smooth) and to match the beam to the downstream lattice.
- 6) A proper setting of high $\beta_{x,y}$ and $\Delta\mu_{x,y} \simeq \pi/2$ has to be set in the area to allow geometric collimation.

All quadrupoles involved have bipolar power supplies for a larger acceptance in case of largely mismatched beam from the injector. Four quadrupoles along the upstream L1 (see Figure 2.2) are used for point 1. They naturally produce a high $\beta_y = 68$ m at the end of BC1, where we have therefore placed the vertical RF deflector (point 2). Downstream of BC1, 5 quadrupoles distributed over 2.5 m with an average integrated strength of $kl = 0.18 \text{ m}^{-1}$ build up a low- β

symmetric optics, as shown in Figure 4.2, with $\Delta\mu_{x,y} = 2\pi/3$ over the following 10 m (points 3 and 5). The beam waist is at the central screen where $\beta_{x,y} = 3$ m. Collimators are near each of the outer two screens (point 6), although $\beta_{x,y} = 12$ m at the collimators' location is not as large as desired. Due to the optics symmetry, the collimators are identical (saving costs), with cylindrical apertures to collimate both planes at the same location and sufficiently long to guarantee a full absorption, so avoiding the usual spoiler plus absorber scheme. Since the distance between the screens is proportional to $\beta_{x,y}$ at the collimators, the total length of the insertion is a compromise between available space and collimation efficiency. Not to add space in the s -direction, a dipole magnet (spectrometer) is inserted between the last two screens. It deflects the beam horizontally in the dispersive line to characterize the electron beam energy distribution. A FODO cell is added upstream of the dipole (this is switched off during the machine operation), downstream of it in the dispersive line and also in the straight line. The first two FODO cells balance the geometric and the chromatic contribution to the particle motion (point 4) in order to improve the energy measurement resolution. The third FODO cell completes the matching to the downstream linac. The betatron phase advance built up in this region also allows a suitable trajectory correction scheme made of 4 BPMs and 6 corrector magnets per plane (combined devices). The scheme allows one to measure the residual dispersion after BC1, to build a straight line along the 5 matching quadrupoles, to measure the residual field of the spectrometer magnet and to properly launch the beam into the succeeding linac.

A careful design of the quadrupole focusing downstream of the deflector has to be carried out because, in the case of a fully compressed and deflected beam, the magnets are traversed by a vertically large size beam with up to 2% rms energy spread. The large energy spread might induce emittance degradation by means of chromatic aberration. At the same time, the dipole-like kick of the quadrupoles traversed off-axis affects not only the motion of the bunch centroid (trajectory distortion) but also the linear dependence of the RF deflecting kick with the longitudinal position inside the bunch. In other words, the path of particles distant from the quadrupole axis could be distorted by the quadrupole field, possibly reducing the magnification factor of the deflecting process at the screen. For this reason, the optics are designed so that the maximum quadrupole kick $kl\Delta y \approx 50$ μ rad is much smaller than the maximum deflector vertical kick, $zeV_{RF}\omega_{RF}/(Ec)$, for $z = 500$ μ m, corresponding to 1 mrad. Particle cross-over between adjacent slices due to quadrupole focusing is therefore excluded. The projected emittances $\epsilon_{x,y}$ can be measured by scanning the strength of the last matching quadrupole and looking to the beam size at the second screen, or with the 3-screens technique without changing the nominal optics set for beam transport. The bunch is vertically deflected according to the

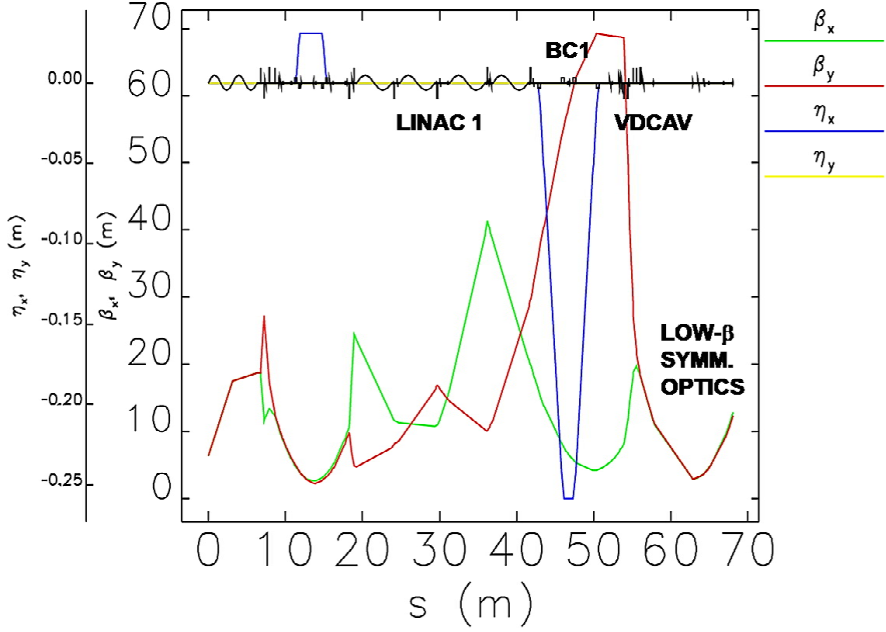


Figure 4.2: Optics from the FERMI Gun to the BC1 area.

product of the RF kick from the deflector and the effective length S_y [81]:

$$\langle \Delta y \rangle = \left(\frac{eV_{\perp}}{E} \sin \phi_{RF} \right) \left(\sqrt{\beta_D \beta_S} \sin \Delta \mu_{DS} \right) \sim \tilde{y}' \cdot \tilde{L} \quad (4.16)$$

The effective length \tilde{L} is 5 m, 14 m and 22 m from the 1st to the 3rd screen, respectively. The last one should therefore be used for bunch length measurements. At this point, linear transport analysis translates a 1 ps fwhm long bunch into a 6.7 mm vertical spot size. Since the non-deflected rms beam size is 0.1 mm, we should be able to resolve $(6.7/3.5) \cdot 0.1 = 15$ longitudinal slices (we have used a factor 3.5 between the standard deviation and the full width of a hard-edge distribution). A conservative picture of 10 slices equivalent to 100 fs resolution at the energy of 350 MeV could be considered to reduce the bunch length measurement error down to 1% [81] or just in case of shorter bunches.

The slice horizontal emittance is foreseen to be measured with a quadrupole scan at the 2nd screen, taking advantage of the natural beam waist at this location. The expected minimum horizontal beam size is 60 μm ; therefore a 10 μm

rms screen+CCD resolution has been specified. The quadratic behavior of the rms beam size σ_x^2 vs. the quadrupole strength can be analytically predicted. During the scan, a bunch length in the range 0.5–1.5 ps is expected to be translated into a vertical spot size in the range 4–8 mm.

As a check of the linear analysis used so far, the `elegant` code [82] has been used to track a 350 pC, 1 ps fwhm long bunch compressed 10 times in BC1. Figure 4.3 shows the simulation result for the bunch length measurement with the RF vertical deflector in the BC1 area, after bunch length compression by a factor of 10. Current profile (left plot) and deflected beam at the 3rd screen (right plot) are illustrated. Figure 4.4 depicts the simulation of the slice horizontal emittance measurement performed with quadrupole scan, after vertical deflection and bunch length compression by a factor of 10. The 6.5 mm bunch length at the 3rd screen, shown in Figure 4.3 and the slice horizontal emittance measurement at the 2nd screen, shown in Figure 4.4, are in full agreement with the afore-mentioned analytical predictions.

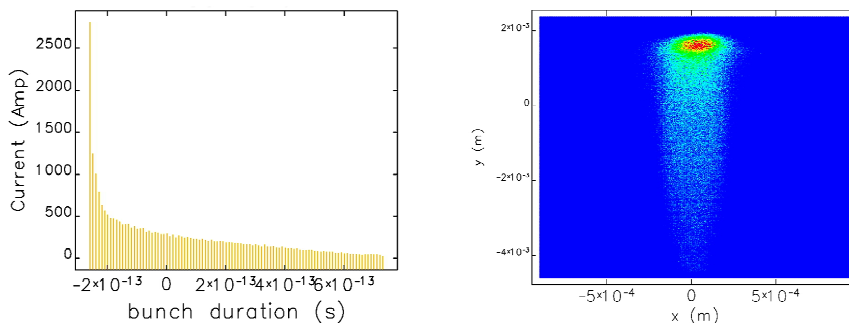


Figure 4.3: Simulation of the bunch length measurement with the RF vertical deflector in the BC1 area. Left plot is the histogram reproducing the beam current profile. It can be reconstructed from the projection of the bunch on the screen after deflection, as shown in the right plot. The simulation assumes a 350 pC bunch, compressed by a factor 10 in BC1.

4.2.2 Design of a Dispersive Diagnostic Line

The FERMI@Elettra beam delivery system includes five spectrometer lines (see Figure 2.2) in which the beam energy distribution is characterized by analyzing the transverse profile collected on a screen, in the bending plane. The minimum relative energy deviation $\delta = (E_0 - E_1)/E_0$ between two particles with mean energy E_0 and E_1 corresponds to the physical separation Δ of the two particle

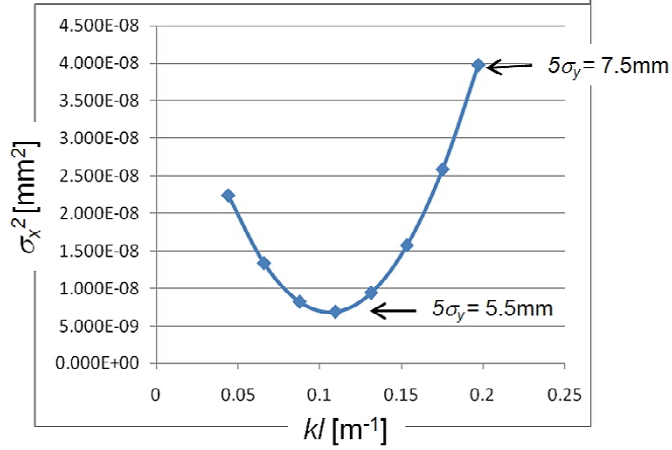


Figure 4.4: Simulation of the slice horizontal emittance measurement with quadrupole scan. The curve shows σ_x^2 vs. quadrupole strength at the 2nd screen and it refers to one of the central slices in the bunch. The horizontal geometric emittance and the Twiss parameters for each of the bunch slices are extracted from the fit of the quadratic behaviour of the squared slice horizontal beam size vs. the integrated quadrupole strength.

projections onto the screen:

$$\delta = \frac{2\Delta}{\eta} \quad (4.17)$$

where η is dispersion at the screen location. By definition, eq.4.17 shows the intrinsic resolution of the energy deviation measurement. In case of a sector dipole magnet with bending angle θ , the intrinsic resolution is maximized by placing the screen at the optimum distance $s_M = \beta_0/\alpha_0$ [53] from the center of the dipole magnet, where the Twiss parameters are computed in the dipole center. Following this prescription and by including a beam finite geometric emittance, eq.4.17 becomes:

$$\delta = \frac{\sqrt{\epsilon}}{\sqrt{\beta} \sin(\theta/2)} \quad (4.18)$$

and one also finds $s_M = \frac{\eta^{(s_M)}}{\eta'^{(s_M)}}$. The beam size as determined by the geometric and chromatic contribution of the particle motion is:

$$\sigma = \sqrt{\epsilon\beta + (\eta\sigma_\delta)^2} \equiv \eta\sigma_\delta\sqrt{1 + \kappa^2} \quad (4.19)$$

where we have introduced the error coefficient $\kappa = \sqrt{\epsilon\beta}/\eta\sigma_\delta$. Given the pure chromatic beam size $\sigma_0 = \eta\sigma_\delta$, the relative error of the energy spread measurement induced by the betatron motion is:

$$\frac{\Delta E}{E_0} = \frac{\sigma - \sigma_0}{\sigma_0} = \sqrt{1 + \kappa^2} - 1 \quad (4.20)$$

Eq. 4.20 defines the intrinsic energy resolution of the spectrometer line. For a more complicated system than a dipole magnet followed by a drift section, the optical resolution power of a spectrometer line can also be evaluated in terms of ratio $\eta/\sqrt{\beta}$ at the screen location. This ratio does not depend from the beam parameters, but only from the beam line optics design. Thus, the effective resolution of a spectrometer line is always optimized for $\eta/\sqrt{\beta} \gg 1$. This condition might set important constraints on the beam line design and, at the same time, it assumes that the electron beam is perfectly matched to the design optics of the lattice. Figure 4.5 shows the nominal optics from the injector end to the BC1 spectrometer line. The spectrometer is a 0.5 m long rectangular dipole; the bending angle is 25 deg. The screen is placed at 1.75 m from the dipole exit flange. The optical functions of interest are depicted in Table 4.2.

Table 4.2: Design optics functions of the BC1 dispersive line.

	Center of dipole magnet	Screen	Unit
β_x	32.0	0.05	m
α_x	-10.0	3.4	
β_y	2.3	30	m
α_y	2.2	-42.6	
η_x	0.1	0.5	m
η'_x	0.4	0.05	

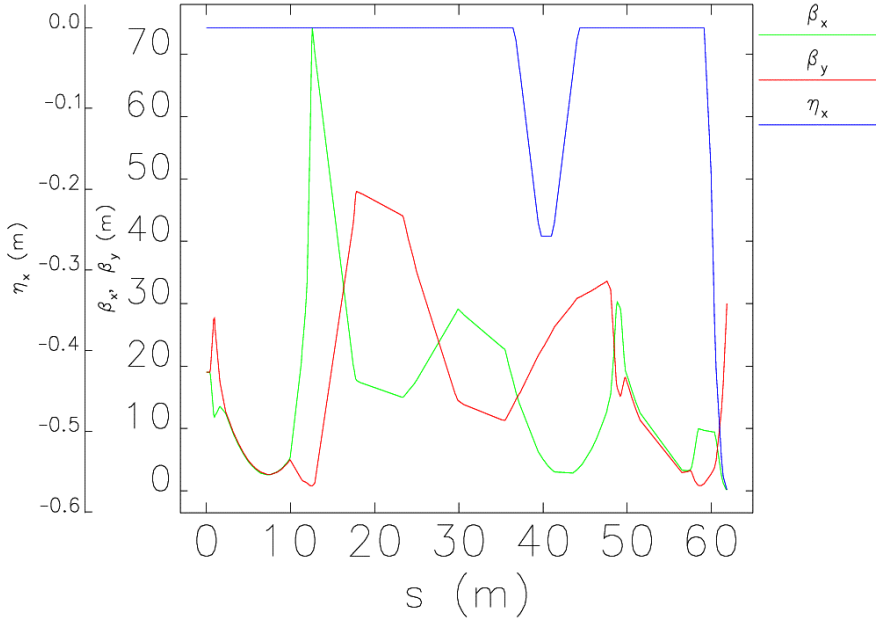


Figure 4.5: Optics functions from the injector exit to the end of the BC1 spectrometer line.

A BPM has been installed immediately downstream of the spectrometer magnet. The BPM ($\eta_x/\sqrt{\beta_x} = 0.09m^{1/2}$) is thought to be used to find the accelerating crest of the upstream linac over a wide range of RF phases by looking to the bunch centroid position. Albeit limited in energy range, the absolute energy measurement at the screen ($\eta_x/\sqrt{\beta_x} = 0.8m^{1/2}$) has a higher resolution than at the BPM. The measurement accuracy is mainly limited by the screen+CCD system resolution, $\Delta_{SC} = 20\ \mu\text{m}$ [83], so that the energy measurement relative accuracy is $\Delta_{SC}/\eta_x = 4 \cdot 10^{-5}$ (this has to be compared with eq.4.20). The expected 0.1% mean energy jitter can thus clearly be detected both at the screen and at the BPM. Figure 4.6 plots eq. 4.20 that is the (intrinsic) error of the measurement of relative energy spread due to the contribution of the betatron motion to the chromatic beam size detected at the screen, in the horizontal plane, as function of the measurement central value. The total energy spread $\sigma_{\delta,tot}$ will be in the range 0.5–2% for the mean energy in the range 100–350 MeV. The lowest energy

is possibly achieved by turning off the RF in L1.

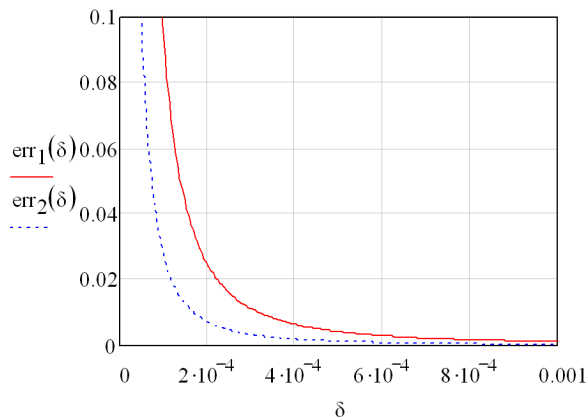


Figure 4.6: Relative error of the energy spread measurement vs. central value (dimensionless parameters). The solid line is for the beam mean energy of 100, the dotted line is for 350 MeV.

In principle, the slice or even the uncorrelated energy spread could be measured in a spectrometer line from the dispersive projected image of the beam on the screen, under critical conditions of the beam optics, energy distribution and diagnostics resolution. The concept of correlated, uncorrelated and slice energy spread have already been given in Section 3.1.2. They are schematically recalled here in Figure 4.7 and their geometric interpretation in the longitudinal phase space is given in order to quantify the dispersive line diagnostic performance. A linear correlation in the longitudinal phase space is assumed; such a correlation, $\Delta\delta_{corr}$, is also called energy chirp. The thickness of the area occupied by the particles is the uncorrelated energy spread, $\Delta\delta_{uncorr}$. It can be measured as a projection on the energy axis only if the correlation is removed. The projection of a small longitudinal portion of the bunch gives the slice energy spread, $\Delta\delta_{SL}$. Notice that, as long as a correlation is present, the slice energy spread does not really coincide with the uncorrelated one, even for zero slice length. In Figure 4.7 the temporal coordinate is substituted by the phase $\phi = \omega_{RF}t$, where ω_{RF} is the linac angular radio-frequency. In this way, all variables in the Figure are dimensionless and geometric considerations can be easily applied to the normalized longitudinal phase space. In particular, we define the linear energy

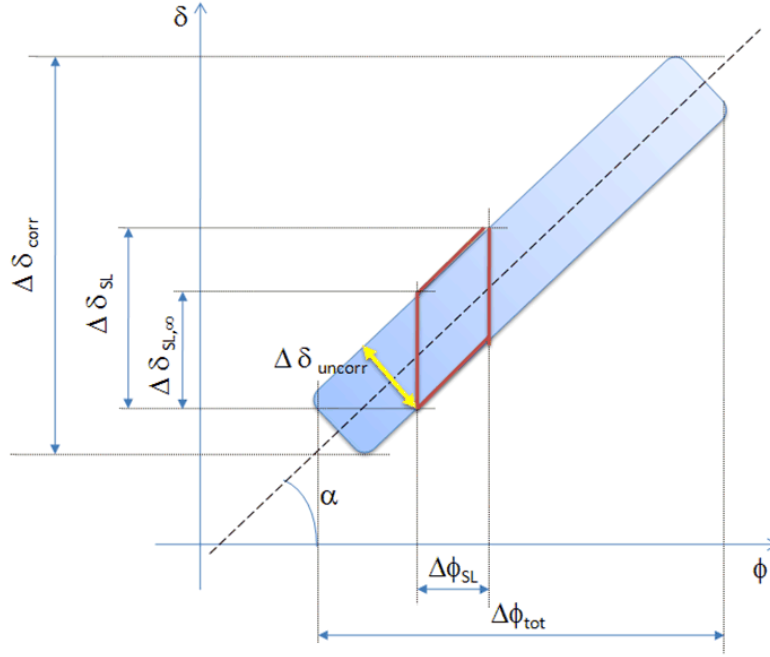


Figure 4.7: Longitudinal phase space with linear energy chirp (conceptual).

chirp $\alpha = d\delta/d\phi$ and the uncorrelated and slice energy spread as function of it:

$$\begin{aligned}\Delta\delta_{uncorr} &= \Delta\delta_{SL,\infty} \cos \alpha \\ \Delta\delta_{SL,\infty} &= \Delta\delta_{SL} - \Delta\phi_{SL} \tan \alpha\end{aligned}\quad (4.21)$$

$\Delta\delta_{uncorr}$ coincides with $\Delta\delta_{SL}$ which only if the energy chirp is sufficiently small, namely $\alpha \ll 1$ and $\tan \alpha \ll \frac{\Delta\delta_{SL}}{\Delta\phi_{SL}}$, finally implies:

$$\alpha \ll \frac{\Delta\delta_{uncorr}}{\Delta\phi_{SL}} \approx \frac{\Delta\delta_{SL}}{\Delta\phi_{SL}}\quad (4.22)$$

When eq.4.22 is satisfied, the energy chirp is negligible with respect to the intrinsic spread of the beam energy that is the total energy spread actually coincides with the slice energy spread. In this case, a simple spectrometer magnet followed by a screen can be used to measure the slice energy spread. Table 4.3 compares the values of the l.h.s and r.h.s. of eq.4.22 for all the five spectrometer lines of the FERMI@Elettra lattice, according to the beam parameters listed in

Table 2.2 for the configuration of FEL1 Operation. The slice length is defined as 1/30 of the fwhm bunch length. Table 4.3 shows that, according to eq.4.22, only in the laser heater spectrometer line, when the injector is run on-crest, the measurement of energy spread is an effective way to detect the slice one. In reality, the on-crest acceleration in the injector superimposes the sin-like RF curvature to the beam energy distribution, so that the longitudinal phase space is no more linear and eq.4.22 only applies to the beam core, which is dispersed on the accelerating crest. On the contrary, in the BC1 area a large $\sim 1\%$ rms and mostly linear energy chirp exists for the bunch length compression. Unfortunately, such a large chirp completely masks the slice energy spread. For this reason, a vertical RF deflecting cavity has been foreseen in the BC1 area to reconstruct the longitudinal phase space [81, 84] and to make a direct measurement of the slice energy spread.

Table 4.3: Design parameters of the beam longitudinal phase space in the FERMI dispersive lines.

Spectrometer Line	$\Delta\phi_{FW}$ [S-deg]	$\Delta\delta_{tot}$	$\Delta\delta_{uncorr}$	α	$\Delta\delta_{uncorr}/\Delta\phi_{SL}$	$\Delta\delta_{uncorr} \equiv \Delta\delta_{SL}$
Gun	0.188	0.025	$6 \cdot 10^{-4}$	0.13	0.10	No
LH	0.188	0.006	$2 \cdot 10^{-4}$	0.03	0.25	Yes
BC1	0.019	0.100	$5 \cdot 10^{-4}$	5.26	0.83	No
DBD	0.019	0.005	$2 \cdot 10^{-4}$	0.26	0.33	No
MBD	0.019	0.005	$2 \cdot 10^{-4}$	0.26	0.33	No

With the vertical deflector, the longitudinal phase space can be reconstructed at the screen. The target size accommodates up to a 2% energy spread, 10 ps fwhm long bunch. The resolution of the measurement of the slice energy spread $\sigma_{\delta,sl}$ is limited by Δ_{SC} to 14 keV rms at 350 MeV. At the same time, eq.4.20 predicts that a relative slice energy spread, $\sigma_{\delta,sl}$, not smaller than $1 \cdot 10^{-4}$ could be measured to avoid in turn a big error ($> 10\%$) due to the contribution of the geometric optics. So, our best guess for the measurement of the slice energy spread is $\sigma_{\delta,sl} = 30 \text{ keV} \pm 12 \text{ keV}$ at 350 MeV. Since the correlated energy spread does not substantially change through BC1 (CSR contribution to it is pretty small) and in the approximation of the longitudinal emittance preservation, eq.3.17 states that the uncorrelated energy spread, σ_{δ} , increases by the same factor of which the bunch length, σ_t , is reduced. According to particle tracking results of the FERMI injector [29], the uncorrelated energy spread at 100 MeV is expected to be close to 3 keV rms. So, assuming a linear bunch length compression by a factor of 10 in BC1, the measurement of 30 keV in the succeeding spectrometer line would be an indirect measurement of the uncorrelated energy spread at the injector level.

One could finally wonder if the slice energy spread measured with the vertical RF deflector is sufficiently close to the uncorrelated energy spread. Figure 4.8 is a sketch of the image displayed at the screen after the beam vertical deflection. The horizontal displacement of the longitudinal slices is proportional to their energy deviation, $\Delta\delta_{sep}$, through the dispersion function. The slice horizontal width is proportional to the slice energy spread, $\Delta\delta_{SL}$. Hence, the linear chirp is sufficiently small if the slices lateral displacement is much smaller than the slice horizontal width:

$$\Delta x_{sep} \ll \Delta x_{SL} \implies \eta_x \Delta\delta_{sep} \ll \eta_x \Delta\delta_{SL} \implies \alpha \Delta\phi_{SL} \ll 4\sigma_{\delta,SL} \approx \Delta\delta_{uncorr} \quad (4.23)$$

The final form of eq.4.23 is clearly independent of the dispersion and puts a constraint on the energy chirp. By inserting in eq.4.23 the values in Table 4.3 for the BC1 spectrometer line, we obtain: $3.3 \cdot 10^{-3} \ll 2.0 \cdot 10^{-3}$, which is clearly false. Thus, the slice energy spread measured by dividing the bunch duration into 30 slices cannot be interpreted as pure uncorrelated one, unless the number of slices resolved at the screen is increased at least by a factor of 3.

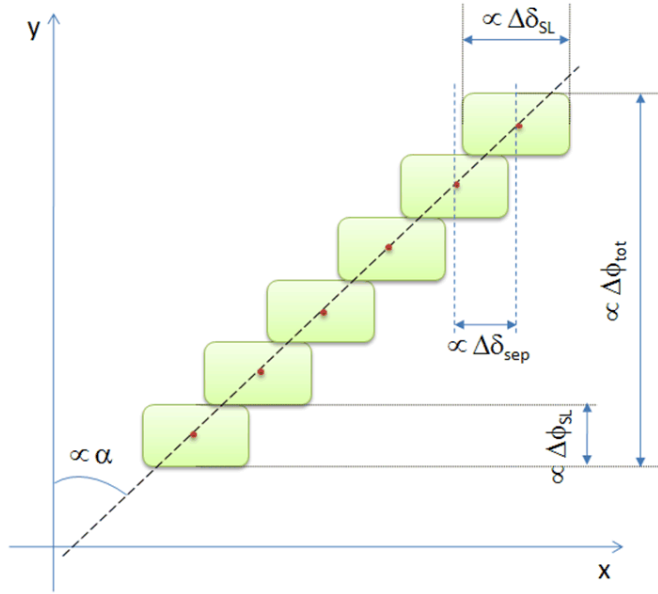


Figure 4.8: Reconstruction of the longitudinal phase space (conceptual). The beam is vertically deflected and then dispersed on a screen in a horizontal spectrometer line.

4.2.3 Screen Resolution

The diagnostic lines depicted so far are thought to be at fixed beam energy, since they do not include any active accelerating element. We now want to consider the beam acceleration along the linac. One of the most sensitive diagnostics to the beam energy change is the screen system that is primarily used to measure the transverse profile of the electron beam. Figure 4.9 shows the evolution of the geometric rms beam size and consequently the required screen resolution.

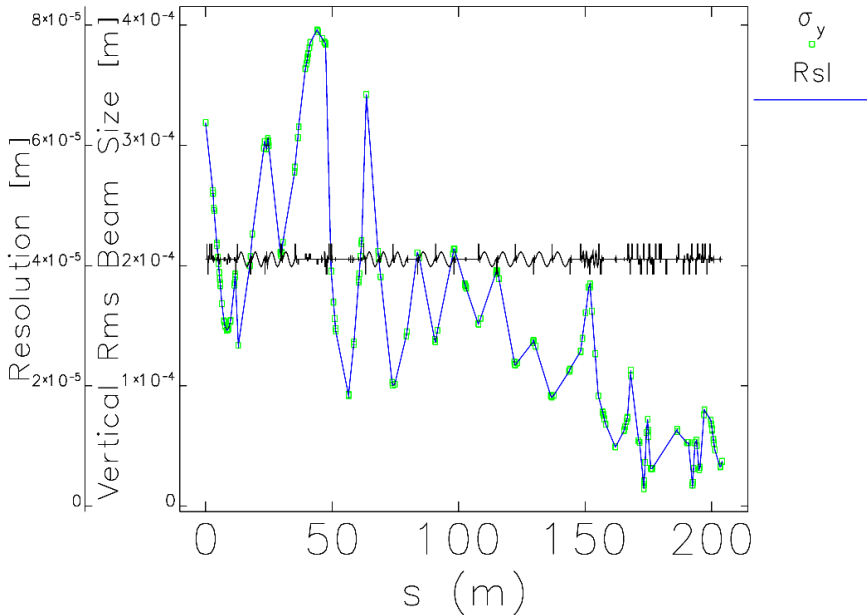


Figure 4.9: Vertical rms beam size and screen resolution from the injector end (100 MeV) to the undulator (1.5 GeV) in FERMI@Elettra. The black line sketches the FERMI layout.

To illustrate this point we recall that, since ϵ_N is an invariant, eq.3.8 determines the energy dependence of the (standard deviation of) beam size, $\sigma = \sqrt{\beta\epsilon}$, when chromatic contributions are neglected. In the realistic assumption of a constant accelerating gradient ($E \sim s$) and for a given average betatron function $\bar{\beta}$ along the accelerator, we have $\sigma \sim 1/\sqrt{s}$. In the FERMI@Elettra linac, $\bar{\beta} \approx 20$ m (see Figure 2.3) and eq.3.8 pushes the resolution of the screen systems

down to the $5\ \mu\text{m}$ level at 1.2–1.5 GeV. The two curves overlap but with different scales, since the rms resolution is defined as 1/5 of the beam size. The normalized emittance is conserved so that the curve is dominated by the oscillating behaviour of the vertical betatron function (compare with Figure 2.3) and by the adiabatic damping of the geometric emittance. The tighter screen resolution is asked to be approximately $5\ \mu\text{m}$ in the Spreader, where the strong quadrupole focusing and the high energy make the beam transverse size very small. Thus, a small betatron function at very high energy could be a limiting factor to the measurement accuracy of the beam transverse size.

4.2.4 Geometric Collimation

Control of beam losses in particle accelerators is often mandatory to protect equipment. This includes preventing halo particles traveling at large amplitudes and eventually hitting the vacuum chamber creating secondary showers. The halo is usually intercepted by absorbing metal blocks called collimators; they locally restrict the vacuum chamber physical aperture without affecting the main beam. The main beam is defined as the ensemble of particles whose trajectory in the pseudocanonical transverse phase space (u, u') , with $u = x, y$, is contained in an ellipse of area ϵ_u , ϵ_u being the transverse geometrical emittance of the beam. By definition, the halo particles have betatron oscillation amplitudes larger than $\sqrt{\epsilon_u \beta_u}$, β_u being the betatron function. To intercept both large amplitude and large angle particles both a primary and a secondary collimator are needed. In the literature, a Collimation System (CS) design usually includes a spoiler and an absorber; the purpose of the spoiler is to increase the transverse footprint of any unwanted particles before they are stopped in the absorber. The present scheme relies instead on a CS consisting of two fully absorbing apertures in the beam path, such as, e.g., a 20 cm long Cu block whose stopping power for electron beams up to the GeV range is high [85].

Collimation systems are used both on linear [86–91] and on circular accelerators [92–94] to minimize background in physics detectors and to limit the irradiation of equipment, possibly leading to demagnetization of undulator permanent magnets. The need of high luminosities in colliders and in linac-based FELs obtained with high beam intensities makes these problems even more serious. 1-D and 2-D detailed analytical studies and particle tracking simulations of CS for circular accelerators are available in the literature. The guiding principle for positioning the secondary collimators in circular accelerators is thought to have been first given in [95] and independently developed in [96, 97]. More recent general principles for two-stage, spoiler plus absorber collimation in circular accelerators have been extensively examined in [98–100]. The optimization criteria of the CS contained in the mentioned references assume the quasi-periodic par-

ticle motion in a storage ring. The choice of the working point, normally clear of resonances in the tune diagram, justifies the assumption that particles touch the primary collimator at their outermost spatial extension. This is not necessarily true in a linac, since particles might reach the primary collimator with a small offset but still with a large angular divergence. The quasi-periodic motion also carries the requirement of a secondary collimator with a larger aperture than that of the first, because particles that do not interact with the primary collimator must not be affected by the secondary one. This is not the case when using full-absorption collimators that are therefore allowed to have the same aperture.

Before illustrating the geometric CS of the FERMI@Elettra linac, a brief review of how the collimation process is described in the literature is given. In [98] the phase advance $\Delta\mu$ between the primary and the secondary collimator is the critical quantity to be chosen in order to minimize the excursion of the particles scattered by the primary collimator:

$$\Delta\mu_{opt} = 2\text{arc sin} \left(\sqrt{\frac{1}{2} \frac{H}{L+H}} \right) \quad (4.24)$$

where L is the normalized half aperture of the primary collimator and H is the normalized step back of the secondary one. In [99, 100] the phase advance between the primary and the secondary collimator is derived by considering the minimum kick that a particle has to receive in the primary collimator in order to be intercepted by the secondary one:

$$\cos \Delta\mu_{opt} = \frac{n_1}{n_2} \quad (4.25)$$

where n_1 and n_2 are the half apertures (in the normalized phase space) of the primary and of the secondary collimator, respectively. By definition, $L > H$ in eq.4.24 and $n_2 > n_1$ in eq.4.25 to prevent particles from hitting the secondary collimator before hitting the primary one. The optimum design of a two-stage, fully absorbing CS in a single-pass linac driving a FEL is presented in [88, 89], where the largest clearance between the collimated beam and the undulator vacuum chamber is defined by a phase advance of $\pi/2$ between the primary and the secondary collimator. A comparison of the CS performance for linac-based FELs is reported in [96], where the effectiveness of the collimation system is quantified by means of particle tracking results in terms of the fraction of initial halo particles that survive the CS. Particle tracking plays a role also in [91, 92, 101] where the *inefficiency* η_c is defined as the ratio of the number $N_i(A_{cut})$ of particles traveling at amplitudes larger than the cut amplitude A_{cut} over the number N_{imp} of particles impacting the collimator; A_{cut} is given by the vacuum

chamber aperture downstream of the CS:

$$\eta_c = \frac{N_i(A_{cut})}{N_{imp}} \quad (4.26)$$

As mentioned before, the above criteria are not necessarily always appropriate to motion in single-pass accelerators, in which angular divergence rather than offset is the primary cause for far-out halo buildup. The present study produces a 1-D analytical expression for the efficiency of a fully absorbing, two-stage collimation system in a single-pass linac that is independent of the number of particles impacting the CS and of their transverse distribution. The expression is a function of the collimators aperture, the vacuum chamber aperture downstream of the CS and the optical functions. Unlike the definition given in eq.4.26, the efficiency is proportional to the number of particles stopped by the real CS over those stopped by the ideal CS and, unlike the prescriptions of eq.4.24 and eq.4.25, the efficiency depends not only on the phase advance between the primary and the secondary collimator but also explicitly on the collimator aperture and the betatron function value. As a result, for some optics and aperture settings, the predicted optimum phase advance in between the primary and the secondary collimator differs from $\pi/2$. Finally, a more general collimation index is defined that also describes the case of a real CS with an acceptance smaller (bigger cleaning capability) than the ideal one.

The analytical approach assumes linear, uncoupled, non-chromatic optics. The case study of low- β symmetric optics defined over a drift space as shown in Figure 4.10 is considered. This choice reflects the optics design in the BC1 diagnostic region, as shown in Figure 4.2. The aim is, given an arbitrary halo particle distribution, to minimize the fraction of halo particles surviving the CS. The result of the analytical approach is then checked against particle tracking with the `elegant` code.

The collimation acceptance is defined in the normalized transverse phase space with particle coordinates:

$$\begin{aligned} X(\mu) &= \sqrt{\epsilon} \cos(\mu + \phi) = \frac{x}{\sqrt{\beta}} \\ X'(\mu) &= \frac{dX}{d\mu} = -\sqrt{\epsilon} \sin(\mu + \phi) = \left(\sqrt{\beta} \frac{dx}{ds} + \alpha \frac{x}{\sqrt{\beta}} \right) \end{aligned} \quad (4.27)$$

where X will be replaced by Y when appropriate. The notation refers to the usual Twiss functions α, β , betatron phase advance (μ), and particle invariant (ϵ) for the plane of interest. This transformation reduces the betatron oscillations to a simple harmonic motion. The simple geometric considerations depicted in Figure 4.11 show that, for a given collimation half aperture g , a phase advance

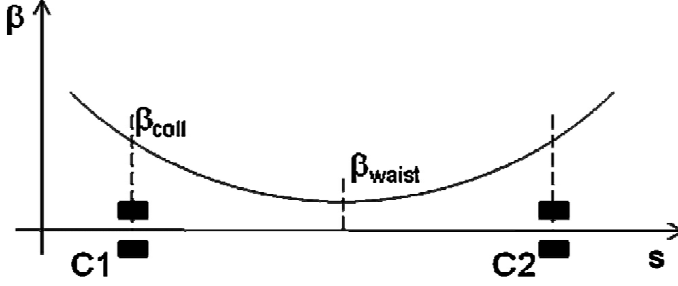


Figure 4.10: Schematic of a two-stage collimation system with low- β symmetric optics.

$\Delta\mu = \pi/2$ between the primary (C1) and the secondary (C2) collimator maximizes the probability of intercepting particles having large betatron amplitude. The circular phase space described by eq.4.27 is represented at the C2 location and limited in spatial position by the collimator half aperture $g/\sqrt{\beta} = |\overline{IO}|$. For a generic phase advance $\Delta\mu$ in between the collimators, the shadow of C1 at the location of C2 is represented by the inclined lines $|\overline{EF}|$, $|\overline{GH}|$ tangent to the circumference. The area $a(\Delta\mu)$ of the parallelogram EFGH is the CS acceptance. By simple geometric considerations (see Figure 4.11) we can infer that:

$$a(\Delta\mu) = 2g(\overline{EM} + \overline{IM} + \overline{HI})/\sqrt{\beta} = 4g^2|\sin \Delta\mu|/\beta \quad (4.28)$$

The parallelogram base \overline{EH} increases monotonically from $2g/\sqrt{\beta}$ to $+\infty$ as $\Delta\mu$ goes from $\pi/2$ to 0 (while its height remains $2g/\sqrt{\beta}$). The minimum acceptance for a given collimator half aperture is therefore the area ABCD corresponding to $\Delta\mu = \pi/2$, $a_{min} = 4g^2/\beta$. For any $g \neq 0$, $a(\Delta\mu) \geq a_{min} > 0$ and $\Delta\mu = \pi/2$ allows one to obtain the same acceptance but with the largest half aperture. This is usually a major goal in order not to restrict the accelerator vacuum chamber and, for this reason, we can set $a_{opt} \equiv a_{min} = 4g^2/\beta$. We propose to define the “collimation efficiency as function of the relative phase advance” between the primary and the secondary collimator as follows:

$$\xi_{coll}(\Delta\mu) = \frac{1/a(\Delta\mu)}{1/a_{min}} = |\sin \Delta\mu| \quad (4.29)$$

where the symbol ξ is used for the collimation efficiency instead of η , in the

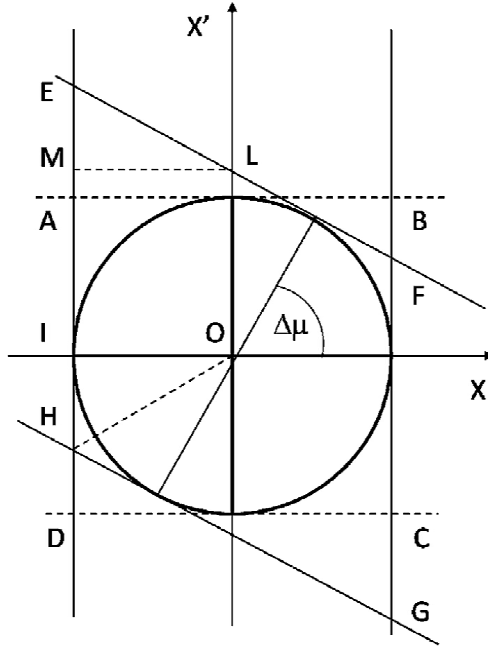


Figure 4.11: Two-stage collimation system acceptance in the normalized phase space.

literature usually referred to signify the collimation inefficiency. For any given incoming beam, the quantity $1/a_{min}$ is supposed to define the optimum number N_{opt} of particles stopped by the CS. Hence, $\xi_{coll}(\Delta\mu)$ can be interpreted as the ratio of the number N_{real} of particles stopped by the real CS over the optimum number N_{opt} .

The CS acceptance has to be fixed according to the area in the transverse plane (x, y) to be protected from stray particles. Inside the vacuum chamber, for simplicity assumed as cylindrical, a safety clearance area of width $\Delta = R - r \geq 0$ is defined. The main goal of the CS is to prevent particles traveling through the real space in the shaded region $(R - r)$ of Figure 4.12. Here, $R = \overline{OA}$ is the chamber radius; $r = \overline{OC}$ is the beam-stay-clear radius; a clearance ring of width $\Delta = \overline{BC}$ prevents particles from hitting the vacuum chamber surface. The collimator half aperture footprint $g = \overline{OD}$ is also projected on the (x, y) plane (not to scale). With reference to Figure 4.12, the optimum collimator acceptance

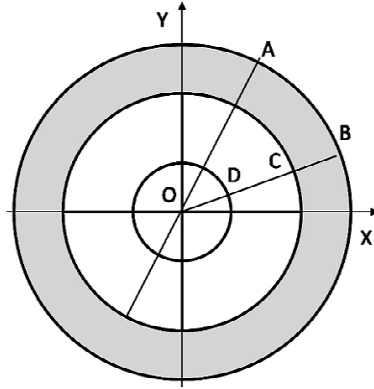


Figure 4.12: Cross section of the undulator vacuum shadowed by collimators.

a_{opt} can be defined for any $\Delta_{opt} > 0$ as follows [88, 89]:

$$a_{opt} = \frac{(R - \Delta_{opt})^2}{2\beta_0} = \frac{r_{opt}^2}{2\beta_0} \quad (4.30)$$

where β_0 is the maximum betatron function over the layout region to be protected by particle hits. The optimum collimator half aperture is then calculated for a given betatron function β_{coll} at the collimator. One has:

$$g_{opt} = \sqrt{a_{opt}\beta_{coll}} \quad (4.31)$$

Once a_{opt} is fixed by eq.4.30, then g_{opt} is also specified. However, the practical lower limit of the collimator half aperture is usually determined by the effect of the transverse wake field in the collimator on the main beam dynamics [102, 103] and the real half aperture g may happen to become larger than g_{opt} . Now, we assume $r = \sqrt{2\beta_0 a} = g\sqrt{2\beta_0/\beta_{coll}}$ to be the radius of the CS defined by the real acceptance a or, equivalently, by the real gap g , is different from the optimum value r_{opt} in eq.4.30. For any $0 \leq \Delta \leq \Delta_{opt}$, one can define the ‘‘collimation efficiency as function of the collimator half aperture’’ as follows:

$$\tilde{\zeta}_{coll}(r) = \frac{R^2 - r^2}{R^2 - r_{opt}^2} \quad (4.32)$$

By definition, $0 \leq \zeta(r) \leq 1$ and it describes the ratio of the clearance area defined by the real CS over its nominal value. The optimum case of unity efficiency is given by $r = r_{opt}$, when particles are stopped exactly at the desired amplitude r_{opt} . When $r = R$, the CS does not shadow the downstream vacuum chamber, all particles are allowed to hit the chamber and therefore the efficiency is zero.

In order to characterize the expected CS performance both in terms of the phase advance between the primary and the secondary collimator and of their half aperture, we propose the following definition of "collimation index" as the product of the two efficiencies in eq.4.29 and in eq.4.32:

$$\chi_{coll} = \frac{R^2 - r^2}{R^2 - r_{opt}^2} |\sin \Delta\mu| \quad (4.33)$$

The physical meaning of eq.4.33 is the following.

(i) For any width of the clearance area $0 \leq \Delta \leq \Delta_{opt}$ we have $0 \leq \chi \leq 1$ and χ can be interpreted as general collimation efficiency. In this case, the relative phase advance that gives the (local) maximum of collimation efficiency is $\pi/2$. Alternatively, if the phase advance is fixed, the collimation efficiency is maximum for $\Delta = \Delta_{opt}$.

(ii) For any width of the clearance area $\Delta_{opt} < \Delta \leq R$, χ_{coll} can be greater than 1, in which case it describes a CS that, for the same incoming beam, is stopping more particles than in the ideal case.

(iii) A null phase advance leads to zero efficiency because it implies that one collimator only is active; thus, for any finite collimator half aperture there is no cleaning of particle angular divergence. Alternatively, a clearance area of width $\Delta = 0$ leads to zero efficiency because, for any phase advance between the collimators, it allows particles to travel at amplitudes as large as R in the downstream vacuum chamber.

Eq.4.33 can be made more explicit by substituting eq.4.30 into eq.4.32 and then giving the explicit dependence of β_{coll} on the lattice geometry. A simple case is given by the two-stage CS in the presence of low- β symmetric optics, as shown in Figure 4.10. This is clearly the case of the FERMI optics in the linac diagnostic areas (see Section 2.3). If $\check{\beta}$ is the betatron function at the waist and Δs is the CS half length, then we have:

$$\left\{ \begin{array}{l} \beta(\Delta s) = \check{\beta} + \frac{\Delta s^2}{\check{\beta}} \\ \Delta\mu(\Delta s) = 2 \arctan\left(\frac{\Delta s}{\check{\beta}}\right) \end{array} \right. \Rightarrow \left\{ \begin{array}{l} \Delta s = \sqrt{\check{\beta}(\beta(\Delta s) - \check{\beta})} \\ \Delta\mu(\Delta s) = 2 \arctan\left(\sqrt{\frac{\beta(\Delta s) - \check{\beta}}{\check{\beta}}}\right) \end{array} \right. \quad (4.34)$$

finally giving:

$$\beta(\Delta s) = \beta_{coll} = \check{\beta} \left[1 + \tan^2\left(\frac{\Delta\mu}{2}\right) \right] \quad (4.35)$$

where $0 \leq \Delta\mu \leq \pi$. Substituting eqs.4.30, 4.31 and 4.33 into 4.35, we obtain:

$$\chi_{coll} = \frac{R^2 - g^2 \frac{\beta_0}{\beta} (1 + \cos \Delta\mu)}{R^2 - r_{opt}^2} \sin \Delta\mu \quad (4.36)$$

Let us now assume that the geometrical or optical parameters of the CS might not be free parameters because of wake field effect, space limitations, costs, or specific optics set for diagnostic purposes. Owing to the trigonometric functions in 4.36 and for any $r_{opt} \leq r \leq R$, the maximum of collimation efficiency does not necessarily occur at the $\pi/2$ phase advance. For example, if the collimator is defined with a half aperture larger than its optimum value, a wider phase advance could be adopted to obtain larger betatron functions at the collimators. Figure 4.13 shows the collimation index χ_{coll} as defined in eq.4.36, as a function of the CS phase advance $\Delta\mu$. The solid curve refers to the optimum set of parameters (nominal collimator half-aperture 1.4 mm): $\chi_{coll} = 1$ at 90 deg. The dotted curve and the dashed curve refer to a smaller (1.2 mm) and a bigger (1.6 mm) collimator half aperture, respectively. In these cases, χ_{coll} can be restored to 1 at 71.4 deg and at 104.4 deg phase advance, respectively. The bottom line shows the betatron function at the collimators location. Table 4.4 lists the fixed parameters used for the calculation: the vacuum chamber radius and the clearance aperture downstream of the CS, the betatron function at the waist and at its maximum downstream of the CS. Table 4.5 summarizes the parameters that vary when different curves are considered. The proposed scenario well fits the optics parameter and layout of the CS in the FERMI@Elettra diagnostic areas, located downstream of BC1 and of the whole linac.

Table 4.4: Fixed parameters of the 2-stage collimation system.

Parameter	Value	Unit
R	3.5	mm
Δ/R	0.2	
β_0	12	m
β_{waist}	3	m

The validity of the analytical results shown in Figure 4.13 and in Table 4.5 has been benchmarked with particle tracking. As mentioned before, eqs.4.33 and 4.36 were defined, for any given incoming beam, as the ratio of quantities proportional to the number of particles stopped by the real CS over the design value. Similarly, the collimation performance extracted from simulation results is here determined by the ratio of the number of particles stopped by the real CS

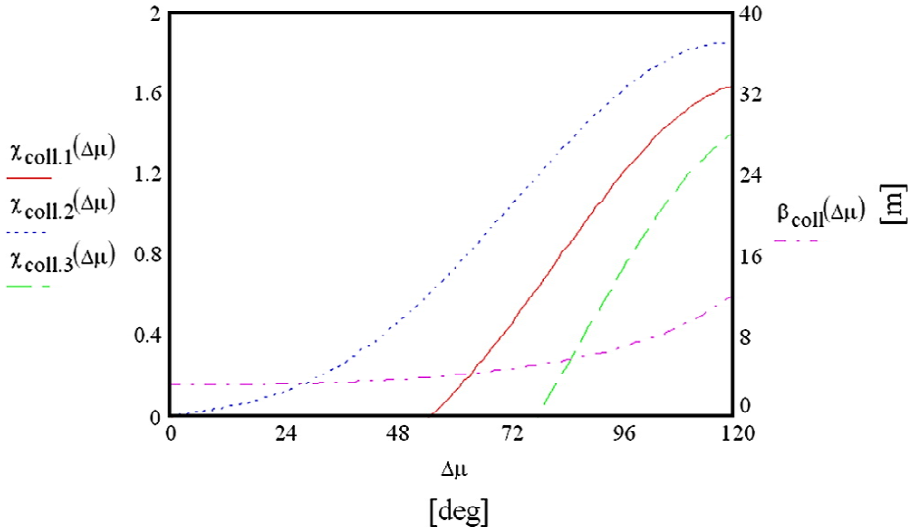


Figure 4.13: Collimation index χ_{coll} vs. relative betatron phase advance between the two fully absorbing geometric collimators.

Table 4.5: Optics parameters to restore the optimum collimation defined by $\chi_{coll} = 1$.

Collimator half aperture [mm]	Optimum phase advance [deg]	Δs [m]	β_{coll} [m]
1.4	90	3.0	6.0
1.2	71.4	2.16	4.6
1.6	104.4	3.87	7.98

over the number of particles stopped by the nominal layout, both evaluated at the downstream location where $\beta = \beta_0$:

$$\chi_{sim}(\beta_0) = \frac{N_{real}}{N_{opt}} \quad (4.37)$$

The 0.7 nC charge of the main beam at the entrance of the CS has a symmetric Gaussian distribution in (x, x') and (y, y') with a 3-sigma cutoff in phase space.

Its rms geometric emittance is $0.91 \cdot 10^{-8}$ mm mrad. The 0.3 nC charge halo beam is depicted by a symmetric Gaussian particle distribution in (x, x') and (y, y') , centered on the main beam axis and extending at radius twice that of the main beam. The mean energy is 250 MeV and rms energy spread of 0.1%; no energy chirp is considered. The whole beam is represented by 10^5 particle self-generated by elegant and matched to the lattice optics. Figure 4.14 shows the particle distribution after horizontal collimation for the CS parameters listed in Tables 4.4 and 4.5, half aperture 1.4 mm.

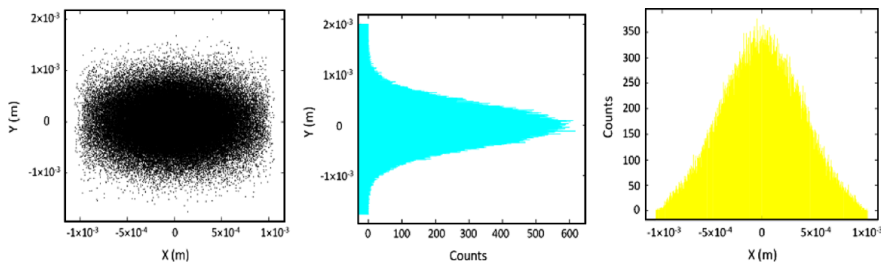


Figure 4.14: Particle distribution after horizontal collimation. From left to right: physical transverse plane (x, y) observed downstream of the CS, where $\beta = \beta_0 = 12$ m; vertical particle distribution with $\sigma_y = 0.415$ mm; horizontal particle distribution with $\sigma_x = 0.388$ mm. The absorbing coefficient predicted by elegant code for 10^5 initial particles is 3.3%.

The optimum cleaning is defined by the two-stage CS as described by the geometrical parameters listed in Table 4.4 and in Table 4.5, for a nominal collimator half aperture of 1.4 mm and a relative phase advance of 90 deg. The two collimators C1 and C2 are identical, rectangular and perfectly absorbing. In this ideal case, the percentage of stopped particles is $N_{opt} = 3.3\%$ and this defines the unity collimation efficiency (in other words, it is supposed the user wants to stop exactly this amount of particles). We now assume that the installed collimators have a half aperture different from the nominal. If the magnetic lattice cannot be changed – for example, due to stronger constraints on the optics or if there is no space available for a different configuration of the CS –, then the collimation efficiency changes.

Table 4.6 shows that the collimation performance simulated by elegant agrees with the analytical prediction both for smaller and larger half apertures than the nominal one, with a discrepancy of 6% and 20%, respectively (numbers in parentheses refer to the 2-D collimation performed with rectangular jaws; in this

case, the 2-D collimation index is calculated as the product of the two 1-D ones). Several runs with different seeding numbers generating the initial particle distribution show fluctuations within 10% of χ_{sim} that are intrinsic to the tracking procedure; this uncertainty reduces the discrepancy between χ_{sim} and χ_{coll} .

As a final check, the optics is rematched in elegant for the 1.2 and 1.6 mm half apertures to re-establish the unity collimation efficiency according to the analytical prescriptions in Table 4.5. The resulting collimation efficiencies are listed in Table 4.7; they converge towards the (nominal) unity value with a discrepancy smaller than 9%.

Table 4.6: Simulated and analytical collimation performance for $\pi/2$ phase advance.

Collimator half aperture [mm]	$\Delta\mu_{C1-C2}$ [deg]	Particles stopped [%]	$\sigma(\beta_0)$ [μm]	χ_{sim} Eq.4.36	χ_{coll} Eq.4.33
1.4	90	3.3 (6.7)	391	1.0 (1.0)	1.0 (1.0)
1.2	90	7.9 (15.3)	369	1.4 (2.3)	1.5 (2.3)
1.6	90	1.3 (2.5)	404	0.6 (0.4)	0.5 (0.3)

Table 4.7: Simulated and analytical collimation performance for optimum phase advance.

Collimator half aperture [mm]	$\Delta\mu_{C1-C2}$ [deg]	Particles stopped [%]	$\sigma(\beta_0)$ [μm]	χ_{sim} Eq.4.36	χ_{coll} Eq.4.33
1.4	90	3.3 (6.7)	391	1.0 (1.0)	1.0 (1.0)
1.2	71.4	3.6 (7.5)	395	1.4 (2.3)	1.09 (1.12)
1.6	104.4	3.5 (6.9)	388	0.6 (0.4)	0.6 (1.03)

As already mentioned, eq.4.36 well suits to the low- β symmetric optics that was designed for the BC1 diagnostic area. Geometric collimation of the electron beam has to be installed downstream of BC1 to clean up the halo particles that could be generated during the bunch length compression because of energy- or optics-mismatch. According to eq.4.36, a two-stage, full absorbing CS with half-aperture of 2 mm and relative phase advance $\Delta\mu_{x,y} = 2\pi/3$ between the two collimators, in each transverse plane, completely shadows the undulator chamber with minimum half-gap of 3.5 mm in the vertical plane. A clearance distance from the inner chamber surface of 20% of the inner radius was assumed. The real device installed in the FERMI linac, downstream of the BC1 magnetic

chicane and also at the linac end, has two other optional half-apertures of 3 and 4 mm radius to make the CS more flexible in terms of beam acceptance. Nominally, these larger apertures do not shadow the undulator chamber but are still able to stop particles traveling at amplitudes larger than the mentioned gap. The real efficiency and stopping power of the CS should then be verified by tracking more detailed halo particle distributions and, of course, during commissioning.

4.3 Conclusions

The analytical evaluation of the effect of the magnetic field errors, magnet misalignments and chromatic aberrations in the presence of linear and nonlinear fields on the transverse beam dynamics in the FERMI@Elettra linac has been presented. Using the beam matrix formalism and theory of field expansion introduced in Section 3.2, the specifications for the magnets field quality and alignment have been given in order to limit the emittance dilution to 1% for each individual error source. Then, in the assumption of linear optics transport, the design of a dispersion-free, straight diagnostic line and of a dispersive diagnostic line has been presented. With particular attention to the FERMI@Elettra lattice, the BC1 region for electron beam diagnostic and production has been discussed. The optics requirements coming from the beam diagnostic performance have been integrated into the optics design. So, the intrinsic resolution of the mean energy and energy spread measurement has been evaluated. The possibility of measuring the correlated, uncorrelated and slice energy spread at all the dispersive lines of the FERMI@Elettra lattice has also been investigated. The measurement of several beam parameters has been simulated with particle tracking. Finally, a two-stage station for beam geometric collimation, integrated into the straight diagnostic line, has been discussed. The collimation efficiency has been analytically defined and the theoretical prediction for the BC1 case study agrees well with the result of particle tracking.

Chapter 5

Machine Design and Electron Beam Collective Effects

This Chapter¹ deals with the collective effects of the electron beam during its transport from the injector end to the undulator, including the magnetic bunch length compression. The collective effects are due the interaction of the particle distribution with the electromagnetic field generated by the distribution itself. Under certain assumptions for the electron beam parameters and strength of the collective effects, the beam dynamics in the presence of these perturbations can be predicted analytically, as shown in Chapter 3. So, the SC forces are parametrized by the laminarity parameter; the effects of the structural wake fields are evaluated for relatively short bunches; the gain of the so-called microbunching instability is computed in the linear regime. However, when the theoretical model presents some lack of accuracy – for example, when it relies on approximations that are not satisfied by more realistic beam parameters –, particle tracking codes are used to support the design of the accelerator system. This happens for the short-range SC forces that might corrupt, for very high charge densities, the linear theory of compression. The effect of the structural wake fields on the longitudinal and on the transverse beam dynamics is characterized in terms of the correlations established between the particles' coordinates along

¹This Chapter is based on the following works: *Formation of electron bunches for harmonic cascade X-ray free electron lasers*, Phys. Rev. Special Topics – Accel. and Beams, **9**, 120701 (2006), by M. Cornacchia, S. Di Mitri, G. Penco and A. A. Zholents. *Single-bunch emittance preservation in the presence of trajectory jitter for FERMI@Elettra seeded FEL*, Nucl. Instr. and Methods in Phys. Research A, **604** (2009) 457–465, by P. Craievich, S. Di Mitri and A. A. Zholents. *Design and simulation challenges for FERMI@Elettra*, Nucl. Instr. and Methods in Phys. Research A, **608** (2009) 19–27, by S. Di Mitri et al. *Comparative study of the FERMI@Elettra linac, with one and two-stage electron bunch length compression*, THPB03 in Proc. of Free Electron Laser Conf. 2010, Malmo, Sweden, by S. Di Mitri et al.

the bunch. The interplay of LSC force and the coherent emission of synchrotron radiation in the presence of magnetic compression is simulated to investigate the nonlinear regime of the microbunching instability. In most of the mentioned cases, a cure for the minimization of the collective effect perturbation due to collective effects is proposed and its feasibility verified with analytical methods and/or particle tracking simulations.

5.1 Short-Range Space Charge Forces

The importance of short-range SC forces on the electron beam dynamics along the FERMI linac is here investigated by means of the laminarity parameter defined by eq.3.54. The laminarity parameter is computed along the beam line on the basis of the beam parameters provided by the particle tracking. Linac regions where the laminarity parameter is much higher than 1 could therefore be investigated with dedicated codes that also provide the simulation of the 3-D SC forces. We consider the two following scenarios for FERMI@Elettra: a 350 pC bunch compressed to reach 0.5 kA and a 800 pC bunch compressed to reach 1 kA. In both scenarios, $\epsilon_{th} = 0.6$ mm mrad, $\gamma' = 39.1$ (corresponding to 20 MV/m); one- or two-stage compression can be adopted equivalently. The transition energy computed with eq.3.55 is, respectively, 500 MeV and 1 GeV. Since the beam energy at BC2 – where the maximum peak current is finally reached – is approximately 600 MeV, we can state that the beam dynamics is not space charge dominated in the case of low charge/two-stage compression (this has a threshold at 500 MeV) and only weakly dominated in the high charge/two-stage compression (this has a threshold at 1 GeV). Instead, the one-stage compression is performed with BC1 at the energy of 350 MeV that is well below the computed thresholds for the low as well as the high charge scenario. Accordingly, a careful study of the 3-D beam dynamics in the presence of SC forces has been carried out for the one-stage compression. This study is reported in Section 5.5.

Figure 5.1 shows the laminarity parameter, eq.3.54 with $\Omega = 0$, computed on the basis of the particle tracking in the FERMI linac, performed with the `elegant` code, from the injector end to the linac end, in the configuration of one-stage compression. No external solenoid focusing is considered. A conservative average accelerating gradient of 16 MV/m is adopted. The beam parameters listed in Table 2.2 for FEL1 Commissioning and Operation are used. The laminarity parameter and the peak current are computed as the average value over the bunch core, which runs over $\sim 80\%$ of the total bunch length. CSR and linac wake fields collective effects are included. In agreement with the previous estimations, we find that the beam dynamics in the high charge configuration is much more strongly affected from SC forces than at low charge.

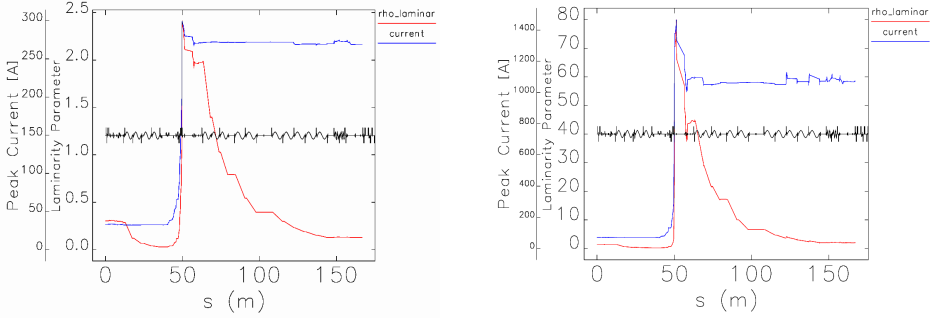


Figure 5.1: Laminarity parameter along the FERMI linac. Left: 350 pC compressed by a factor of 6.5. Right: 800 pC compressed by a factor of 10. In both cases, $\rho_L \gg 1$ immediately downstream of BC1 (notice that the vertical scales are different in the two plots), exactly where the peak current in the bunch core rises to 1 kA. Then ρ_L falls down with $\sim \gamma^{-2}$ dependence.

5.2 Longitudinal Structural Wake Field

5.2.1 Energy Loss

Relying on the analytical model depicted in Section 3.3.2, we are now going to evaluate the effect of the longitudinal structural wake field on the electron energy distribution along the FERMI linac. The longitudinal wake potential induces a total energy loss of the electron beam so that the relative energy change at the bunch length coordinate \bar{z} is [59]:

$$\delta_w(\bar{z}) = -\frac{e^2 L}{\gamma m c^2} \int_0^\infty w(z) n(\bar{z} - z) dz \quad (5.1)$$

where $n(\bar{z} - z)$ is the longitudinal particle distribution with normalization $\int_{-\infty}^\infty n(z) dz = N$ (N is the total number of electrons in the bunch). As an example, for a uniform longitudinal bunch profile, one has $n(z) = N / (2\sqrt{3}\sigma_z)$ for $|z| \leq \sqrt{3}\sigma_z$ and $n(z) = 0$ for $|z| > \sqrt{3}\sigma_z$. If the constant wake function in eq.3.58 is used, then eq.5.1 yields a linear wake-induced energy change along the bunch coordinate:

$$\delta_w(\bar{z}) = -\frac{2Nr_e L}{\gamma a^2} \left(1 + \frac{\bar{z}}{\sqrt{3}\sigma_z} \right) \quad (5.2)$$

where we have used the identity $Z_0 c \epsilon_0 = 1$; $r_e = 2.82 \cdot 10^{-15}$ m is the classical electron radius. It is straightforward to calculate the standard deviation of the

wake-induced relative energy loss:

$$\sqrt{\langle \delta_w(\bar{z})^2 \rangle} = -\frac{2}{\sqrt{3}} \frac{Nr_e L}{\gamma a^2} \quad (5.3)$$

Eq.5.3 can be used to roughly estimate the energy loss induced by the geometric longitudinal wake field in the FERMI linac. Taking into account the specific iris radius and length of the various accelerating structures, we obtain a total loss of approximately 10 MeV. Since the uncorrelated energy spread is a few order of magnitudes smaller than this, the energy loss translates into correlated energy spread. In the linear approximation, it could be removed by running off-crest some accelerating structures at the end of the linac in order to compensate this additional $\sim 1\%$ energy chirp.

The estimation can be made more accurate by considering the exponential behaviour of the wake functions in eqs. 3.60–3.62. The non-exponential terms in eq.3.62 were added to fit the analytical wake function of the BTW structures in case of bunches longer than 1.5 mm; they are neglected in the following treatment. By substituting eq.3.59 in eq.5.1, we integrate by parts with the change of variable $u = \sqrt{z/s_0}$ and we finally find the following expression for the induced average energy change per electron, normalized to the beam mean energy:

$$\langle \delta_w \rangle = -\frac{4}{\sqrt{3}} \frac{Nr_e L s_0}{a^2 \gamma \sigma_z} \left[1 - \left(1 + \sqrt{\frac{2\sqrt{3}\sigma_z}{s_0}} \right) e^{-\sqrt{\frac{2\sqrt{3}\sigma_z}{s_0}}} \right] \quad (5.4)$$

With this result, the total energy loss in the FERMI linac is expected to be 15.6 MeV.

5.2.2 Cubic Energy Chirp

The effect of the structural longitudinal wake field in terms of energy loss has been estimated for FERMI@Elettra in the previous Section. The standard theory of compensation of the quadratic energy chirp during magnetic bunch length compression has already been exposed in Section 3.2.2. We now move to discuss the more subtle effect of a cubic energy chirp. A significant cubic energy chirp has three main disrupting consequences: i) it reduces the efficiency of the magnetic compression for the bunch core, since during the compression, the edges "attract" particles from the core reducing the current in this region; ii) it induces current spikes at the edges that may be dangerous sources of CSR, with a direct impact on the transverse emittance and on the energy distribution; iii) wake field excited by a leading edge spike may cause additional energy spread in the low gap undulator vacuum chambers.

The sign of the cubic energy chirp in the photo-injector is mainly determined by SC forces. It is always negative for a flat-top charge distribution [30]. After the interaction with longitudinal wake fields, this sign is reversed at the entrance of the second compressor, enhancing the energy-position correlation of the bunch edges with respect to the core. The edges are there over-compressed producing current spikes. On the contrary, a negative cubic chirp at the chicane provides under-compression of the edges. For these reasons the sign of the cubic term is related to the topology of the longitudinal phase space and to the final current profile. This is illustrated in Figure 5.2.

For a given charge and bunch length, the interaction of the cubic chirp coming from the injector with the longitudinal wake field of the succeeding linac cannot be arbitrarily manipulated. However, the user has one more degree of freedom to manage the cubic chirp before reaching the magnetic compressor, that is by setting the harmonic cavity a few X-band degrees away from the usual decelerating crest. In some cases this knob may be weak and a significant increase is needed in the amplitude of the cavity voltage. For a one-stage compression the following parameters are defined: $k = 2\pi/\lambda_{RF}$ is the RF wave number and λ_{RF} is the RF wavelength; U_0 is the voltage amplitude of a first linac accelerating on-crest (L0 for FERMI); U_1 is the amplitude of a second linac (L1) with off-crest acceleration at phase ϕ_1 , referred to the crest of the RF wave; U_x and ϕ_x are the amplitude and phase of the RF harmonic cavity. Given the initial energy E_0 , the final energy of the particle at coordinate z from the centroid is given by:

$$E_f = E_0 + U_0 \sin(k_s z) + U_1 \sin(k_s z + \phi_1) + U_x \sin(k_x z + \phi_x) \quad (5.5)$$

The cubic energy chirp is simply computed as the third consecutive derivative of eq.5.5. We now assume that the longitudinal wake field is negligible in the linac section upstream of the compressor. Thus, the cubic chirp is canceled if $\Delta E''_{z=0} = 0$ that is:

$$U_x \cos \phi_x = - \left(\frac{k_s}{k_x} \right)^3 (U_0 + U_1 \cos \phi_1) \quad (5.6)$$

So far, we do not consider the 2nd order dynamics in the magnetic compressor. With zero cubic chirp, the quadratic chirp is canceled in the equation for $\Delta E''_{z=0} = 0$ by imposing:

$$\tan \phi_x = \frac{k_x}{k_s} \left(\frac{U_0 + U_1 \sin \phi_1}{U_0 + U_1 \cos \phi_1} \right) \quad (5.7)$$

Hence, eqs.5.6 and 5.7 define the space where parameters of the harmonic cavity can be moved in order to linearize the longitudinal phase space up to the 3rd

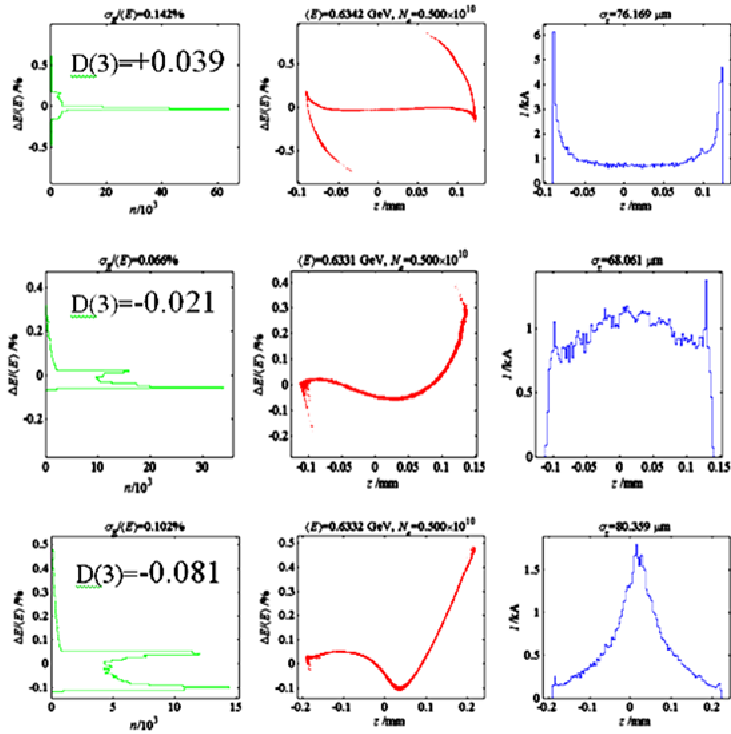


Figure 5.2: Longitudinal dynamics in the presence of cubic energy chirp. The energy distribution (left), the longitudinal phase space (center) and the corresponding current profile (right) generated by LiTrack [104] tracking code are shown, in the presence of three different values of the cubic energy chirp, $D(3)$, in units of 0.01 mm^{-3} , at the entrance of BC1. The positive sign is related to an over-compression of the bunch edges (top), while a negative sign is related to their under-compression (bottom).

order. If the 2^{nd} order dynamics in the magnetic chicane is considered instead, U_x is fixed by eq.3.51 and ϕ_x is computed from eq.5.6.

We are now going to include the longitudinal wake field into our analysis. Using a parabolic electron density distribution with 10 ps length (fwhm value) and with a total charge of 0.8 nC, the wake potential induced by the L0 and L1 accelerating structures (for a total length of 30 m) is shown in Figure 5.3. The black line is the actual calculation and the blue line is fit with a polynomial up

to 3rd power (the artificial vertical offset in the blue line is made to avoid the overlap of the two curves). The result is fit by the 3rd order polynomial:

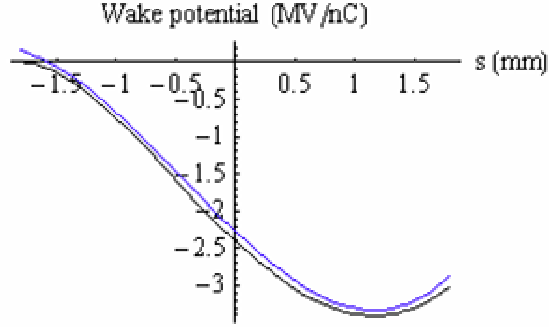


Figure 5.3: Wake potential for 0.8 nC bunch with parabolic density distribution.

$$w_z(z) = \frac{k^3 a_3}{3!} z^3 + \frac{k^2 a_2}{2!} z^2 + k a_1 z + a_0 \quad (5.8)$$

where $a_0 \approx -2.38$ MV/nC, $a_1 \approx -24.2$ MV/nC, $a_2 \approx 144$ MV/nC and $a_3 \approx 5000$ MV/nC. The RF wave number k is introduced for convenience in order to give dimensions of wake potential to the coefficients a_0 , a_1 , a_2 and a_3 . When $w_z(z)Q$ – where Q is the bunch charge – is added to the energy gain in eq. 5.5, it modifies all derivatives of the equation for $\Delta E'_{z=0} = 0$ with the addition of Qka_1 , $Qk^2 a_2$ and $Qk^3 a_3$ in the first, second and third derivative, respectively. Again, the quadratic chirp (second derivative) becomes zero when:

$$U_x \sin \phi_x = - \left(\frac{k_s}{k_x} \right)^2 (U_0 + U_1 \sin \phi_1 - Qa_2) \quad (5.9)$$

With this result, the first derivative can be written as:

$$\Delta E'_{z=0} = k_s U_1 \cos \phi_1 + \frac{k_s^2}{k_x} [U_0 + U_1 \sin \phi_1 - Qa_2] \tan \phi_x + Qk_s a_1 \quad (5.10)$$

This expression can be used to redefine the energy chirp used for magnetic bunch length compression in the presence of longitudinal wake field. With zero

quadratic chirp as in eq. 5.9, the cubic energy chirp in eq. 5.5 now takes the following form:

$$\Delta E''_{z=0} = -k_s^3 (U_0 + U_1 \cos \phi_1 + Qa_3) + k_x k_s^2 \tan \phi_x (U_0 + U_1 \sin \phi_1 - Qa_2) \quad (5.11)$$

As a numerical example, in FERMI@Elettra we use $k_s = 2\pi/100 \text{ mm}^{-1}$, $Q=0.8 \text{ nC}$ and a typical accelerator set-up with $\phi_x = 0$ and $\Delta E'_{z=0} = 3.3 \text{ MV/mm}$. With the fitted values of the afore-mentioned wake potential coefficients, eq. 5.10 gives $U_1 \cos \phi_1 = 76.1 \text{ MV}$. This is to be compared in eq.5.11 with $Qa_3 \approx 5000 \text{ MV}$. Thus, we have demonstrated that the cubic energy chirp in the FERMI linac is totally dominated by a contribution from the longitudinal wake potential, rather than by higher order terms from the RF curvature. For the FERMI@Elettra case, eqs. 3.51, eq.5.11 and the constraint of a null cubic chirp $\Delta E''_{z=0} = 0$ are used to analytically determine the X-band cavity voltage and phase setting. Simulations confirm the analysis and the X-band cavity is therefore specified to have a nominal peak voltage of 20 MV to linearize the longitudinal phase space up to the 2nd order during the bunch length compression. The RF phase is usually shifted by approximately 4 X-band degrees from the decelerating crest to cancel the cubic energy chirp. Some small adjustments to the voltage and to the phase could be necessary in the simulations with respect to the present analysis, depending on the cubic energy chirp coming from the injector and on the effective compression factor. A tuning range 19–22 MV is actually specified in order to allow some flexibility in the compression scheme and magnetic chicane bending angle.

Since the cubic energy chirp is responsible for the appearance of a bifurcation in the phase space after the bunch compressor and this phase space distortion in turn leads to spikes in the peak current at the edges of the electron bunch, it is desirable to minimize a_3 . One way to achieve this is to use a density distribution other than the parabolic one considered so far. For example, a distribution with a linearly ramped peak current as shown in the next Section gives a wake potential with a significantly reduced cubic chirp $a_3 \approx 890 \text{ MV/nC}$. This is one of the motivations leading to the technique of current shaping discussed in the following Section.

5.2.3 Current Shaping

The basic premise for current shaping is that the output bunch configuration is largely pre-determined by the input bunch configuration and that therefore it is possible to find a unique electron density distribution at the beginning of the linac that produces a flat-flat distribution at the end of the linac. Finding this distribution can be relatively easy. One just needs to reverse the problem, i.e. start at the end of the linac and move backwards towards the beginning of

the linac. Eq.5.12 shows that for a given electron density λ_z and wake function w_z , the electron energy at the end of a section of the linac, defined as δ_f (with z_f being the electron coordinate taken with respect to the bunch center), can be determined using the electron energy δ_i and the coordinate z_i at the beginning of the section:

$$\delta_f(z_f) = \delta_i(z_i) + eU \cos(kz_i + \phi) - LQ \int_{z_i}^{+\infty} w_z(z_i - z') \lambda_z(z') dz' \quad (5.12)$$

where U, ϕ, L define the RF voltage, phase and length of the linac section, k is the wave number, e is the electron charge and Q is the bunch charge. For a relativistic beam the electron distribution function λ_z does not change during acceleration, i.e. $z_i = z_f$, and, therefore, eq.5.12 can be used to define $\delta_i(z_i)$ as a function of $\delta_f(z_f = z_i)$. Thus, beginning with a desirable electron distribution at the end of the linac section, one can find the distribution at the beginning of the linac section that will eventually make it.

A different situation arises in a bunch compressor where the electron coordinate at the end of the bunch compressor $z_f(\delta_f)$ becomes a function of the electron coordinates z_i and energy δ_i at the beginning of the bunch compressor:

$$z_f(\delta_f) = z_i(\delta_i) + R_{56}\delta_i + T_{566}\delta_i^2 + f_{CSR}(z_i, \delta_i) \quad (5.13)$$

where R_{56}, T_{566} are first and second order time-of-flight parameters and a function f_{CSR} describes changes related to the CSR effects. In the case of a smooth electron density distribution, the emission of synchrotron radiation is coherent at frequencies $\omega \leq c/l_b$, where c is the speed of light and l_b is the bunch length. Since the loss of electron energy due to CSR is negligible with respect to that induced by the longitudinal wake field in the linac, one can ignore CSR and assume that the electron energy is not affected in the magnets of the bunch compressor, i.e. $\delta_f = \delta_i$ (this assumption will be justified later on for the FERMI case study). Then, the electron coordinate at the beginning of the bunch compressor can be found using the electron coordinate at the end of the bunch compressor using eq.5.13.

The above considerations justify a concept of reverse tracking demonstrated in Figure 5.4. For each group of plots, the left image shows the longitudinal phase space, while the right one shows the corresponding current profile. The code was run with input particle distribution shown at the top line of each group; the final particle distribution is at the bottom line of each group. The result of this tracking (bottom right section) agrees well with the initial distribution (top left section).

In the next step, a desirable flat-flat distribution is set up at the end of the accelerator. Starting with this distribution and tracking it backward, the nearly linear ramped peak current shown in Figure 5.5 is obtained at the start of the

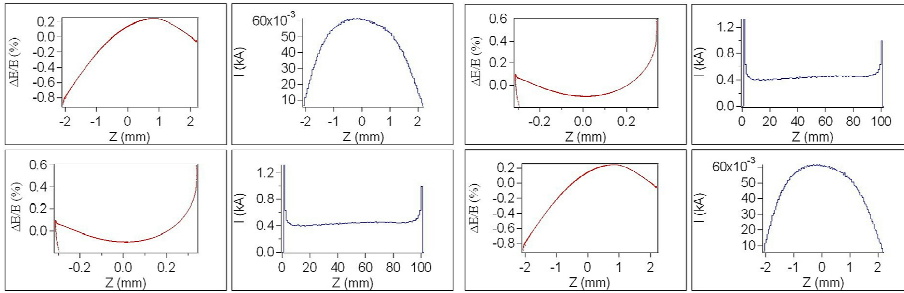


Figure 5.4: Conceptual demonstration of the reverse particle tracking. Left plot shows the result of conventional forward particle tracking obtained with LiTrack starting with the particle distribution at the beginning of the linac. Right plot shows the reverse tracking starting with the distribution obtained at the end of the first tracking (see top right and bottom left sections).

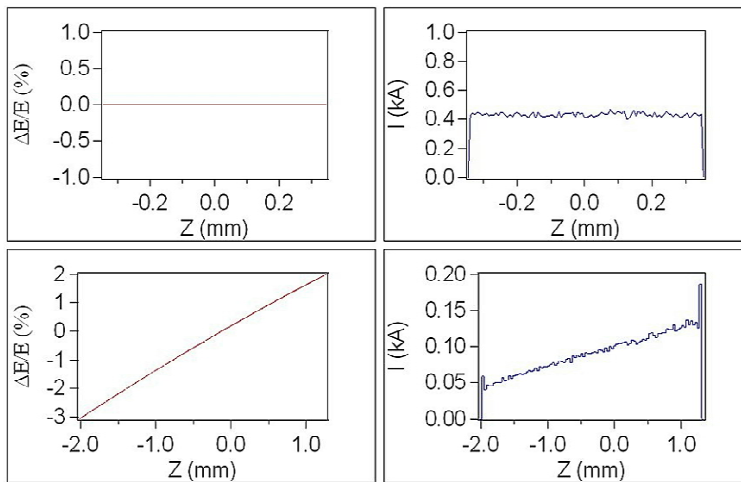


Figure 5.5: Reverse tracking applied to the FERMI@Elettra linac. It begins with flat-flat distribution at the end of the accelerator (top line) and moves towards beginning of the accelerator (bottom line).

accelerator. This result can be understood if one uses the wake function for an accelerating structure consisting of an array of cells, eq.3.59:

$$w_z(z) = A \frac{Z_0 c}{\pi a^2} e^{-\sqrt{z/s_0}} \quad (5.14)$$

and convolutes it with the linear ramped peak current distribution shown with the red line in Figure 5.6 to obtain the wake potential:

$$W_z(z) = -L \int w_z(z - z') \lambda_z(z') dz' \quad (5.15)$$

shown with the red line in Figure 5.6. Here a is the iris radius, $Z_0 = 377\Omega$ and $A \approx 1$ and s_0 are fitting coefficients. On the left side, the density distribution with a linear ramped peak current. On the right side, the corresponding wake potential calculated for $a=9.73$ mm, $s_0=1.28$ mm and $L=30$ m. The red line shows a desirable ideal distribution and its associated wake potential. The black line shows the realistic density distribution obtained in the studies of the photo-injector using the laser pulse with a quadratic ramp in the intensity and the wake potential that corresponds to that distribution. The part under the red line contains approximately 40% of the total charge under the black line. As seen in Figure 5.6, the wake potential is highly linear and this is why the final distribution is flat in energy.

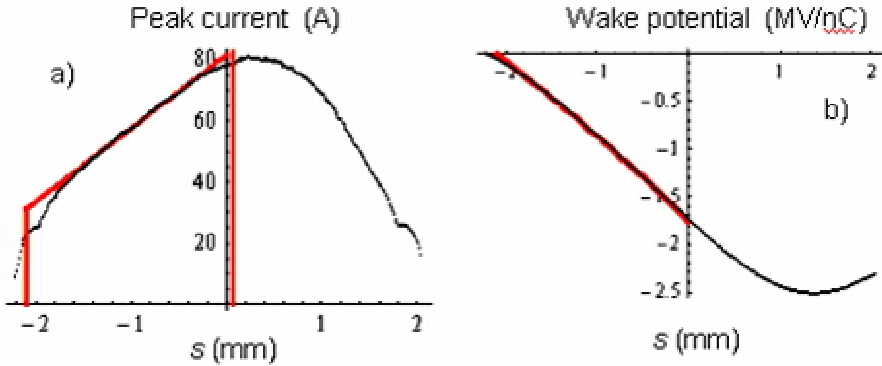


Figure 5.6: Linear ramped peak current (left) and corresponding wake potential (right).

Producing a linearly ramped electron bunch current at the exit of the injector is somewhat of a challenge because of the strong nonlinearity of the SC fields at

low energy. The longitudinal blow-up of the electrons from the cathode to the first accelerating structure, poses a limit to the ramping fraction of the bunch that meets the current linearity requirement. A fourth-degree polynomial distribution was found to offer the best cancellation of the high orders nonlinear contributions of the SC field, and thus increases the bunch fraction that follows a linear ramp. This cancellation helps preserving the linearity of the fields in the space-charge dominated part of acceleration.

Now we consider a condition that allows a conversion of a linear ramped peak current at the beginning of the accelerator into the flat distribution at the end of the compression. The compression factor can be defined as:

$$C = I_a / I_b \quad (5.16)$$

where I_a is the peak current after compression and I_b is the peak current before compression. The transformation from a linear ramped peak current $I_b = I_{b0} + I'_b z$ to the flat distribution $I_a = I_{a0} = \text{const.}$ can be obtained with:

$$C^{-1} = I_{b0} / I_{a0} + z I'_b / I_{a0} \quad (5.17)$$

i.e. with a compression factor that gradually decreases from the head to the tail of the electron bunch. On the other hand $C^{-1} = 1 + h R_{56}$, where $h = d(\Delta E / E) / dz$ is the energy chirp in the electron bunch. Thus, eq.5.17 can be realized if one uses the energy chirp with a quadratic component, i.e. $h = h_0 + h' z$, where:

$$h' = \frac{1}{R_{56}} \frac{I'_b}{I_{a0}} \quad (5.18)$$

This result can easily be generalized. For example, in some cases a distribution with the maximum peak current at the head of the bunch gradually reducing towards the tail can be beneficial for HGHG FELs, i.e. one may want $I_a = I_{a0} - I'_a z$. Performing a similar analysis, one can find that this distribution can be obtained with a slight modification to the quadratic energy chirp:

$$h' = \frac{1}{R_{56}} \left(\frac{I'_b}{I_{a0}} + \frac{I'_a I_{b0}}{I_{a0}^2} \right) \quad (5.19)$$

The peak current spikes at the edges of the compressed electron bunches are largely due to the compressor second order time-of-flight parameter T_{566} and the cubic chirp in the electron energy distribution $\mu = d^3 E / dz^3$. Both of them cause a bifurcation in the phase space whose example is shown in Figure 5.2. Controlling μ is likely the only way to control the bifurcation for a given R_{56} since T_{566} is often bound to $T_{566} \approx -3R_{56}/2$ if sextupoles are no used in the bunch compressor. Figure 5.7 shows a typical example that demonstrates how

the change in μ from -0.008 MeV/mm^3 to -0.088 MeV/mm^3 in the electron energy distribution created in the injector removes the bifurcation after the bunch compressor. Related to that is a drop of the spikes in the peak current from $\sim 5 \text{ kA}$ in the first case to approximately no spikes condition in the second case. Apart from the cubic energy chirp, the same initial distributions were used in both cases.

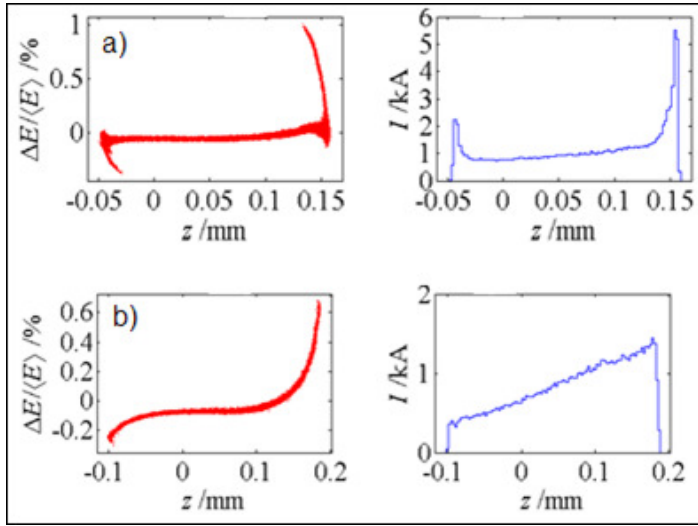


Figure 5.7: Effect of the cubic energy chirp on the longitudinal phase space (left) and peak current distribution (right) in FERMI@Elettra for a ramped final current profile (the higher current is in the bunch tail).

It should be pointed out that the distribution in Figure 5.7, top plot is flat in energy and in peak current, while the distribution in Figure 5.7, bottom plot is neither flat in the energy nor it is flat in the peak current. By using a cubic energy chirp as a knob one can obtain either flat-flat distributions or distributions without spikes rather routinely, but not both features at the same time. Simply having just one knob is not enough. However, one can effectively employ the peak current distribution in the gun to provide required μ using the wake fields. In the case of strong wake fields this method was found to be much more effective than correction using a high harmonic cavity [36, 37].

The electrons sitting at the edges of the electron bunch often deviate in energy from the energy of most other electrons. This feature can be exploited in a complementary procedure for the removal of the spikes in the peak current if the electron distribution in the phase space has a characteristic S-type shape, like one shown in Figure 5.8 (we note that the S-shaped distribution in the longitudinal phase space at the end of the linac appears rather naturally when ramped peak current in the injector is used). Then, it is possible to dissolve clusters of electrons at the edges of the electron bunch by sending the electron beam through a lattice with properly adjusted time-of-flight parameter R_{56} . Typically a “dog-leg” type lattice is used to connect the linac to the FEL undulator line, so that adjustments in bunch length through R_{56} manipulation can be easily done there. The application of this technique to the FERMI@Elettra case study is shown in Figure 5.8. A further discussion of the Spreader optics as related to collective instabilities is given in Section 5.4. The eL_{egant} code has been used

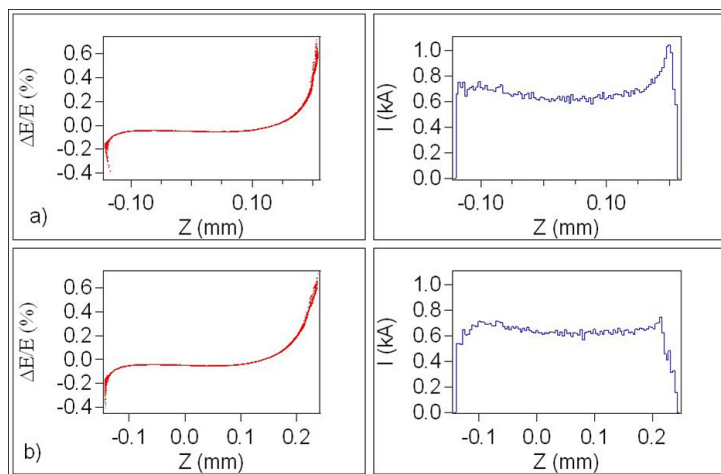


Figure 5.8: Removal of current spikes using R_{56} adjustment in the Spreader.

in order to obtain the electron distribution in the longitudinal phase space and a histogram of the electron peak current at the entrance of the FEL, verifying the validity of all the techniques described here. These calculations have been performed for FERMI@Elettra linac set in the two-stage compression scheme with machine and the beam parameters described in Table 2.2 for the FEL1 Operation mode. A ramped peak current distribution at the entrance of the linac has been

used, as shown with the black line in Figure 5.6. The result of these calculations is shown in Figure 5.9. We note that these calculations included CSR effects in the bunch compressors.

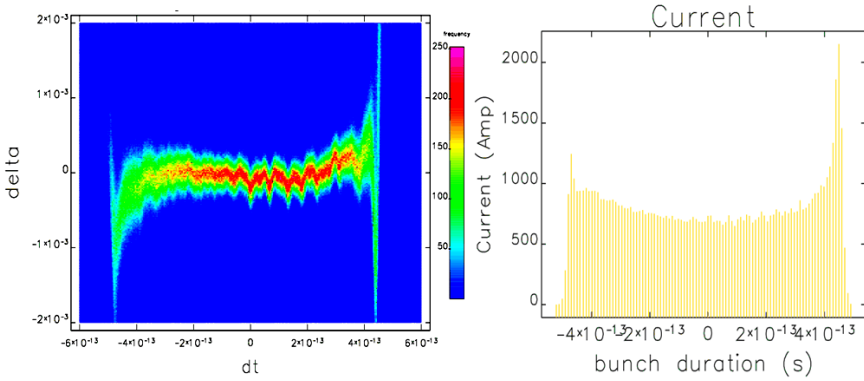


Figure 5.9: Longitudinal phase space (left) and current profile (right) at the entrance of the FERMI@Elettra undulator. elegant particle tracking results starting from 0.8 nC charge, linearly ramped current profile at the injector exit. The two-stage compression scheme has been implemented. Collective effects have been included in the simulation.

5.3 Transverse Structural Wake Field

5.3.1 Emittance Growth

The growth of the single bunch projected emittance accompanied by the characteristic bending of the electron bunch into a banana-like shape induced by the short range transverse wake field has been extensively treated in the literature for linear colliders with regard to the luminosity loss [105–107]. Trajectory bumps to minimize the projected emittance growth were introduced in [107–111]. Furthermore, the impact of trajectory jitter on the single bunch dynamics in the presence of a transverse wake field has been investigated in [106, 112–115], still with regard to projected emittance growth and luminosity loss in colliders. FELs are sensitive to the projected emittance growth as are linear colliders. The FEL power relies on the energy exchange between the electrons and the light beam along the undulator chain; this interaction is made possible when

the two beams overlap. For HGHG FELs, this happens in the modulator, where the external seeding laser has to superimpose on the electron bunch, as well as in the succeeding radiator modules, where the electrons should overlap with the coherent radiation emitted. It has been shown in [116] that the FERMI FEL is sensitive to the projected emittance growth generated by the transverse displacement of longitudinal slices of the bunch. However, owing to the fact that the ~ 100 fs seeded laser is much shorter than the ~ 1 ps electron bunch, a bigger projected emittance could be tolerated if the slice transverse mismatch is sufficiently small in the region of the bunch where photons and electrons overlap. At the same time, the distortion of the electron bunch shape in the (t, x) and (t, y) plane (banana shape) should be sufficiently small along the whole undulator chain so that electrons and photons travel on the same axis.

The transverse kick induced by the dipole wake potential along the bunch is always proportional to the total charge of the bunch, it is linear with the linac-to-beam relative displacement and, opposite to the longitudinal wake potential, its strength increases with the bunch length (at a certain charge). Accordingly, it imposes an upper limit to the bunch length that is based on the single bunch emittance growth. In order to evaluate this limitation, we recall the approximate transverse emittance dilution through an accelerating structure of length L , due to a coherent betatron oscillation of amplitude Δ [105]:

$$\frac{\Delta\epsilon}{\epsilon} \approx \left(\frac{\pi r_e}{Z_0 c} \right)^2 \frac{N^2 \langle w \rangle^2 L^2 \beta}{2\gamma_i \gamma_f \epsilon} \Delta^2 \quad (5.20)$$

This is predominantly a linear time-correlated emittance growth and can be corrected. The wake field, $\langle w \rangle$, is expressed here as the approximate average transverse wake function over the bunch given by eqs.3.64–3.66, evaluated at $\bar{z} = 2\sqrt{3}\sigma_z$. In FERMI, the misalignment tolerance is $|\Delta| \leq 300 \mu\text{m}$ in order to ensure $\Delta\epsilon/\epsilon \leq 1\%$ per cavity. At the same time, the FERMI electron bunch and the accelerating structures are not short enough to completely fit into the approximated eq.3.57, so that eq.5.20 underestimates the real effect. In this case, the machine design and alignment tolerances are made more robust and reliable by particle tracking studies that include the geometric wake functions and all realistic alignment errors. The effect of the wake field can therefore be integrated into the machine error budget.

5.3.2 Single-Bunch Transverse Wake Field Instability

The operation of X-ray FELs requires small emittance electron beams. Although both SASE FELs and seeded FELs are mostly sensitive to slice emittance, it is also important that relative transverse offsets of different slices or slice-to-slice variations along the electron bunch remain within strictly defined limits. Therefore

any significant growth of the projected emittance in the linac under the influence of the linac geometric wake fields should be minimized. Computer codes like PLACET, MTRACK and MBTRACK [117–120] adopt the Courant Snyder variables to calculate the growth of the bunch slice coordinates caused by a random misalignment of various machine components in the presence of the geometric transverse wake fields. It has also been demonstrated that this instability can be compensated with trajectory bumps. In a similar way, it has been shown in [121, 122] that the single bunch emittance growth in the FERMI@Elettra linac calculated with `elegant` is in good agreement with a prediction obtained on the basis of a theory developed in [123, 124].

Relying on this basis, this Section addresses the impact of trajectory jitter on the degradation of the projected emittance induced by short range geometric transverse wake fields during a single pass of the electron bunch through the FERMI@Elettra linac. Special care is devoted to the incoherent part of the trajectory growth due to random misalignment of quadrupole magnets and accelerating structures. This Section shows that control over the transverse wake field instability can be gained in a reliable way in the FERMI@Elettra linac by applying local trajectory bumps even in the presence of a shot-to-shot trajectory jitter. The instability analysis is focused on the correlation of the slice transverse offset with its longitudinal position along the bunch. A specific Self-Describing Data Sets (SDDS) [82] script working with Courant-Snyder variables is written to evaluate the residual banana shape after instability suppression in the presence of shot-to-shot trajectory jitter. A statistical parameter for each bunch slice is introduced; its maximum value over all slices determines the projected emittance growth under the effect of trajectory jitter in terms of the slice transverse phase space mismatch. For completeness, well known methods of evaluation of the projected emittance and of the banana shape are included and the consistency of all methods is demonstrated for FERMI@Elettra. A by-product of this study is the capability of specifying the tolerances on trajectory jitters for the FERMI@Elettra linac. As a first step, the FERMI@Elettra trajectory correction scheme is presented and the most important contributions to the trajectory distortion are discussed. They are:

- i) misalignment of magnetic elements, linac RF phase and voltage errors, beam launching error. All these errors determine the machine error budget;
- ii) trajectory distortion induced by the emission of CSR in the BC1 and BC2 magnetic chicanes;
- iii) effective trajectory distortion induced by the banana shape.

Simulations including all these effects show that the global trajectory correction provided through a response matrix algorithm is not sufficient to damp the

transverse wake field instability; for this reason local trajectory bumps are applied (with success) to suppress it. The validity of the trajectory manipulation described so far is also checked in the presence of shot-to-shot trajectory jitter. The following sources of trajectory jitter are considered:

- a) beam launching error jitter;
- b) quadrupole magnet mechanical vibration and power supply current ripple;
- c) jitter of the residual dispersion induced by misaligned quadrupoles;
- d) energy jitter translating into trajectory jitter through residual dispersion.

The projected emittance at the linac end is evaluated and its dependence on the beam launching error jitter is shown. As an alternative method for the analysis of the instability, the simulation of the banana shape for all jittered runs is presented. Finally, the Courant-Snyder variables are introduced to describe the phase space mismatch of each longitudinal slice of the bunch in the presence of trajectory jitter. All three methods – projected emittance, banana shape, Courant-Snyder amplitude – give consistent results. Concluding remarks are given about the expected impact of the instability in the presence of trajectory jitter on the FERMI@Elettra FEL performance.

It is well known that an electron traveling off axis in an accelerating module excites the short range geometric transverse wake field that affects in turn trailing electrons. This has a result that the bunch tail oscillates with respect to the bunch head forming in the (t, x) and in the (t, y) planes a characteristic banana shape. Persistence of the slice oscillations along the linac and their amplification may cause the conversion of the bunch time duration into the transverse dimension (beam break up). So, the displaced bunch tail adds a contribution to the projection of the beam size on the transverse plane that is the projected emittance is increased.

The transverse motion of a relativistic electron in the linac in the presence of the short-range geometric transverse wake field is described by an ordinary 2^{nd} order differential equation in the complete form. The l.h.s. of this equation is the homogeneous equation for the betatron motion in the horizontal or vertical plane; the r.h.s. contains the convolution of the transverse wake function with the local current distribution and is also linearly proportional to the relative displacement of the particle from the axis of the accelerating structure [123, 124]:

$$\frac{1}{\gamma(\sigma)} \frac{\partial}{\partial \sigma} \left[\gamma(\sigma) \frac{\partial}{\partial \sigma} x(\sigma, \gamma) \right] + \kappa(\sigma)^2 x(\sigma, \gamma) = \epsilon(\sigma) \int_{-inf}^{\zeta} w_n^1(\zeta - \zeta') F(\zeta') [x(\sigma, \zeta') - d_c(\sigma)] d\zeta' \quad (5.21)$$

where $\sigma = s/L$ is the distance from the linac entrance normalized with the total linac length L ; $\zeta = z/l_b$ is the longitudinal bunch coordinate at location σ measured after the arrival of the bunch head, normalized with the full width bunch length; $F(\zeta) = I(\zeta)/I_{pk}$ is the local current normalized with the maximum peak current along the bunch; $\kappa = kL$ is the average normalized focusing strength k integrated along the linac length L ; $w_n^1(\zeta)$ is the transverse wake function normalized with the wake amplitude; d_c is the transverse offset of the beam respect to the linac axis. Finally, $\epsilon(\sigma) = \epsilon_r (\gamma_0/\gamma(\sigma))$ is the factor coupling the particle betatron motion (described by the homogeneous form of the previous equation) to the wake field driving term. It is given by [123]:

$$\epsilon_r = \frac{4\pi\epsilon_0}{I_A} \frac{w_n(1)I_{pk}l_bL^2}{\gamma(0)} \quad (5.22)$$

where $I_A=17$ kA is the Alfvén current, $w_n(1)$ is the wake function normalized to its amplitude and computed for the particle at the bunch tail, I_{pk} is the peak current. Thus, according to eqs.5.21 and 5.22, the transverse kick induced by the dipole wake potential along the bunch is always proportional to the total charge of the bunch, it is linear with the linac-to-beam relative displacement and, as opposite to the longitudinal wake potential, its strength is proportional to the bunch length, for a given charge.

The FERMI@Elettra linac lattice is simulated with `elegant` by adopting the static machine error setting shown in Table 5.1. This includes errors on the dipoles and quadrupoles main integrated field component $b_i l$, element misalignments, magnet tilt angles, beam launching error and accelerating structure phase and voltage errors. All values are rms taken over a Gaussian distribution with a 3 sigma cut-off. The emittance growth induced by the transverse wake field instability depends on the errors affecting the machine optics (quadrupole misalignment and gradient error) and the acceleration (phase and voltage errors). The trajectory correction scheme foresees 24 steering magnets (correctors) in both the transverse planes and 31 BPMs whose rms single-shot resolution is specified as 20 μm . A pair of horizontal and vertical correctors and one BPM are placed after each accelerating structure. The `elegant` “global” method for trajectory correction that minimizes the BPM position readings is implemented by using the trajectory response matrix computed by the code itself. For illustration, only one set of errors – randomly chosen over a meaningful sample of error seeds – is shown in the following. A discussion of the statistical distribution of the trajectory distortion over a large number of random seeds can be found in [122, 125 and 126]. Simulations were performed with $2 \cdot 10^5$ particles divided into 30 longitudinal slices. The particle spatial distribution is approximately Gaussian in the transverse dimensions; the initial current profile has an approximate linear ramp, as described in Section 5.2, from the bunch head to

Table 5.1: FERMI error budget.

	$\Delta(b_i l)/b_i l$ [%]	$\Delta x, \Delta y$ [μm]	Δz [μm]	Roll Angle [mrad]
Dipole	0.01	150	150	0.5
Quadrupole	0.01	150	150	0.5
BPM	–		150	–
Acc. Structure	–	300	150	–
Acc. Str. Voltage Error		0.1%		
Acc. Str. Phase Error		0.1 deg S-band		
Beam Launching Error	$\Delta x, \Delta y = 150\mu\text{m}, \Delta x', \Delta y' = 10\mu\text{rad}$			

the tail and it flattens out after the bunch length compression. The longitudinal phase space has an energy chirp that increases to $\sim 1\%$ at BC1 and diminishes to $\sim 0.1\%$ at the linac end. CSR is emitted in the dipoles of the magnetic chicanes of the two compressors. CSR emission causes a diminishing of the beam mean energy. Hence, the bunch centroid shifts to a trajectory that is a few 100's μm away from that defined by the nominal energy. A more important contribution to the trajectory distortion comes from the transverse wake field. An ideal trajectory correction sets the centroid trajectory to zero, but due to the wake field, head and tail particles perform different, uncorrected betatron oscillations. The trajectory correction efficiency is therefore degraded by the banana shape dynamics as compared to the case of a rigid beam. The residual centroid dispersion generated by a misaligned accelerating structure grows resonantly with s and it becomes large at the end of the 150 m long FERMI linac.

Even after correction, the residual trajectory distortion induces an important emittance dilution at the linac end. The projected emittances in Figure 5.12 blow up as the beam enters the BTW structures that start at the linac longitudinal coordinate of approximately 80 m (see also the linac layout in Figure 2.2). The emittance blow up can be suppressed through local trajectory bumps [107–110]. Their simulation is shown in Figure 5.13. The bumps technique looks for an empirical “golden” trajectory for which all the kicks generated by the transverse wake field compensate each other and the banana shape is finally canceled. When applying the local bumps, the steering magnets force the beam on a distorted trajectory but still keeping the beam off axis excursion less than 500 μm . Six steerers and six BPMs distributed along the BTW linac are used for the bumps. The maximum variation of the steerer strengths with respect to the nominal set up is 0.2 mrad. The emittances are finally compensated, as shown in Figure 5.14. In practice, the implementation of the local bumps in

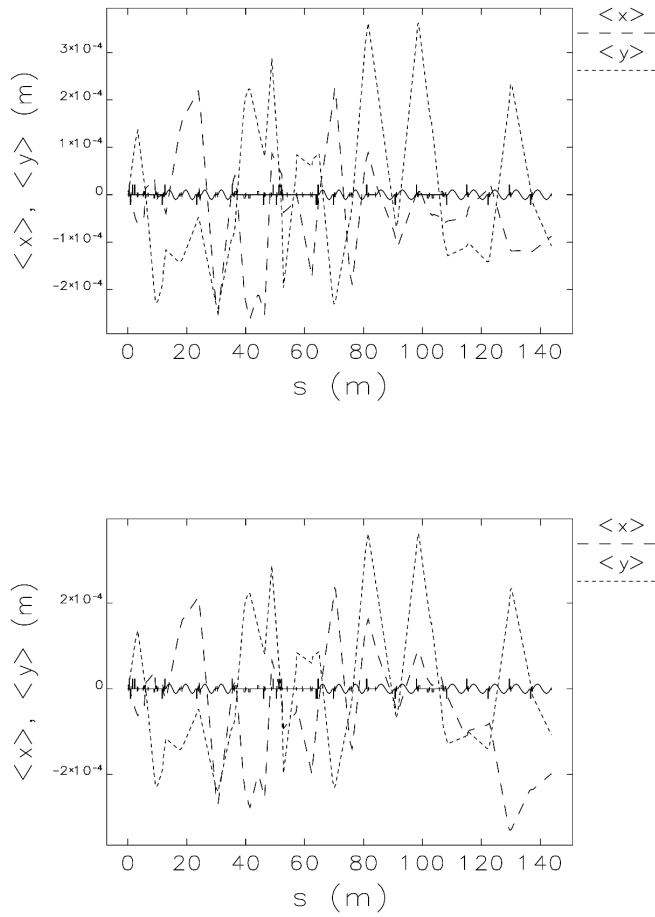


Figure 5.10: Trajectory correction along the FERMI linac. The trajectory distortion in the bare lattice with no collective effects (top) is compared with that in the presence of CSR only (bottom). Field errors, gradient errors and element misalignments are included in the simulation (solid line at the plot center is a sketch of the machine layout).

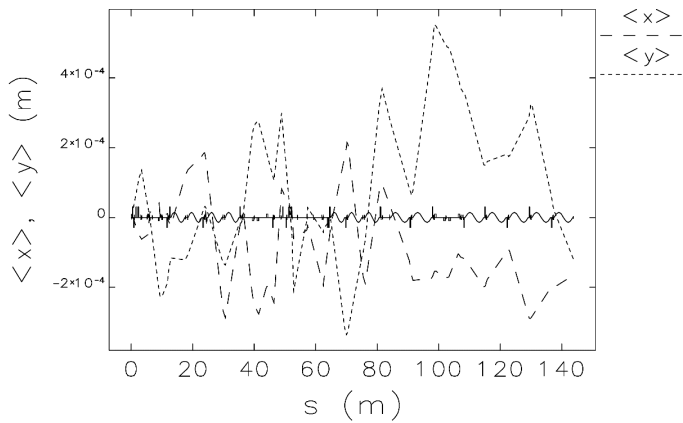


Figure 5.11: Trajectory correction along the FERMI linac when CSR and transverse wake field are all included (compare with Figure 5.10). The trajectory correction is performed with `elephant` by using the “global” correction method. Field errors, gradient errors and element misalignments are included in the simulation (solid line at the plot center is a sketch of the machine layout). The CSR induced trajectory distortion can be neglected with respect to the wake field contribution that is especially important in the last part of the linac, which is made of the high impedance BTW accelerating structures.

the FERMI@Elettra linac foresees the characterization of the transverse beam profile as a function of the bunch longitudinal coordinate projected on screens separated by a proper phase advance. This will be done in the diagnostic section downstream the linac by means of RF deflectors [81], in the horizontal and vertical plane.

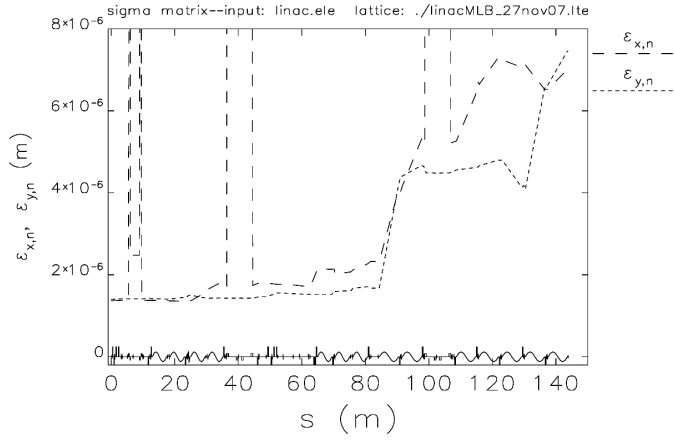


Figure 5.12: Single-bunch transverse wake field instability in the FERMI@Elettra linac. The transverse projected emittances blow up as the 0.8 nC beam enters into the BTW accelerating structures. A 300 μm rms lateral misalignment of the structures is considered.

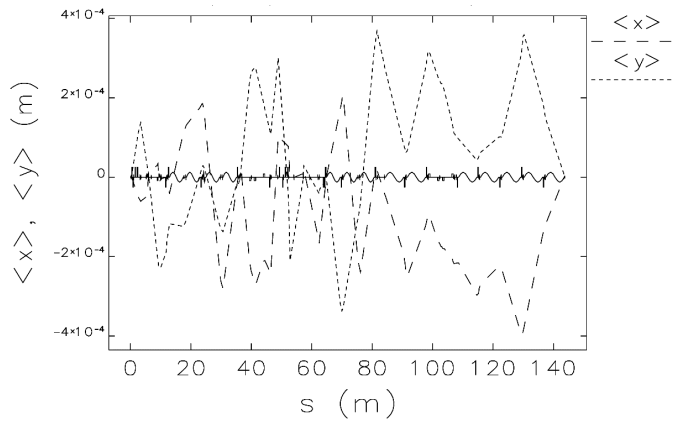


Figure 5.13: Trajectory bumps along the FERMI linac.

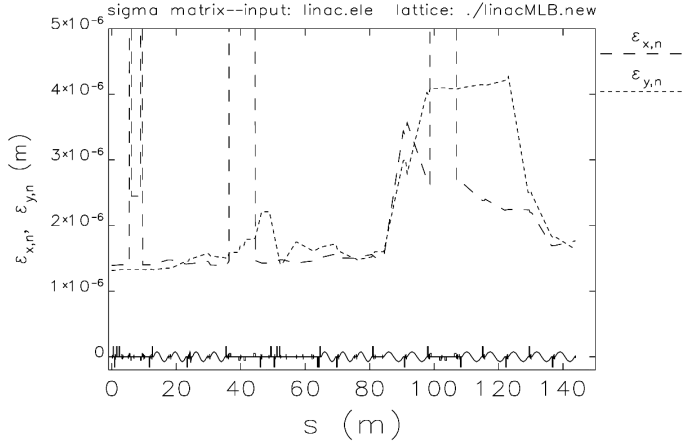


Figure 5.14: Suppression of single-bunch transverse wake field instability in the FERMI linac. Some trajectory manipulation is done as depicted in Figure 5.13.

5.3.3 Slice Centroid Courant-Snyder Amplitude

Owing to its local property, the efficacy of the local bumps technique depends on the specific machine configuration (i.e., misalignment of elements) and beam optics (i.e., bunch centroid position and angular divergence) at the locations where the bumps are applied. Accordingly, shot-to-shot trajectory jitter may affect the scheme efficacy by changing the bunch centroid transverse coordinates at the location of the bumps. The aim of this Section is to evaluate a realistic budget for the sources of trajectory jitter in the FERMI@Elettra linac.

The jitter budget is estimated by considering that the shot-to-shot jitter of the bunch centroid position and angular divergence at the injector end should not exceed a small fraction of the beam size and divergence, respectively, if the machine is properly tuned. As an example, the nominal betatron functions at the FERMI linac entrance are $\beta_x = \beta_y = 19$ m. These values coupled with the rms geometric emittances of $\epsilon_x = \epsilon_y = 7.65$ nm rad (equivalent to a normalized emittance of 1.5 mm mrad, at the energy of 100 MeV) give an rms beam size $\sigma = \sqrt{\epsilon\beta} \simeq 380$ μ m in both planes. The rms variation of the launching position is taken as 10% of the rms beam size; that is, 38 μ m. The launching angular divergence is related to the launching position through the injector optics. The trajectory distortion generated by an angular kick θ_k at a longitudinal position s_k

in the lattice and observed at a downstream position s_0 is given by eq.3.19 (valid for both the transverse planes). We adopt here the new naming for $\Delta u' = \theta_k$ and for the locations s_0 and s_k . The corresponding distortion of the angular divergence at position s_0 is therefore given by:

$$x'_0 = \frac{dx_0}{ds} = -\theta_k \frac{\sqrt{\beta_k}}{\sqrt{\beta_0}} [\alpha_0 \sin(\Delta\mu_{k0}) + \cos(\Delta\mu_{k0})] \quad (5.23)$$

In FERMI, $\alpha_0 = 0$ and $\Delta\mu_{k0} \approx \pi/4$. With these numbers, eq.5.23 gives $x'_0 = \frac{x_0}{\beta_0} \cot(\Delta\mu_{k0}) = x_0/19$ m. Thus, the launching error jitter is simulated by moving the position and the angular divergence of the bunch centroid at the linac entrance over a Gaussian distribution with standard deviation $\sigma_0 = 38 \mu\text{m}$ and $\sigma'_0 = 2 \mu\text{rad}$, with a 3 sigma cutoff.

Other contributions to the trajectory jitter are: quadrupole vibrations, short-term magnetic field stability and shot-to-shot variation of the residual dispersion. As for the quadrupole vibrations, rms vibration amplitude of $0.5 \mu\text{m}$ in the range 1–100 Hz (FERMI will nominally operate at 50 Hz) leads to an rms variation of the induced angular kick per quadrupole of:

$$\Delta\theta_{k,v} = \frac{\Delta \int B(s)ds}{B_0\rho} = kl_q\Delta r \approx 0.1\mu\text{rad} \quad (5.24)$$

where k is the quadrupole normalized strength, typically not larger than 2 m^{-2} , $l_q=0.1$ m is the quadrupole magnetic length and $\Delta r=0.5 \mu\text{m}$ is the rms vibration amplitude.

The relative short term (<100 Hz) stability of the quadrupole gradient is essentially the stability of the current signal provided by the power supply; it is specified to be equal or smaller than 10^{-4} . The rms variation of the induced angular kick is therefore:

$$\Delta\theta_{k,ps} \leq 10^{-4} \cdot \theta_k = 10^{-4} \cdot kl_qR \approx 20\text{nrad} \quad (5.25)$$

where a particle offset $R=0.5$ mm inside the quadrupole magnet is considered.

When the quadrupole magnet is traversed off axis, a shot-to-shot variation of its integrated gradient excites residual dispersion that contributes to the shot-to-shot trajectory distortion. Dispersion induced in both transverse planes by the quadrupole gradient variation is estimated in thin lens approximation by:

$$\eta_r = \frac{1}{\rho K} \left[1 - \cos\left(\sqrt{Kl_q}\right) \right] \simeq \frac{1}{\rho K} \left[\frac{1}{2} Kl_q^2 \right] \simeq \frac{l_q^2}{2\rho} = \frac{l_q\theta_k}{2} \quad (5.26)$$

where $\rho = \frac{l_q}{\theta_k}$ is the curvature radius induced by the quadrupole magnetic field when the magnet is traversed off axis and $K = \left(\frac{1}{\rho^2} - k\right)$. A similar consideration gives for the derivative of the residual dispersion $\Delta\eta'_r \approx \theta_k$. Given eq.5.25,

the maximum induced residual dispersion and its derivative is therefore of the order of:

$$\begin{aligned}\Delta\eta_r &\simeq \frac{l_q}{2}\Delta\theta_k \approx 1 \text{ nm} \\ \Delta\eta'_r &\simeq \theta_{k,ps} \approx 100 \text{ } \mu\text{rad}\end{aligned}\tag{5.27}$$

The relative energy spread in the FERMI@Elettra linac does not exceed 2%, so that the maximum trajectory variation induced by the residual dispersion never exceeds a few μrad . Finally, an energy jitter of 0.1% rms is taken into account. It couples with the residual dispersion and its first derivative, therefore leading to an effective trajectory jitter. Even assuming a 10 mm large dispersion and 1 mrad first derivative propagating through the machine, we would obtain a jitter of the trajectory offset and divergence smaller than 10 μm and 1 μrad , respectively.

elegant simulations are performed with the trajectory jitter budget listed in Table 5.2. The jitter budget includes launching error jitter, quadrupole vibrations and energy jitter. The residual dispersion functions and their induced trajectory distortion are taken into account.

Table 5.2: Trajectory jitter budget.

	Position [μm]	Divergence [μrad]
Beam		
Launching	38	2
Quadrupole		
Vibration Ampl.	0.5	–

The reference trajectory along the FERMI@Elettra linac is defined by the golden trajectory shown in Figure 5.10, top plot. A shot-to-shot trajectory jitter is then superimposed to it. We want to evaluate if the transverse wake field instability remains suppressed by the trajectory local bumps in the presence of trajectory jitter. Three methods for the evaluation of the instability effect on the electron distribution are presented: evaluation of the projected emittance, of the banana shape and the definition of a new parameter for each slice of the bunch that is related to the slice phase space mismatch induced by the instability. A rotational symmetry of the accelerating structures around their longitudinal axis is assumed in the simulations. The geometric transverse wake field in the accelerating structures is taken as uniform over the whole transverse beam size, that is, we use a simple dipole wake. Hence, the slice emittance is preserved, while the projected emittance is not because the wake field drives a bunch tail oscillation relative to the bunch head; in this way, a correlation is established between

the longitudinal slice position and its lateral displacement.

Let us reasonably assume the following approximation that is the full width transverse beam size, in each plane, is covered by four standard deviations (σ) of the particle position distribution. The beam standard deviation at the linac end is approximately $100 \mu\text{m}$. The tolerance on the beam size growth induced by instability is now fixed so that it is sufficiently smaller than the total beam size, namely the bunch tail centroid should not laterally exceed the head centroid by more than 1σ , as it is sketched in Figure 5.15. In this limit case, the total projected beam size becomes $5\sigma_0$ that we re-define equal to $4\sigma_{eff}$. The relative growth of the beam size is therefore:

$$\frac{\Delta\sigma}{\sigma} = \frac{\sigma_{eff} - \sigma_0}{\sigma_0} = 25\% \quad (5.28)$$

Figure 5.15 shows the schematic of the beam size growth described by eq.5.28. Since $\sigma = \sqrt{\beta\epsilon}$, where ϵ is the projected geometric emittance, the relative variation of the beam size is half of relative variation of the emittance. In other words, the projected emittance growth after instability suppression must be less than 50%.

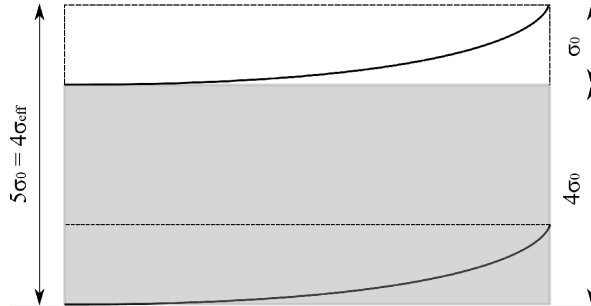


Figure 5.15: Beam affected by transverse wake field instability (conceptual).

As a preliminary study, particle tracking simulations are performed to evaluate the sensitivity of the projected emittance growth, specified at the linac end, to the launching error jitter. Figure 5.16 shows the normalized emittances when the launching coordinates of the bunch centroid move along an ellipse of semi-axes

$x = 76 \mu\text{m}$ and $x' = 4 \mu\text{rad}$ (two times bigger the rms launching error specified in Table 5.2) in the (x, x') phase space. Same considerations apply to the vertical plane. The maximum emittance growth is 44% in the horizontal plane and 64% in the vertical plane. The lack of periodicity in the data depends from the static errors set in the initial configuration; in other words, the machine errors corrupt the dependence of the trajectory from the periodic launching condition; this fact in turn reflects into a non-periodic dependence of the wake field effect or of the projected emittance growth on the initial betatron phase of the beam centroid.

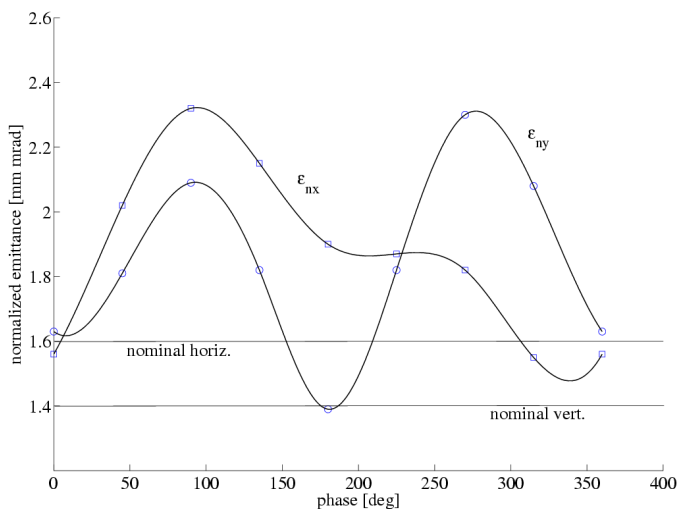


Figure 5.16: Final normalized projected emittances in the presence of trajectory jitter in the FERMI linac. The only trajectory jitter source considered here is the variation of the electron beam launching at the linac entrance (injector exit). The phase along the abscissa is the betatron phase difference with respect to the nominal set point (in each plane).

Now we want to investigate the projected emittance dilution induced by the lateral slices offset. It can be quantified by means of the transverse deviation of the bunch tail with respect to the head, in units of unperturbed rms beam size: $R_x = |x_{head}x_{tail}|/\sigma_x$ (same applies in the vertical plane). Figure 5.17 shows the banana shape jitter (slice centroid lateral deviation vs. bunch duration in 100 fs units) over 50 runs generated by the trajectory jitter budget in Table 5.2; bunch head is on the left. Averaging over all these runs we obtain $\langle R_x \rangle = 0.2$ for the horizontal plane and $\langle R_y \rangle = 0.8$ for the vertical plane. Notice that $R_x \leq 0.9$ and

$R_y \leq 1.6$ over the whole sample of trajectories considered.

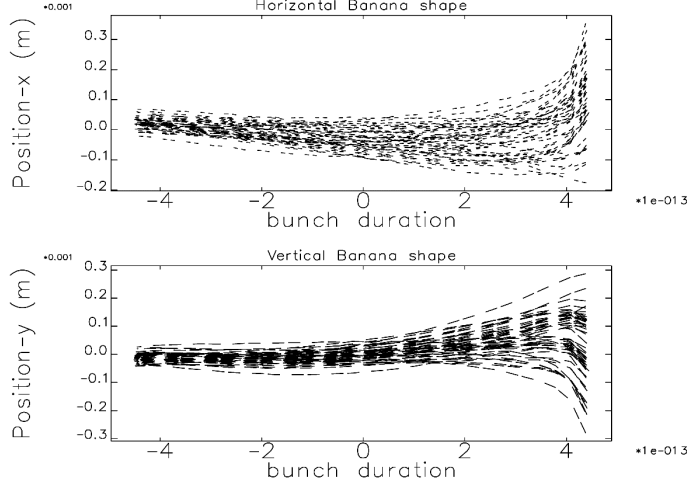


Figure 5.17: Final banana shape affected by trajectory jitter.

Consistently with the constraint in eq.5.28 for the suppressed transverse wake field instability, one should have $R_{x,y} \leq 1$. We point out that if the instability is suppressed at the linac end, then the slice centroid transverse offset and divergence are small. Hence the bunch tends to maintain its shape in the (t, x) and (t, y) plane at any point of the line downstream. On the contrary, if the banana shape is pronounced, the slice optics in the bunch tail is mismatched to the magnetic lattice. Then, the bunch tail starts additional betatron oscillations around the head axis and the banana shape at any point downstream will depend on the Twiss parameters at the point of observation. The Courant-Snyder amplitude of the slice centroid is here introduced as a parameter to characterize the instability (same applies to the vertical plane):

$$\epsilon_{SC} = \gamma_x x_{cm}^2 + 2\alpha_x x_{cm} x'_{cm} + \beta_x x_{cm}'^2 \quad (5.29)$$

ϵ_{SC} is a constant of motion in absence of frictional forces such as geometric wake fields and emission of radiation; this is just the case for the beam transport downstream of the linac, where also coherent and incoherent synchrotron radiation is neglected. ϵ_{SC} provides a measurement of the amplitude of motion that is independent of betatron phase. Its square root is proportional to the

amplitudes of the slice centroid motion $x_{SC}(s)$ that describes the banana shape:

$$\begin{cases} x_{SC}(s) = \sqrt{\epsilon_{SC,x} \beta_x(s)} \cos \Delta\mu_x \\ x'_{SC}(s) = -\sqrt{\frac{\epsilon_{SC,x}}{\beta_x(s)}} [\alpha_x(s) \cos \Delta\mu_x + \sin \delta\mu_x] \end{cases} \quad (5.30)$$

In general, x_{SC} is the linear superposition of three main contributions sketched in Figure 5.18: i) the betatron motion, $x_{S\beta}$, generated by focusing of misaligned quadrupoles; ii) the trajectory distortion, x_{ST} ; iii) the transverse wake field effect, x_{SW} . Notice that $x_{offset} = x_{S\beta} + x_{ST}$ is approximately the same for all slices along the bunch. Regarding the instability, only the motion relative to the bunch head is of interest:

$$x_{SW} = x_{SC} - x_{S\beta} - x_{ST} = x_{SC} - x_{offset} \quad (5.31)$$

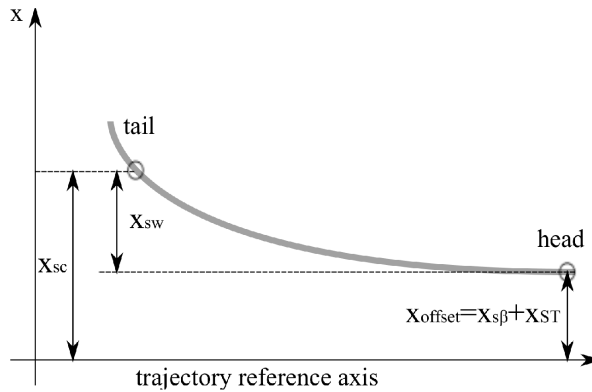


Figure 5.18: Slice centroid motion in the presence of transverse wake field instability.

We now define a new slice centroid amplitude relative to the motion of the bunch head:

$$\epsilon_{SW,x} = \gamma_x (x_{SC} - x_{offset})^2 + 2\alpha_x (x_{SC} - x_{offset})(x'_{SC} - x'_{offset}) + \beta_x (x'_{SC} - x'_{offset})^2 \quad (5.32)$$

The effect of the trajectory jitter on the scheme for the suppression of the instability can be evaluated by looking to the shot-to-shot variation of the centroid amplitude $\epsilon_{SW,x}$ over the bunch duration. In fact, we require that the standard

deviation (over all jitter runs) of the slice lateral deviation be less than the rms (over all particles) beam size $\sigma_x = \sqrt{\beta_x \epsilon_x}$:

$$\frac{\sigma_{x,SC}}{\sigma_x} \leq 1 \quad (5.33)$$

Since x_{offset} is a constant, we can write:

$$\begin{aligned} \sigma_{x,SC} &= \sqrt{\langle x_{SC}^2 - \bar{x}_{SC}^2 \rangle} \simeq \sqrt{\frac{1}{N} \sum_{i=1}^N (x_{SW}^i - \bar{x}_{SW})^2} = \\ &= \sqrt{\frac{1}{N} \sum_{i=1}^N \left[\sqrt{\beta_x \epsilon_{SW,x}^i} \cos \phi_x - \frac{1}{N} \sum_{i=1}^N \sqrt{\beta_x \epsilon_{SW,x}^i} \cos \phi_x \right]^2} = \\ &= \sqrt{\beta_x} \cos \phi_x \sqrt{\frac{1}{N} \sum_{i=1}^N \left[\sqrt{\epsilon_{SW,x}^i} - \frac{1}{N} \sum_{i=1}^N \sqrt{\epsilon_{SW,x}^i} \right]^2} \end{aligned} \quad (5.34)$$

In eq.5.34 the betatron function has been extracted from the summation under two reasonable assumptions: first, the slice Twiss parameters are the same as the projected ones even in case of slice lateral displacement; second, the slice Twiss parameters remain constant over all jittered runs. We now redefine the variable $\sqrt{\epsilon_{SW,x}^i} \equiv Q_x^i$. Given $\cos \phi_x \leq 1$, it is possible to make the condition in eq.5.33 more stringent by defining the new instability threshold as the ratio between the standard deviation of Q_x^i and the square root of the rms projected (unperturbed) emittance:

$$\frac{\sigma_{Q,x}}{\sqrt{\epsilon_x}} \leq 1 \quad (5.35)$$

Figure 5.19 shows the ratio defined by eq.5.35 along the bunch duration for the jitter budget specified in Table 5.2. Again, the reduced effectiveness of the instability suppression due to trajectory jitter is more pronounced in the vertical plane than in the horizontal plane.

Unlike the computation of the projected emittance and of the banana shape profile, the slice centroid amplitude offers a deeper and more complete understanding of the instability behaviour in the presence of trajectory jitter. That is, the projected emittance analysis does not contain the information on the slice particle distribution. Presumably, the emittance growth, more pronounced in the vertical plane than in the horizontal, could be due to a small portion of the bunch tail that is not participating in the seeded FEL process. In particular, only a few 100's of fs in the bunch core over a total duration of approximately 1 ps are going to be seeded in the modulator. If 40% – 60% emittance growth predicted by the simulation comes from the bunch tail slice offset, then it would not affect the FERMI FEL performance. Similar considerations apply to the parameter $R_{x,y}$ that works with the projection of the banana shape onto the plane

of interest, not with individual slice dynamics. Moreover, the jitter of the slice centroid position and divergence are treated separately. In this case, the instability suppression can only be evaluated by means of a function properly defined in terms of both the slice centroid position and divergence. This function is the slice centroid Courant-Snyder amplitude $\epsilon_{SW,x}$ defined in eq.5.32. When eq.5.35 is applied to each slice of the bunch, it is possible to predict which portion of the electron bunch can be safely used for the seeded FEL operation even in the presence of trajectory jitter. Figure 5.19 shows that, for the specific linac error set up considered, the vertical plane is more affected from the transverse wake field than the horizontal. However, the transverse motion of only a very small portion of the bunch tail is really affected by the trajectory jitter. Owing to the fact that the condition 5.35 is widely satisfied for most of the bunch slices (about 80% of the bunch duration in both planes), we do not expect any important effect of the jitter on the FERMI FEL performance if the tolerances in Table 5.1 and 5.2 are respected.

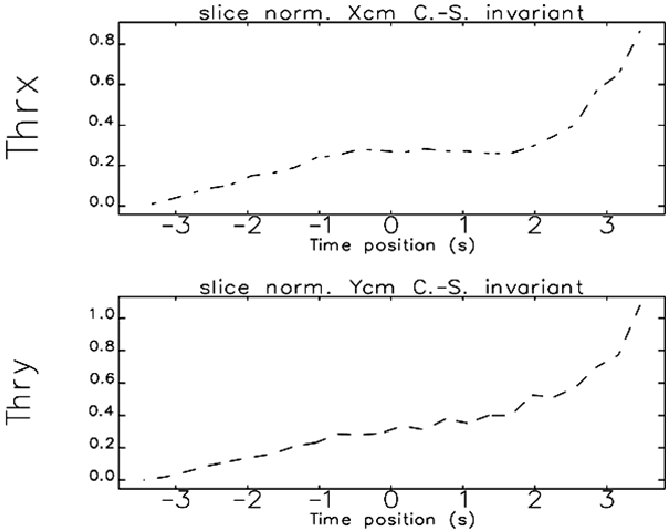


Figure 5.19: Ratio defined as in eq.5.35 vs. bunch duration (in 100 fs unit), at the end of the FERMI linac.

5.4 Coherent Synchrotron Radiation Instability

5.4.1 Energy Loss

In order to achieve high peak current and small energy spread at the undulator, the electron beam longitudinal phase space has to be manipulated in the linac. The high peak current is normally achieved by using a series of RF accelerating structures and at least one magnetic chicane, which all together make up the bunch length compression system, as discussed in Section 3.2.2. Emission of CSR in the chicane dipoles is the most evident perturbation to the beam energy distribution and, indirectly, to the beam emittance. In order to provide a deeper understanding of the CSR wake field discussed in Section 3.3.3, we follow [127] to give a conceptual interpretation of the CSR field emission. Then, we identify the regime of CSR emission for the FERMI case, in order to correctly compute the CSR effect in the assumption of a uniform charge distribution (step function). Finally, we show our application of the CSR theory to the case of a more realistic charge distribution, also in the presence of vacuum chamber shielding effect.

Following [127], two segments of the ultra-relativistic bunch, spaced at a distance $s \sim l_b$ (“tail” and “head”) and moving in an arc \widehat{AB} as shown in Figure 5.20, are considered. The electron and photon trajectory path length difference is called “slippage length”, s_L ²:

$$s_L = \widehat{AB} - \overline{AB} = R\theta - 2R \sin(\theta/2) \approx \frac{R\theta^3}{24} \quad (5.36)$$

Since it is, by definition, the maximum cooperation length over the bending magnet, it determines the regime of CSR emission, steady state or transient, as will be shown in the following. It also determines other two important geometrical parameters:

$$\theta = 2 \left(\frac{3s}{R} \right)^{1/3}, d = \overline{AB} \sin(\theta/2) = 2R \sin^2(\theta/2) = 2 \left(9s^2 R \right)^{1/3} \quad (5.37)$$

We will now restrict our analysis to the 1-D, longitudinal beam dynamics in the presence of CSR. This approximation does include neither the effects of the transverse distribution on the CSR fields nor the field variation across the beam. It is valid for a transverse beam size $\sigma_r \ll \sigma_z^{2/3} R^{1/3}$. We notice that this condition is well satisfied in the FERMI compressors where $\sigma_r \leq 200 \mu\text{m}$ and $\sigma_z^{2/3} R^{1/3} \geq 2 \text{ mm}$. The magnitude of the transverse electric field that acts on the head particle

²this classical geometric relation was already well-known to Ipparco in the Antique Greece, ~ 100 B.C. More precisely, it is valid for $\gamma \gg 1$ where the relativistic correction is given by the additional terms $R\theta/(2\gamma^2)$.

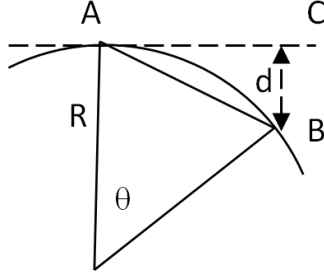


Figure 5.20: A geometrical diagram for an electron bunch motion in the bending magnet.

can be estimated as the field of the line-charge λ_z , with total charge Q , produced at the characteristic distance d [71]:

$$E_{\perp} \simeq \frac{1}{4\pi\epsilon_0} \frac{2Q\lambda_z}{d} \quad (5.38)$$

Because this field was radiated at point A, its direction at point B is perpendicular to the line \overline{AC} . Thus, the head particle experiences the longitudinal force:

$$F_{\parallel} = \frac{eE_{\perp}\theta}{4\pi\epsilon_0} = \frac{2eQ\lambda_z\theta}{4\pi\epsilon_0 d} = \frac{1}{4\pi\epsilon_0} \frac{2eQ\lambda_z}{3^{1/3}s_L^{1/3}R^{2/3}} \quad (5.39)$$

As already depicted in Section 3.3.3, the energy loss per unit length of the reference particle in the steady state regime of CSR emission is:

$$\frac{dE}{dz} = - \int_{-\infty}^{\infty} \lambda_z(z) F_{\parallel}(z) dz = - \frac{1}{4\pi\epsilon_0} \frac{e^2 N^2}{3^{1/3} R^{2/3} l_b^{4/3}} \quad (5.40)$$

where N is the number of particles per bunch and a uniform longitudinal density distribution $\lambda_z = N/l_b$ is assumed. The afore-mentioned conditions ensure that the bunch is sufficiently short that the radiation of the tail particles overtakes the head particles before the electron bunch leaves the magnet; at the same time, the magnet is so long that the transient behavior of CSR emission at its edges is negligible. This is one of the usual scenarios for magnetic compressors in linac-based FELs.

The FERMI BC1 and BC2 retarded angle $\gamma\theta$ is always bigger than 50 rad, the slippage length s_L is usually smaller than 140 μm and the nominal electron bunch length l_b is equal or longer than 150 μm (fwhm value). So, for $\gamma\theta \gg 1$

and $l_b \geq s_L$, the beam is emitting CSR in the long magnet, long bunch regime described by eq.3.74. At the highest charge of 0.8 nC, eq.3.74 predicts a total energy loss of 0.5 MeV that is 0.16% only of the mean energy at BC1. This value is comparable with the specified shot-to-shot mean energy jitter of the electron beam at the BC1 location.

We now enlarge the discussion to the possible scenarios of a very short bunch. To estimate the energy loss in this case, we will use the electron density distribution with the flat-top and smooth transitions at the edges with characteristic width of $\sim 2\sigma_0$ described by the *erf* function. The plot of this distribution is shown in Figure 5.21, with the assumption that the length of each transition occupies $\sim 10\%$ of the main body. The function is normalized to 1. The abscissa is in ps unit.

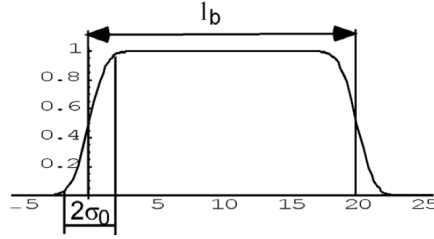


Figure 5.21: Longitudinal electron bunch density described by the *erf* function.

In this case, eq.3.68 becomes:

$$W_{CSR}^{SS}(z) = -\frac{1}{4\pi\epsilon_0} \frac{2e}{3^{1/3}R^{2/3}} \int_{-\infty}^z \frac{1}{(z-z')^{1/3}} \frac{1}{\sqrt{2\pi}\sigma_0} \left(e^{-\frac{z'^2}{2\sigma_0^2}} - e^{-\frac{(z'-l_b)^2}{2\sigma_0^2}} \right) dz' \quad (5.41)$$

This integral can be evaluated in analytical functions. The product $W_{CSR,SS}$ times the bend magnet length is plotted in Figure 5.22 for bending magnet length of 0.5 m, bending angle of 0.053 rad and $\sigma_0 = 20 \mu\text{m}$. One can notice that $W_{CSR,SS} \sim 1/z^{1/3}$ over the entire length of the bunch excluding the edges. The magnitude of the variation from head to tail for a 0.8 nC, 50 μm bunch length is approximately 0.2 MeV and 0.4 MeV for a larger bending angle as large as 0.095 rad. This result is to be compared with the 15.6 MeV energy loss induced by the longitudinal wake field in the FERMI linac (see Section 5.2). Thus, this study concludes that the CSR affects the FERMI electron bunch energy distribution much less than the linac geometric longitudinal wake field.

In practice, the electron bunch moves inside the vacuum chamber that acts

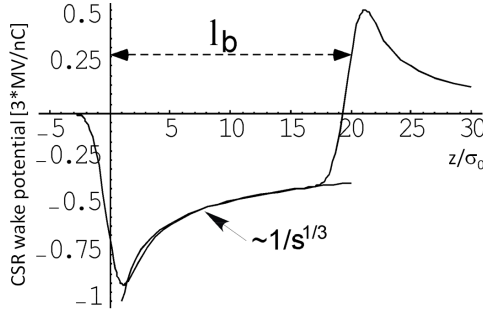


Figure 5.22: CSR wake potential.

as a waveguide for the radiation. Not all spectral components of the CSR propagate in the waveguide and therefore the actual radiating energy is smaller than in a free space environment. For an estimation of the shielding effect of vacuum chamber, the recipe suggested in [128] is used:

$$\frac{\Delta E_{shielded}}{\Delta E_{free\ space}} \simeq 4.2 \left(\frac{n_{th}}{n_c} \right)^{5/6} \exp \left(-\frac{2n_{th}}{n_c} \right), n_{th} > n_c \quad (5.42)$$

Here $n_{th} = \sqrt{2/3} (\pi R / \Delta)^{3/2}$ is the threshold harmonic number for a propagating radiation, Δ is the vacuum chamber total gap, $n_c = R / \sigma_c$ is the characteristic harmonic number for a Gaussian longitudinal density distribution with the rms value of σ_c . For a uniform stepped density distribution, $\sigma_c \simeq l_b / 3.22$ with l_b the distribution length. The meaning of n_c is that the spectral component of the radiation with harmonic numbers beyond n_c is incoherent. Figure 5.23 shows the calculated effect of shielding for vacuum chamber with $\Delta=8$ mm. However, because of the very wide vacuum chamber in BC1 and BC2 (inner radius is 35 mm wide), most of the CSR emission is not shielded when a bunch length of the order of 1 ps is considered.

5.4.2 Emittance Growth

The energy loss induced by CSR is inversely proportional to the bunch length. Since in a magnetic chicane the bunch length reaches its minimum already in the third magnet, the global CSR effect is dominated by the energy spread induced in the second half of the chicane. Given the CSR induced energy spread $\sigma_{\delta, CSR}$,

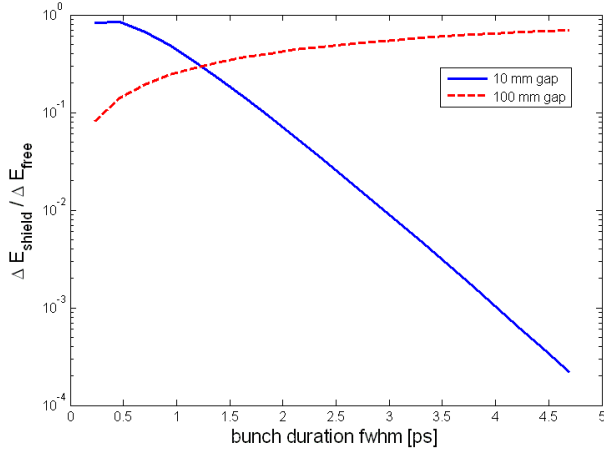


Figure 5.23: Suppression of CSR by the vacuum chamber shielding.

i.e. computed with one of eqs. 3.71, 3.72 or 3.75, eq.3.31 can be used to estimate the projected emittance growth induced by CSR in the presence of chromatic filamentation:

$$\frac{\Delta\epsilon}{\epsilon_0} \simeq \frac{1}{2} \frac{\beta}{\epsilon} \theta^2 \sigma_{\delta,CSR}^2 \quad (5.43)$$

It is possible to recognize here the chromatic nature of the CSR transverse kick angle, $\theta\sigma_{\delta,CSR}$, where for a small bending angle ($\theta \ll 1$) the first derivative of the dispersion function behaves such as $\eta' \approx \theta$. Due to the β -dependence of the emittance growth, a proper optics design can help to reduce the impact of CSR emission on the electron beam transverse dynamics by counteracting the CSR emission especially in the last two bending magnets of the chicane. This formalism, however, does not take into account the motion in phase space of the bunch slices that causes such emittance blow up. In fact, an energy/position correlation along the bunch is established by CSR emission. An optics system can be designed to remove this correlation, finally canceling the consequent emittance dilution. Also, the potential influence of SC forces during magnetic compression on the electron beam dynamics should be evaluated. A benchmark of 1-D and 3-D modeling including a more exhaustive, numerical treatment of CSR instability also in the presence of SC forces during magnetic compression is presented in the following.

5.4.3 Optics Design to Suppress CSR Instability

Owing to the β -dependence shown by eq.5.43, the CSR induced projected emittance growth expected at the magnetic compressor exit is reduced by a strong focusing of the electron beam in the bending plane, especially where the CSR emission is stronger that is in the third and fourth dipole magnet of the chicane. The physical meaning of this is given by the well-known relation between the Twiss parameters:

$$\beta\gamma = 1 + \alpha^2 \quad (5.44)$$

and by recalling that the geometric transverse rms beam size and angular divergence are given, respectively, by $\sigma = \sqrt{\epsilon\beta}$ and $\sigma' = \sqrt{\epsilon\gamma}$. So, for any α , a small β -function corresponds to a high beam angular divergence. If this is large enough, the CSR kick is largely dispersed in the particle divergence distribution – the perturbed beam divergence is computed as the squared sum of the unperturbed beam divergence and the CSR kick, that can therefore be neglected – and no relevant CSR effect is observed in the bending plane. For this reason, the horizontal betatron function is forced below 5 m in the second half of the FERMI magnetic chicanes BC1 and BC2, as shown in Figure 4.2. This configuration limits the relative projected emittance growth to $\sim 10\%$.

The CSR instability is not only studied for design the compression process, but also for design the beam transport in the high energy transfer line that is usually included in the machine to bring the electron beam from the linac end to one or more undulator lines. Basically, all what is necessary is to contain the effect of CSR on the emittance by employing a scheme of emittance preservation that we are going to explain now. The CSR induced projected emittance growth is actually the result of the bunch slices misalignment in the transverse phase space. This misalignment is meant to be a spatial and an angular offset of each slice centroid respect to the others. This offset is correlated with the z-coordinate along the bunch. In principle, the emittance growth can be completely canceled out if this correlation is removed. The spatial (angular) offset evaluated at a certain point of the lattice is the product of η_x (η'_x), or equivalently the linear transport matrix element R_{16} (R_{26}), with the CSR induced energy change, integrated over the beam path. In general, this kind of product has two contributions dealing with the uncorrelated and correlated energy change in the dispersive region; they lead to incoherent and coherent emittance growth, respectively [129]:

$$\langle \Delta x^2 \rangle_{incoh} = \int_{path} R_{16}^2(s) \frac{d\sigma_\delta^2(s)}{ds} ds \quad (5.45)$$

$$\langle \Delta x^2 \rangle_{coh} = \left(\int_{path} R_{16}(s) \frac{d\sigma_\delta(s)}{ds} ds \right)^2 \quad (5.46)$$

The angular kick error $\langle \Delta x'^2 \rangle$ is calculated with the same formulas, just substituting R_{16} with R_{26} . Eq.5.45 is the integral of a positive quantity and therefore it cannot be made null in any case. Instead, the sign of the integrand in eq.5.46 can change along the beam path and, if a proper linac optics is set, it can be zero at the end of the path. This is the case for CSR emission. If a π betatron phase advance is built up between two points of the lattice at which the beam is emitting CSR in identical conditions, then eq.5.46 is the integral of an odd function over a half-period and its value is zero [130]. We are now going to explain this optics scheme in detail for the FERMI Spreader design.

Let δ_{CSR} be the relative energy loss due to CSR for an electron in the first bend magnet of the Spreader scheme shown in Figure 5.24, right plot (b). Then the kick to the electron trajectory due to this energy loss at the end of the first magnet, in the thin lens approximation, can be written as:

$$\delta'_x = \eta'_x \delta_{CSR} \quad (5.47)$$

where η'_x is the derivative of the dispersion function at the exit of the magnet. Since we use $-I$ transport between the magnets (namely, a π betatron phase advance in the bending plane), then at the entrance of the second magnet this kick changes sign and also the derivative of the dispersion function changes sign. Thus, the kick of the second magnet to the electron trajectory is $\eta'_x \delta_{CSR}$. We assume that the electrons' longitudinal position inside the bunch is fixed and that, therefore, the CSR causes the same amount of the energy loss in the second magnet as in the first magnet (as well as in the third and fourth magnets). After another $-I$ transport, the kick due to the CSR in the third magnet is $-\eta'_x \delta_{CSR}$; the kick from the fourth magnet is the same as in the third one, $-\eta'_x \delta_{CSR}$. At the end, the total kick due to the CSR induced energy loss in the dispersive region is:

$$\delta x' = 2\eta'_x \delta_{CSR} - 2\eta'_x \delta_{CSR} = 0 \quad (5.48)$$

We see here that the electron emerges with zero kick, and therefore, there must be no emittance excitation. In practice, however, the electron bunch is not completely frozen and there is a slight re-arrangement of electrons within the electron bunch. Certainly, this compromises the scheme, but not much. In all circumstances, the above described scheme is probably the best what one can do in order to contain the emittance excitation.

By the way, we notice that a similar analysis repeated for an angular Spreader like that in Figure 5.24, left plot (a), shows that the angle of the trajectory acquired in the central magnet should be twice as large as the one in either of the side magnets. Although both Spreader schemes work in principle, the parallel Spreader is chosen for FERMI@Elettra, that has a small non-zero $R_{56} = 2.8$ mm. It is easy to modify it by using the second quadrupole (of four) in each achromat. These quadrupoles are separated by a unit transfer matrix and located near

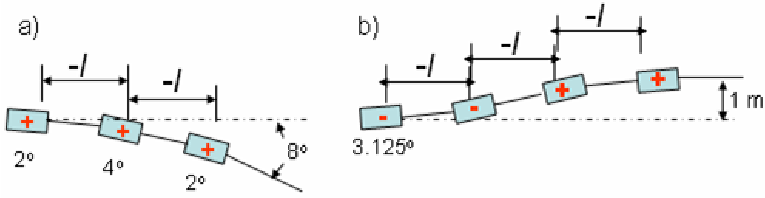


Figure 5.24: Angular (a) and parallel (b) Spreader (conceptual).

to the positive and negative peaks of the dispersion function. Thus, one can simultaneously change their gradients and produce a dispersion bump localized between the quadrupoles. By controlling this bump, one would be able to regulate the R_{56} of the Spreader making it to be exactly zero or any other reasonable value. In fact, we propose to keep it slightly positive in some cases in order to disperse the electrons in the spikes of the peak current at the edges of the electron bunch. Figure 5.8, already shown in a previous Section, illustrates the idea. Top of the Figure shows the original distribution, without energy variation in the main part and significant energy variation of the opposite sign in the tails. At its bottom we see what happens when we increase R_{56} from 2.8 mm to 7 mm. We disperse the electrons in the back spike more strongly and produce the anticipated reduction in the peak current.

5.4.4 Numerical Methods

Three particle tracking codes are used to support the analytical study of CSR instability and for mutual benchmarking. They are elegant [82], IMPACT [131] and CSRTrack3D [132]. The flexibility of these codes allows the investigation of the FERMI compression scheme and CSR effects independently from the analytical approximation for the magnet length ($\gamma\phi \gg 1$ or $\ll 1$) or bunch length ($\sigma_z \gg$ or $\ll R\phi^3/24$), already discussed in Section 3.3.3. Moreover, the codes allow the simulation of an arbitrary longitudinal current profile since they convolve the CSR wake function with the actual current profile at the entrance of the magnetic chicane. elegant implements a 1-D CSR steady-state and transient force approximation for an arbitrary line-charge distribution as a function of the position in the bunch and in the magnet; the charge distribution is assumed unchanged at retarded times [72]. The 1-D model ($\sigma_r \ll \sigma_z^{2/3} R^{1/3}$, where R is

the orbit radius of curvature) does include neither the effects of the transverse distribution on the CSR fields nor the field variation across the beam. However, these approximations fit well with the bunch length compression scheme in FERMI@Elettra. IMPACT computes quasi-static 3-D SC forces in the linac with the exception of CSR which is treated with the same 1-D algorithm as in elegant. Figure 5.25 shows the good agreement of the slice emittance predicted by IMPACT, which was run for FERMI at LBNL, and elegant, for a 0.8 nC, 10 ps long bunch compressed by a factor of 10 in BC1. This agreement demonstrates that SC forces in the range 100–350 MeV, simulated in IMPACT but not in elegant, do not affect the compression substantially. CSRTrack3D, which was run for FERMI at SLAC, treats sub-bunches of variant shape traveling on non-linear trajectories in the compressor. The simulation result in Figure 5.25 shows that the slice emittance of the bunch compressed by a factor 10 is somehow affected, not drastically, by CSR.

In conclusion, a specification of 1.0 mm mrad and 1.5 mm mrad for the slice and projected normalized emittance, respectively, can finally be established for a compression factor of 10 in the one- as well as in the two-stage compression scheme (see next Section for a comparative study of these two scenarios). These values include a $\sim 20\%$ margin with respect to the simulation results and are compatible with the FEL ultimate goal of 4 nm wavelength output, for which $\gamma\epsilon \leq \gamma\lambda/4\pi \simeq 2$ mm mrad at 1.5 GeV. The significant slice emittance growth shown by Figure 5.25 at the bunch edges is not really a limiting factor to the FEL performance because those portions of the electron bunch are not foreseen to interact with the external seeding laser, primarily because of the expected arrival time jitter of 150 fs (rms value) of the electron bunch with respect to the laser. In the presence of such jitter, only the bunch core, approximately 600 fs long, will be involved in the FEL generation. On one hand, the particle distribution at the bunch edges suffers more than the bunch core of nonlinear energy chirp, which leads to local over-compression and optics mismatch. Thus, we expect a stronger effect of the CSR instability in those regions. On the other hand, the very ends of the bunch usually contain a smaller number of particles than the bunch core. This implies a bigger uncertainty in the computation of the beam slice parameters by the tracking codes due to numerical sampling errors.

5.5 Microbunching Instability

5.5.1 Energy Spread

So far we have considered collective effects with a typical scale of the order of the electron bunch length. We have demonstrated that at this scale we can neglect the energy loss induced by CSR by virtue of the dominant dynamics established

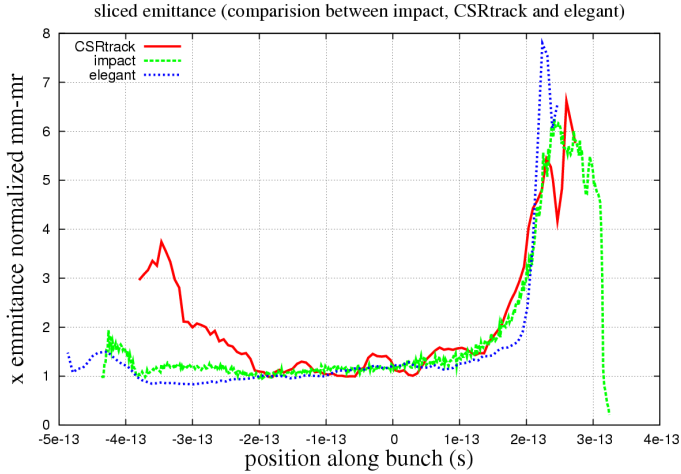


Figure 5.25: Codes benchmarking slice emittance for $C = 10$ in the FERMI magnetic chicane BC1. We find a good agreement of the slice emittance predicted by IMPACT (thick dotted line), which was run for FERMI at LBNL, and `elegant` (sparse dotted line), for a 0.8 nC charge beam. This agreement demonstrates that SC forces in the range 100–350 MeV, simulated in IMPACT but not in `elegant`, do not affect the compression substantially. The CSRTrack3D result (solid line) shows that the slice emittance is somehow affected, albeit not drastically, by CSR.

by the linac geometric wake fields. We can also ignore LSC effects [38, 74–78, 127, 133, 134] because they are weak in the relativistic electron bunch with a smooth density distribution. But at a scale much smaller than the bunch length both these effects gain significance. At this scale shielding is not important at all and any microstructures within the bunch will cause CSR as in a free space. The same microstructures will induce LSC forces which over time will produce energy modulation of electrons within the electron bunch. Together, LSC and CSR give rise to so-called microbunching instability [38, 78, 127]. This is a rather fundamental instability that takes its roots in a shot noise of electrons. Shot noise is responsible for initial microbunching of electrons. The microbunching induces LSC forces and they produce energy modulation of electrons. Then, energy modulation is transformed into spatial modulation with increased magnitude of microbunching when the electron bunch propagates through the magnets of

the bunch compressor(s). At the same time, increased microbunching gives rise to increased intensity. The entire machine acts as gigantic amplifier of the initial noise in a direct similarity with the process of self amplified spontaneous emission in FELs. What one gets at the end is an electron beam with significant fragmentation in the longitudinal phase space that reflects both a modulated current profile and an increase of the slice momentum spread which, if it is too large, reduces the gain and increases the bandwidth of the FEL.

Simulation of the microbunching instability with particle tracking codes requires a large number of macroparticles. For example, the microbunching amplitude, b , due to shot noise in an electron beam with peak current I_b within the bandwidth $\Delta\lambda$ can be estimated:

$$b = \sqrt{\frac{ec}{I_b\Delta\lambda}} \quad (5.49)$$

For $I_b = 75$ A and $\Delta\lambda = 10 \mu\text{m}$ this formula gives $b = 2.52 \cdot 10^{-4}$. Typically, the microbunching due to granularity of the distribution of macro-particles is much larger. For example, we calculate for a 6 ps long electron bunch (fwhm) with 10^6 macroparticles, $b = 1.3 \cdot 10^{-2}$, which is approximately 50 times larger than the real shot noise. The particle tracking codes `elegant` and `IMPACT` are used in order to get around this problem. A completely different approach is also pursued, namely a technique that follows the evolution of the distribution function using Vlasov's kinetic equation [135]. This was implemented in a code developed and run for FERMI at LBNL. Ideally this technique is absolutely free from computational noise, although some noise can be introduced on which, due to the final size of the grid, the initial distribution function is defined. However, in practice, this noise can be easily kept below the sensitivity level. Last but not least, we use the analytical linear theory [78] to estimate the gain of the microbunching and the energy spread caused by the instability. The tracking codes results and the analytical evaluation converge with small discrepancy when applied to the beam dynamics in FERMI@Elettra. In the case of comparison of the simulation results with the linear theory, it becomes apparent that a true result will likely be different because of the anticipation that the linear model should fail at the high frequency end of the noise spectra. Nevertheless, even in the analytical case we want to present a simple transparent result which gives a correct assessment of the magnitude of the effect.

Eq. 3.85 is applied to the two-stage compression scheme of FERMI@Elettra, whose set of machine and electron beam parameters are listed in Table 5.3. The instability gain vs. uncompressed modulation wavelength at the end of BC1 is shown in Figure 5.26, left plot, while the total one at the linac end is shown in Figure 5.26, right plot. Comparison of the two plots show that most of the microbunching instability gain in FERMI@Elettra occurs after BC2. Hence, one

can effectively suppress it by using only BC1 for bunch compression. This is a potentially attractive option that however involves many different aspects of the electron beam dynamics. The next chapter is dedicated to such investigation.

Table 5.3: FERMI parameters used to calculate the microbunching instability gain.

Parameter	Value	Units
Uncorrel. Energy Spread (rms)	2	keV
Initial Beam Energy	100	MeV
Beam Energy at BC1	320	MeV
R_{56} of BC1	-26	mm
Lin. Compression Factor in BC1	4.5	
Peak Current after BC1	350	A
Linac Length up to BC1	30	m
Lin. Compression Factor in BC2	2.5	
Beam Energy at BC2	600	MeV
R_{56} of BC2	-16	mm
Peak Current after BC2	800	A
Linac Length up to BC2	50	m
Linac Length after BC2	70	m

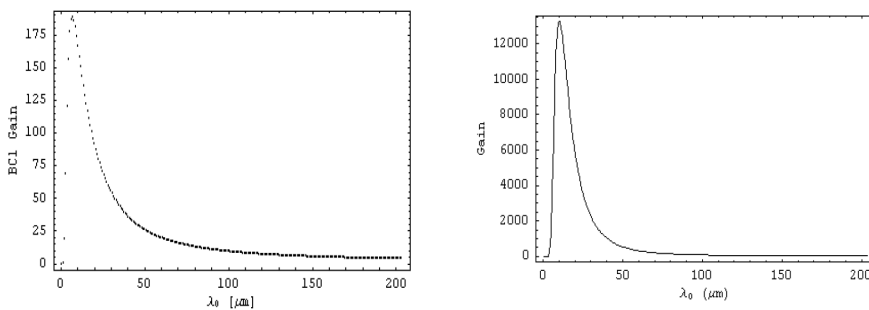


Figure 5.26: Two-stage compression gain function at BC1 end (left) and at linac end (right).

The slice energy spread in the electron bunch after BC2 can be calculated

by assuming that the energy spread induced by the microbunching instability will eventually become uncorrelated energy spread. We assumed an initial shot noise with a constant spectral power and calculate the initial bunching according to the formula:

$$|b|^2 = \frac{\sigma_I^2}{I_b^2} = \frac{2e}{I_b} \Delta\nu \quad (5.50)$$

where $\Delta\nu$ is the bandwidth. Then, we convolute it with spectral gain function $G(\lambda)$ shown in Figure 5.26, right plot, to obtain:

$$\left(\frac{\sigma_E}{E_0}\right)^2 = \frac{2ec}{I_b} \int G(\lambda)^2 \frac{d\lambda}{\lambda^2} \quad (5.51)$$

Here we used a substitution $\Delta\nu = c\Delta\lambda/\lambda^2$. This gives us a large value, $\sigma_E = 4.3$ MeV, which is one order of magnitude larger than the FERMI FEL specification of 150 keV rms.

5.5.2 Landau Damping

Eq. 3.84 shows that the gain of the microbunching instability is very sensitive to the uncorrelated energy spread in the electron beam. Typically, even a modest increase in the uncorrelated energy spread weakens the instability because of the Landau damping effect. In order to underline the importance of Landau damping, Figure 5.27 shows the damping coefficient for a Gaussian energy distribution, eq.3.85, as function of the compressed modulation wavelength: the dashed curve reproduces the damping provided at BC1 by the natural 2 keV rms energy spread of the beam. The other two curves are for 10 keV and 30 keV rms, respectively. The laser heater was proposed in [38] in order to have an efficient control over the uncorrelated energy spread with the ability to increase it beyond the original small level. The laser heater consists of an undulator located in a magnetic chicane where a laser interacts with the electron beam, causing an energy modulation within the bunch on the scale of the optical wavelength. The corresponding density modulation is negligible and the coherent energy/position correlation is smeared by the particle motion in the chicane. The reason is that, if the following condition is satisfied, $\sigma'_x \cdot |R_{52}| \geq 780\text{nm}/2\pi$ (780 nm is the seed laser wavelength), then electrons with different divergences will follow different paths independently of their longitudinal position. In FERMI we have $\sigma'_x = 26 \cdot 10^{-6}$ and $|R_{52}| = 25$ mm; the condition for decoherence, $\sigma'_x \cdot |R_{52}| = 650$ nm, is therefore satisfied. In the following it is simply assumed that the laser heater provides additional energy spread which adds in quadrature to the uncorrelated one generated by the photoinjector.

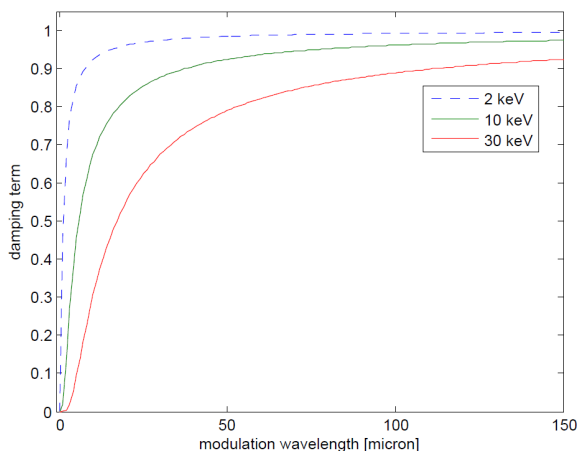


Figure 5.27: Gaussian damping coefficient vs. compressed modulation wavelength.

In order to demonstrate the effect of the laser heater we compute the spectral gain function for a few different setting of the laser heater and plot them in Figure 5.28. It is seen here that the larger the energy spread added by the laser heater the more efficient is the suppression of the gain at the high frequency end of the spectra. We also compute the uncorrelated energy spread at the end of the linac as a function of the energy spread added by the laser heater only with the beam and accelerator parameters listed in Table 5.3. The analytical result is shown in Figure 5.29. The calculation is simplified by the fact that the interaction between the laser and the electron beam is weak because the required energy spread is small. In this case the changes in laser and beam dimensions along the interaction region can be neglected. Even the slippage effect is negligible because the slippage length is small with respect to the electron and laser pulse length. The heating process is therefore well described by the small gain theory with a single mode [136].

Figure 5.29 shows a minimum. For beam heating weaker than that minimum, the instability is not suppressed and the final uncorrelated energy spread grows because of the energy modulation cumulated at the linac end at very short wavelengths. For stronger beam heating, instead, the final uncorrelated energy spread is dominated by that induced by the laser heater. Owing to the (approximate) preservation of the longitudinal emittance during bunch length compression, the final energy spread is linearly proportional to the initial one and this explains the linear behaviour in the right part of the plot. The point of minimum

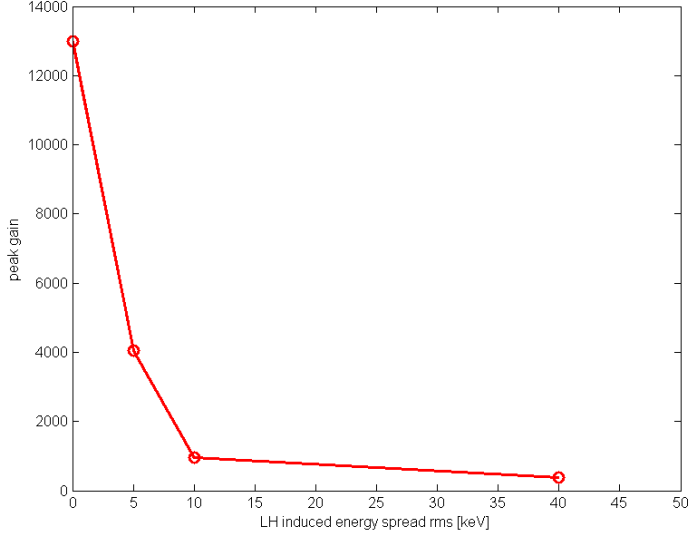


Figure 5.28: Spectral gain function for several beam heating levels.

is the best one at which the machine should be tuned because, although the instability is not fully damped, it is kept well under control by the beam heating and the final energy spread is within the FEL specification. According to Figure 5.29, the energy spread induced by the laser heater should be in the range 8–12 keV rms.

As an alternative to the beam heating, energy modulation and transverse emittance excitation induced by CSR can be moderated, in principle, with an appropriate design of the compressor lattice. Although transverse microbunching radiative effects excite emittance directly [137, 138], an indirect emittance excitation via longitudinal-to-transverse coupling typically dominates them. This coupling is characterized by the function:

$$H = \gamma_x \eta_x^2 + 2\alpha_x \eta_x \eta_x' + \beta_x \eta_x'^2 \quad (5.52)$$

where γ_x , α_x and β_x are the horizontal Twiss functions and η_x , η_x' are the horizontal dispersion function and its derivative (here we assume a chicane in the horizontal plane.) Using H , we write for the emittance contribution due to CSR:

$$\Delta\epsilon_x \approx H\delta^2 \quad (5.53)$$

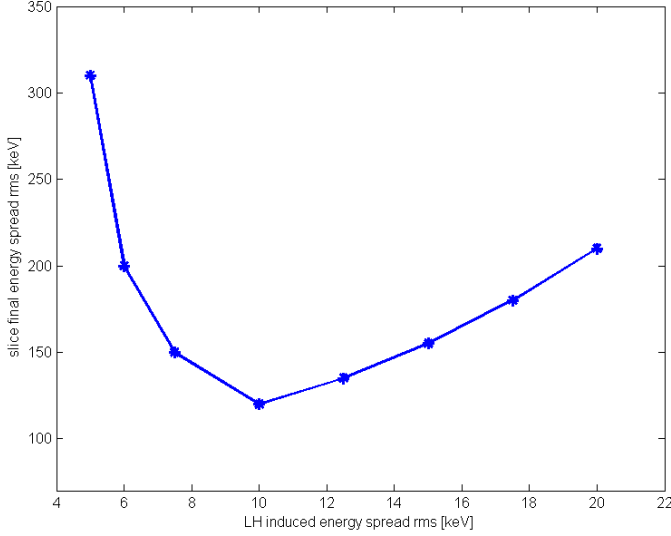


Figure 5.29: Final uncorrelated energy spread vs. energy spread added by the laser heater. This analytical computation is for the two-stage compression scheme in FERMI@Elettra.

where δ is the spread of the energy losses caused by CSR, which is proportional to the value defined in eq.5.40. It is obvious from eq.5.53 that the lattice with small H gives less emittance excitation. Since the strongest CSR is expected in the third and fourth bending magnet of the chicane where the electron bunch is the shortest, we pursue the FERMI BC1 design with reduced H in this magnet. Now we would like to give the argument why we may not want to get the smallest possible H . While moving through the chicane bending magnets, the electrons with different amplitudes of the betatron oscillations follow different paths with path lengths described by the following equation:

$$\delta l = \int_0^s \frac{x(s')}{R} ds' = x_0 \int_0^s \frac{C(s')}{R} ds' + x'_0 \int_0^s \frac{S(s')}{R} ds' \quad (5.54)$$

Here x_0, x'_0 are the electron spatial and angular coordinate at the beginning of the chicane and $C(s), S(s)$ are the cos-like and sin-like trajectory functions. It can be shown that the rms value of Δl taken over the electrons in any given slice of the electron bunch is related to the electron beam emittance through the

function H , i.e.:

$$\Delta l_{rms} \approx \sqrt{H\epsilon_x} \quad (5.55)$$

Thus, the lattice with large H spreads slice electrons more apart than the lattice with small H and washes out the microbunching more effectively. In fact, without accounting for this effect, the gain of the microbunching instability would be significantly overestimated. This effect is very similar to the effect of the Landau damping due to the energy spread. Because of the last argument, we design the BC1 lattice such as the magnitude of H in the last bend of the chicane can vary at least within a factor of four. It will give us some flexibility to maneuver between such tasks as containing the emittance excitation due to CSR that benefits from smaller H and containing energy spread growth due to the microbunching instability that benefits from larger H .

5.5.3 Numerical Methods

The sources of microbunching instability include initial density modulations arising from non-uniformity of the photo-cathode laser profile and shot noise. Unfortunately, simulations of shot noise are affected by unphysical numerical sampling anomalies introduced by tracking codes when the particle flow is not sufficiently smooth. In FERMI, this might artificially increase the instability gain by a factor $\sqrt{N_{real}/N_{sim}} \leq 100$, depending on the number of particles in the real bunch, N_{real} , and in the simulation, N_{sim} . For this reason, three different noise suppression strategies have been adopted and benchmarked: i) a smoothed initial particle distribution is taken as start for elegant [139]; the particle binning is then filtered during the simulation. Several tens of million particles representing a 0.8 nC, 10 ps long bunch were tracked on parallel computing platforms to resolve the final modulation at wavelengths of 1-10 μm ; ii) IMPACT tracked 1 billion particles, thus reducing the numerical sampling noise by brute force. The convergence of the final result for the increasing number of macroparticles was demonstrated in [140]; iii) a 2-D direct Vlasov solver code was used that is much less sensitive to numerical noise than PIC codes. The 4-D emittance smearing effect is simulated by adding a filter, as shown in [141, 142].

elegant demonstrates [139] that FERMI is very sensitive to small initial density modulations and that the instability enters into the nonlinear regime as the beam is fully compressed in BC2. The longitudinal phase space becomes folded and sub-harmonics of the density and energy modulation appear. Consequently, the uncorrelated energy spread produced in the injector region has to be increased with a laser heater. Based on these results and on the afore-mentioned analytical evaluations, elegant was used to define the physical requirements for the laser heater; they are summarized in Table 5.4.

IMPACT and the Vlasov solver predict [141] that a minimum beam heating of 10 and 15 keV rms, respectively, is necessary to suppress the microbunching instability in the one- and two-stage compression scheme. This leads to a final slice energy spread of 110 and 180 keV rms, respectively, with a nominal uncertainty of about 15% from code to code.

Table 5.4: Parameters of laser heater for FERMI@Elettra.

Parameter	Value	Units
Nr. of Undulator Periods	12	
Undulator Period Length	50	mm
Undulator Parameter k	0.487	
Laser Peak Power	13	MW
Laser Wavelength	780	nm
Laser Waist	0.912	mm
Chicane Bending Angle	3	deg

In spite of the results obtained so far, the microbunching instability study still presents some challenges. First, the Vlasov solver agrees well with the linear analytical solution of the integral equation for the bunching factor for a compression factor of 3.5, as shown in [135]. However, entrance into the nonlinear regime is predicted by that code when the compression factor reaches 10 [141]. Unfortunately, the analytical treatment of the nonlinear regime remains a work in progress [143] and no nonlinear analytic treatment of the microbunching instability exists at present for codes benchmarking. Second, the initial seed perturbations for the instability are currently not well determined, both in configuration and in velocity space. Moreover, complications from the bunch compression process, which can lead to “cross-talk” amongst different modulation frequencies, make it difficult to extract the frequency-resolved gain curve. Finally, a fully resolved 3-D simulation of microbunching instability can only be accomplished with massive parallel computing resources that are impractical for the machine fine tuning. As mentioned before, only IMPACT implements 3-D SC forces, while `elegant` and Vlasov solver adopt a 1-D LSC impedance. However, the substantial agreement between the codes suggests that the 3-D SC effect (which is expected to mitigate the microbunching instability) is probably masked by the differences in the computational methods and in the treatment of the numerical noise.

5.6 Conclusions

Analytical evaluations and simulations with particle tracking of electron beam collective effects in a single-pass, S-band linac have been carried out. A quantitative study for the FERMI@Elettra electron beam delivery system from the injector end to the undulator, including the magnetic bunch length compression has been done. The strength of the short-range SC forces has been evaluated through the laminarity parameter computed as function of the electron beam parameters along the line. It has been shown that SC forces might corrupt the quasi-laminar particle motion and therefore should be taken into account during the one-stage magnetic compression of the bunch length, even at energies at which the electrons are ultra-relativistic. The effect of the structural longitudinal and transverse wake field on the electron beam energy distribution and projected emittance, respectively, has been studied. Shaping of the initial current profile has been proposed to alter the longitudinal wake potential and make it almost linear. In this way, the longitudinal wake field can be used to cancel out the linear energy chirp required for magnetic compression; moreover, nonlinear contributions to the energy chirp are minimized. It has been proposed to suppress the head-tail instability induced by the transverse wake with trajectory manipulation along the linac (emittance bumps). Then, a trajectory jitter study has been done in order to specify the magnets' alignment and vibration tolerances that do not affect this correction scheme. Finally, the CSR effect on the transverse emittance and the microbunching instability linear gain has been computed and compared with particle tracking results. The optics design allows for the compensation of the CSR effect by means of a suitable optics arrangement in the magnetic chicanes and in the Spreader. As for the microbunching instability, it enters into the nonlinear regime when the two-stage compression is adopted. This study therefore justifies the implementation of a laser heater to Landau damp the instability and to keep the slice energy spread within the FEL specifications.

Chapter 6

Schemes of Magnetic Bunch Length Compression

This Chapter¹ discusses some general principles for the design of the magnetic compression scheme of the electron bunch duration for a seeded FEL. Although neither a general receipt nor an obvious solution exist for this problem, our considerations start from the FEL requirements about the final peak current and bunch length of the electron beam. We stress that the seeding option for the FEL imposes some constraints on the bunch length that are not usually present in a SASE FEL design. Once the machine working point - in terms of compression factor and electron beam parameters - has been determined, some discussions about the impact of the compression scheme on the suppression of the microbunching instability are presented. Finally, the feasibility of the proposed scheme(s) is demonstrated with particle tracking.

6.1 Working Point

We consider the machine working point as the ensemble of parameters that define the bunch length compression factor and the final electron beam parameters. We start from the requirement for the output photon pulse duration, whose minimum value is usually specified by fast dynamics experiments. In a seeded FEL, this is approximately the duration of the external seeding laser. It is 100 fs long in FERMI@Elettra. The final electron bunch duration has to be long enough

¹This Chapter is based on the following work: *Suppression of microbunching instability with magnetic bunch length compression in a linac-based fel*, Phys. Rev. Special Topics – Accel. and Beams, **13**, 010702 (2010), by S. Di Mitri, M. Cornacchia, S. Spampinati and S. V. Milton.

to accommodate the seeding pulse and the arrival time jitter of the electrons with respect to the seed laser. In a two-stage harmonic cascade such as FERMI FEL2, which is implementing the fresh bunch technique to reach the smallest wavelength of 4 nm, the seeding laser pulse length actually counts for two. If we estimate a final time jitter of 150 fs (rms value), the electron bunch duration in FERMI cannot be shorter than approximately 600 fs fwhm (100 fs additional margin has been taken to avoid longitudinal overlap of the two seeding pulses interacting, respectively, in the first and in the second stage of the harmonic cascade). At the same time, the electron bunch peak current is usually determined by the users' specification for the number of photons per pulse, which is particularly important for experiments of nonlinear dynamics. Simulations of the FEL process in FERMI show that the goal of 10^{12} photons per pulse at 4 nm fundamental wavelength can be achieved with a peak current as high as 900 A [29]. The total charge is therefore determined by the peak current times the final bunch length, in the approximation of an ideal hard edge current profile. Actually, a factor usually equal to or smaller than 0.8 has to be included in this calculation that takes into account the real efficiency of the bunch length compression process. As already shown in this Thesis, this efficiency is limited by the nonlinear longitudinal dynamics introduced by (residual) high order energy chirps during the magnetic compression. The total electron charge in FERMI has therefore been fixed at 800 pC. We point out that by limiting the final bunch duration to the strict minimum value of 500 fs (the shot-to-shot stability of the FEL output intensity would then be suffering because of less space along the bunch left for accommodating the time jitter with respect to the seed laser) and assuming a compression efficiency of 0.9, the beam charge out of the injector could be in principle diminished to 450 pC. Some optimizations in this sense could be carried out in a future tuning of the FERMI FEL, if they turn out to be compatible with the users' experimental program.

The electron bunch length before compression is determined by the final bunch length times the (effective) compression factor. For the same peak current, the degrading effect of structural wake fields and CSR emission is minimized by the shortest duration, smallest charge of the electron bunch. The minimum electron bunch duration out of the RF photo-injector is often limited to a few ps by the photo-injector pulse shaping and repulsive SC forces. In general, a too short bunch at non-relativistic velocities suffers from transverse emittance degradation due to SC forces that must be counteracted with external focusing. At the same time, the charge density cannot be arbitrarily diluted by enlarging the transverse laser spot size because the minimum emittance achievable (the so-called thermal emittance) is proportional to its radius. At the end, a 3-D charge density that permits full control of the transverse and longitudinal emittance should be chosen. The specification on the transverse (slice) emit-

tance comes from the FEL requirement in order to reach saturation at the shortest wavelength. The FERMI FEL2 performance goal sets this value to 1 mm mrad normalized emittance at 1.5 GeV. Assuming an emittance degradation not bigger than 20% along the whole beam transport and compression, the injector should provide a slice emittance of approximately 0.8 mm mrad. Particle tracking studies show that this goal is achieved with 800 pC charge distributed along 10 ps (fwhm value) and with a photo-injector laser radius of 0.7 mm [29]. In conclusion, the total compression factor is fixed by the ratio of the final vs. the initial electron bunch duration that is 11 in case of FERMI. Relying on this theory, a working point for the FERMI magnetic compressors can be fixed, as it is depicted in Table 6.1. This is consistent with the electron beam specifications in Table 2.2.

Table 6.1: Main linac and magnetic chicanes nominal setting.

Peak Current	300 A	800 A	Units
L1 RF phase	-25	-27.5	S-band deg
BC1 bending angle	0.085	0.068	rad
BC1 R_{56}	-40.9	-26.3	mm
BC1 Lin. Compr. Factor	6.5	4.5	
L2, L3 RF phase	0	-20, 0	S-band deg
BC2 bending angle	0	0.050	rad
BC2 R_{56}	0	-14.2	mm
BC2 Lin. Compr. Factor	0	2.5	

The FERMI moderate compression factor of 10 could be achieved either with a one-stage or a two-stage magnetic compression scheme. Nevertheless, the two schemes might lead to some differences in the final current shaping, transverse emittance and energy distribution, mainly due to a different balance of the strength of collective effects such as CSR emission and microbunching instability. In the following, the issue of the emittance preservation is recalled with a special attention to the slice and the projected dynamics. The impact of the compression scheme on the development of the microbunching instability is treated in the next Section.

At the first stage of optimization, the horizontal, vertical and longitudinal particle motion are assumed to be uncoupled. The particle configuration generated in each plane at the end of the injector is taken as a reference, since the electrons are already ultra-relativistic and the particle spatial distribution is frozen for any practical purpose. Assuming that the injector is able to produce a beam whose parameters satisfy the FEL performance, the beam transport and manip-

ulation in the main linac should not degrade the area in each 2-D phase space by more than $\sim 20\%$. Simulations indicate that this threshold can be satisfied for the longitudinal core of the bunch, while it is harder to apply it when also the bunch edges are included. These regions are characterized by a lower charge density, therefore they are subjected to a different dynamics at very low energy, where the beam is generated in the presence of important SC forces that strongly depend on the charge density. This different dynamics of the bunch edges with respect to the core leads to a mismatch of the local distribution function (defined in the transverse and in the longitudinal phase space) with respect to the rest of the bunch. Moreover, the finite length of the bunch enhances a nonlinear behaviour of the space charge electric field at the bunch edges that introduces in turn a local nonlinear energy chirp. For all these reasons, particle dynamics in the bunch head and tail is usually studied only with particle tracking codes and the final beam quality is referred to $\sim 80\%$ of the beam population contained in the bunch core.

Figure 6.1 shows the evolution of the projected and slice horizontal emittance along the FERMI electron beam delivery system, from the injector end to the undulator entrance. Perturbative effects such as CSR emission and optical aberrations are included in the particle tracking performed with `elegant`. The same beam parameters and machine set up as in Figure 5.1 are used. Both in the case of low (top) and high (bottom) charge in the one-stage compression, the discrepancy between the slice and the projected emittance originates in the injector (the initial particle file was generated with GPT [144], as described in [29]) and it is preserved along the FERMI linac. The projected emittance bump in correspondence of BC1 is due to slice misalignment induced by the dispersive motion in the BC1 magnetic chicane: a $\sim 1\%$ correlated energy spread, required for bunch length compression, makes different slices to follow different trajectories. Their transverse misalignment translates into the projected emittance growth. This growth is recovered in the case of low charge, weak compression, as the dispersion bump closes at the end of the chicane. It is not, instead, for the high charge case. The (average) slice emittance is preserved as at the injector level in both cases.

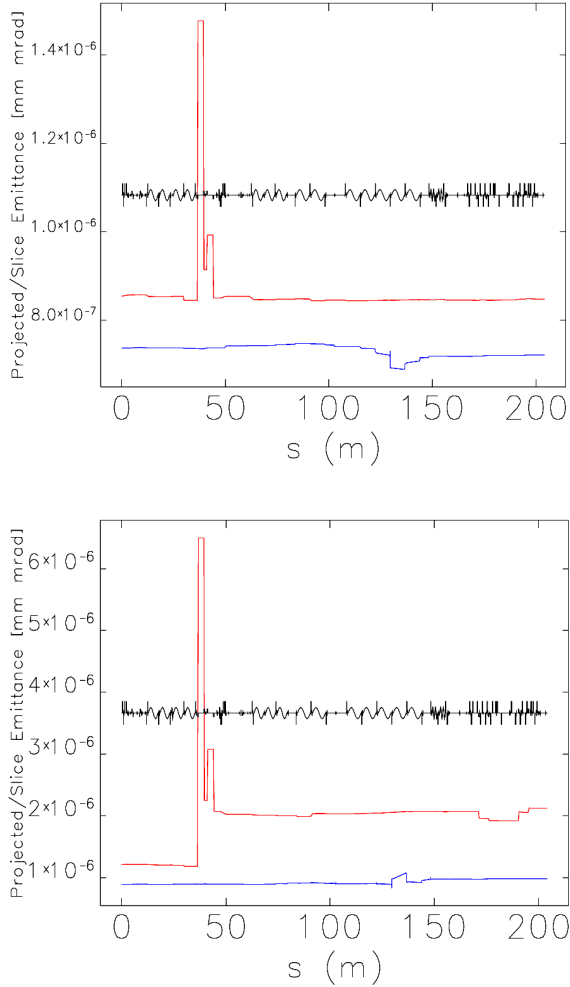


Figure 6.1: Projected and slice horizontal emittance along the FERMI linac. Top plot: projected (upper line) and slice (lower line) emittance along the FERMI linac for $C = 6.5$. Bottom plot: projected (upper line) and slice (lower line) emittance for $C = 10$. The slice emittance is averaged over the entire bunch length divided in 50 slices. The projected emittance is for 100% of the beam population. The (average) slice emittance is preserved as at the injector level in both cases.

6.2 Two-Stage Compression

The amplification of the energy modulation and emittance blow up induced by the microbunching instability in the presence of magnetic bunch length compression has been discussed in the previous Chapter. Some cures such as laser heater and optics tuning in order to mitigate or even suppress the instability have been discussed. We now want to show that a magnetic chicane downstream of the first one could be used for the same purpose, once a different compression scheme than the usual multi-stage is adopted. It will be shown that, after removing the linear energy chirp required for the compression at low energy, an additional and properly tuned R_{56} transport matrix element is able to dilute the initial energy modulation and to suppress the current spikes created by the microbunching instability without affecting the bunch length. A by-product of the study is the observation that a single compressor is more effective than the two-compressors scheme in reducing the unwanted modulations caused by the microbunching instability. The study is based on analytical calculations and on elegant simulation results.

As a preliminary discussion, let us start with a conventional two-stage compression scheme. The FERMI layout is taken as a case study. If the uncorrelated energy spread is included in the physics modeling, the larger the negative R_{56} in BC1 is, the bigger the uncorrelated energy spread out of the chicane will be by virtue of the preservation of the longitudinal emittance and the smaller the compression factor in BC2 should be to maintain the nominal total compression action. If the particle longitudinal cross-over in BC1 is efficient enough, it is expected that no density clusters are enhanced by the dispersive motion in the chicane. Unfortunately, the above statement becomes less and less valid the longer the wavelengths considered. Based on these considerations, we will show that two schemes can alternatively be adopted to smear an initial density modulation. The first is the one-stage compression scheme. In the second, BC2 is re-introduced in the layout but the energy chirp required by the compression in BC1 has to be removed at the entrance of BC2. This approach requires that the sign of R_{56} be equal in BC1 and in BC2. In practice, the scheme evolves towards a one-stage compression in which the final bunch length is determined by BC1 only, while the modulation washing out is made even more effective by BC2.

At first, we calculate the bunching factor at the exit of the first stage of compression, BC1, with a compression factor of 3.5 (slightly relaxed with respect to the nominal value of 4.5 for the two-stage compression in FERMI) established by $R_{56} = -31$ mm and a properly set energy chirp. Then, we consider an additional positive R_{56} transport matrix element (called DC) immediately downstream of BC1. In the latter case, $R_{56} = -33.8$ mm giving $C=4.5$ in BC1 is stronger than in the former case but the total compression factor is re-established by the DC

element that has $R_{56} = 2.9$ mm corresponding to $C=1/3$. Now, two sinusoidal density modulations of amplitude 0.03% at $10 \mu\text{m}$ and 1% at $100 \mu\text{m}$ are considered. The density modulations are superimposed to the initial beam current profile shown in Figure 6.2.

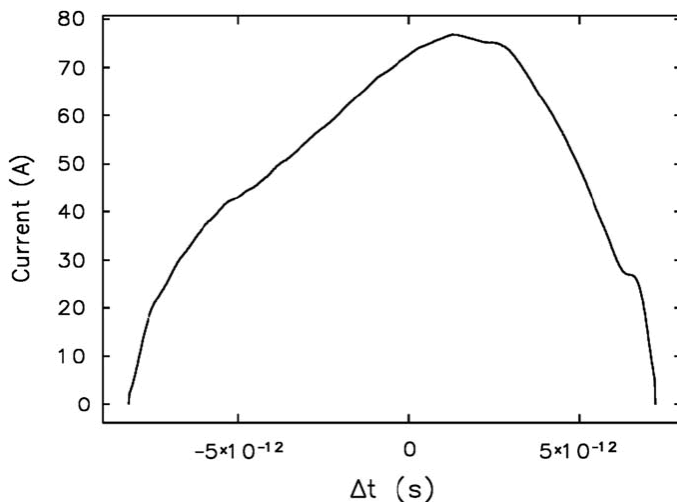


Figure 6.2: Initial unperturbed electron beam current profile. Input file provided by G. Penco (ST).

The two initial density modulations induce energy modulations of amplitude 0.3 keV and 5 keV at the entrance of BC1, at the wavelengths of $10 \mu\text{m}$ and $100 \mu\text{m}$, respectively. Table 6.2 shows the bunching factor calculated with eq.3.80 and eq.3.81, respectively, at the end of compression in the BC1-only and in the BC1+DC scheme. The total compression factor is 3.5 in both cases. As expected, the DC option reduces the bunching by a factor 4.5 at $10 \mu\text{m}$, while it is almost inefficient at $100 \mu\text{m}$ because the longitudinal phase mixing is no longer effective at such a long wavelength. As additional check, an initial density modulation of 0.03% at $100 \mu\text{m}$ is considered. The final bunching is still not affected by the DC option, so demonstrating that the effect of phase mixing is more sensitive to the wavelength than to the modulation amplitude.

On the basis of the results in Table 6.2, one might think of further increasing the positive R_{56} in DC while reducing the negative R_{56} in BC1; in this way the total compression factor is kept constant and the longitudinal phase mixing becomes effective even at longer wavelengths. As a matter of fact, this scheme

Table 6.2: Bunching factor after compression for the BC1-only and the BC1+DC scheme.

Initial Density Modulation	BC1 only	BC1 + DC
0.03% at 10 μm	$9 \cdot 10^{-3}$	$2 \cdot 10^{-3}$
1.00% at 10 μm	0.146	0.188
0.03% at 100 μm	$8 \cdot 10^{-3}$	$11 \cdot 10^{-3}$

is equivalent to a two-stage compressor with unequal weight between BC1 and BC2: the stronger the first chicane is, the more effective the instability suppression becomes. The implications of this preliminary study lead to consider the advantages of a single compressor over two. This is discussed in the next Section.

6.3 One-Stage Compression

The one-stage compression scheme optimizes the suppression of the instability with respect to the two-stage compression for two reasons: firstly, the phase mixing is more effective in BC1 due to the larger R_{56} and to the larger relative energy spread (see eq.3.85). Secondly, the absence of the high energy compressor does not provide the opportunity to transform the energy modulation accumulated by LSC downstream of BC1 into current modulation. These considerations are consistent with the studies presented in [141], where the instability gain function for a single bunch compressor lattice was shown to be significantly lower than in the case of the two bunch-compressor lattices. Owing to the sensitivity of harmonic cascade FELs to the slice energy spread – and of FERMI in particular [15, 16] –, it is important to reduce this parameter to the minimum. A metric to compare the performance between the two lattices is therefore the evaluation of the increase in beam slice energy spread caused by the microbunching instability and seeded by shot noise. This is shown in Figure 6.3 (compare with the analytical prediction in Figure 5.29), where the slice energy spread at the exit of the linac is reported as a function of the slice energy spread at the exit of the laser heater for the two lattices. In both cases the total compression is $C=10.4$ and the peak current 800A. These results have been obtained by using the same 2-D Vlasov solver as in [141] except for a modified and presumably more accurate model of the LSC impedance that includes averaging of the longitudinal electric field over the transverse beam density [142]. The error bars indicate the spread in the outcome corresponding to different seeds used for the generation of shot noise. First simulations with IMPACT and Vlasov solver based on 1-D

impedances [141] (not reported here) show the minimum of the curve in Figure 6.3 to be 9 keV and 15 keV, respectively, for the one-stage and two-stage compression. They predict a final slice energy spread of 120 and 180 keV rms. Now, a more accurate treatment of the transverse dynamics lowers the minimum to 6 keV and 11 keV, providing a final slice energy spread of 80 keV and 140 keV rms. Whatever the modeling used is, a one-stage compression minimizes the amount of uncorrelated energy spread provided by the laser heater, required to suppress the microbunching instability.

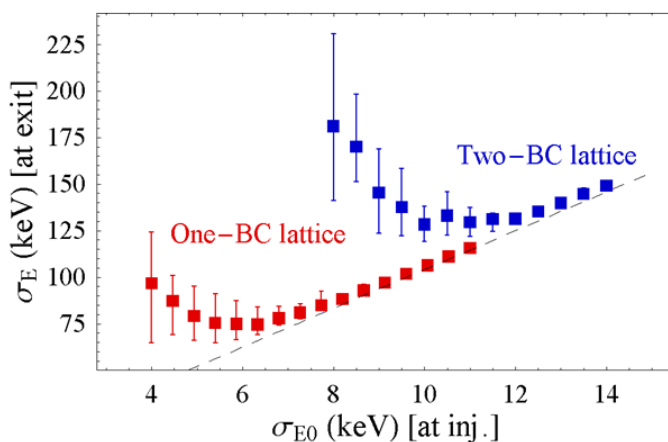


Figure 6.3: Final vs. initial uncorrelated energy spread for one- and two-stage compression in FERMI@Elettra. Vlasov solver simulation result. Figure courtesy of M. Venturini (LBNL).

In spite of the great advantage of suppressing the microbunching instability with minimum energy spread, the shortcoming of a one-stage compression is that a short bunch is affected by longitudinal wake field along a longer path than in the two-stage option, where the path to a short final bunch proceeds in two stages. The wake field corrupts the longitudinal phase space by increasing the energy spread, by reducing the average beam energy and by inducing nonlinearities in the energy distribution. A manipulated current profile, already shown in Figure 6.2, has been successfully studied to overcome this problem. At the same time, a positive aspect of the one-stage compression, performed early enough in the linac, is that of minimizing the effect of the transverse wake field, since the induced wake potential is reduced by a shorter bunch length.

To demonstrate the attraction of the one-stage compression scheme for a realistic model of linac-based FEL and for FERMI in particular, the 6-D tracking of a 5 million particle file is here shown according to the parameters in Table 6.3. All collective effects previously described in this Thesis are included. A uniform beam heating at 100 MeV is also included in the simulation, so that the uncorrelated energy spread before compression is approximately 10 keV rms. Figure 6.4 depicts the properties of the FERMI@Elettra bunch, compressed by a factor 10 in BC1 with $R_{56}=-46$ mm. As already discussed in Section 5.5, 3-D effects are marginal for such compression factor. The initial density modulation of 0.03% at 30 μm wavelength, superimposed to the initial beam, is washed out at the linac end. For comparison, the final bunch after two-stage compression is shown in Figure 6.5. No difference in the slice emittance is apparent for the two cases in Figure 6.6. The projected normalized horizontal emittance for 60% of the particles in the transverse phase space is 0.8 mm mrad. Unlike the one-stage compression, the two-stage allows one to obtain a flat longitudinal phase space ($\sigma_\delta \leq 0.1\%$) and current profile ($\Delta I/I \leq 10\%$ in the bunch core) even for a compression factor in the range 10–30. The current spikes at the bunch edges can be manipulated in both schemes by moving the charges towards the tail, so avoiding high spikes in the head that could excite damaging wake fields in the low-gap undulator vacuum chamber.

Table 6.3: FERMI parameters for the one-stage compression.

Parameter	Value	Units
Initial energy	100	MeV
Energy at BC1	320	MeV
Charge	0.8	nC
Initial peak current	80	A
Initial bunch length, rms	3.71	mm
Final bunch length, rms	0.08	mm
BC1 compression factor	10	
R_{56} in BC1	-46	mm
Initial uncorrelated energy spread, rms	10	keV
Initial modulation amplitude	0.03	%
Initial modulation wavelength	30	μm

From the point of view of the stability, the two-stage compression has the intrinsic advantage of self-stabilizing the shot-to-shot variation of the total compression factor, C . Let us assume an RF and/or a time jitter makes the beam more (less) compressed in BC1; a shorter bunch then generates stronger (weaker)

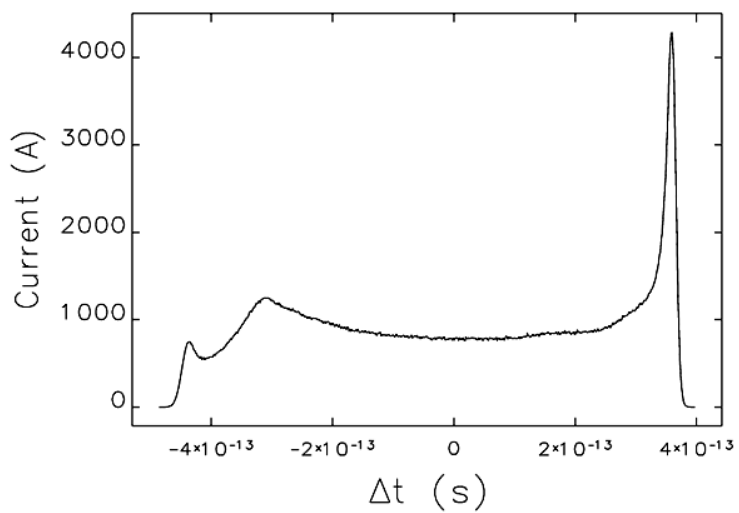
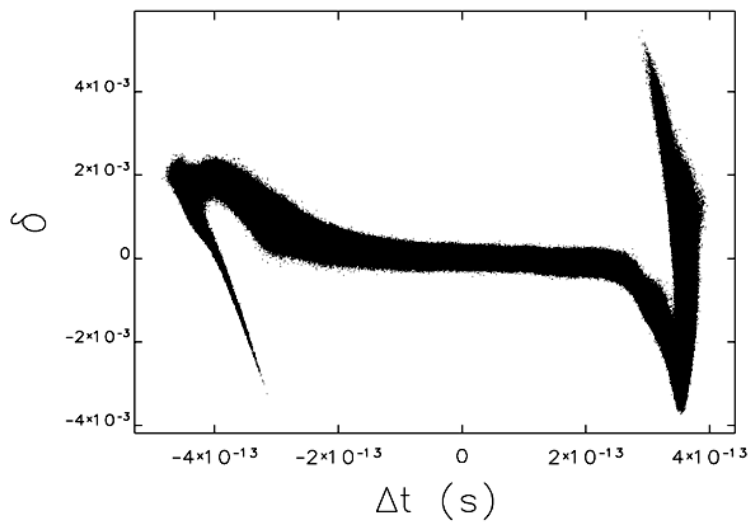


Figure 6.4: Final particle distributions after one-stage compression.

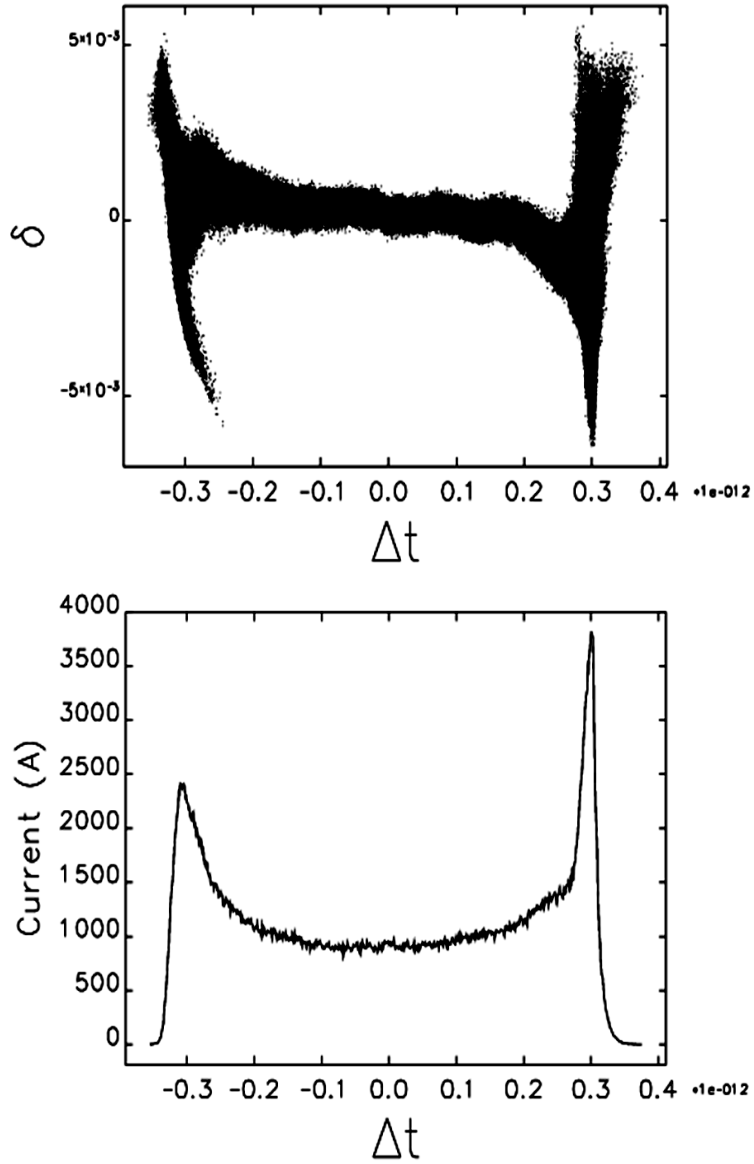


Figure 6.5: Final particle distributions after two-stage compression.

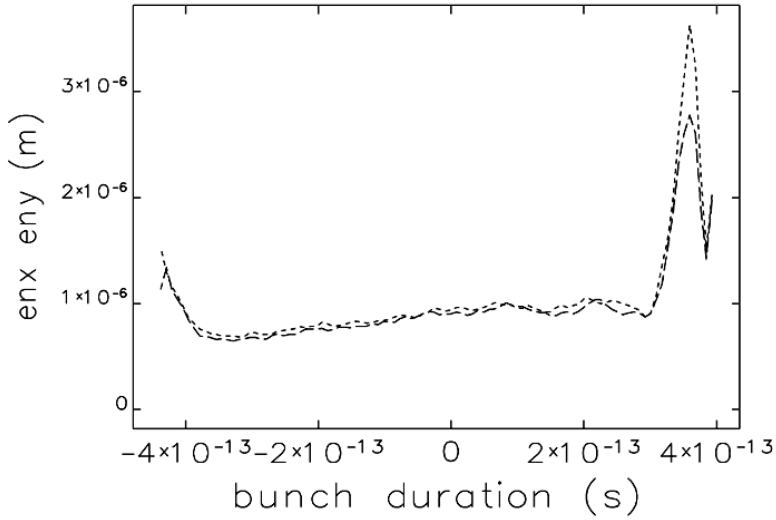


Figure 6.6: Horizontal (dotted line) and vertical (dashed line) slice normalized emittance after one-stage compression.

longitudinal wake field in the succeeding linac so that the energy chirp at BC2 is smaller (bigger). This in turn leads to a weaker (stronger) compression in BC2 that approximately restores the nominal total C . In the one-stage compression, where $C \gg 1$ and the phase is far enough from the accelerating crest, the sensitivity of C to phase jitter is [146]:

$$\frac{\Delta C}{C_0} = -C_0 \frac{\Delta \phi}{\phi_0} \quad (6.1)$$

where the accelerating crest is for $\phi_0 = \pi/2$. Basing on some technical considerations and recent measurements at the Elettra laboratory, an admissible value for the shot-to-shot variation of the FERMI linac RF phase is 0.1 degree S-Band and 0.1% for the peak voltage (rms values). Given the phase jitter $\Delta \phi \leq 0.1$ deg and the energy jitter $\Delta E/E_0 \leq 0.1\%$, their relation:

$$\frac{\Delta E}{E_0} = \Delta \phi \cos \phi_0 \quad (6.2)$$

sets a new constraint on the maximum L1 off-crest phasing, finally fixed to -25

deg. This prescription goes in the same direction of a final beam energy equal or bigger than 1.2 GeV and of an energy spread smaller than 2% at BC1. So, using this prescription in eq. 6.1, we find a shot-to-shot jitter in C of 4% in the one-stage compression. This result is fairly compatible with the FEL requirement of a final peak current jitter $\Delta I/I \leq 10\%$. For completeness, we report in Table 6.4 the tolerance budget for the one-stage and two-stage compression as already computed in [29], whereas the one-stage scenario is updated with the aforementioned prescriptions on the RF phase of L1.

Table 6.4: Jitter tolerance budget for the one- and two-stage compression scheme.

Parameter	Two-stage	One-stage
L1 phase [deg]	0.10	0.10
X-band phase [deg]	0.30	0.35
L2 phase [deg]	0.10	0.20
L3 phase [deg]	0.10	0.15
L4 phase [deg]	0.10	0.10
L1 voltage [%]	0.10	0.10
X-band voltage [%]	0.50	0.30
L2 voltage [%]	0.10	0.15
L3 voltage [%]	0.10	0.08
L4 voltage [%]	0.05	0.05
Gun timing [fs]	250	350
Charge [%]	3.0	5.0
BC1 dipole field [%]	0.02	0.01
BC2 dipole field [%]	0.02	

6.4 Enhanced Phase Mixing

As anticipated at the beginning of this Section, we also want to show an alternative compression scheme that is even more effective than a pure single compressor in suppressing the beam microbunching. It requires that the correlated energy spread, needed for bunch length compression in BC1, be removed before passing through a second chicane. When this happens, the rotation of the longitudinal phase space can be made large enough so that phase mixing is maximized in the second chicane. At the same time, the second chicane does not change the overall bunch length that therefore depends on the R_{56} in BC1 only.

Its only task is to smear the microbunching modulations. In this case the energy and density modulation washing out is more efficiently provided by two magnetic chicanes having R_{56} of the *same sign*. In fact, the energy modulation smearing is induced by a complete rotation of the longitudinal phase space; the two chicanes must therefore stretch the particles in the same direction.

To illustrate this process, we consider a line-charge that has a Gaussian energy distribution with $\langle E \rangle = 320$ MeV and $\sigma_E = 10$ keV. A linear energy chirp of 0.036 ps^{-1} and an energy modulation with amplitude $A_E = 1\%$ and wavelength $\lambda_E = 30 \text{ }\mu\text{m}$ are superimposed to it. The linear transport matrix formalism is used to propagate the line-charge through drift sections and R_{56} elements. Figure 6.7 shows that, after the linear energy chirp is removed, the residual energy chirp changes sign over one modulation period, so that particles lying on opposite fronts of the modulation can be (de-)compressed in BC2 by the same factor: the longitudinal phase space becomes folded and the initial energy modulation is removed, turning into an almost totally uncorrelated energy spread. This is shown in Figure 6.8. At the same time, the particle cross-over in the z coordinate damps the initial current spikes, therefore suppressing the microbunching instability.

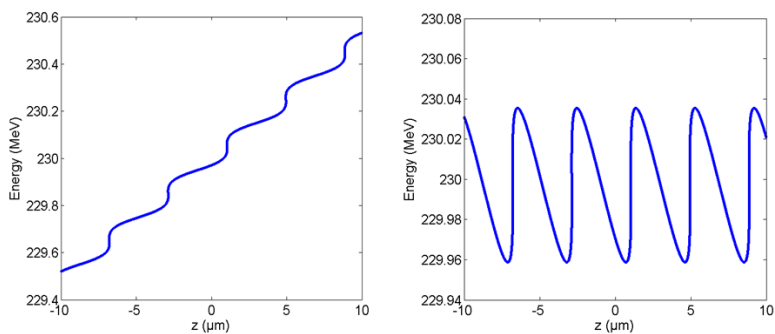


Figure 6.7: Longitudinal phase space before (left) and after (right) energy chirp removal.

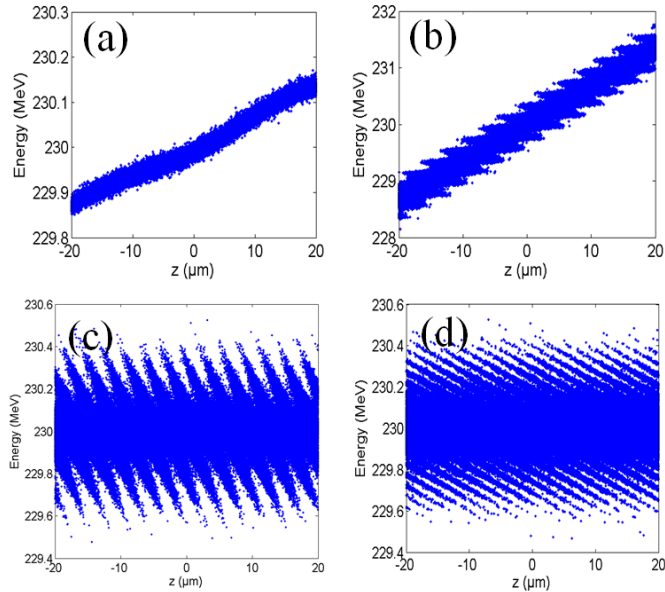


Figure 6.8: Longitudinal phase space evolution during enhanced phase mixing. (a) An energy modulation is superimposed to the linear energy chirp entering BC1 (10 keV rms uncorrelated energy spread). (b) As a result of the bunch length compression in BC1, the longitudinal phase space looks rotated. (c) The longitudinal phase space is flattened by removing the linear energy chirp. (d) A further rotation allows the particles to longitudinally cross-over. Tracking code developed by S. Spampinati (ST).

Figure 6.9 shows the instability gain function for the one-stage compression scheme and for the enhanced phase mixing (where $R_{56} = -30$ mm in BC2) in FERMI@Elettra. BC1 is at 320 MeV, BC2 is at 600 MeV and they are separated by a 30 m long S-band linac. By virtue of the off-crest phasing of this linac, the energy chirp required for compression in BC1 is removed before the beam enters BC2. In the latter case, the gain is clearly reduced and it practically goes to zero for initial wavelengths shorter than $100 \mu\text{m}$. Particle tracking is carried out with elegant in order to obtain a complete and realistic picture of the dynamics discussed so far, including LSC, CSR and longitudinal structural wake fields, and to support the analytical result in Figure 6.9. The FERMI linac RF phasing is re-adjusted to cancel the linear chirp at BC2. Figure 6.10 and 6.11 show a portion of the bunch core at the entrance and at the exit, respectively, of BC2 characterized by $R_{56} = -30$ mm. At the end, the longitudinal phase space becomes folded,

the energy spread is uncorrelated, for any practical purposes, on the slice scale of microns and the charge clusters are largely suppressed. To make the dynamics more evident, an initial modulation amplitude of 1% is introduced at $30\ \mu\text{m}$ wavelength, corresponding to an initial bunching factor of $7 \cdot 10^{-2}$. After BC2, the bunching factor calculated for $3\ \mu\text{m}$ wavelength shrinks to approximately $3 \cdot 10^{-5}$. CSR introduces some energy deviation between particles of different bunch slices. Since this happens in a dispersive region, it may increase the particle transverse invariant. At the same time, the phase space rotation leads to particle longitudinal crossover between adjacent slices, finally affecting the horizontal slice emittance. Figure 6.12 shows the slice emittance at the exit of BC2 ($R_{56} = -30\ \text{mm}$), after the linear energy chirp removal; the bunch head is for negative time coordinates. The short dashed line is for the horizontal emittance, the long dashed line is for the vertical emittance. The projected normalized horizontal emittance for 60% of the particles in the transverse phase space is 2 mm mrad.

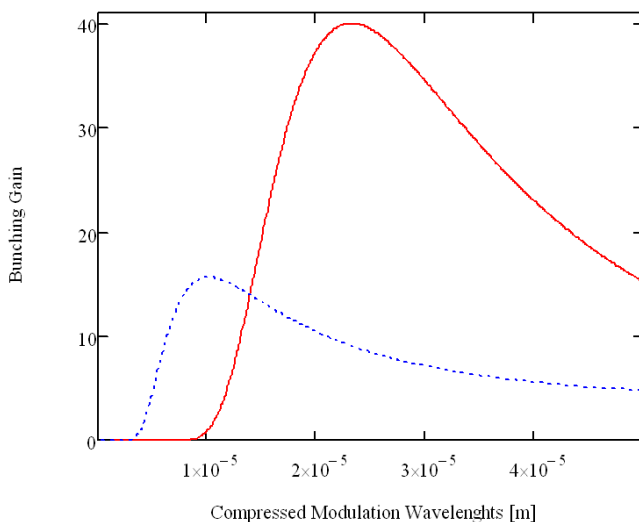


Figure 6.9: Instability gain vs. compressed modulation wavelength for one-stage compression (dotted line) and enhanced phase mixing (solid line). The wavelength in the abscissa axis is computed as the modulation wavelength before the total compression.

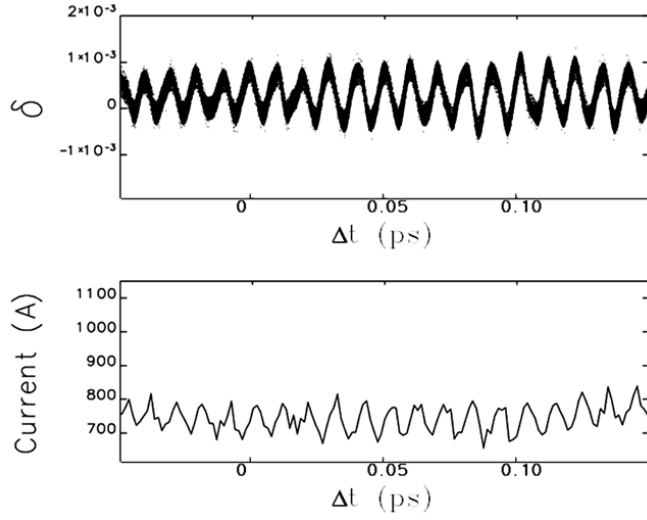


Figure 6.10: Particle distributions of the bunch core at the entrance of BC2.

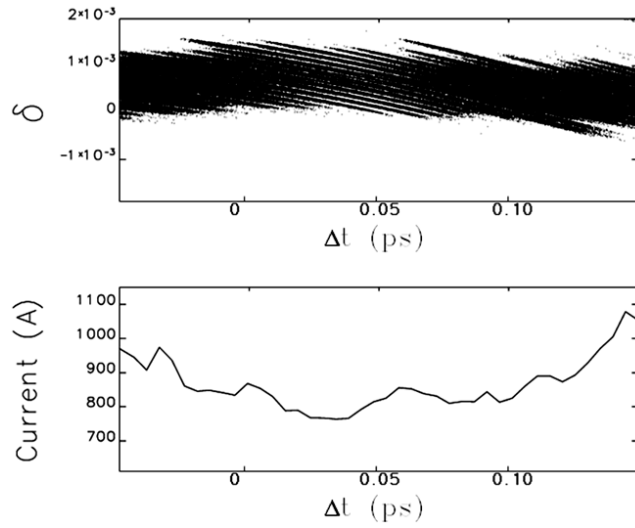


Figure 6.11: Particle distributions of the bunch core downstream of BC2.

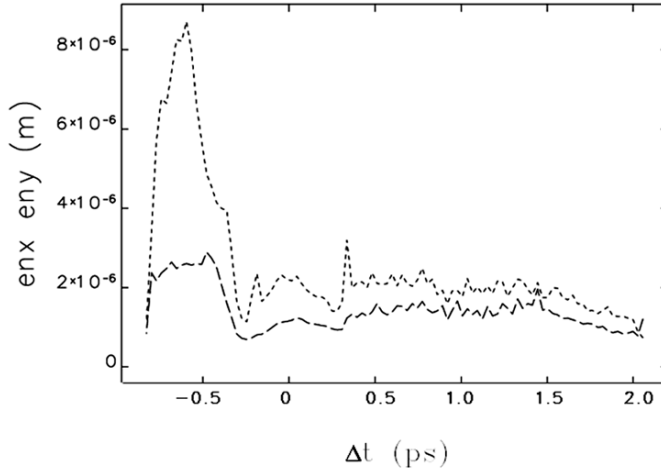


Figure 6.12: Slice emittances after enhanced phase mixing.

6.5 Conclusions

Some guidelines for the design of the magnetic compression scheme have been given, according to the requirements expressed from the FEL performance goal. The principles depicted in this Chapter refer to the specific case of a seeded X-ray FEL and only magnetic compression of the bunch length has been considered. The effect of magnetic bunch length compression on the microbunching instability development in a linac-based FEL has been investigated. In particular, the reduction of the instability gain by particle longitudinal phase mixing has been demonstrated analytically. It has been shown that the efficiency in removing the beam microbunching is much more sensitive to the initial modulation wavelength than to the amplitude. The natural consequence of this dynamics is the adoption of a single compression scheme. The feasibility of this scheme has been demonstrated by means of a 3-D particle tracking for the FERMI@Elettra FEL, with promising results for the preservation of the beam quality. In addition to this, a different promising configuration shows up. If the linear energy chirp at the exit of BC1 could be removed by dedicated accelerating structures, then particle longitudinal crossover is enhanced in BC2. The effect is optimized by two chicanes, BC1 and BC2, with the same sign of R_{56} . As a result, the energy modulation is damped, together with the associated current

spikes. The FERMI@Elettra case study has been analyzed in some details. The 1-D beam transport has been verified against the 3-D particle tracking performed with `elegant`, including collective effects, for a compression factor of 10 in BC1. The study shows that this alternative scheme of compression is successful and even more efficient than the single compression for initial modulations whose wavelength is of the order of tens of μm . It may even be applicable to longer wavelengths and/or higher compression factors, although these more extreme situations need to be confirmed by further investigations.

Chapter 7

Electron Beam Control

In this Chapter we describe methods and experimental results related to the control of the longitudinal (acceleration, energy distribution, bunch length compression and microbunching instability) and transverse (optics matching, transport and trajectory control) electron beam dynamics in the FERMI@Eletra beam delivery system. This Chapter is based on the commissioning experiments we carried out from September 2009 to December 2010 [147, 148], when the first lasing of FERMI FEL1 was observed. During the commissioning we have developed some high level software for optics matching, transport, trajectory control and dispersion measurement. We have provided support to the development of other codes devoted to the energy measurement, emittance measurement and transverse phase space reconstruction [149]. We extensively used all the mentioned software and a description of our measurements and comparison with the machine model is reported in the following.

7.1 Longitudinal Phase Space

The longitudinal phase space of the electron beam is investigated both for the projected and the slice beam parameters. Here, we focus on the characterization of the particle energy distribution and measurement of the bunch length by using the beam projection on the screen of the LH spectrometer line. This is shown in Figure 7.1. Once the beam is centered on the screen, its mean energy is simply computed from the dipole magnet calibration table (current vs. energy), which has an accuracy better than 10^{-4} . According to the design optics of the LH spectrometer line, the resolution for the energy measurement is $4 \cdot 10^{-3}$. A quadrupole magnet in front of the spectrometer is used to shrink the horizontal betatron function at the screen location, so minimizing the geometric contribu-

tion to the image at the screen, while the horizontal dispersion is left to reach 1.7 m. As expected, by turning on the quadrupole upstream of the spectrometer, the energy spread value diminishes because the energy measurement error is minimized.

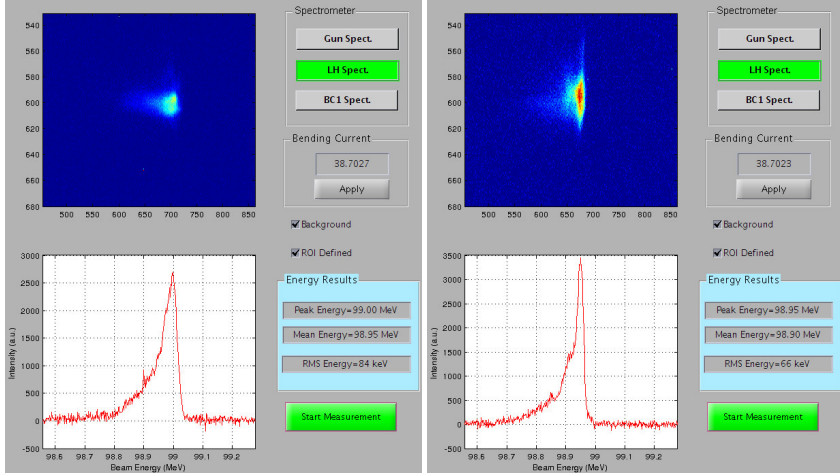


Figure 7.1: Energy measurement in LH spectrometer line. The energy spread is computed as the ratio between the horizontal size at the screen and the theoretical value of the dispersion at the same location. The dedicated quadrupole in front of the spectrometer is turned off (left) and on (right). Doing this, the measured energy spread reduces from 84 keV to 66 keV rms.

The bunch length is measured in the LH spectrometer line by taking the horizontal beam size Δx (fwhm) at the screen. We set the L1 RF phase for on-crest acceleration. Now, assuming that the particles lie on a perfectly sinusoidal RF potential, Δx can be related to the bunch length, Δz , and to the local dispersion function, η_x , as follows:

$$\Delta z = \frac{\lambda_{RF}}{\pi} \arccos \left(\left| \frac{\Delta x}{\eta_x} - 1 \right| \right) \quad (7.1)$$

The assumption of a beam symmetrically distributed across the RF crest is verified thanks to an occasional vertical deflection observed at the screen, which generates a half-moon shape in the (x, y) plane. The beam horizontal extension at the screen is 17.6 mm. The bunch length is therefore evaluated with eq. 7.1 to

be in the range of 5.7–6.2 ps. The biggest measurement uncertainty comes from the mean energy jitter of the electron beam. Other bunch length measurements provided by a Cherenkov detector at the Gun exit and simulation results using space charge codes are in agreement with the present value [147].

7.2 Trajectory Control

The FERMI electron beam delivery system has no explicit coupling elements and it consists only of dipole and quadrupole magnets. For each plane, the point-to-point transfer map between any two points 1 and 2 is given by:

$$\begin{pmatrix} x \\ x' \end{pmatrix}_2 = \begin{pmatrix} R_{11} & R_{12} \\ R_{21} & R_{22} \end{pmatrix} \begin{pmatrix} x \\ x' \end{pmatrix}_1 \quad (7.2)$$

Let the initial point 1 be at a corrector and the final point 2 at a BPM. Two measurements are required to determine R_{12} that is the position of the beam with the nominal trajectory $(x, x')_2$ and after the beam is kicked by an angle θ , $(x, x' + \theta)_2$. The difference in the BPM reading between the two measurements is $R_{12} = \Delta x / \theta$. In practice, to decrease the sensitivity to the measurement error one introduces a series of large betatron oscillations by varying the corrector's strength in steps. This is the procedure implemented in a MATLAB [150] tool that allows the measurement of the direct Trajectory Response Matrix (TRM) of any portion of the FERMI lattice. In principle, any combination of correctors and BPMs can be chosen. The corrector's strength is varied by an arbitrary step, usually of 0.03 mrad to have at least 20 micron displacement at any BPM downstream. During the measurement of the TRM, five kicks with positive and negative sign are applied to each corrector: if the BPM differential response has a discrepancy larger than 10% of the absolute value for negative and positive kicks, then an error message is sent to the user. In this way, the linearity of the TRM is checked out and identification and exclusion of bad BPMs can be carried out for good convergence of the steering algorithms.

The position of the beam centroid is usually forced onto the reference axis, which should coincide with the zero reading of the BPMs. Some uncertainties are still associated with the electronic center and/or mechanical alignment of the BPMs. If the BPM offsets are not known *a priori* and possibly larger than the alignment specifications (see Table 5.1), a better strategy is to reduce the rms strength of the correctors and to pay less attention to the absolute trajectory reading. A technique based on the Singular Value Decomposition (SVD) [151] allows the reduction of the rms strength of the correctors while maintaining a set of constraints. For this reason it is adopted in the FERMI trajectory manipulation

tool. Suppose we want to solve the linear equation:

$$\Delta x = A \cdot \theta \quad (7.3)$$

where the vector $\Delta x = (\Delta x_1, \Delta x_2, \dots, \Delta x_M)$ describes the desired correction at M BPMs and $\theta = (\theta_1, \theta_2, \dots, \theta_N)$ are the excitation strengths of N correctors that we want to determine to satisfy the constraints described by Δx . If $M \geq N$, we can decompose the matrix A as:

$$A = U \cdot \begin{pmatrix} w_1 & 0 & \dots & 0 \\ 0 & w_2 & \dots & 0 \\ & \dots & \dots & \\ 0 & 0 & \dots & w_n \end{pmatrix} \cdot V^t \quad (7.4)$$

The column vectors of the $M \times N$ matrix U and the $N \times N$ matrix V are orthonormal, $U^t \cdot U = I_N$ and $V^t \cdot V = I_N$, where I_N denotes the $N \times N$ unity matrix. The decomposition of eq.7.4 is performed by a mathematical package of MATLAB. We now want to consider three different cases. First, $N = M$. In this case the matrix A is square and we can write down a formal solution for the corrector strengths vector:

$$\theta = A^{-1} \cdot \Delta x = V \cdot \begin{pmatrix} 1/w_1 & 0 & \dots & 0 \\ 0 & 1/w_2 & \dots & 0 \\ & \dots & \dots & \\ 0 & 0 & \dots & 1/w_n \end{pmatrix} \cdot U^t \cdot \Delta x \quad (7.5)$$

If none of the w_i is zero, this is the unique solution of the problem. If one or more of the w_i are zero, the equation may not have an exact solution, but for these w_i one can simply replace $1/w_i$ by zero and with this replacement eq.7.5 still gives the solution in a least square sense. This means it minimizes the distance $r = |A \cdot \theta - \Delta x|$. Furthermore, the solution vector θ so obtained is the solution with the smallest possible length $|\theta|^2$. Next, we consider the case for which $M < N$. In this case, we can simply add rows with zeroes to the vectors and matrices of eq.7.3 until the matrix is square and then apply the SVD formalism, as described above. In this case, there is at least one zero eigenvalue w_i for every row of zeroes added. Finally, in the case of $M > N$, SVD works just as well. In general, the w_i will not be zero and the SVD solution will agree with the result of a least-square fit. If there are still some small values of w_i , these indicate a degeneracy in A that is a BPM is not very sensitive to a certain corrector's strength. Hence, the corresponding $1/w_i$ should be set to zero, as before. We point out that the corresponding column in V describes a linear combination of corrector excitations, which does not affect the constraints.

Such a formalism is implemented in the MATLAB-based trajectory feedback for FERMI that is routinely used both for trajectory correction (the user stops the

feedback once the constraints are satisfied) and feedback operation at approximately 1 Hz. In particular, the program is capable of displaying any response matrix, as well as its inversion using either regular SVD, Truncated Singular Value Decomposition (TSVD) [152] or Tikhonov regularized SVD [153]. It is also possible to view the singular values for all three inversion options. Still for the TSVD, the given tolerance specifies how small singular values will be included in the inversion. In case the matrix rank is lower than both the number of actuators or sensors, some singular values should be removed in order for the inversion to produce a matrix with non-infinite elements. For the Tikhonov inversion option, small singular values are scaled up which allows inversion of low rank matrices. The Tikhonov parameter will determine the focus of the correction parameter: a value of zero will mean no weight is given to the amplitude of corrector changes when the solution is computed. An increasing value will increase the weight on the norm of corrector changes. In order to give preference to a particular solution with desirable properties – small corrector strengths in our case –, the regularization term is included in the minimization of the following norm:

$$\| A\theta - \Delta x \|^2 + \|\Gamma\theta\|^2 \quad (7.6)$$

for some suitable chosen Tikhonov matrix, Γ . In our feedback tool, $\Gamma = q \cdot I$, where $q = 1, \dots, n$ is a positive integer that underlines the importance of minimizing the corrector strengths with respect to satisfying the trajectory constraints. More in detail, given the singular value decomposition of A as in eq.7.4 with singular values w_i , the Tikhonov regularized solution can be expressed as:

$$\tilde{\theta} = VDU^t \Delta x \quad (7.7)$$

where D has diagonal values $D_{ii} = \frac{w_i}{w_i^2 + q^2}$ and is zero elsewhere.

In addition, the trajectory feedback tool has some important capabilities to optimize the trajectory control:

- i) the TRM can be visualized in a 3-D contour plot to identify areas of particularly high or poor BPMs sensitivity to the correctors;
- ii) a theoretical TRM, direct or inverted, computed by `elegant`, can be imported, compared with the corresponding measured one via the visualization tool and used for trajectory correction;
- iii) experimental and theoretical TRMs can be merged for global trajectory manipulation.

Since the feedback tool manages the correctors' normalized strength in *mrاد* and not the correctors' supplying current in Ampere, the corrector magnets must

be configured for the correct energy. Currently this is done on the feedback startup: in case of a large change in the klystron voltage or phase for the accelerating structures, the beam energy must be updated. In case it would be necessary to measure a response matrix for the power supply currents, an additional script can be run before starting the feedback in order to be able to select power supplies as actuators. The tool is also used to launch successive feedback loops on the beam line. The possible interference of one loop with each other is avoided by verifying the orthogonality of the TRMs. This is done by merging the matrices into a global one, representing it graphically and verifying that the different blocks are diagonal.

Up to three feedback loops in both planes have been run continuously for a few hours: the first TRM was a merged version of the experimental matrix for the injector (in each plane, 2-by-2) and of the theoretical matrix for the rest of the linac (in each plane, 27-by-27); the second TRM is measured and applied to correct the trajectory in the Spreader (in each plane, 11-by-11); the third one is measured and applied to the undulator chain (in each plane, 7-by-7). The resulting trajectory correction for both planes is shown in Figure 7.2. Some large position values correspond to bad BPMs reading.

We stress that the efficient trajectory correction in the linac with a relatively large theoretical TRM is an indirect proof of the agreement between the theoretical optics (quadrupole set) and the real one adopted in the machine. The importance of this result relies on the fact that accuracy of the model is vital for basic optics checkout and requires, for example, accurate representation of magnetic field strengths. As an example, Figure 7.3 compares the horizontal measured (top) and theoretical (bottom) TRM relative to the steering elements from the LH area to the BC1 spectrometer line. In spite of small differences in correspondence of elements at the beginning of the beam line where the LH matching quadrupoles are located, the theoretical matrix was successfully used for trajectory correction as well as the experimental one.

Trajectory correction with the theoretical TRM is shown in Figure 7.4. The horizontal axis runs along the machine, from the Gun exit to the BC1 spectrometer line (approximately at the longitudinal coordinate of 60 m). BPMs used for these measurements are made of striplines and a single shot resolution of $5 \mu\text{m}$ rms for a charge higher than 50 pC has been measured [154]. This is well below the physical specification of $20 \mu\text{m}$ rms. The short-term trajectory jitter is usually in the range 10–20 μm rms (again within the physical specification).

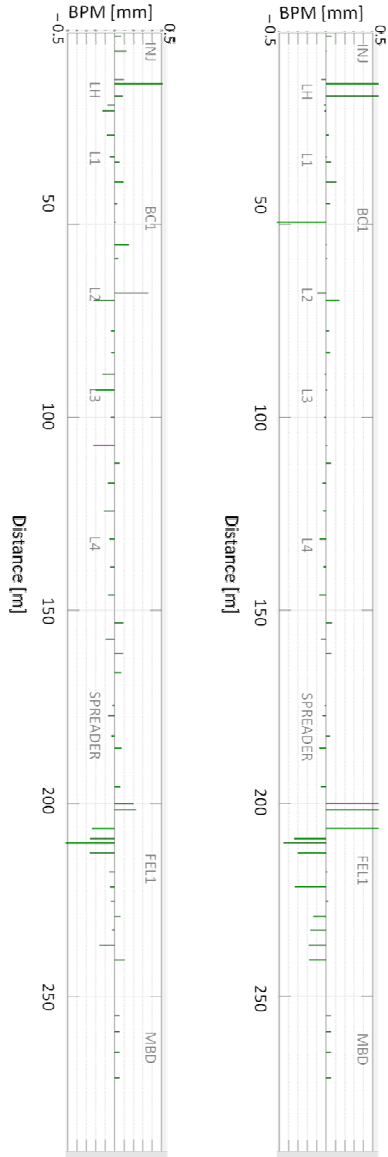


Figure 7.2: Global trajectory correction in the horizontal (top) and vertical plane (bottom).

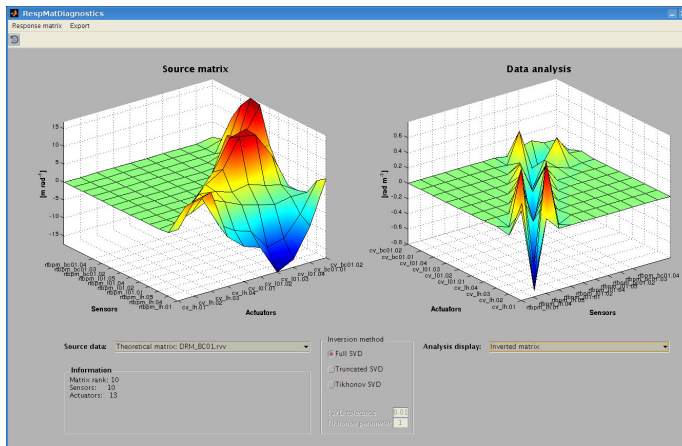
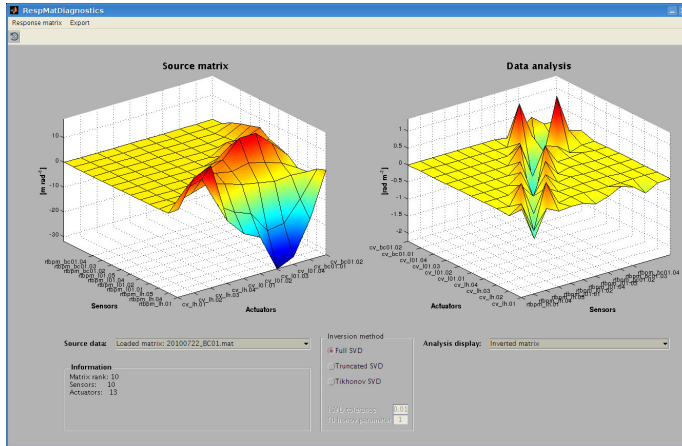


Figure 7.3: Measured (top) and theoretical (bottom) TRM. The direct matrix is made of 13 correctors per plane ($M=13$) and 11 BPMs ($N=11$) and it is shown in the left side of each plot. The matrix inverted with regular SVD is shown on the right side.

During the commissioning, BPM offsets have been found by looking for the maximum charge transport efficiency through the whole line. In some cases, offsets between 1 and 2 mm have been identified such as in the proximity of the LH, BC1 and DBD spectrometer magnets, but also in straight sections at the end of L2 and L4. In the meantime, the offsets are virtually zeroed via software control. Then, TRMs are applied for trajectory correction. Even when starting from 2 mm displacement at some locations, the trajectory converges well to 10 μm level over all BPMs in a few seconds, the velocity of convergence depending from the feedback gain set by the user.

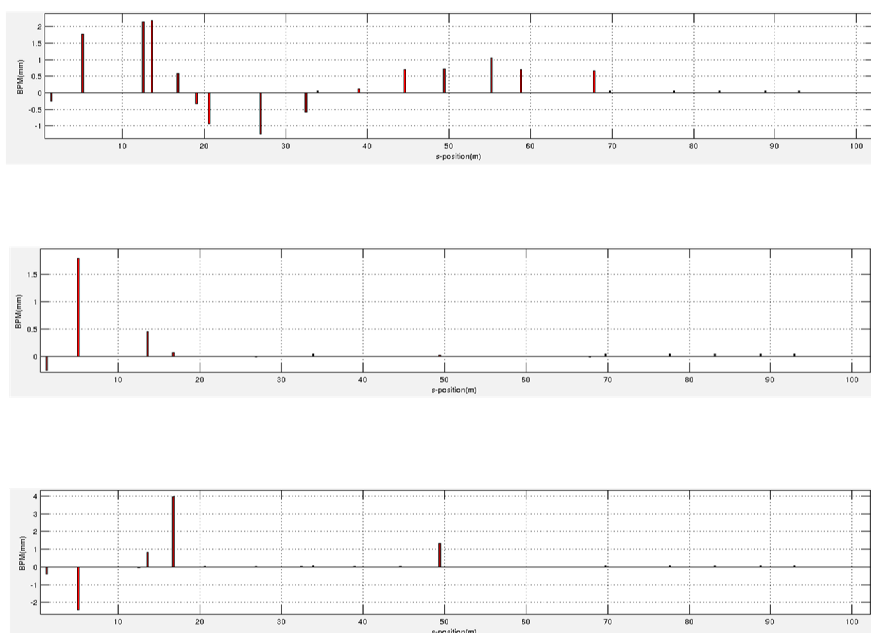


Figure 7.4: Local trajectory correction. Top: vertical plane before correction; the vertical scale is [-1.5, 2.5] mm. Middle: vertical plane after correction with the theoretical matrix shown in Figure 7.3; the first two BPMs in the injector are excluded from the steering algorithm, while all others read beam position around 10 μm . The vertical scale is [-0.5, 2.0] mm. Bottom: horizontal plane after correction. The vertical scale is [-2.5, 4.0] mm.

The feedback is also used to create closed trajectory bumps to minimize

the projected emittance dilution due to transverse wake field instability. This optimization was partially carried out along L3 and L4, characterized by the strongest impedance over the whole linac. Preliminary results depict a reduction of the normalized projected emittance from 10 ± 1 mm mrad before the implementation of trajectory bumps to $3 - 4 \pm 0.3$ mm mrad, in both planes, after the bump. The electron beam has 350 pC total charge distributed over 6 ps (fwhm value) and an emittance of approximately 1.5 mm mrad at the exit of the injector. A similar trajectory manipulation is also done along L1 to compensate an unwanted vertical deflection observed at the screen of the BC1 spectrometer line. Possible sources of the vertical head-tail deflection might be identified in the RF kick given by the vertical coupler of the injector accelerating structures as well as in transverse wake field kick in L0 or L1. The model does not foresee any strong effect from the impedances, unless the BPMs and the accelerating structures are misaligned by more than 1 mm; so, we are led to think of time-dependent RF kicks at very low energy. Figure 7.5 shows the beam transverse spot size at the screen of the BC1 spectrometer line. The screen shows a half-moon shape in the vertical plane (left plot). The horizontal axis is proportional to the particle energy while the vertical one, in the presence of deflection, is proportional to the particle phase. The screen is reproducing the particle longitudinal phase space and the shape represents the electron bunch lying on the RF crest of the upstream linac. This shape is therefore representing the on-crest acceleration in L1. The vertical deflection is suppressed after a vertical offset of $400 \mu\text{m}$ is imposed across L1. The trajectory bump is implemented by using the theoretical TRM shown in Figure 7.3. So, we think we were compensating the vertical banana shape by exciting vertical transverse wake field in L1.

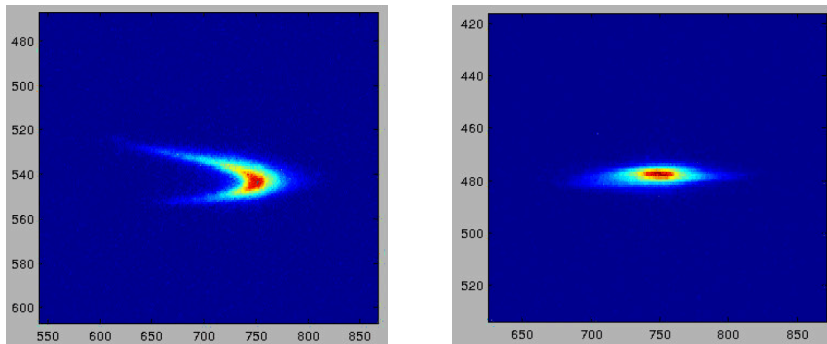


Figure 7.5: Suppression of vertical banana shape (left) with trajectory bump (right). Axes scales are pixels.

7.3 Residual Dispersion

The dispersion function along the FERMI linac is measured by changing the beam energy through the high voltage of the selected klystron and monitoring the trajectory changes at the BPMs downstream. Dispersion is computed, in each plane, as $R_{16} = \Delta x / (\Delta E / E_0)$. Figure 7.6 shows the dispersion function from the very first BPM at the Gun exit to the linac end. It is obtained by varying the high voltage of the RF plant supplying the two accelerating structures of L0 by $\pm 1.5\%$ in seven steps. The linearity of the beam mean energy with the high voltage within this range of variation has previously been verified at the LH spectrometer line. The trajectory is corrected everywhere as shown in Figure 7.4. Our measurements show that the dispersion function is non-zero along the linac in both planes, but with larger excursion in the vertical plane. This could be a consequence of the propagation of a residual dispersion at the linac entrance. It is also consistent with our afore-mentioned guess of a vertical time-dependent RF kick at the entrance of L0. The horizontal dispersion downstream of BC1 is in the 1–5 mm range. Its contribution to the horizontal projected emittance can be estimated with eq. 3.20. This predicts an emittance growth of only 4% for a residual dispersion of 2 mm, unperturbed normalized emittance of 1.5 mm mrad, energy spread of 0.8% (like that used for compression during commissioning) and nominal betatron function of 3 m at the location of emittance measurement. In this case, we do not expect any relevant contribution to the emittance growth during compression. However, other measurements have been carried out in which the horizontal dispersion reaches 10 mm in the same region. In this case, the emittance measurement, which assumes a pure geometric beam size at the screen, is affected by the chromatic particle motion and the effective error on the emittance measurement is of the order of 100%.

Figure 7.6 also shows the closure of the horizontal dispersion bump in BC1, where the two lines in each window refer to the case of BC1 at 0.05 rad and at 0 rad. Notice that the chicane seems to give an unexpected contribution in the vertical plane as well. The effect of the bunch compressor on the dispersion function has been systematically investigated by scanning the compressor strength, as shown in Figure 7.8. The agreement with the model is satisfactory at these early stages. The dispersion bump introduced by the BC1 magnetic chicane is reasonably well closed after the 4-th dipole and, for bending angles up to 0.12 rad, the residual trajectory distortion remains within the 10 μm level at the two BPMs downstream of BC1. The bend magnets trim coils correct the trajectory to the level of 20 μm . These correct for the magnet-to-magnet differences that could in principle corrupt the achromaticity of the chicane.

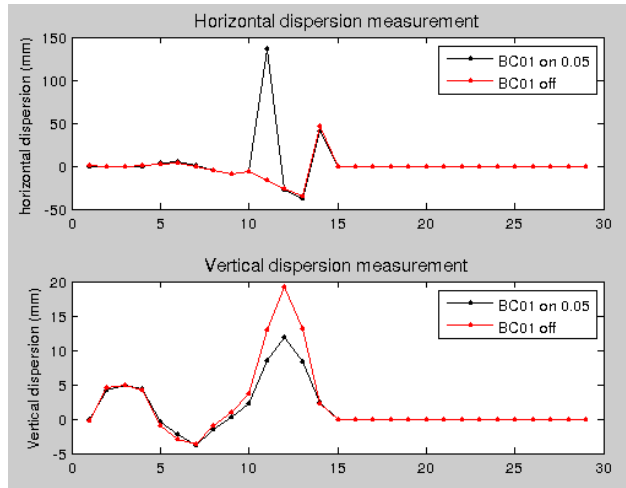


Figure 7.6: Dispersion function up to BC1 area. The abscissa is the BPM number along the linac.

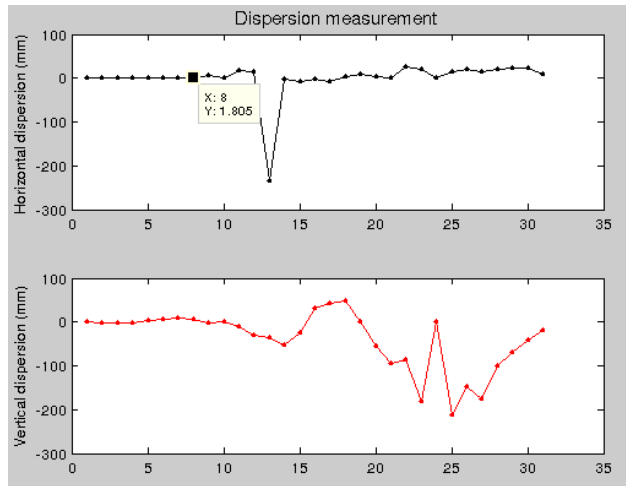


Figure 7.7: Dispersion function up to linac end. The abscissa is the BPM number along the linac (two more BPMs have been added at the beginning of the beam line with respect to Figure 7.6).

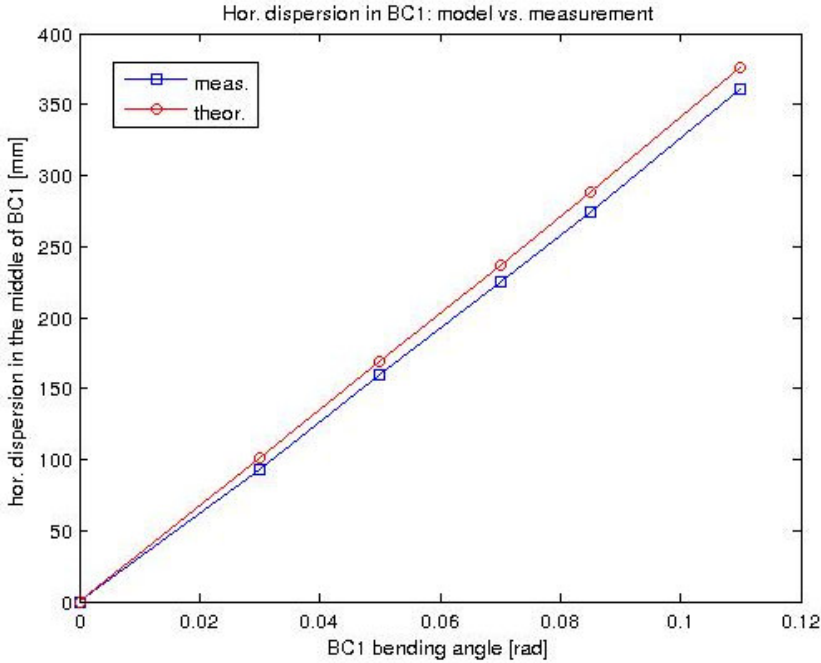


Figure 7.8: Dispersion function in the middle of BC1 vs. bending angle.

7.4 Optics Matching

The goal of matching is to impose to the beam the design optics functions at a certain point of the lattice. For this purpose a set of quadrupoles is used. During the FERMI commissioning, optics matching is routinely performed at the entrance of the LH area and then repeated in the BC1 area, downstream of the chicane and at the linac end (TLS area). In order to perform the matching, the Twiss parameters of the beam must be known at the entrance of the matching section. To achieve this, the Twiss parameters are measured via the quadrupole scan technique. Doing this, the quadrupole strength is varied and the beam size measured with a YAG or an OTR screen target. Once the measurement is done, the Twiss parameters are back-propagated up to a reference point by running elegant with a reverse-ordered lattice file and the quadrupole strengths are acquired from the running accelerator. The initial conditions for the Twiss param-

eters of the beam are so available for estimating the optical functions along the whole accelerator and performing the desired matching with `elegant`. The user can inspect the matching result before actually setting the calculated quadrupole strengths to the machine. If the resulting matching is not good enough, the user can iterate the matching procedure starting with the previous result. All the intermediate data and results are exchanged via SDDS format files and can be plotted also with standard SDDS based tools.

Although simple in principle, all these steps are rather involved to be done by hand from a Linux shell. The matching procedure has thus been coded in a MATLAB GUI, exploiting the possibility to invoke system commands [155, 156]. Since MATLAB is an interpreted language, it is fast and straightforward to test and modify the procedure during commissioning shifts. At this stage of development, we use traditional SDDS toolkit plot utilities since we are quite acquainted to them and we can directly compare the live data with results and plots from off-line simulations. The matching procedure works reliably. It generally converges in a couple of iterations. The speed of the matching procedure is acceptable and is in the order of 10 to 20 seconds. It is mainly affected by the speed of the actual matching algorithm performed by `elegant`. The matching tool provides to the user information about the quadrupole strengths required for matching, the expected Twiss parameters along the lattice after matching and in particular at the entrance of the quadrupole used for emittance measurement. Also, a theoretical mismatch parameter [52] is computed. This is used as an indicator of the convergence of the matching loop performed by `elegant` to the optics constraints fixed by the model. Figure 7.9 shows such a typical data set. So, first step is to verify that the computation, starting from the Twiss parameters of the presumably mismatched beam, succeeded that is the theoretical mismatch parameter is close to 1 in both planes. If this is the case, the computed solution is applied to the machine. The user can immediately guess if the beam is approaching the optics design by looking to the beam spot at the three screens of the diagnostic section in LH, BC1 or TLS. According to the nominal optics and for similar emittance in the horizontal and vertical plane, the beam is expected to be round, have a waist at the screen in the middle and being identical at the outer screens. Figure 7.10 shows the beam spot at the YAG screens in the LH diagnostic area. The beam is propagating through the lattice from left to right plot of Figure 7.10. The theoretical mismatch parameter is very close to the target value of 1 in both planes. Finally, the new beam optics is measured again and another small MATLAB GUI allows the computation of the experimental mismatch parameter, including errors affecting the measurement of emittance and Twiss parameters.

Statistics of the experimental mismatch parameter, mainly collected during measurements in LH and BC1 area, provide a satisfactory overview for the

```

**** MKP_BC1DIAG = MSCR_BC01.02 (goal: bxy=11.864,axy=1.732)

```

ElementName	betax m	betay m	alphax	alphay
MKP_Q_BC1.3	6.644148e+00	4.671170e+01	-9.175543e-01	-2.924557e-01
MKP_Q_BC1.4	6.286891e+00	5.579206e+01	4.740009e-01	-1.165276e+01
MKP_Q_BC1.5	9.956434e+00	3.941277e+01	-3.197791e+00	1.204507e+01
MKP_Q_BC1.6	1.477122e+01	2.473704e+01	-5.942306e+00	1.452744e+01
MKP_Q_BC1.7	1.679712e+01	1.719119e+01	-1.717811e+00	6.151304e+00
MKP_BC1DIAG	1.082959e+01	1.056349e+01	1.639552e+00	1.628037e+00

theoretical mismatch parameter bmagx	parameter bmagy
1.006043e+00	1.006043e+00

ElementName	ElementParameter	ParameterValue
Q_BC01.03	K1	3.403775e+00
Q_BC01.04	K1	-5.307315e+00
Q_BC01.05	K1	-1.856487e+00
Q_BC01.06	K1	4.500000e+00
Q_BC01.07	K1	2.644266e+00
Q_BC01.08	K1	0.000000e+00
Q_BC01.09	K1	0.000000e+00

Figure 7.9: Optics matching output data.

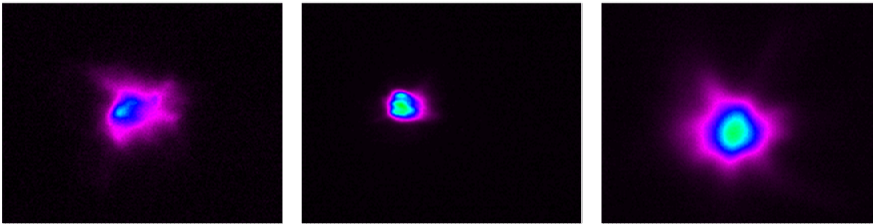


Figure 7.10: Beam spot at the screens of LH area after matching. Rms beam size is approximately 200 μm at the outer screens (first and third image) and 140 μm in the middle screen (second image), in both planes. The beam is round and has a waist at the middle of the section as required from the design optics.

matching procedure. The horizontal mismatch parameter is in the range $[1.005 \pm 0.001, 1.075 \pm 0.020]$, with mean value of 1.03. The vertical mismatch parameter is in the range $[1.002 \pm 0.002, 1.117 \pm 0.124]$, with mean value of 1.05. The vertical parameter assumes higher values during matching in the BC1 area with respect to the LH area. In general, we notice that the quality of the matching seems to depend mainly on the goodness of the initial emittance and beam parameters measurement. Noisy or odd-shaped beams are more difficult to match. After having matched the beam, we load the theoretical optics on the lattice. Once the optics is matched in the LH area, the beam is transported to the BC1 section almost instantly, requiring only small trajectory adjustments with the correctors. Without any further matching in the BC1 area, the experimental mismatch parameter is pretty good, 1.011 and 1.004 in the horizontal and in the vertical plane, respectively. Since the model is also includes BC1 dipole magnets vertical focusing and cavity end RF focusing, the good optics transport is also a confirmation of the correct modeling of such effects on the particle motion. However, we stress that the optics transport is not always so straightforward. Especially in the last two runs of commissioning (from September to December 2010), we have recognized an incorrect optics transport from LH to BC1, independently from the magnetic chicane settings. This bug is still under investigation. The same optical transport, but this time requiring bigger efforts to maximize the transport efficiency with trajectory correction, is repeated after matching in BC1 to upload the nominal optics up to linac end and, again, after matching in TLS to upload the nominal optics in the Spreader. Before imposing the nominal optics to the machine, the matching tool provides data and plots about the present optics along the lattice, the optics expected after applying but starting from the measured Twiss parameters and the nominal optics as a reference. If the mismatch parameter is very close to 1 at the beginning of the line, then the expected optics will be very similar to the nominal one.

7.5 Emittance Studies

In spite of the relatively smooth beam transport through the linac, we observe an important and not expected projected emittance growth during bunch length compression in BC1. Further investigations are required to understand this effect in detail. So far, we have collected some data that we are going to interpret, also with the support of simulations. The nominal optics adopted in FERMI from LH to BC1 area is shown in Figure 4.2. Figure 7.11 shows the emittance measurements performed in LH and BC1 area with quadrupole scan technique. Usually, more than 7 values of quadrupole strength and at least 3 images per strength are recorded. Gaussian fitting is applied to the projection of each col-

lected image in the horizontal and in the vertical plane, taking 100% of the pixels. The measurement is therefore providing a 100% statistical projected emittance. Background subtraction is also usually done during the measurement. Two sets of measurements are represented by solid/yellow and dashed/pink line, respectively. The projected emittance is shown as function of the machine configuration and measurement location, as indicated in the abscissa axis. Machine reproducibility and measurement errors lead us to limit the measurement accuracy to ± 0.1 mm mrad normalized emittance, in both planes.

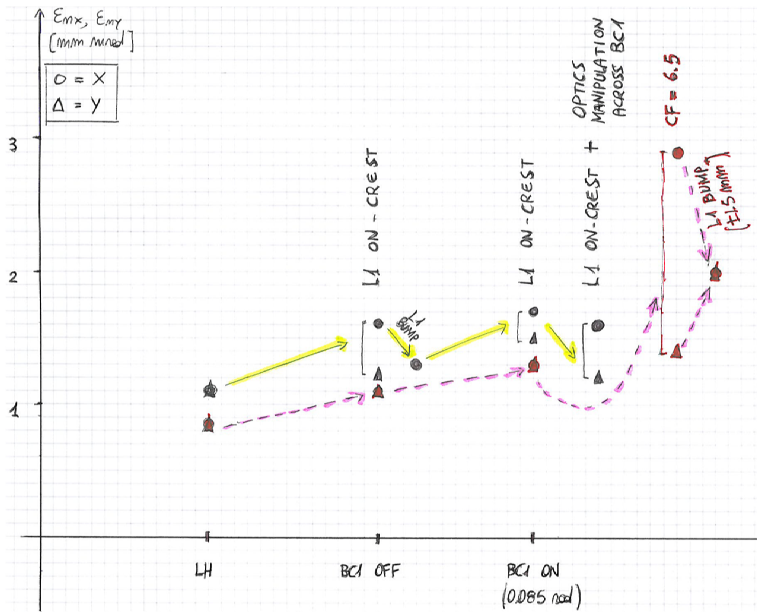


Figure 7.11: Emittance measurements at fixed compression factor.

In the first set of measurements (yellow line) there is a net increase in the horizontal emittance when the beam passes from LH at 100 MeV to BC1 at 350 MeV. BC1 is at zero bending angle. Since the energy spread is relatively small, 0.1%, we neglect chromatic aberrations and residual dispersion. Instead, we suspect transverse wake field generated in L1 or upstream is displacing the bunch tail with respect to the head. Notice that during the measurement the beam is forced to pass at the zero reading of all BPMs in L1. In fact, a $200 \mu\text{m}$ horizontal offset in L1 reduces the horizontal emittance closer to the initial value, which is approximately 1.2 mm mrad. As BC1 is turned on at 0.085 rad bending angle, with new optics tuning for this option, both horizontal and vertical emittances slightly

grow. No compression is expected so far because the beam is still running on crest in L1. However, an uncertainty on the effective residual (and nonlinear, due to the RF curvature) energy chirp at the entrance of BC1 could explain a local compression of the bunch head. Since the bigger growth is in the horizontal plane, we suspect a CSR contribution from some energy and/or optics mismatched end of the bunch. After some optics manipulation across BC1, some reduction is observed, especially in the vertical plane. This could indicate the vertical plane suffers from chromatic aberration in the matching quadrupoles downstream of BC1, in the presence of an energy mismatched end of the bunch. As a last step, a smoother optics through the BC1 area seems to slightly reduce such an effect. In the second set of measurements (pink line) there is 20% emittance growth in both planes from LH to BC1 off and then again to BC1 on. This time, when compressing the beam by a factor of 6.5 (linear theoretical), the horizontal emittance blows up by a factor of 2.2. CSR might be acting here, although an emittance growth smaller than 10% is predicted from `elegant` for a compression factor up to 10. The blow up is then strongly minimized by big trajectory bumps of ± 1.5 mm in L1. The final growth is by a factor of 1.5. The vertical emittance is affected by the trajectory bumps as well. We also report of a third set of measurements (not shown here), in which the same mean energy and energy spread at BC1 is achieved than during compression, but with energy chirp of opposite sign. So, while the emittance grew again by a factor of 2 during compression, it is observed no emittance growth at all during bunch lengthening. These additional measurements confirm a CSR effect during compression and seem to remove any suspicion of residual dispersion when the energy spread is high but no compression is going on. Another campaign of emittance studies was made by varying the compression factor. The same compression factor, analytically computed in the linear approximation, is implemented with BC1 at 0.085 rad bending angle first, at 0.050 rad then, by varying the L1 RF phase. Also, a new optics with smaller betatron functions and smoother optics across BC1 is adopted. This is shown in Figure 7.12. For any fixed BC1 setting, the new optics mitigates the emittance growth only for $C > 6.4$, where $\epsilon_{n,x}$ passes from 4.1 to 3.2 mm mrad. The same mitigating effect is observed in the vertical plane. We suspect this is an indication the vertical emittance is suffering from chromatic aberration. Although simulations for a perfectly matched beam predicts the absence of any second order emittance growth, chromatic aberration could play a role for optically mismatched slices. Finally, the nominal optics with smaller bending angle in BC1 and larger energy chirp to restore the same compression factor reduces the horizontal emittance of a big amount, from 3.2 to 2.2 mm mrad for $C = 6.4$. In this case, the smaller bending angle is expected to mitigate CSR and this is confirmed by the measurements. An `elegant` simulation of the CSR instability and the second order aberration with a self-generated particle beam,

perfectly energy and optically matched to the standard optics lattice, does not predict any important emittance growth. Some small growth becomes evident when using a GPT generated input beam with slice optics greatly mismatched. The simulation results listed in Table 7.1 refer to an ideal 350 pC, 5 ps fwhm long, elegant-generated beam, with an initial normalized projected emittances of 1.0 mm mrad. The optics mismatch is reproduced by changing a quadrupole setting on purpose. The output normalized projected emittances are listed in Table 7.1, considering either CSR only (1st order tracking), chromatic aberration only (2nd order tracking) or both these effects at the same time. Due to the limited number of particles used, $2 \cdot 10^4$, we limit the accuracy of our results to 0.1 mm mrad. The first value in each Table cell is for the horizontal plane, the second is for the vertical. The simulations result indicate that a big optics mismatch along the whole bunch or part of it, can enhance CSR induced emittance growth up to factor of approximately 2. However, a factor of about 5 is gained in the horizontal plane and a factor of 2 in the vertical plane from chromatic aberration only. This dominates the CSR contribution as well. The same simulations have been repeated with the new optics. Due to the different quadrupole strengths, here the mismatch induces even higher betatron functions and, therefore, stronger effects from chromatic aberration. However, the same CSR effect than with nominal optics is substantially confirmed, while the chromatic aberration effect in the vertical plane is minimized, as expected (1.5 mm mrad instead of 2.5 mm mrad vertical emittance).

Table 7.1: Emittance simulation study with standard optics.

	CSR	Chrom. Aberration	CSR+Chrom. Aberration
C = 1 (L1 on crest)	1.0, 1.0	1.1, 1.0	1.2, 1.0
C = 6.4 (L1 +25 deg)	1.8, 1.1	5.2, 2.1	5.2, 2.1
C = 10 (L1 +28 deg)	2.5, 1.2	-	5.5, 2.5
C = 1/5 (L1 -25 deg)	1.0, 1.1	6.6, 2.5	4.5, 2.5

7.6 Microbunching Instability

We conclude this Chapter with a few notes on experimental evidence for CSR and the microbunching instability. As discussed above, a contribution from CSR is suspected from the fast increase of the horizontal emittance during compression. Owing to the non-linearized longitudinal phase space at the entrance of BC1 (the X-band structure is not installed yet), the elegant simulation predicts a 1 kA, 20 fs long current spike at the bunch head for $C > 3$. If the slice optics of this spike is not well matched to the lattice, it could become the natural source

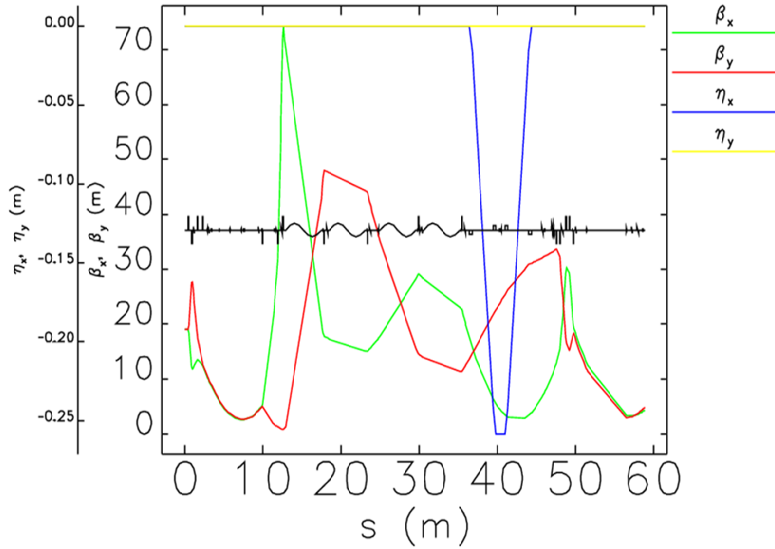


Figure 7.12: New optics from the LH to the BC1 area. The center line sketches the FERMI layout.

of the projected emittance blow up depicted in Figure 7.11. Some coherent optical radiation emission is also observed at the second screen downstream of BC1, where the beam is expected to reach a waist. This is shown in Figure 7.13 in which the beam is compressed by a factor of 4. As the computed compression factor reaches the value of 3 or higher, we obtain a fragmented image at the OTR target (middle plot). Saturation of the screen system with the OTR target can be interpreted as coherent optical transition radiation emitted by a very short current spike or extended microbunching along the whole bunch duration. At the moment, we cannot distinguish between these two possible sources. The fragmented image disappears when using the YAG target (left plot) or by inserting an OTR foil upstream of it to introduce an emittance smearing effect (right plot). Another evidence of microbunching instability is shown in Figure 7.14. Here the beam spot is collected at the last screen of the FERMI electron ebeam delivery system, in front of the main beam dump. The horizontal dispersion is left to reach several meters so that we are effectively projecting the particle energy distribution on the horizontal plane. The total energy spread is expected to be of the order of 0.3% rms. The BC1 linear compression factor is 6.4. Most of the 350

pC beam charge is collected in the brighter spot, approximately in the middle of the dispersed image. The several mm's long tail on the left side corresponds to higher energy particles. A periodic structure is clearly visible in the high energy region and even more in the low energy portion of the bunch. This image reveals an energy modulation distributed along the whole bunch duration, as predicted by the simulation studies in Section 5.5. Further and more systematic investigations on microbunching instability will be carried out during commissioning in 2011.

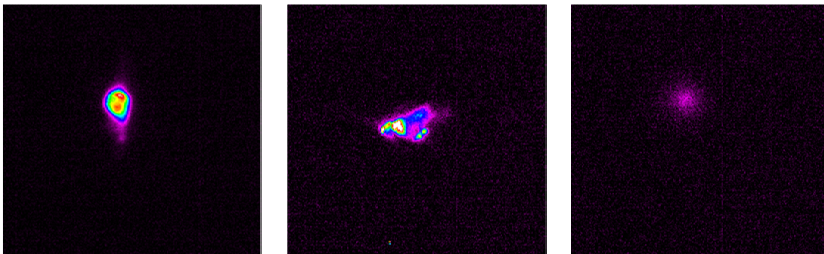


Figure 7.13: Evidences of COTR during compression.

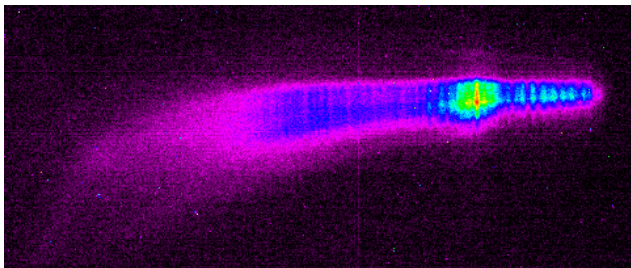


Figure 7.14: Evidences of energy modulation at the main dump.

7.7 Conclusions

We have reported about the commissioning of the FERMI@Elettra electron beam delivery system. Methods and experimental results concerning the control of the longitudinal (acceleration, energy distribution, bunch length compression and microbunching instability) and transverse (optics matching, transport and trajectory control) electron beam dynamics in FERMI have been shown. The longitudinal phase space of the electron beam has been characterized at the beginning of the FERMI commissioning with a simple spectrometer line. Optics has revealed to be an important ingredient for the characterization of the electron beam energy distribution since it optimizes the resolution of the energy measurement. Starting from experimental Twiss parameters of the electron beam, the optics matching and transport through the whole line has been performed with the `elegant` code, which includes the description of the real accelerating gradients and the RF edge focusing of the structures. The mismatch parameter usually corresponds to a projected emittance growth smaller than 1% in both planes. `elegant` has also been used to generate for the trajectory theoretical response matrices to correct the real beam trajectory in the linac and in the high energy transfer line. The matrices are imported in a trajectory feedback tool. This is also able to measure experimental response matrices. The theoretical and the experimental ones can be merged for a global trajectory correction along the whole line. The BPMs integrated into the feedback tool read the beam position at the frequency of 10 Hz and their reading is forced to the value determined by the user by the corrector magnets. In this way, the feedback works as a trajectory correction tool as well. It has been verified that the magnetic chicane BC1 does affect neither the trajectory nor the dispersion in the succeeding lattice. The dispersion bump in the chicane has been measured and agrees well with the theoretical expectation. An important horizontal emittance growth appears during the magnetic bunch length compression, especially for compression factors larger than 3. Off-line simulation studies indicate that CSR might be the main responsible of this emittance degradation, especially in the presence of nonlinear compression (the X-band cavity to linearize the longitudinal phase space during compression has not been installed yet) and potential slice optics mismatch. Some evidence for the microbunching instability has been detected for compression factors larger than 3. They are COTR emission downstream of BC1 and an energy modulation of the compressed electron beam. At the end, a comparison of the theoretical expectation and measured values for many electron beam parameters has been produced and summarized in a table of parameters. The uncompressed beam has been well characterized experimentally. A good agreement with the model has been achieved. The uncompressed beam still deviates from the model as for the projected emittance measured after BC1. Fur-

ther investigations are needed to accomplish a full understanding of the physics developing in BC1. Nevertheless, the electron beam quality has revealed to be more than sufficient to generate the first coherent harmonic generation in seeded configuration at 43 nm (FEL fundamental output) in December 2010, after one year, calendar time, of machine commissioning. Table 7.2 shows the comparison of the main electron beam parameters as they have been measured during the commissioning and the model prediction.

Table 7.2: Design and measured main electron beam parameters.

Parameter	Model	Measurement	Unit
Charge	350	350	pC
Charge jitter (rms)	4	0.5	%
PI laser radius	0.7	0.7	mm
PI pulse duration (fwhm)	5.0	5.0 ± 0.1	ps
Bunch duration (fwhm)	6.0	6.0 ± 0.5	ps
$\epsilon_{N,x}, \epsilon_{N,y}$ in LH area	0.8, 0.8	$0.8 \pm 0.1, 0.9 \pm 0.1$	mm mrad
$\epsilon_{N,x}, \epsilon_{N,y}$ in BC1 area, $C = 1$	1.0, 1.0	$1.3 \pm 0.1, 1.2 \pm 0.1$	mm mrad
$\epsilon_{N,x}, \epsilon_{N,y}$ in BC1 area, $C = 6.4$	1.1, 1.1	$2.0 \pm 0.1, 1.4 \pm 0.1$	mm mrad
$\epsilon_{N,x}, \epsilon_{N,y}$ at linac end, $C = 6.4$	1.5, 1.5	$3.5 \pm 0.5, 2.9 \pm 0.1$	mm mrad
$B_{mag,x}, B_{mag,y}$ in LH area	1., 0, 1.0	$1.005 \pm 0.003, 1.001 \pm 0.002$	
$B_{mag,x}, B_{mag,y}$ in BC1 area	1., 0, 1.0	$1.010 \pm 0.004, 1.000 \pm 0.001$	
$\langle E \rangle$ out of Gun	5.0	$4.5 - 4.9 \pm 0.1$	MeV
$\sigma_{\delta,tot}$ out of Gun (rms)	40	$28 - 44 \pm 5$	keV
$\langle E \rangle$ out of L0 (on crest)	96	$95 - 102 \pm 0.02$	MeV
$\sigma_{\delta,tot}$ out of L0 (rms)	45	$43 - 89 \pm 20$	keV
$\langle E \rangle$ out of L1 (on crest)	345	$349 - 357 \pm 0.01$	MeV
$\sigma_{\delta,tot}$ out of L1 (rms)	200	$\geq 135 \pm 12$	keV
$\langle E \rangle$ out of L4	1200	$\leq 1210 \pm 0.06$	MeV
$\sigma_{\delta,tot}$ out of L4 (rms)	1200	$\geq 900 \pm 60$	keV
$\langle E \rangle$ jitter out of Gun	5	6	keV
$\langle E \rangle$ jitter out of L0	9.6	9	keV
$\langle E \rangle$ jitter out of L1	300	660	keV
$\langle E \rangle$ 6hs-stability out of L1 (p2p)	0.3	1.0	MeV
$\sigma_{\delta,tot}$ 6hs-stability out of L1 (p2p)	0.3	0.15	keV
Trajectory jitter (rms)	20	$10 - 30 \pm 5$	μm

Chapter 8

Concluding Remarks and Outlook

8.1 General Remarks for Seeded FELs

The operation of X-ray FELs relies on extremely high quality electron beams. Two FEL projects, LCLS at SLAC [33] and FLASH at DESY [157], employing the technique of SASE, define the state-of-the-art situation: peak current of few kiloamperes, normalized emittance of 1 mm mrad or less and an energy spread of 1 MeV or less [11]. The creation of electron bunches with these parameters is a difficult and elaborate process consisting of the electron bunch production, acceleration and compression. The main phenomena affecting the electron beam quality include chromatic aberrations, magnetic field errors and magnets misalignment, SC forces, wake fields and CSR. Demanding for the electron beam quality at least as much as, maybe more than, SASE FELs are those FELs that are designed to generate fully temporally coherent X-rays. Among these, the HGHG FELs employ a laser to seed the radiation at a lower harmonic of the FEL fundamental output. FERMI@Elettra belongs to this new generation of light sources. When the electron beam energy is not high enough to ensure a FEL fundamental emission resonant at the desired X-ray wavelength, two (or more) FEL cascades are adopted to reach the goal. So, FERMI FEL1 is a standard HGHG FEL, while FERMI FEL2 employs a double cascade. In this case the radiation produced in one cascade by one group of electrons proceeds ahead and interacts with other electrons from the same bunch in the next cascade. Thus, relatively long electron bunches are needed to accommodate this technique. The FEL gain is ensured by a high peak current that implies a constant value (flat profile) over most of the bunch length. At the same time, one must make sure that there is

no frequency chirp in the signal, or as little as possible. This chirp can be caused either by energy modulation along the electron bunch or by frequency chirp in the seeding laser. Thus, a flat longitudinal phase space of the electron beam has to be provided at the undulator entrance. At the end, in a HGHG FEL the goal is to obtain an electron beam with “flat-flat” distribution, i.e. flat in both peak current and energy.

It has been shown in this Thesis that in the presence of a longitudinal structural wake field, the degree of linearity of the final longitudinal phase space depends on the initial current profile. In FERMI, a flat longitudinal phase space is ensured by the linearity of the initial current ramp. If this is not perfect, residual higher order energy chirps might reduce the effective compression factor, enlarge the FEL spectral output bandwidth [158] (via a quadratic component of energy chirp) and create current spikes at the bunch edges during compression (via a cubic component of energy chirp) (see also [159]). These lead to further detrimental effects on the energy spread and emittance due to enhanced CSR and wake fields. It has been shown that these terms can be further minimized by adjusting the harmonic cavity RF voltage and phase.

At a scale much shorter than the bunch length, CSR, LSC and the dispersive motion in the magnetic chicanes lead to an amplification of initial small energy or density perturbations, even at the Schottky noise level, driving the microbunching instability. The final longitudinal phase space is typically modulated at wavelengths of the order of $1 \mu\text{m}$. In the presence of two-stage magnetic compression, the instability enters into the nonlinear regime that is the folded structure of the longitudinal phase space has important harmonic contents. Although the microbunching instability seems to be well suited to enforce the FEL amplification, there is not any practical way to keep it under control, yet. Instead, Landau damping induced by a large transverse emittance and large relative uncorrelated energy spread would allow partial or total suppression of the instability. In fact, they act as a low-pass filter for the spectral content of the final energy and current modulation. In FERMI, a laser heater has been adopted to increase the uncorrelated energy spread at low energy. Due to the relatively low beam energy at the undulator and to the FEL sensitivity to the relative energy spread, a careful control of the beam heating to a few keV level is required in order to reduce the instability strength. In practice, a compromise between strong heating to suppress the microbunching instability and small relative energy spread for an efficient FEL process has to be reached.

All these considerations underline that a not so high electron energy of 1.5 GeV makes the FERMI HGHG FEL particularly sensitive to any nonlinear effect in the particle longitudinal phase space. As for the transverse dynamics, instead, the geometric emittance of the 100's pC charged beam is adiabatically damped to the level of 0.3 nm rad so that, for an average betatron function of

10 m, the scale of the transverse beam size is 50 micron. This allows to relax the tolerances on the accelerator alignment and any source of transverse emittance growth (i.e., residual dispersion, magnets field quality, CSR effect, etc...) and trajectory jitter (i.e., ground and magnet vibrations, beam launching, etc...) with respect to much higher energy machines such as LCLS. However, because of the weaker beam rigidity, the transverse wake field instability, whose strength is made particularly important because of the small iris of the accelerating structures installed in FERMI, becomes a real issue, especially at the nominal high charge of 800 pC. A careful control of the beam trajectory along the linac and dedicated diagnostics with high resolution (screens, RF deflectors) are therefore required to minimize the projected emittance growth. If the head-tail instability is strong enough, any seeded FEL power emission would suffer of it because of the lack in the transverse overlap of the electron beam and the seed laser. The other major issue affecting the transverse emittance of the electron beam is the CSR emission in the bends of the magnetic chicanes and of the high energy transfer line. In this case, almost all the CSR effect can be recovered by a suitable optics arrangement, such as a high beam angular divergence at the single source point (in BC1 and BC2) and -I transport matrix between consecutive (and identical) sources of CSR emission (in the Spreader). When a quite linear compression is implemented and pretty far from the point of full-compression, the slice emittance is expected to be preserved as at the injector level, even for high compression factors.

8.2 Machine Design

The FERMI linac layout is designed in order to minimize any source of 6-D emittance dilution. The high impedance BTW accelerating structures are positioned in the last two linac sections L3 and L4, in the energy range 0.6–1.5 GeV, so that their longitudinal wake field is used to remove the energy chirp required upstream for bunch length compression and the effect of transverse wake field is minimized by the higher energy, shorter bunch obtained after compression.

The electron energy at BC1 ranges between 330 and 310 MeV for a linear compression factor from 5 to 10. On the one hand, such energies are high enough to avoid repulsive nonlinear SC forces during compression that would otherwise degrade the 6-D beam emittance, on the other hand, BC1 is desired to be at as low energy as possible to enhance energy Landau damping in order to minimize the impact of the microbunching instability. In the two-stage compression scheme, the energy at BC2 is approximately 600 MeV. This choice balances the conflicting requirements of minimizing the CSR instability – by adopting small $R_{56} \approx -20$ mm and large energy spread $\sigma_\delta \approx 1\%$ – and that of can-

celing the correlated energy spread needed for compression in the two-stage scheme. The CSR effect in BC2 can be evaluated as in the following. Since the electron bunch emits in the long bunch, long magnet approximation, the CSR induced energy spread goes like $\sigma_{\delta,CSR} \sim (4 \ln \gamma \theta - 2)/\gamma$. The CSR induced emittance growth has therefore the following dependence on the beam energy, $\Delta\epsilon/\epsilon \sim \gamma \sigma_{\delta,CSR}^2 \sim (4 \ln \gamma \theta)^2/\gamma$ (for a Gaussian short bunch radiating in a long magnet we would have $\Delta\epsilon/\epsilon \sim 1/\gamma$). So, we only gain a factor of 2 in emittance growth by ideally moving BC2 from 300 MeV to 1 GeV. The intermediate energy of 600 MeV has finally been chosen for the FERMI case. It primarily allows the beam to be fully compressed early enough to minimize the transverse wake field effect in L4. At the same time, all five BTW structures in L4 are run on-crest to maximize the final energy and, at the same time, their geometric longitudinal wake field removes the energy chirp required for compression in BC2. The threshold of 2% rms energy spread at the entrance of both chicanes sets tight but still realistic tolerances on the magnetic field homogeneity in the chicane dipole magnets. A good field homogeneity is required to avoid chromatic emittance dilution. The two-stage configuration allows FERMI@Elettra to extend the total compression factor up to 50, if needed. The chicane bending angle can reach a maximum operational value of 0.12 rad, so providing a (linear) compression factor of 10–30 in BC1 and 2–5 in BC2.

Owing to the combined action of LSC, CSR and dispersive motion in the compressors, FERMI@Elettra acts like a huge amplifier of small initial density and energy modulations. The frequency cutoff of the microbunching instability gain is determined by the uncorrelated energy spread and transverse emittance that allow particle phase mixing in the longitudinal and transverse phase space, respectively. Linear analysis of the instability starting from shot noise predicts a final slice energy spread of a few MeV's, which is one order of magnitude bigger than the FEL specification. The energy spread can be reduced to the 100 keV level (rms value) by using a laser heater at low energy, that is increasing the uncorrelated energy spread from the natural 2 keV level up to 10 keV. Owing to the sensitivity of FERMI FEL performance to the slice energy spread, the specified beam heating is a compromise between the effective reduction of the instability gain and the maximum energy spread tolerated by the FEL. The analysis shows that the efficiency in removing the beam microbunching by Landau damping is much more sensitive to the initial modulation wavelength than to the amplitude.

A compromise has also to be reached about the optics design of BC1 and BC2, in which the magnitude of the H -function in the last bend of the chicane can vary within at least a factor of four. This will give us some flexibility to maneuver between such tasks as containing the emittance excitation due to CSR that benefits from smaller H and containing energy spread growth due to the

microbunching instability that benefits from larger H . Numerical simulations of the microbunching instability support and complete the linear analysis. They are a multi-scale dynamics problem because even fluctuations on a small scale can lead to global instabilities and fine-scale structure formation. `elegant` tracking demonstrates the high sensitivity of FERMI to even very small initial density modulations and confirms that most of the instability gain is cumulated just after BC2. In addition to the linear analysis, it also shows that the instability enters into the nonlinear regime after BC2. IMPACT and Vlasov solver predict that a minimum beam heating of ~ 10 keV is necessary to suppress the instability in the two-stage compression scheme, whereas 12 keV rms was predicted by the analytical treatment of the instability. So, the final slice energy spread would be in the range 80–150 keV rms, which is still compatible with the FEL production. The substantial agreement of 1-D and 3-D codes simulating the CSR instability in BC1 and the microbunching instability along the whole linac suggests that the 3-D SC effect, if present, is small and probably masked by the differences in the computational methods of the numerical noise.

We have also investigated compression schemes alternative to the two-stage, in order to more effectively suppress the microbunching instability and compatible with the present FERMI layout. They are the one-stage compression and the so-called enhanced phase mixing. The feasibility of one-stage compression and its compatibility with the FERMI@Elettra FEL requirements is demonstrated by means of 1-D and 3-D particle tracking, with promising results for the preservation of the beam quality. In addition to this, a different promising configuration shows up. If the linear energy chirp at the exit of BC1 is removed by dedicated accelerating structures, then particle longitudinal crossover in BC2 is enhanced. The effect is optimized by two chicanes, BC1 and BC2, with the same sign of R_{56} . As a result, the energy modulation is damped, together with the associated current spikes. The beam transport has been verified with `elegant` particle tracking, including collective effects, for a compression factor of 10 in BC1. The study shows that the enhanced phase mixing is successful and even more efficient than the one-stage compression for initial modulations whose wavelength is of the order of tens of μm . It may even be applicable to longer wavelengths and/or higher compression factors, although these more extreme situations need to be confirmed by further investigations.

The diagnostic part of the FERMI linac layout relies on the design of a compact multi-purpose optics insertion. This aims to reach a satisfactory compromise between beam diagnostic, production, collimation and space saving. It is based on a low-beta symmetric optics over $2\pi/3$ betatron phase advance. A betatron mismatch parameter ≤ 1.05 and maximum residual dispersion of the order of $\eta \approx 1$ mm, $\eta' \approx 1$ mrad are expected. Total shadowing of the undulator vacuum chamber, including 20% safety margin on the 7 mm gap, is ensured

by the definitively small collimators' iris radius of 2 mm. A dedicated optics for collimation with bigger $\beta_{x,y}$ would have been desired. However, a different arrangement of quadrupole magnets would have required more space or, alternatively, the CS should have to be moved further downstream in a dedicated optics insertion. In general, modifications to the present magnetic lattice are possible but probably not in the picture of a sole optics for beam diagnostic and transport. The straight line is intersected by a spectrometer line for the characterization of the beam longitudinal phase space. Here, an energy resolution in the range $10^{-4} - 10^{-5}$ is available.

8.3 Electron Beam Quality and Control

In the nominal design, to be fully implemented by the end of 2011, the final electron bunch duration is fixed to 900 fs fwhm to accommodate 150 fs rms arrival time jitter between the seed laser and the electron beam [29] and an up to 200 fs long seed pulse. A peak current of 800 A is achieved by compressing the bunch length of the initial 0.8 nC charged beam by a factor of 11. The compression efficiency is limited by nonlinearities in the longitudinal phase space, mostly due to the geometric longitudinal wake field in the accelerating structures (for a parabolic current profile, a quadratic energy chirp $\approx 0.02 \text{ MV}/ps^2$ and a cubic energy chirp $\approx 165 \text{ MV}/ps^3$ are induced at the entrance of BC1) and the second-order energy/path length dependence in the magnetic chicane ($T_{566} \leq 60 \text{ mm}$). Compression inefficiency translates into high order energy chirp, large correlated energy spread and current spikes at the bunch edges of the final beam. On the bunch length scale, CSR corrupts the longitudinal phase space much less than the longitudinal wake field: 0.5 MeV energy loss induced by CSR can effectively be neglected with respect to 15.6 MeV dissipated by the linac wake field. The flatness in the current profile, $\Delta I/I \leq 12\%$, and in the longitudinal phase space, $\sigma_{\delta,tot} \leq \rho = 1.5 \cdot 10^{-3}$, are simultaneously recovered by means of a linearly ramped current profile at the gun exit to generate linear longitudinal wake potential in the succeeding linac, while an RF X-band structure shall be used in decelerating mode to cancel the quadratic and cubic energy chirp during compression in BC1. An additional fine manipulation of the current profile is possible through R_{56} tuning, at the mm level, in the Spreader.

After accurate machine tuning, an rms projected emittance smaller than 2 mm mrad is expected at the entrance of the undulator. This is computed over 100% of the charge. A value closer to 1 mm mrad is predicted for approximately 80% of the charge in the bunch core. The initial 0.8 mm mrad emittance [29], provided by the injector at 100 MeV, is primarily affected by the geometric transverse wake field in the accelerating structures of L3 and L4, which have the re-

markably small iris radius of 5 mm. Trajectory bumps must be implemented along the linac to cancel the banana shape at the end of acceleration. Approximately 50% projected emittance blow up due to wake field can be tolerated by the FEL process. Simulation studies show that most of this blow up concerns trailing electrons, which occupy only 20% of bunch duration and therefore are not necessary involved in the interaction with a 100 fs long seed laser. Trajectory jitter smaller than 20 μm rms is tolerated in order not to corrupt the trajectory manipulation that counteracts the transverse wake field instability.

The second main source of emittance dilution is CSR emission in the compressors. This happens as in free space since there is no radiation shielding from the 70 mm wide vacuum chamber for a bunch duration equal or shorter than 1 ps. Theoretical evaluations and simulation results agree on a maximum emittance blow up of 20% once the horizontal betatron function in the second half of the chicane is shrunk to the 1 m level. It is important to notice that such projected emittance growth is essentially due to the slice emittance blow up in the bunch edges, where current spikes may appear corresponding to high slice energy spread and slice mismatched optics. A dedicated $-I$ transport matrix is implemented in the Spreader to cancel any CSR effect on the transverse emittance. Chromatic aberrations dilute the vertical emittance up to 15% (the main source is quadrupole focusing in the BC1 area) in the conservative scenario of complete filamentation that, however, is not expected to develop in the FERMI lattice. All other sources of emittance dilution are forced to a negligible level by the specifications of the magnet field quality and alignment. The specifications are computed for producing 1% projected emittance growth from each independent error source. Unlike the projected emittance, the slice emittance in the bunch core – we define a slice 30 fs long so that the seed pulse covers from one to three of them – is preserved as at the 0.8 mm mrad injector level. A safety value of 1 mm mrad is kept as the reference since it is still compatible with HGHG FEL production even at 4 nm fundamental output wavelength.

During one year of commissioning, from September 2009 to December 2010, a 350 pC electron beam has been generated, transported through the whole beam line with $\geq 97\%$ efficiency and seeded to generate the first FEL output signal in the coherent harmonic generation mode. A peak signal at the fundamental wavelength of 43 nm has been detected, as well as signals up to the 15th harmonic, with the narrowest fwhm bandwidth of 21 meV. Although priority was given to the RF conditioning and simple beam transport to ensure generation of an FEL signal within the deadline of December 2010, rough machine tuning and preliminary studies of electron beam dynamics have been carried out. Our initial contribution has concerned the characterization of the longitudinal phase space of the initial beam by means of projection imaging in the LH spectrometer line. So, bunch length, mean energy and energy spread are

measured on the basis of the beam line design optics. Then, we focused on the development of methods for slow (~ 1 Hz) trajectory correction and feedback. A MATLAB-based tool manipulates the trajectory with theoretical as well as experimental response matrices. The tool ensures freedom in setting correction algorithms, weights on the eigenvalues of the inverted matrices, speed of convergence of the correction loop and merging different matrices. Trajectory manipulation by imposing several constraints on the BPMs reading and correctors strength was successful, even using a global matrix correcting from the injector to the linac end as well as three parallel feedback loops covering from the injector to the FEL1 undulator line. Trajectory bumps along the linac are routinely implemented. They limit the projected emittance dilution to 20% downstream of L1 and reduce the normalized emittances from ~ 10 mm mrad to ~ 3 – 4 mm mrad at the linac end (~ 2 mm mrad emittances are measured in the BC1 area). So, a strong sensitivity of the projected emittances to the trajectory is experimentally confirmed. Trajectory correction to $20 \mu\text{m}$ level is normally achieved, with trajectory short-term jitter at $10 \mu\text{m}$ level.

The dispersion function has been measured along the linac for several configurations of magnetic focusing and RF acceleration. The dispersion in the middle of BC1 is in good agreement with the theoretical value. Closure of the BC1 dispersion bump has also been verified. A large 100 mm vertical dispersion propagates parasitically along the linac. We suspect the main source of this effect is a time-dependent RF kick given by the vertical coupler of the injector. If so, a suitable steering at low energy would allow to compensate for these unexpected dispersion bumps.

A MATLAB-based tool for optics matching and transport has been developed that also takes advantage of specific SDDS-to-TANGO MATLAB scripts to interface `elegant` with the real magnet devices. The matching procedure is routinely performed in LH, BC1 and TLS area and it works reliably. A theoretical solution is obtained in a few tens of seconds. Graphical and text data are provided by the tool to the user to check the level of convergence and the accuracy of the matching loop. By virtue of the low- β symmetric optics downstream of each matching section, the user can immediately verify whether the theoretical solution is correctly applied to the machine by looking to the beam sizes at three consecutive screens. Statistics of the experimental mismatch parameter, mainly collected during measurements in LH and BC1 area, gives the horizontal one in the range $[1.005 \pm 0.001, 1.075 \pm 0.020]$, with mean value of 1.03. The vertical mismatch parameter is in the range $[1.002 \pm 0.002, 1.117 \pm 0.124]$, with mean value of 1.05. In general, we notice that the quality of the matching depends mainly on the goodness of the initial emittance and beam parameters measurement. Noisy or odd-shaped beams are more difficult to match. After having matched the beam, we load the theoretical optics on the lattice. Once the optics

is matched in the LH area, the beam is transported to the BC1 section almost instantly, requiring only small trajectory adjustments with the correctors. In one of the best cases of simple optics transport, the experimental mismatch parameter in BC1 area is 1.011 and 1.004 in the horizontal and in the vertical plane, respectively. Since the model is also including the vertical focusing of the BC1 dipole magnets and cavity end RF focusing, the good optics transport is also a confirmation of the correct modeling of such effects on the particle motion. A good week-by-week reproducibility of the machine optics has been confirmed.

Projected emittance studies have been carried out in the BC1 area, for several configurations of the magnetic chicane. While elegant simulations do not predict any important emittance growth during compression, we have measured some emittance blow up due to energy and/or optically mismatched beam passing through the compressor. Second order simulations with mismatched optics show that CSR and chromatic aberration seem to justify the measurement results. In addition to this, we guess some head-tail effect is coming from the injector, in both planes. Trajectory manipulation allows to minimize the emittance blow up downstream of L1 with no compression. As for the BC1 area, the CSR instability would dominate the horizontal beam dynamics providing an emittance growth by a factor of 2 for $C = 6.4$, while chromatic aberration would dominate the vertical with a blow up of a factor of 5 for $\sigma_\delta \sim 1\%$. This interpretation is supported by several measurement campaigns with BC1 on, off and in bunch lengthening mode. A residual dispersion effect in the horizontal plane is not excluded at all, but, in this case, it would invalidate the emittance measurement itself that assumes a pure betatron particle motion. More in detail, $\epsilon_{n,x}$ grows by 20% for $C < 3$, in agreement with simulations. But, for $C > 6$, up to a factor of 1.8 is gained. Since the CSR instability depends on the initial emittance as $\sim 1/\epsilon_x$, we have normalized the relative growth to the initial value for different measurements at different compression factors and found that the measured absolute emittance growth coincide with 0.1 mm mrad error. Finally, we expect that a new optics with smaller β_x across BC1 chicane, smaller β_y over the BC1 matching quadrupoles, BC1 bending angle of 0.052 rad, 1.5% energy spread and a compression factor of 5, would allow a large reduction of the emittance growth (we expect $<20\%$) with respect to the present status.

Evidence of the microbunching instability has been collected downstream of BC1 for $C \geq 3$. COTR appears in this case, it is smeared by a YAG target or by inserting an OTR foil upstream. Also, some energy modulation has been detected in the dispersive line in front of the main beam dump. Since the laser heater is not implemented yet, some bunching development is expected to happen along the machine even starting from shot noise.

8.4 Outlook

In the last 20 years, an important part of the accelerator physics community has been focusing on the design, optimization and construction of VUV, soft and hard X-ray FELs. These powerful light sources, driven by linacs, show enough flexibility in the output photon properties to cover a broad range of experimental programs. Two big families of FEL generation schemes can be recognized in the SASE and seeded FEL production. Although both these schemes can be in principle implemented in the same facility, every laboratory involved in this business starts with specializing its own project on the basis of the requirements expressed by its own science case. SASE FEL might be considered a good choice to achieve very short pulses at wavelengths in the nm range and below with a 10's GeV energy linac. HGHG FEL is intended to be an improvement with respect to SASE in terms of spectral purity, but it is currently limited to a few nm output wavelength in the fundamental because of the available seed laser technology. The HGHG scheme could become a practical choice for much shorter wavelengths, as in the SASE case, if and when a seed laser became available at 10's nm wavelength. Some recent scientific programs are already looking to the High Harmonic Generation technique to make this possibility a reality. At the moment, the harmonic cascade implemented in a HGHG FEL is probably the only way to allow a 1 GeV machine reaching 1–5 nm fundamental output wavelength with hundreds of MW peak power and more than 10^{12} photons per pulse. Of course, also a SASE FEL might have an important harmonic content, but in this case the undulator must be much longer than in a seeded FEL (we can estimate at least by a factor of 2 to reach saturation, with the same electron beam) and therefore with higher costs. In a seeded FEL, the time and spectral properties of the output photon pulse are dominated by the seed laser quality. Unfortunately, the higher the harmonic up-shifting from the seed laser wavelength, the tighter is the constraint on the slice relative energy spread at the undulator entrance. We have the impression this is the most critical issue on which a 1 GeV, X-ray HGHG FEL design should be focused.

The most challenging FEL option of FERMI@Elettra implements the HGHG with fresh bunch technique. This requires a bunch length of approximately 1 ps and, for 800 A peak current, 800 pC total charge. This unavoidable high charge for the double cascade scheme might reveal as a limiting factor for the ultimate FEL performance because it seems to be quite difficult to ensure a high brightness and uniform particle distribution over such duration at the undulator entrance. An arrival time jitter between the seed laser and the electron beam possibly to 10 fs level would reduce the final bunch duration and thus relax the electron beam quality requirements, especially in terms of energy and current flatness. Also, there are some expectations about the potential success of the

optics design to suppress the CSR induced emittance growth in the presence of large bending angles. This special optics arrangement (-I transport matrix) can reveal particularly useful for the design of the high energy transfer line that, in all linac-based FEL projects, brings the electron beam to the undulator line(s) with at least one dog-leg lattice. If the CSR effect is canceled, the electron beam quality is totally preserved and large bending angles would become allowed thus reducing the total length of the undulator and experimental hall buildings. The impact on the total cost of a FEL project would then be really important. A major uncertainty that future FEL projects could be facing is the impact of the microbunching instability on the FEL performance. The instability mechanism is already known, but the nonlinear development of it is not treated analytically yet (time consuming and complex numerical methods are currently used). As already mentioned, lower energy machines are more sensitive to the growth of energy spread induced by this instability and the implementation of a laser heater at low energy seems now to be mandatory for almost all this kind of projects. However, the scheme of enhanced phase mixing could be one possible, simpler and cheaper solution than the laser heater to suppress the energy and current modulation. This scheme is thought to be feasible for moderate compression factors in one-stage, but it also gives an FEL project the possibility of achieving full compression with a two-stage compression. As a bottom line, we think that one really new and challenging goal for the next future linac-based FELs is to drive the microbunching instability on purpose and keep it under control in order to enhance the desired bunching at the undulator entrance.

Bibliography

- [1] G. N. Kulipanov, *Phys. Usp.* **50** (2007) 368–376.
- [2] H. Motz, *J. Appl. Phys.* **22** (1951) 527–535.
- [3] H. Motz, W. Thon and R. N. Whitehurst, *J. Appl. Phys.* **24** (1953) 826–833.
- [4] J. M. Madey, *J. Appl. Phys.* **42** (1971) 1906–1913.
- [5] R. Coisson and F. De Martini, *Quantum Electronics* **9** (1982) 939.
- [6] R. Bonifacio et al., *Nucl. Instrum. and Meth. A* **296** (1990) 787.
- [7] L.H. Yu, *Phys. Rev. A* **44** (1991) 5178.
- [8] I. Ben-Zvi, K. M. Yang, L. H. Yu, *Nucl. Instr. and Meth. in Phys. Res., Sect. A* **318** (1992) 726.
- [9] L.H. Yu et al., *Science* **289** (2000) 932.
- [10] R. Scheffield, *Physics of Particle Accelerators*, AIP Vol.**184** (1989) 1500–1531.
- [11] P. Emma, *Proc. of Part. Accel. Conf., Dallas, Texas, USA*, WAG01 (1995).
- [12] TESLA TDR, DESY 2000-011 (2001).
- [13] K. J. Kim, *Nucl. Instrum. Meth. A* **250**, (1986) 396 and *Phys. Rev. Letters* **57**, (1986) 1871.
- [14] R. Bonifacio, C. Pellegrini and L. M. Narduci, *Opt. Comm.* **50** (1984) 373.
- [15] G. De Ninno, W. Fawley, W. Graves, G. Penn, ST/F-TN-05/23 (2005).
- [16] G. De Ninno, E. Allaria, *PRL*, **99**, 014801 (2007) and ST/F-TN-09/03 (2009).
- [17] M. Cornacchia, S. Di Mitri, G. Penco and A. A. Zholents, *Phys. Rev. Special Topics - Accel. and Beams*, **9**, 120701 (2006).

- [18] S. Di Mitri et al., Nucl. Instr. and Methods in Phys. Res., Sect. A **608** (2009) 19–27.
- [19] P. Craievich, S. Di Mitri and A. A. Zholents, Nucl. Instr. and Methods in Phys. Res., Sect. A **604** (2009) 457–465.
- [20] S. Di Mitri, M. Cornacchia, S. Spampinati and S. V. Milton, Phys. Rev. Special Topics - Accel. and Beams, **13**, 010702 (2010).
- [21] S. Di Mitri, Phys. Rev. Special Topics - Accel. and Beams, **13**, 052801 (2010).
- [22] C. Pellegrini, Nucl. Instr. and Meth. A **445** (2000) 124.
- [23] H. Haus, Quantum Electronics, IEEE Journal of 17 (1981) 1427, ISSN 0018-9197.
- [24] G. Dattoli, A. Marino, A. Renieri and F. Romanelli, IEEE J. Quantum Electron. QE-17, (1981) 1371.
- [25] E. L. Saldin, E. A. Schneidmiller and M. V. Yurkov, Nucl. Instr. And Methods in Phys. Research., Sect. A **490** (2002).
- [26] L.H. Yu et al., Phys. Rev. Lett. **91**, 074801 (2003).
- [27] G. De Ninno et al., Phys. Rev. Lett. **101**, 053902 (2008).
- [28] C. Bocchetta et al., *FERMI@Elettra: A Free Electron Laser for EUV and Soft X-Ray Radiation*, Synchr. Rad. News **18N6** (2005) 30–35.
- [29] C. Bocchetta et al., *FERMI@Elettra Conceptual Design Report* (2007) <http://www.elettra.trieste.it/FERMI/index.php?n=Main.CDRdocument>
- [30] M. Cornacchia et al., *FERMI@Elettra Accelerator Technical Optimization Final Report*, ST/F-TN-06/15 (2006).
- [31] M. Svandrlik et al., Proc. of EPAC 2006, THPLS033, Edimburgh, UK.
- [32] D. Palmer, *The Next Generation photo-injector*, Stanford University dissertation (1998).
- [33] LCLS CDR, SLAC Report No. SLAC-R-593 (2002).
- [34] B. E. Carlsten, Nucl. Instr. and Methods in Phys. Res., Sect. A **285** (1989) 313–319.
- [35] M. Ferrario et al., Phys. Rev. Letters, **99** 234801 (2007).

- [36] D. Dowell et al., in Proc. of the 1995 Part. Accel. Conf., Dallas, Texas, USA (1995).
- [37] P. Emma, LCLS-TN-01-1 (2001).
- [38] E. L. Saldin, E. A. Schneidmiller and M. Yurkov, TESLA-FEL2003-02 (2003).
- [39] J. M. Byrd et al., Proc. of Linac Conf., Knoxville, Tennessee, USA, THP007 (2006).
- [40] M. Borland, J. Lewellen and S. Milton, Proc. of the 20th Intern. Linac Conf., THC05, Monterey, California (2000).
- [41] Yu, L. H., et al., Nucl. Instr. and Methods in Phys. Res., Sect. A **393** (1997) 96-99.
- [42] S. Sasaki, K. Miyata and T. Takada, J. Appl. Phys., Vol. **31** (1992) 1794–1796.
- [43] S. Reiche et al., in Proc. of PAC 2007, TUPMS038, Albuquerque, NM, USA (2007).
- [44] W.M.Fawley, LBNL-49625 (2002).
- [45] J. D. Lawson, The Physics of Charges Particles, Clarendon, Oxford (Oxford University Press, 1977).
- [46] A. J. Lichtenberg, Phase Space Dynamics of Particles, Wiley, New York (1969).
- [47] P. Lapostolle, Proc. of the 1st Int. Conf. on Ion Sources, Saclay (1969).
- [48] M. Weiss, Proc. of CERN Acc. School, CERN 87–10, Aarhus (1986) 162.
- [49] L. C. Teng, NAL Rep. FN 221-0100, Batavia, Illinois (1971).
- [50] J. Buon, Proc. of CERN Acc. School, CERN 94–01, Univ. of Jyvaskyla, Finland (1994) 89.
- [51] R. D. Ruth, SLAC-PUB-5091 (1989).
- [52] M. Sands, SLAC-AP-85 (1991).
- [53] H. Wiedemann, Particle Accelerator Physics, Vol. I, Springer (2003).
- [54] R. W. Assmann and A. Chao, in Proc. of PAC'97, 9V014, Vancouver, B.C., Canada (1997).

- [55] J. Rossbach and P. Schmuser, Proc. of CERN Acc. School, CERN 94-01, Vol.I, Geneva (1994) 17-33.
- [56] J. Tanabe, SLAC-R-754 (2005).
- [57] P. J. Bryant, Proc. of CERN Acc. School, CERN 94-01, Vol.I, Geneva (1994) 207-216.
- [58] M. Ferrario, V. Fusco, C. Ronsivalle, L. Serafini and C. Vaccarezza, New J. Phys. **8** (2006) 295.
- [59] L. Palumbo, V. G. Vaccaro and M. Zobov, LNF-94/041 (P) (1994).
- [60] K. L. F. Bane and M. Sands, SLAC-PUB-95-7074 (1994).
- [61] K. L. F. Bane, in Workshop on the Phys. and Appl. of High Bright. Electr. Beams, Erice, Italy (2005) and SLAC-PUB-11829 (2006).
- [62] K. L. F. Bane et al., SLAC-PUB-7862 (1994).
- [63] P. Craievich, T. Weiland and I. Zagorodnov, Nucl. Instr. and Meth. in Phys. Res., Sect. A **558** (2006) 58-61.
- [64] K. L. F. Bane et al., SLAC-PUB-9663 (2003).
- [65] A. W. Chao, B. Tichter and C.-Y. Yao, SLAC-PUB-2498 (1980).
- [66] L. I. Schiff, Rev. Sci. Instr. **17** (1946) 6.
- [67] J. S. Nodvick and D. S. Saxon, Phys. Rev. **96** (1954) 180.
- [68] R. L. Warnock and P. Morton, Part. Accel. **25** (1990) 113.
- [69] J. B. Murphy, S. Krinsky, and R. L. Gluckstern, Proc. of Part. Accel. Conf. 1995, (1995) 2980 and in Part. Accel. **57** (1997) 9.
- [70] E. L. Saldin, E. A. Schneidmiller, and M. V. Yurkov, Nucl. Instrum. Meth. Phys. Res., Sect. A **398** (1997) 373.
- [71] Ya. S. Derbenev, J. Rossbach, E. L. Saldin, and V. D. Shiltsev, DESY-TESLA-FEL-95-05 (1995).
- [72] M. Borland, Phys. Rev. Special Topics - Accel. and Beams, **4**, 070701 (2001).
- [73] E. L. Saldin, E. A. Schneidmiller and M. V. Yurkov, Proc. of PAC'97, Vancouver, B.C., Canada (1997) 1658.

- [74] T. ShafTan and Z. Huang, *Phys. Rev. Special Topics - Accel. and Beams*, **7**, 080702 (2004).
- [75] T. ShafTan et al., in *Proc. of PAC 2003, TPAG030, Portland, Oregon* (2003).
- [76] T. ShafTan et al., *Nucl. Instrum. Meth. Phys. Res., Sect. A*, **528** (2004) 397.
- [77] Z. Huang and K.-J. Kim, *Phys. Rev. Special Topics - Accel. and Beams*, **5**, 074401 (2002).
- [78] Z. Huang, M. Borland, P. Emma, J. Wu, C. Limborg, G. Stupakov, and J. Welch, *Phys. Rev. Special Topics - Accel. Beams*, **7**, 074401 (2004).
- [79] Ming Xie, *Nucl. Instrum. Meth. Phys. Res., Sect. A* **445**, (2000) 59.
- [80] L. H. Yu and S. Krinsky, *Nucl. Instrum. Meth. Phys. Res., Sect. A* **285**, (1989) 119.
- [81] P. Craievich, S. Di Mitri, M. Ferianis, M. Veronese, M. Petronio and D. Alesini, *Proc. of DIPAC 2007, TUPC10, Venice, Italy* (2007).
- [82] M. Borland, *APS LS-287* (2000).
- [83] L. Badano, private communications (2009).
- [84] P. Craievich et al., *Proc. of EPAC'08, TUPC080, Genoa, Italy* (2008).
- [85] S. Ferry, C. Bontoiu, P. Craievich, S. Di Mitri, and E. Karantzoulis, *Proc. of PAC'09, WE6RFP043, Vancouver, Canada* (2009).
- [86] P. Tenenbaum, P. Emma, L. Keller, Y. Nosochkov, T. O. Raubenheimer, and M. Woodley, *Report No. SLAC-PUB-8934* (2001).
- [87] F. Jackson, D. Angal-Kalinin, A. Latina, D. Schulte, R. J. Barlow, and A. Toader, *Proc. of PAC'07, THPMN073, Albuquerque, New Mexico* (2007).
- [88] H. Schlarb, *Proc. of EPAC'02, TUPRI054, Paris, France* (2002) 2706.
- [89] T. Kamps, *Proc. of FEL'04, TUPOS02, Trieste, Italy* (2004).
- [90] P. Emma, D. Dowell, C. Limborg, J. Schmerge, and J. Wu, *Proc. of EPAC'06, MOPCH048, Edinburgh, Scotland* (2006).
- [91] I. Agapov et al., *Phys. Rev. Special Topics - Accel. Beams* **12**, 081001 (2009).
- [92] R. Assmann et al., *Proc. of EPAC'06, TUODFI01, Edinburgh, Scotland* (2006).

- [93] M. Tomizawa, A. Molodzhentsev, and M. Shirakata, Proc. of PAC'07, TUPAN051, Albuquerque, New Mexico (2007).
- [94] A. I. Drozhdin et al., Proc. of PAC'07, TUPAS016, Albuquerque, New Mexico (2007).
- [95] L. C. Teng, Report No. FN-196/0400 (1969).
- [96] J. B. Jeanneret, SL/EA/Note Report No. 90-01 (1990).
- [97] LHC Study Group, CERN Report No. 91/-03 (1991) 115–125.
- [98] P. J. Bryant and E. Klein, CERN Report No. SL/92-40 (AP) (1992).
- [99] T. Trenkler and J. B. Jeanneret, Part. Accel. **50** (1995) 287.
- [100] J. B. Jeanneret, Phys. Rev. Special Topics - Accel. Beams **1**, 081001 (1998).
- [101] R. Assmann, J. B. Jeanneret, and D. Kaltchev, Proc. of EPAC'02, Paris, France (2002) 293.
- [102] I. Zagorodnov and T. Weil, TESLA Report No. 2003-23 (2003).
- [103] Y. Suetsugu, K. Shibata, A. Morishige, Y. Suzuki, and M. Tsuchiya, Phys. Rev. Special Topics - Accel. Beams **9**, 103501 (2006).
- [104] K. Bane, P. Emma, PAC'05, FPAT091, Knoxville, Tennessee (2005).
- [105] P. Emma, LCC-0021 (1999).
- [106] R. Wanzenberg, Proc. of LINAC'96, WE103, Geneva, Switzerland (1996).
- [107] P. Tenenbaum, SLAC-TN-04-038 (2004).
- [108] J. Seeman et al., SLAC-PUB-5705 (1992).
- [109] C. Adolphsen et al., Proc. of PAC'93, Washington DC, (1993) 0417.
- [110] R. W. Assmann et al., SLAC/AP-103 (1997).
- [111] P. Eliasson and D. Schulte, Phys. Rev. Special Topics - Accel. Beams, **11**, 011002 (2008).
- [112] C. Adolphsen et al., Proc. of PAC'95, WAB08, Dallas, Texas 1995).
- [113] R. W. Assmann et al., Proc. of LINAC'96, TUP54, Geneva, Switzerland (1996).
- [114] G. Guignard et al., Proc. of PAC'97, 8W015, Vancouver, Canada (1997).

- [115] N. Leros and D. Schulte, Proc. of PAC'01, TPPH014, Chicago, Illinois (2001).
- [116] G. Penn et al., ST/F-TN-06/01 (2006).
- [117] G. Guignard, CERN-SL/91-19 (AP) (1991).
- [118] G. Guignard and J. Hagel, Proc. of EPAC'96, WEP015G, Sitges, Barcelona, Espana (1996).
- [119] E. T. D'Amico et al., Proc. of PAC'01, RPAH082, Chicago, Illinois (2001.)
- [120] J. Resta-Lopez et al., Proc. of EPAC'08, MOPP027, Genoa, Italy (2008).
- [121] P. Craievich, S. Di Mitri, Proc. of FEL'05, THPP044, Paolo Alto, California (2005).
- [122] P. Craievich, S. Di Mitri, Proc. of EPAC'06, THPCH044, Edinburgh, Scotland (2006).
- [123] J. Delayen, Phys. Rev. Special Topics - Accel. and Beams, **6**, 084402 (2003).
- [124] J. Delayen, Phys. Rev. Special Topics - Accel. and Beams, **7**, 074402 (2004).
- [125] S. Di Mitri and A. A. Zholents, Proc. of EPAC'08, THPC010, Genoa, Italy (2008).
- [126] S. Di Mitri, ST/F-TN-07/06 (2007).
- [127] S. Heifets, G. Stupakov and S. Krinsky, Phys. Rev. Special Topics - Accel. Beams **5**, 064401 (2002).
- [128] R. Li, C. L. Bohn and J. J. Bisognano, Particle Accelerator Conference (1997) 1644.
- [129] P. Emma and R. Brinkmann, SLAC-PUB-7554 (1997).
- [130] D. Douglas, JLAB-TN-98-012 (1998).
- [131] J. Qiang, S. Lidia, R. D. Ryne and C. Limborg-Deprey, Phys. Rev. Special Topics - Accel. Beams, **9**, 044204 (2006).
- [132] M. Dohlus and T. Limberg in Proc. of the FEL Conf. 2004, M0C0S05, Trieste, Italy.
- [133] M. Huning, P. Piot, H. Schlarb, Nucl. Instrum. Meth. Phys. Res., Sect. A, **475** (2001) 348.

- [134] K. Tian et al., Phys. Rev. Special Topics - Accel. Beams, **9**, 014201 (2006).
- [135] M. Venturini et al., LBNL Report, Berkeley, LBNL-60513 (2006).
- [136] G. Dattoli and A. Renieri, Laser Handbook, Vol.4 (1985).
- [137] Ya.S. Derbenev, V. D. Shiltsev, FERMILAB-TM-1974, SLAC-PUB 7181 (1996).
- [138]] R. Li, Particle Accelerator Conference, New York, (1999) 118.
- [139] M. Borland, Phys. Rev. Special Topics - Accel. Beams, **11** 030701 (2008).
- [140] I. Pogorelov et al., in Proc. of ICAP'06, WEPPP02, Chamonix, France (2006).
- [141] M. Venturini et al., Phys. Rev. Special Topics - Accel. Beams, **10** 104401 (2007).
- [142] M. Venturini, R. Warnock and A. A. Zholents, Phys. Rev. Special Topics - Accel. Beams, **10** 054403 (2007).
- [143] M. Venturini, in Proc. of the Second Workshop on Microbunching Instability, LBNL, /<https://www.elettra.trieste.it/FERMI/> (2008).
- [144] S. B. van der Geer et al., /<http://www.pulsar.nl/gptS>.
- [145] S. Di Mitri et al., in Proc. of FEL Conf. 2010, THPB03, Malmo, Sweden.
- [146] A. Kabel, M. Dohlus and T. Limberg, in Proc. of EPAC'98, THP34G, Stockholm, Sweden (1998).
- [147] G. Penco et al., in Proc. of of IPAC 2010, TUOARA02, Tsukuba, Japan.
- [148] S. Di Mitri et al., in Proc. of FEL Conf. 2010, MOPA02, Malmo, Sweden.
- [149] The main authors of the mentioned MATLAB scripts are G. Penco, M. Trovo', S. Ferry and S. Krecic.
- [150] <http://www.mathworks.com/products/matlab>
- [151] L. N. Trefethen, Numerical and Linear Algebra, Philadelphia Society for Industrial and Applied Mathematics. ISBN 978-0-89871-361-9 (1997).
- [152] P. C. Hansen, The truncated SVD as a method for regularization, BIT 27, (1987) 534-553.

- [153] A. N. Tychonoff, Solution of incorrectly formulated problems and the regularization method, Doklady Akademij Nauk SSSR 151, (1963) 501–504. Translated in Soviet Mathematics 4, 1035–1038.
- [154] S. Bassanese, private communications (2010).
- [155] C. Scafuri, in Proc. of ICALEPCS 2009, Kobe, Japan.
- [156] S. Di Mitri, G. Penco, C. Scafuri, in Proc. of IPAC 2010, TUPE019, Tsukuba, Japan.
- [157] FLASH Free Electron Laser, <http://flash.desy.de/>
- [158] W. Fawley, G. Penn, ST/F-TN-06/07 (2006).
- [159] P. Emma and A. C. Kabel, EPAC'04, MOPKF081, Lucerne, Switzerland.

Summary

In classical electromagnetism, a charged particle radiates energy in the form of electromagnetic radiation when it is subject to a force. This effect is the principle behind many useful sources of radiation such as electron synchrotrons and linear accelerators. The main figures of merit of synchrotron radiation sources are (narrow) spectral bandwidth, photon wavelength tunability and brilliance. The periodic motion of particles in a synchrotron makes these machines well-suited for a stable emission at high repetition rate. However, in addition to the synchrotron radiation and complementary to that, a strong need has emerged over the last few years for a source of radiation with extremely high brilliance, close to full coherence, a bandwidth approaching the Fourier limit and a stable and well characterized temporal structure in the femtosecond time domain. Such a source is the single-pass Free Electron Laser (FEL) that, due to Doppler frequency up-shifting of emitted radiation by relativistic electrons, is particularly well-suited to generate short wavelength X-ray pulses with peak brilliance many orders of magnitude higher than that generated in modern synchrotrons and with sub-picosecond pulse lengths. There are currently no alternative sources that have such high pulse energies and short durations. The investigation domain opened by the new FEL sources covers essentially all basic science fields giving access to explorations of matter in practically unexplored regimes. The scientific opportunities will in fact impact studies of a large number of disciplines encompassing material and biomaterial science, nanoscience, plasma physics, molecular and cluster femto- and nano- physics and chemistry, as well as having various connections to life, environmental, astrophysical and earth science.

The FEL high brilliance, high intensity and shot-to-shot stability strongly depends on the electron beam source. Delivering a high quality electron beam and machine flexibility to serve a broad range of potential applications imposes severe requirements on the final electron beam parameters and the machine design. To meet these requirements, the need of a linac design based on extensive studies of possible perturbations that may affect the electron beam dynamics, of means to correct them and of parameter optimization has emerged. In this sense,

the realization of a valid machine design is a fundamental and critical step for the success of a FEL project. Because of the special sensitivity of the FEL generation to the electron beam emittance, relative energy spread and trajectory control [15, 16], this Thesis has focused on the design strategies to control these parameters. Some aspects of the machine study have been developed for the specific FEL scheme known as harmonic generation. In fact, we can identify two general ways to generate X-rays with a FEL. The Self Amplified Spontaneous Emission (SASE) [22–25] relies on the interaction of electrons and photons that are emitted by the electron beam itself. Since the electron bunching starts to grow from the natural noise of the initial electron distribution, the SASE output radiation is relatively poor in longitudinal coherence. In the High Gain Harmonic Generation (HG) scheme [5–9, 26, 27], instead, the initial energy modulation is driven by an external seed laser. It is then transformed into density bunching in a dispersive section inserted in the undulator chain. In this case, the output FEL properties reflect the high longitudinal coherence of the seed laser. The machine design of a single-pass linac-based FEL and the related electron beam dynamics has been presented in this Thesis. The specific case of a HG FEL has been treated. Then, the general principles have been applied, for a quantitative analysis, to the FERMI@Elettra FEL case study. Some experimental results of the recent FERMI commissioning have been discussed and compared with the model predictions.

The FERMI@Elettra single-pass linac-based FEL at the Elettra Laboratory of Sincrotrone Trieste [28, 29] is one of the FEL based European projects, designed to become the international user facility in Italy for scientific investigations with ultra high brilliance X-ray pulses of ultra-fast and ultra-high resolution processes in material science and physical biosciences. With a peak brightness of about 6 orders of magnitude greater than third generation sources, full transverse coherence, (close to) transform limited bandwidth, pulse lengths of the order of a picosecond or less, variable polarization and energy tunability, the FERMI source is a powerful tool for scientific exploration in a wide spectrum of disciplines. The coherence properties will open up new perspectives for single shot imaging, allowing to study the dynamics of chemical reactions and other phenomena through single pulse coherent diffraction imaging with a spatial resolution in the nanometer domain. The high peak power will allow studying nonlinear multi-photon processes in a regime never explored before, dilute samples that are of paramount importance in atmospheric, astrophysical and environmental physics as well as in the characterization of nano-size materials. The short pulse duration will open the door to visualizing ultra-fast intra-atomic and electronic dynamics. So, the ultra-bright, ultra-short pulses will allow single photon pulse experiments to collect images at time scales faster than radiation damage. This in turn will open the possibility of studying the morphol-

ogy and the structure of bio-systems unstable under X-ray radiation exposure. Last but not least, the choice of harmonic generation by an external seed laser is dictated by the scientific applications and the flexibility that such choice entails. As the seed laser determines the duration, bandwidth, and wavelength of the output radiation, all are tunable and controllable, covering a wide spectral range. The seed laser furthermore provides a reference signal throughout the FERMI facility (including the experimental beamlines) to facilitate the femtosecond level precision timing and synchronization of all systems. The seeded FEL driven by an external laser is therefore particularly suitable for pump-probe synchronization at time scales well below one picosecond. The choice of design parameters allows FERMI to generate FEL radiation with a wide range of characteristics tailored to match a diversity of experimental requirements, ranging from single shot, short (≤ 50 fs), high brilliance, time-resolved experiments to ultra-fast pump-probe experiments, to high resolution experiments with close to transform-limited radiation on the 10's fs time scale.

This thesis starts from the assumption that a high brightness electron beam is generated in a photo-injector at energies lower than 100 MeV. The primary goal of the machine design is that of preserving the 6-D electron beam emittance as at the injector level. The emittance is a measure of the phase space domain occupied by the beam. The transverse emittance has to be small enough to allow the production of a spatially coherent photon beam at the desired wavelength. The longitudinal emittance or more precisely the energy spread, for a given electron bunch duration, has to be small enough to permit the saturation of the FEL intensity within a reasonable undulator length. A small energy spread also ensures a small bandwidth of the output photon pulse and a high harmonic content. Typical electron beam parameters of the fourth generation – very high brightness – linac-based FELs (from infrared to X-rays spectral range) are listed in the following and the FERMI@Elettra nominal parameters are put in parenthesis: 0.2–1 nC charge (0.8 nC), 1–3 mm mrad normalized emittance (1.5 mm mrad), 0.5–3 kA peak current (0.8 kA), 0.05–0.1 % relative energy spread (0.1%) and 1–50 GeV final electron energy (1.5 GeV). In contrast to linear colliders, where particle collisions effectively integrate over the entire bunch length, the X-ray FEL concerns only very short fractions of the electron bunch length. The integration length is given by the FEL slippage length that is the electron-to-photon longitudinal slippage over the length of undulator, prior to FEL power saturation. The slippage length is typically in the range 1–30 μm , a small fraction of the total bunch length.

The original contributions of this Thesis are structured as follows. Chapter 2 is an introduction to the FERMI@Elettra layout based on the FERMI Technical Design Study. Apart from little manipulations of some formulas, Chapter 3 introduces for the Reader's convenience well-established theoretical tools which

are used in the the following Chapters to describe the electron beam dynamics and the 6-D emittance degradation. The validity of the theoretical models for the FERMI case study is discussed. Chapter 4 deals with the machine design from the point of view of the single particle dynamics, including the specification of the magnetic field tolerances and alignment, the optics design of diagnostic and production lattice and geometric collimation. Chapter 5 describes the impact of collective effects on the electron beam dynamics such as wake fields, space charge forces and emission of coherent synchrotron radiation. Chapter 6 is focused on the determination of the machine working point in terms of bunch length compression factor and final electron beam parameters. Finally, Chapter 7 reports about the FERMI@Elettra commissioning results that are highly relevant for a comparison with the theoretical and simulation studies carried out in the previous Chapters.

In Chapter 2, the main parameters and layout of the FERMI@Elettra single-pass FEL have been introduced. Due to the relatively low energy of the electron beam, ranging from 0.9 GeV to 1.5 GeV, the harmonic up-shifting of an initial seed signal is an obliged choice for FERMI in order to reach the FEL fundamental emission at wavelengths as short as 4 nm. However, the seeding interaction puts a tight constraint on the maximum slice energy spread of the electron beam at the undulator entrance that is approximately 150 keV (rms value), only a factor of 5 bigger than the minimum theoretical uncorrelated energy spread expected after bunch length compression. Peak power saturation at the fundamental wavelength is ensured by the several hundred's Ampere electron beam with a normalized slice emittance equal or smaller than 1 mm mrad. The S-band, normal conducting Elettra linac has been upgraded with other 7 accelerating structures from CERN. Only the Elettra structures should be able to provide the remarkable accelerating gradient of 25 MV/m, instead of 15 MV/m in the others, by virtue of the SLED system for RF pulse length compression. Unfortunately, the BTW structures have irises with inner radius of only 5 mm, instead of the 9 mm in the TW structures. Such a small radius excites strong longitudinal and transverse wake fields that have to be carefully considered in the machine design and study of the electron beam dynamics. A movable, achromatic, four dipoles magnetic chicane has been designed to manage the magnetic bunch length compression. Two of these chicanes, BC1 and BC2, are integrated in the linac magnetic lattice. A 30 m long transfer line brings the high energy electron beam to the parallel undulator lines of FEL1 and FEL2. The electron beam is finally dumped in the horizontal plane, while the emitted photons are transmitted to the downstream photon beam lines for experiments.

Chapter 3 contains the theoretical tools for describing the single particle and electron beam collective motion in a single-pass linac; their applicability to the FERMI case study has been discussed. Liouville's theorem illustrates the pri-

mary goal of 6-D electron beam emittance preservation as at the injector level. The high beam quality that is required from the FEL process is expressed in terms of the Liouville transverse emittance and energy spread. In reality, the applicability of Liouville's theorem to the beam transport and bunch length compression in a linac-based FEL is invalidated by several single particle and collective frictional forces. These degrade time-projected or local (in the z -coordinate) beam parameters. To investigate such different effects, the concept of projected and slice emittance has been introduced for the transverse motion. The definition of correlated, uncorrelated and slice energy spread has been given for the longitudinal motion. The rms emittance has also been introduced as a statistical measure of the particle spread in the phase space. In fact, most of the measurements of the electron beam parameters deal with that, not with the Liouville one. Unfortunately, unlike the latter, the former is diluted by chromatic filamentation. Because of the relatively high energy spread required for the magnetic bunch length compression, chromatic filamentation might develop in the presence of beam optics mismatch or magnetic field errors. Nevertheless, the beam matrix formalism allows one to determine the design tolerances in terms of mismatch parameter, magnet alignment and field quality to avoid an emittance dilution beyond the specifications. As for the longitudinal dynamics, the theory of magnetic bunch length compression has been expanded up to the second order in the particle coordinates. It has been shown how the second order energy chirp and path length-to-energy correlation term limit the compression efficiency and, therefore, the minimum bunch length achievable with a magnetic chicane. A higher harmonic RF cavity has therefore been introduced in order to cancel out the second order terms in the longitudinal particle motion.

The analytical treatment of the most important collective effects has also been given. The interaction of the electron beam with the image charge field in the accelerating structures has been described in terms of the longitudinal and transverse wake potential. The beam dynamics in the presence of the electromagnetic self-field has been investigated through the laminarity parameter. This could be used to identify the linac regions in which short range space charge forces corrupt the quasi-laminar particle motion due to very high charge density. This is expected to happen, for example, during the bunch length compression, even at high energy. The space charge forces are then modeled with a longitudinal wake function that induces an energy modulation at wavelength much shorter than the bunch length. It is transformed into density modulation in the chicanes' dispersive region, thus enhancing the emission of coherent synchrotron radiation that, in turn, amplifies the initial energy modulation. This self-amplifying process is called the microbunching instability and degrades both the energy and the particle density distribution. Formulas for the computation of the linear gain, in the one- and two-stage compression scheme have been given. A very

similar process is at the basis of the FEL instability. The 1-D modeling of the FEL generation has been sketched and the requirements on the electron beam quality have been deduced from the basic formulas, essentially for the peak current, transverse emittance and relative energy spread.

The analytical evaluation of the effect of the magnetic field errors, magnet misalignments and chromatic aberrations in the presence of linear and non-linear fields on the transverse beam dynamics in the FERMI@Elettra linac has been presented. Using the beam matrix formalism and theory of field expansion introduced in Section 3.2, the specifications for the magnets field quality and alignment have been given in order to limit the emittance dilution to 1% for each individual error source. Then, in the assumption of linear optics transport, the design of a dispersion-free, straight diagnostic line and of a dispersive diagnostic line has been presented. With particular attention to the FERMI@Elettra lattice, the BC1 region for electron beam diagnostic and transport has been discussed. The optics requirements coming from the beam diagnostic performance have been integrated in the optics design. So, the intrinsic resolution of the mean energy and energy spread measurement has been evaluated. The possibility of measuring the correlated, uncorrelated and slice energy spread at all the dispersive lines of the FERMI@Elettra lattice has been investigated. The measurement of several beam parameters has been simulated with particle tracking. Finally, a two-stage station for beam geometric collimation, integrated into the straight diagnostic line, has been discussed. The collimation efficiency has been analytically defined and the theoretical prediction for the BC1 case study agrees well with the result of particle tracking.

Analytical evaluations and simulations with particle tracking of electron beam collective effects in a single-pass, S-band linac have been carried out. A quantitative study for the FERMI@Elettra electron beam delivery system from the injector end to the undulator, including the magnetic bunch length compression has been done. The effect of the structural longitudinal and transverse wake field on the electron beam energy distribution and projected emittance, respectively, has been studied. Shaping of the initial current profile has been proposed to alter the longitudinal wake potential and make it almost linear. In this way, the longitudinal wake field can be used to cancel out the linear energy chirp required for magnetic compression; moreover, nonlinear contributions to the energy chirp are minimized. It has been proposed to suppress the head-tail instability induced by the transverse wake with trajectory manipulation along the linac (emittance bumps). Then, a trajectory jitter study has been done in order to specify the magnet alignment and vibration tolerances that do not affect this correction scheme. Finally, the CSR effect on the transverse emittance and the microbunching instability linear gain has been computed and compared with particle tracking results. The optics design allows the compensation of the CSR

effect by means of a suitable optics arrangement in the magnetic chicanes and in the Spreader. As for the microbunching instability, it enters into the nonlinear regime when a two-stage compression is adopted. This study therefore justifies the implementation of a laser heater to Landau damp the instability and to keep the slice energy spread within the FEL specifications.

Some guidelines for the design of the magnetic compressor scheme have been given, according to the requirements based on the FEL performance goal. The principles depicted in this Chapter refer to the specific case of a seeded X-ray FEL and only magnetic compression of the bunch length has been considered. The design parameters for the FERMI magnetic compressors have been made explicit as a case study of the previous theory. After that, the effect of the magnetic bunch length compression on the microbunching instability development in a linac-based FEL has been investigated. In particular, the reduction of the instability gain by particle longitudinal phase mixing has been demonstrated analytically. It has been shown that the efficiency in removing the beam microbunching is much more sensitive to the initial modulation wavelength than to the amplitude. The natural consequence of this dynamics is the adoption of a single stage of compression. The feasibility of this scheme has been demonstrated by means of 3-D particle tracking for the FERMI@Elettra FEL, with promising results for the preservation of the beam quality. In addition to this, a different promising configuration shows up. If the linear energy chirp at the exit of BC1 could be removed by dedicated accelerating structures, then particle longitudinal crossover is enhanced in BC2. The effect is optimized by two chicanes, BC1 and BC2, with the same sign of R_{56} . As a result, the energy modulation is damped, together with the associated current spikes. The FERMI@Elettra case study has been analyzed in some details. The 1-D beam transport has been verified against the 3-D particle tracking performed with *elegant*, including collective effects, for a compression factor of 10 in BC1. The study shows that this alternative scheme of compression is successful and even more efficient than the single compression for initial modulations whose wavelength is of the order of tens of μm . It may even be applicable to longer wavelengths and/or higher compression factors, although these more extreme situations need to be confirmed by further investigations.

We have reported about the commissioning of the FERMI@Elettra electron beam delivery system. Methods and experimental results concerning the control of the longitudinal (acceleration, energy distribution, bunch length compression and microbunching instability) and transverse (optics matching, transport and trajectory control) electron beam dynamics in FERMI have been shown. The longitudinal phase space of the electron beam has been characterized at the beginning of the FERMI commissioning with a simple spectrometer line. Optics has revealed to be an important ingredient for the characterization of the electron

beam energy distribution since it optimizes the resolution of the energy measurement. Starting from experimental Twiss parameters of the electron beam, the optics matching and transport through the whole line has been performed with the `elegant` code, which includes the description of the real accelerating gradients and the RF edge focusing of the structures. The mismatch parameter usually describes a projected emittance growth smaller than 1% in both planes. `elegant` has also been used to generate trajectory theoretical response matrices to correct the real beam trajectory in the linac and in the high energy transfer line. The matrices are imported in a trajectory feedback tool. This is also able to measure experimental response matrices. The theoretical and the experimental ones can be merged for a global trajectory correction along the whole line. The BPMs integrated into the feedback tool read the beam position at the frequency of 10 Hz and their reading is by the corrector magnets forced to the value determined by the user. In this way, the feedback works as a trajectory correction tool as well. It has been verified that the magnetic chicane BC1 does affect neither the trajectory nor the dispersion in the succeeding lattice. The dispersion bump in the chicane has been measured and agrees well with the theoretical expectation. An important horizontal emittance growth appears during the magnetic bunch length compression, especially for compression factors larger than 3. Off-line simulation studies indicate that CSR might be the main responsible of this emittance degradation, especially in the presence of nonlinear compression (the X-band cavity to linearize the longitudinal phase space during compression has not been installed yet) and potential slice optics mismatch. Some evidence of the microbunching instability has been detected for compression factors larger than 3. They are COTR emission downstream of BC1 and an energy modulation of the compressed electron beam. At the end, a comparison of the theoretical expectation and measured values for many electron beam parameters has been produced and summarized in Table 7.2. The transverse beam dynamics suffers of a normalized emittance degradation during compression in BC1, as mentioned before, and of a further growth due to the transverse wake field effect in the last part of the linac, as predicted by the model. On the other hand, the beam optics seems to be pretty well under control since the mismatch parameter is usually very close to 1. The particle energy distribution is manipulated according to the model along the entire linac. An energy jitter beyond the specification has been measured at the entrance of BC1 and this could be related to the trajectory jitter also observed in a range larger than the specification. So, further investigations are needed to accomplish a full understanding of the physics developing in BC1. Nevertheless, the electron beam quality has revealed to be more than sufficient to generate the first coherent harmonic generation in seeded configuration at 43 nm (FEL fundamental output) in December 2010, after one year (calendar time) of machine commissioning.

Samenvatting

In de klassieke elektromagnetisme, een geladen deeltje straalt energie in de vorm van elektromagnetische straling wanneer het versnelt. Dit effect is het principe achter veel nuttige bronnen van straling, zoals elektronen synchrotrons en lineaire versnellers. De belangrijkste cijfers van verdienste van synchrotron straling bronnen zijn (smalle) spectrale bandbreedte, foton golflengte tunability en schittering. De periodieke beweging van deeltjes in een synchrotron maakt deze machines zeer geschikt voor een stabiele emissie bij hoge herhalingsfrequentie. Echter, in aanvulling op de synchrotron straling en complementair zijn aan dat, heeft een sterke behoefte ontstaan afgelopen jaren voor een bron van straling met extreem hoge schittering, dicht bij volledige samenhang, een bandbreedte het naderen van de Fourier te beperken en met een stabiel en goed gekarakteriseerde temporele structuur in de femtoseconde tijdsdomein. Een dergelijke bron is de single-pass Free Electron Laser (FEL), dat als gevolg van een Doppler frequentie omhoog-shifting van de uitgezonden straling door relativistische elektronen, is bijzonder goed geschikt voor het genereren korte golflengte X-stralen, lichtpulsen met piek schittering veel ordes van grootte hoger dan die welke in de moderne synchrotrons en met sub-picoseconde pulslengten. Er zijn momenteel geen alternatieve bronnen die zulke hoge puls hebben energie en korte looptijden. Het onderzoek domein geopend door de nieuwe FEL bronnen dekt nagenoeg alle fundamentele wetenschapsgebieden die toegang geven tot verkenningen van de materie in vrijwel onontgonnen regimes. De wetenschappelijke mogelijkheden zal in feite impact studies van een groot aantal disciplines, variërend van materialen en biomaterialen wetenschappen, nanowetenschappen, plasmafysica, moleculaire en cluster Femto- en nano-fysica en chemie, alsmede als met verschillende aansluitingen op het leven, het milieu, astrofysische en aardwetenschappen.

De FEL hoge schittering, hoge intensiteit en shot-to-shot stabiliteit hangt sterk af van de elektronenbundel bron. Bereiken van een hoog elektronenbundel kwaliteit en flexibiliteit machine te dienen een breed scala aan mogelijke toepassingen stelt strenge eisen aan de elektronenbundel definitieve parameters

en het ontwerpen van machines. Om te voldoen aan deze eisen, de noodzaak van een Linac ontwerp, gebaseerd op uitgebreide onderzoeken van mogelijke verstoringen die de elektronenbundel van invloed kunnen zijn dynamiek, van de middelen om te corrigeren en optimalisatie van de parameters is ontstaan. In deze zin, de realisatie van een geldig machine ontwerp is een fundamentele en kritische stap voor het succes van een FEL project. Vanwege de bijzondere gevoeligheid van de FEL generatie op de elektronenbundel emittance, relatieve energie te verspreiden en traject controle [15, 16], is dit proefschrift gericht op het ontwerp van strategieën om deze parameters te controleren. Sommige aspecten van de machine studie zijn ontwikkeld voor de specifieke regeling FEL bekend als harmonische generatie. In feite kunnen identificeren we twee algemene manieren om X-ray met een FEL te genereren. Het Zelf Amplified spontane emissie (SASE) [22 tot 25] beroept zich op de interactie van elektronen en fotonen die worden uitgezonden door de elektronenbundel zelf. Aangezien het elektron bunching begint te groeien van de natuurlijke geluid van de oorspronkelijke elektronen verdeling, de SASE output straling is relatief arm in de lengterichting samenhang. In de High Gain harmonische generatie (HGHG regeling) [5 - 9, 26, 27], in plaats daarvan is de eerste energie-modulatie gedreven door een externe zaad laser. Het wordt dan omgezet in dichtheid opeenhoping in een dispersieve passage ingevoegd in de undulator keten. In dit geval, de output FEL eigenschappen weerspiegelen de hoge longitudinale samenhang van het zaad laser. De machine ontwerp van een single-pass Linac gebaseerde FEL en de daarmee samenhangende elektronenbundel dynamiek is gepresenteerd in dit proefschrift. Het specifieke geval van een HGHG FEL is behandeld. Vervolgens hebben de algemene beginselen zijn toegepast, voor een kwantitatieve analyse, de Fermi@Elettra FEL case study. Sommige experimentele resultaten van de recente ingebruikname FERMI zijn besproken en vergeleken met de modelvoorspellingen.

De Fermi@Elettra single-Linac gebaseerde FEL over op het Elettra Laboratorium voor Sincrotrone Trieste [28, 29] is een van de FEL gebaseerde Europese projecten, ontworpen te worden van de internationale gebruikersfaciliteit in Italië voor wetenschappelijk onderzoek, met ultra hoge glans X-ray peulvruchten, van ultra-snelle en ultra-hoge resolutie processen in materiaalkunde en fysieke biowetenschappen. Met een maximale helderheid van ongeveer 6 ordes van grootte hoger dan de derde generatie bronnen, vol dwarse samenhang, (nabij) te transformeren beperkte bandbreedte, pulslengten van de orde van een picoseconde of minder, variabele polarisatie en energie tunability, de Fermi bron is een krachtig hulpmiddel voor wetenschappelijk onderzoek in een breed spectrum van disciplines. De samenhang eigenschappen opent nieuwe perspectieven voor single shot beeldvorming, waardoor de studie van de dynamica van chemische reacties en andere fenomenen door middel van enkele puls samen-

hangende diffractie beeldvorming met een ruimtelijke resolutie in de nanometer-domein of materie onder extreme omstandigheden thermodynamische (warm en dichte materie fasen). De hoge piekvermogen zal het bestuderen van niet-lineaire Multi-foton processen in een regime nooit onderzocht alvorens Verdun monsters van het allergrootste belang zijn in de atmosfeer, astrofysische en milieu natuurkunde als in de karakterisering van nano-afmetingen materialen. De korte pulsduur opent de deur naar het visualiseren van ultra-snelle intratomaire en elektronische dynamiek. Dus zal de ultra-bright, ultra-korte pulsen kunnen enkel foton impuls experimenten om beelden op tijdschalen verzamelen sneller dan stralings schade. Dit zal op zijn beurt de mogelijkheid open om het bestuderen van de morfologie en de structuur van de bio-systemen onstabiel onder X-ray blootstelling aan straling. Last but not least, is de keuze van de harmonische generatie door een externe zaad laser gedictieerd door de wetenschappelijke toepassingen en de flexibiliteit dat dergelijke keuze met zich meebrengt. Als het zaad laser bepaalt de duur, de bandbreedte, en de golflengte van de output straling, zijn allemaal instelbaar en controleerbaar, die een breed spectrum. Het zaad laser geeft bovendien een referentie signaal gedurende de Fermi-faciliteit (met inbegrip van de experimentele bundellijnen) aan de femtoseconde niveau precisie timing en synchronisatie van te vergemakkelijken alle systemen. De geplaatste FEL aangedreven door een externe laser is daarom bijzonder geschikt voor pump-probe synchronisatie op tijdschalen en minder dan een picoseconde. De keuze van het ontwerp parameters kunt FERMI om FEL straling te genereren met een breed scala van kenmerken afgestemd op een diversiteit aan experimentele wensen, variërend van een opname, korte (≤ 50 dollar fs), hoge helderheid, tijd-opgeloste experimenten om ultrasnelle pump-probe experimenten, om hoge Resolutie van experimenten met bijna beperkte straling te transformeren op de 10s fs tijdsschaal.

Dit proefschrift is gebaseerd op de realistische veronderstelling dat een hoge helderheid elektronenbundel wordt gegenereerd in een foto-injector bij energieën van minder dan 100 MeV. Het primaire doel van de machine ontwerp is dat van de 6-D elektronenbundel emittance als bij de injector niveau behouden. De emittance is een maat voor de faseruimte domein bezet door de balk. De dwarse emittance moet klein genoeg zijn om de productie van een ruimtelijk samenhangende fotonenstralen mogelijk op de gewenste golflengte. De longitudinale emittance of meer precies de energie te verspreiden, voor een bepaalde elektron stelletje duur, moet klein genoeg zijn om de verzadiging van de FEL-intensiteit binnen een redelijke undulator lengte. Een kleine energie spreiding zorgt er ook voor een kleine bandbreedte van de output foton impuls en een hoge harmonische inhoud. Typische elektronenbundel parameters van de vierde generatie - zeer hoge helderheid - Linac-based FELs (van infrarood tot en met X-stralen spectrale bereik) zijn opgenomen in het volgende en de Fermi@Elettra nominale

parameters worden gebracht tussen haakjes: 0.2 tot 1 nC heffing (0.8 nC), 1–3 mm mrad genormaliseerd emittance (1.5 mm mrad), 0,5–3 kA piek stroom (0.8 kA), 0,05 tot 0.1% relatieve energie verspreid (0.1%) en 1 tot 50 GeV definitieve elektronpiekenergie (1.5 GeV). In tegenstelling tot lineaire colliders, waar deeltjesbotsingen effectief te integreren over de gehele lengte van bos, de X-ray FEL heeft alleen betrekking op zeer korte fracties van het elektron stelletje lengte. De integratie lengte is gegeven door de FEL ontsporing lengte die het elektron-to-foton longitudinale slippen over de lengte van undulator, voorafgaand aan de macht FEL verzaadiging. De ontsporing lengte is typisch in het bereik 1–30 μ m, een kleine fractie van het totale bos lengte.

De originele bijdragen van deze thesis zijn als volgt opgebouwd. Hoofdstuk 2 is een inleiding tot de Fermi@Elettra indeling op basis van de Fermi Technisch Ontwerp studie. Afgezien van kleine manipulaties van sommige formules, hoofdstuk 3 introduceert voor het gemak van de Reader's gevestigde theoretische gereedschappen die worden gebruikt in de de volgende hoofdstukken aan de elektronenbundel dynamiek en de 6-D emittance degradatie te beschrijven. De geldigheid van de theoretische modellen voor de Fermi casus wordt besproken. Hoofdstuk 4 gaat met de ontwerpen van machines uit het oogpunt van de interne dynamiek deeltje, met inbegrip van de specificatie van het magnetisch veld toleranties en afstemming, de optiek ontwerp van diagnostische en productie rooster en geometrische collimatie. Hoofdstuk 5 beschrijft het effect van collectieve effecten op de elektronenbundel dynamiek zoals wakker velden, ruimte heffing krachten en de emissie van coherente synchrotronstraling. Hoofdstuk 6 is gericht op de bepaling van de machine te werken punt, in termen van de tros lengte compressie factor en de uiteindelijke elektronenbundel parameters. Tot slot, hoofdstuk 7 rapporten over de Fermi @ Elettra inbedrijfstelling resultaten die meer relevant zijn voor een vergelijking met de theoretische en simulatie studies die zijn uitgevoerd in de voorgaande hoofdstukken.

In hoofdstuk 2 worden de belangrijkste parameters en lay-out van de Fermi@Elettra single-pass FEL zijn ingevoerd. Vanwege de relatief lage energie van de elektronenbundel, variërend van 0.9 tot 1.5 GeV, de harmonische up-verschuiving van een eerste zaad-sigitaal is een verplicht keuze voor FERMI om de fundamentele FEL-emissie te bereiken bij een golflengte zo kort 4 nm . Maar, het seeden en interactie legt een strakke beperking van de maximale slice-energie verspreiding van de elektronenbundel op het undulator entree is ongeveer 150 keV (RMS waarde), een factor 5 alleen groter dan de minimale theoretische ongecorrigeerde energie verspreid verwacht na stelletje lengte compressie. Piekvermogen verzaadiging op de fundamentele golflengte wordt verzekerd door het enkele honderden's Ampere elektronenbundel met een genormaliseerde slice emittance gelijk aan of kleiner dan 1 mm mrad. De S-band, heeft een normale

uitvoering van Elettra Linac is opgewaardeerd met 7 andere versnelling structuren van het CERN. Alleen de Elettra structuren moeten in staat zijn om de opmerkelijke versnelling gradiënt van 25 MV/m bieden, in plaats van 15 MV / m in de anderen, op grond van de SLED systeem voor de RF-puls lengte compressie. Helaas is de BTW structuren irissen met inwendige straal van slechts 5 mm, in plaats van de 9 mm in de TW structuren. Zoals een kleine straal Excite sterke lengte-en dwarsrichting wakker velden die moeten zorgvuldig worden overwogen in de machine ontwerp en de studie van de elektronenbundel dynamiek. Een beweegbare, achromatische, vier dipolen magnetische chicane is ontworpen om het bos te beheren lengte magnetische compressie. Twee van deze chicane, BC1 en BC2, zijn geïntegreerd in de Linac magnetische rooster. Een 30 m lange transfer lijn brengt de hoge energie elektronen straal voor de parallelle lijnen van undulator FEL1 en FEL2. De elektronenbundel is eindelijk gedumpt in het horizontale vlak, terwijl de uitgezonden fotonen worden doorgegeven aan de downstream-fotonenstralen lijnen voor experimenten.

Hoofdstuk 3 bevat de theoretische hulpmiddelen voor het beschrijven van de afzonderlijke deeltjes en de elektronenbundel collectieve beweging in een single-pass Linac; hun toepasbaarheid op de Fermi case studie werd besproken. De stelling van Liouville illustreert het primaire doel van de 6-D elektronenbundel emittance bewaring als bij de injector niveau. De hoge kwaliteit van de straal die wordt vereist van de FEL-proces wordt uitgedrukt in termen van dwars emittance de Liouville en energie te verspreiden. In werkelijkheid, de toepasbaarheid van de stelling van de Liouville om de balk vervoer en stel de lengte compressie in een Linac gebaseerde FEL is ontkracht door meerdere afzonderlijke deeltjes en collectieve wrijvingskrachten. Deze degraderen tijd geprojecteerd of lokaal (in de z-coördinaat) bundel parameters. Om te onderzoeken zulke verschillende effecten, is het concept van de geraamde en snijd emittance ingevoerd voor de transversale beweging. De definitie van gecorreleerde, ongecorrleerd en slice-energie verdeeld is gegeven voor de longitudinale beweging. De rms emittance is ook ingevoerd als een statistische maat van het deeltje zich in de fase ruimte. In feite zijn de meeste van de metingen van de elektronenbundel parameters mee omgaan, niet met de Liouville een. Helaas, in tegenstelling tot de laatste, is de voormalige verdund door chromatische filamentatie. Vanwege de relatief hoge energie verspreid vereist van de tros lengte magnetische compressie, kan de chromatische filamentatie te ontwikkelen in de aanwezigheid van de balk optica mismatch of magnetisch veld fouten. Niettemin is de bundel matrix formalisme maakt het mogelijk om de ontwerptoleranties in termen van mismatch parameter, de magneet van de aanpassing en in het veld bepalen van de kwaliteit van een emittance verwatering van het bestek te vermijden. Als voor de longitudinale dynamiek, heeft de theorie van de tros lengte magnetische compressie is uitgebreid tot in de tweede orde in het

deeltje coördinaten. Het is aangetoond hoe de tweede orde energie tijlpen en weglengte-to-energy correlatie termijn beperken de compressie-efficiëntie, en dus de minimale lengte stelletje haalbaar met een magnetische chicane. Het effect van een hogere harmonische RF holte in de lengterichting deeltje is daarom ingevoerd om te annuleren van de tweede orde termen.

De analytische behandeling van de meest belangrijke collectieve gevolgen heeft ook gekregen. De interactie van de elektronenbundel met het beeld heffing veld in de versnelling van structuren is beschreven in termen van lengten en dwarsrichting wakker potentieel. De balk dynamiek in de aanwezigheid van elektromagnetische self-gebied is onderzocht door de laminarity parameter. Dit kan gebruikt worden om de Linac regio's te identificeren waar korte afstand ruimtelading krachten corrupte de quasi-laminaire deeltje beweging op grond van zeer hoge ladingsdichtheid. Verwacht wordt dat dit te gebeuren, bijvoorbeeld tijdens het peloton lengte compressie, zelfs bij hoge energie. De ruimte heffing krachten worden vervolgens gemodelleerd met een longitudinale wakker functie die een energie-modulatie induceert bij golflengte veel korter dan de tros lengte. Het wordt omgezet in de dichtheid modulatie in de chicanes 'dispersieve regio, zodat de verbetering van de emissie van coherente synchrotronstraling die op hun beurt, versterkt het aanvankelijke energieniveau modulatie. Deze zelf-versterkende proces heet microbunching instabiliteit en degradeert zowel de energie en de dichtheid deeltjesverdeling. Formules voor de berekening van de lineaire versterking, in de een-en twee-traps compressie regeling hebben gekregen. Een zeer gelijkaardig proces aan de basis ligt van de FEL instabiliteit. De 1-D modellering van de FEL generatie is geschetst en de eisen aan de elektronenbundel kwaliteit zijn afgeleid uit de basisformules, voornamelijk over de piekstrom, dwars emittance en relatieve energie te verspreiden.

De analytische evaluaties van het effect van het magnetisch veld fouten, magneet onjuiste en chromatische aberraties in de aanwezigheid van lineaire en niet-lineaire velden op de dwarsbalk dynamiek in de Fermi@Elettra Linac is gepresenteerd. Op grond van de balk matrix formalisme en de theorie van het veld expansie geïntroduceerd in sectie ??, de specificaties voor de magneten gebied kwaliteit en afstemming hebben gekregen om de emittance verwatering te beperken tot 1% voor elke individuele fout bron. Dan, in de veronderstelling van lineaire optica vervoer, heeft het ontwerp van een dispersie-vrij, rechte lijn en diagnostische van een dispersieve diagnostische lijn gepresenteerd. Met bijzondere aandacht voor de Fermi @ Elettra rooster, de BC1 regio voor elektronenbundel diagnostische en de productie werd besproken. De optiek eisen uit de bundel diagnostische prestaties zijn geïntegreerd in de optiek ontwerp. Ja, heeft de intrinsieke resolutie van de gemiddelde energie en energie-spread meet geïntegreerd. De mogelijkheid van het meten van de correlatie, ongecorrleerd

en slice energie verspreid op alle lijnen van de dispersieve de Fermi @ Elettra rooster is onderzocht. De meting van de verschillende parameters bundel is gesimuleerd met particle tracking. Ten slotte, heeft een twee-traps station voor bundel geometrische collimatie, geïntegreerd in de rechte lijn diagnostische, zijn besproken. De collimatie-efficiëntie is analytisch gedefinieerd en de theoretische voorspelling voor de BC1 case study komt goed overeen met het resultaat van particle tracking.

Analytische evaluaties en simulaties met particle tracking van de elektronstraal collectieve effecten in een single-pass, S-band Linac zijn uitgevoerd. Een kwantitatieve studie voor de Fermi@Elettra elektronenbundel levering systeem van de injector einde aan de undulator, met inbegrip van de tros lengte magnetische compressie is gedaan. De kracht van de korte-range spatieleading (SC) krachten is geëvalueerd door middel van de laminarity parameter, berekend als functie van de elektronenbundel parameters langs de lijn. Het is aangetoond dat SC krachten zou corrupt de quasi-laminaire deeltje beweging en moet daarom rekening worden gehouden tijdens de one-stage magnetische compressie van het stel lengte, zelfs bij energieën waar de elektronen zijn ultra-relativistische. Het effect van de structurele lengte-en dwarsrichting wakker veld op de elektronenbundel distributie van energie en de verwachte emittance, respectievelijk, is onderzocht. Vormgeving van de oorspronkelijke huidige profiel is voorgesteld om de lengte-as wakker potentiële veranderen en het bijna lineaire maken. Op deze manier kan de longitudinale wakker veld worden gebruikt om te annuleren van de lineaire energieoverdracht chirp die nodig zijn voor magnetische compressie, en bovendien, niet-lineaire bijdragen aan het energie-chirp een minimum worden beperkt. Er is voorgesteld om de kop-staart instabiliteit veroorzaakt door de dwarse wakker worden met manipulatie traject langs de Linac (emittance bulten) te onderdrukken. Dan is er een traject jitter onderzoek is gedaan om de magneten 'uitlijning en trillingen toleranties die geen invloed hebben deze correctie regeling te geven. Ten slotte heeft de MVO-effect op de dwarse emittance en de microbunching instabiliteit lineaire versterking zijn berekend en vergeleken met particle tracking resultaten. De optiek ontwerp maakt de compensatie van het MVO-effect door middel van een geschikte optica regeling in de magnetische chicanes en in de strooier. Als voor de microbunching instabiliteit, gaat het in de niet-lineaire regime toen de twee-traps compressie wordt aangenomen. Deze studie rechtvaardigt daarom de uitvoering van een laser kachel Landau de instabiliteit vochtig en het plakje energie-verspreiding te houden binnen de FEL specificaties.

Enkele richtlijnen voor het ontwerp van de magnetische compressor regeling hebben gekregen, volgens de eisen uitgedrukt van de FEL doel prestaties. De principes weergegeven in dit hoofdstuk wordt verwezen naar het specifieke geval van een uitgezaaid X-ray FEL en alleen magnetische compressie van het

stel lengte is overwogen. Het ontwerp parameters voor de Fermi magnetische compressoren zijn gemaakt expliciet als een case study van de vorige theorie. Na dat het effect van de tros lengte magnetische compressie op de microbunching instabiliteit ontwikkeling in een Linac-based FEL is onderzocht. Met name de vermindering van de de instabiliteit krijgen door deeltjes longitudinale fase mengen is analytisch aangetoond. Het is aangetoond dat de efficiëntie in het verwijderen van de balk is microbunching veel gevoeliger voor de eerste modulatie golflengte dan aan de amplitude. Het natuurlijke gevolg van deze dynamiek is de goedkeuring van een enkele compressie schema. De haalbaarheid van deze regeling is aangetoond door middel van een 3-D deeltje Het bijhouden van de Fermi@Elettra FEL, met veelbelovende resultaten voor het behoud van de balk kwaliteit. Naast deze, een andere veelbelovende configuratie verschijnt. Als de lineaire energieoverdracht piepen bij de uitgang van BC1 kunnen verwijderd worden door speciale structuren te versnellen, dan deeltje longitudinale crossover is verbeterd in BC2. Het effect is geoptimaliseerd door twee chicanes, BC1 en BC2, met dezelfde teken van R_{56} . Als gevolg daarvan is de energie modulatie gedempt, samen met de bijbehorende stroompieken. De Fermi @ Elettra case studie is onderzocht in enkele details. De 1-D Beam vervoer is getoetst de 3-D particle tracking uitgevoerd met elegant, met inbegrip van collectieve effecten, voor een compressie factor van 10 in BC1. De studie toont aan dat dit alternatief systeem van compressie is succesvol en nog efficiënter dan de interne compressie voor de eerste modulaties waarvan de golflengte van de orde van tientallen μm . Het kan zelfs van toepassing zijn op langere golflengten en / of hogere compressie factoren, hoewel deze meer extreme situaties nodig te worden bevestigd door nader onderzoek.

We hebben gerapporteerd over de ingebruikname van de Fermi@Elettra elektronenbundel leveringssysteem. Methoden en experimentele resultaten met betrekking tot de controle van de longitudinale (versnelling, de distributie van energie, stelletje lengte compressie en microbunching instabiliteit) en transversale (optica matching, het vervoer en de traject controle) elektronenbundel dynamiek in FERMI is aangetoond. De longitudinale fase ruimte van de elektronenbundel werd gekenmerkt aan het begin van de Fermi inbedrijfstelling met een eenvoudige spectrometer lijn. Optiek heeft geopenbaard een belangrijk ingrediënt voor de karakterisering van de elektronenbundel de distributie van energie te worden, aangezien het optimaliseert de resolutie van de meting van het energieverbruik. Vanaf experimentele Twiss parameters van de elektronenbundel, de optiek matching en het transport door de gehele lijn is uitgevoerd met de elegant code, die de beschrijving van de echte versnelling van gradienten en de RF rand scherpstellen van de structuren. De mismatch parameter beschrijft meestal een verwachte groei van emittance kleiner dan 1% in beide vlakken. Tfamily elegante is ook gebruikt om de theoretische tra-

ject reactie matrices om de echte bundel baan te corrigeren in de Linac en in de hoge energie-overdracht lijn te genereren. De matrices worden ingevoerd in het traject feedback tool. Dit is ook in staat om experimentele reactie matrices te meten. De theoretische en de experimentele degenen kunnen worden samengevoegd voor een wereldwijde correctie traject langs de gehele lijn. De BPMS geïntegreerd in de feedback tool lees de balk positie op de frequentie van 10 Hz en hun lezing wordt gedwongen door de corrector magneten om de waarde bepaald door de gebruiker. Op deze manier, de feedback werkt als een traject correctie instrument. Het is geverifieerd dat de magnetische chicane BC1 niet noch de baan, noch de spreiding in de volgende rooster beïnvloeden. De dispersie hobbel in de chicane is gemeten en komt goed overeen met de theoretische verwachting. Een belangrijke horizontale emittance groei verschijnt tijdens de tros lengte magnetische compressie, vooral voor compressie factoren groter dan 3. Off-line simulatie studies geven aan dat MVO misschien wel de belangrijkste verantwoordelijke van deze emittance degradatie, vooral in de aanwezigheid van niet-lineaire compressie (de X-band holte naar de longitudinale fase ruimte lineariseren tijdens de compressie is nog niet geïnstalleerd) en de potentiële slice optica mismatch. Sommige bewijzen van microbunching instabiliteit zijn geconstateerd voor compressie factoren groter dan 3. Ze zijn COTR uitstoot stroomafwaarts van BC1 en een energie-modulatie van de gecomprimeerde elektronenbundel. Aan het eind, is een vergelijking van de theoretische verwachting en de gemeten waarden voor veel elektronenbundel parameters zijn geproduceerd en samengevat in een tabel met parameters. De ongecomprimeerde bundel is goed experimenteel gekarakteriseerd. Een goede overeenkomst met het model is bereikt. De ongecomprimeerde bundel wijkt nog steeds uit het model als voor de verwachte emittance gemeten na BC1. Verder onderzoek is nodig om een aanvullend begrip van de fysica te ontwikkelen in de BC1 volbrengen. Niettemin heeft de elektronenbundel kwaliteit bleek te zijn meer dan voldoende om de eerste coherente harmonische generatie in gezaaid configuratie op 43 nm (FEL fundamentele output) te genereren in december 2010, na een jaar, kalender tijd, van de machine inbedrijfstelling. Tabel ?? toont de vergelijking van de belangrijkste elektronenbundel parameters zoals ze zijn gemeten tijdens de inbedrijfstelling en het model voorspelling.

Acknowledgments

I want to thank my promoters Prof. Paul van Loosdrecht of the University of Groningen, Prof. Sytze Brandenburg of the Kernfysisch Versneller Instituut of Groningen and Prof. Parmigiani of the University of Trieste for having given to me the great opportunity of this Ph.D. thesis and for their effort in supervising my work. I also greatly appreciate the support that Hans Beijers (KVI) and the Management of Sincrotrone Trieste gave me to accomplish this thesis.

This thesis and, more in general, my present experience in electron beam dynamics for linac-based FELs relies on the guidance of my three invaluable guru, Max Cornacchia (SLAC and ST, on leave), Alexander Zholents (LBNL) and Paul Emma (SLAC). This thesis is mine as it is theirs. I thank Micheal Borland (ANL) because he taught me how conscious of the physics has to be a code runner. I have finally the opportunity to thank Rene' Bakker for having introduced me to the world of FELs.

I arrived to the production of this thesis only in virtue of the initial generous support of the FERMI@Elettra Project Leaders, Dr. Carlo Bocchetta first, Dr. Stephen Milton then. They allowed and pushed me to collect international experiences in accelerator physics research. Going even back to the origins, I will never forget the persons who inspired in me the passion for accelerator physics, Prof. Franco Cervelli (University of Pisa), Dr. Gaetano Vignola (INFN-LNF, on leave) and Dr. Caterina Biscari (INFN-LNF).

I enjoyed a lot of great helps from my colleagues Enrico Allaria, Sophie Ferry, Stefano Krecic, Giuseppe Penco, Mauro Trovo', during discussions, commissioning and software development. Special acknowledgments go to: Paolo Craievich, who introduced me to the world of wake fields; Simone Spampinati, who supported this thesis with new ideas and analytical calculations regarding microbunching instability; Magnus Sjoström (MAX-lab), who built up a beautiful tool for trajectory manipulation as I wished; Riccardo Bartolini (DLS and Univ. of Oxford) for fundamental discussions on the dispersion measurement. I thank the following colleagues for sharing with me the simulation results about microbunching instability: M. Venturini (LBNL) produced Figure 6.3, J. Qiang

(LBNL) and K. Sonnad (SLAC) contributed to produce Figure 5.25.

I also thank Prof. Sergio Tazzari and Prof. William Barletta for fruitful discussions and their patience in reviewing many draft works related to this thesis. There are many colleagues that I would like to thank because of precious discussions and suggestions that I received from them. I am pleased to remember here Zhirong Huang, Juhao Wu, William Fawley, Martin Dohlus, Torsten Limberg, Gabriele Bassi, Enrica Chiadroni, Daniele Filippetto, Luca Giannessi, Laura Badano, Sandra Biedron, Davide Castronovo, Giovanni De Ninno.

I would like to express my love to my friends and family. My old friends Alessio, Angela, Angelo, Carlo, Carmine, Dennis, Giacomo, Giancarlo, Giuseppe, Iacopo, Luca, Pasquale and Sauro still make my life happy: no one year seems to be passed, as in an extreme time contraction effect. My friends in Trieste, Paolo (Ino), Laura, Walter, Roberta, Felice, Mara, Yolanda, Claudia, Giovanni, Nicolas and Dylan made these recent years a peaceful and consoling period. My soul is devoted to my wife Valentina and my son Giordano. They patiently and firmly suffered, accompanied and supported my long doing during nights and nights of study and writing.

Curriculum Vitae

9 October 1976 Born in Terni, Italy

Educational Record

1990 – 1995 Senior High School (Scientific Lyceum) G. Galilei, Terni, Italy.

1995 – 2000 University of Pisa, Italy. Master Degree in Nuclear and Sub-nuclear Physics. Experimental thesis in Optical Electronics at the National Laboratory of Frascati, Rome, Italy.

Professional Record

2002 – Staff member of the Accelerator Group at Sincrotrone Trieste S.C.p.A.

2002 – 2006 Involved in the operation of Elettra synchrotron light source. In charge of the transfer lines design for the Elettra full energy injection system. Involved in the commissioning of such new system.

2003 – 2009 In charge of the electron beam delivery system design for the FERMI@Elettra Free Electron Laser. Member of the FERMI Commissioning Team. I serve the project leader as physics liaison support for the FERMI layout and electron beam dynamics.

Professional Services

- 2004 – 2008 PhD Supervisor. Teacher at the 2005 Cern Accelerator Advanced School, Trieste, Italy. Contract Professor of Accelerator Physics at the University of Trieste, Department of Physics, Trieste, Italy.
EUROFEL spoke-person for particle collective instabilities and nonlinear motion in linac-based FELs.
- 2007 – 2011 Member of the Organizing and Program Committee of the I (2007), II (2008), III (2010) and IV (2011) Workshop on Microbunching Instability.
Member of the Scientific Advisory Board of the Intern. Part. Accel. Conference 2010, Genoa, Italy.
Member of the Scientific Program Committee of the Free Electron Laser Conference 2010, Malmo, Sweden.
Member of the Scientific Program Committee of the Free Electron Laser Conference 2011, Shanghai, China.

Talks and Collaborations on Invite

- 08/2006 Free Electron Laser Conference 2006, Berlin Germany. *How to obtain high quality electron bunches in the presence of normal conducting linac wakefields.*
- 09/2009 Karlsruhe Institute of Technology, Karlsruhe, Germany. *The 100 nm to 4 nm FERMI@Elettra FEL project.* Introduction to eLlegant for the TBONE project.
- 09/2009 International Conference on Accelerator Computing 2009, San Francisco, California. *Design and Simulation Challenges for the FERMI@Elettra project .*
- 10/2009 Societa' Italiana di Fisica, Bari, Italy. *The 100 nm to 4 nm FERMI@Elettra FEL project.*
- 03/2010 2nd IRUVX-PP Annual Meeting, Hamburg, Germany. *FERMI@Elettra is under commissioning.*
- 01/2011 Kernfysisch Versneller Instituut, Groningen, The Netherlands. *The 100 nm to 4 nm Single-pass, Linac-based FERMI@Elettra FEL.* Introduction to eLlegant for the ZFEL project.
- 03/2011 Pohang Accelerator Laboratory, Pohang, South Korea. *Machine Design in the presence of Structural Wake Fields.* Member of the Review Committee (Accelerator Chair) at the PAL XFEL Beam Dynamics Workshop.

List of Publications

M. Cornacchia, S. Di Mitri, G. Penco and A. A. Zholents, *Formation of Electron Bunches for Harmonic Cascade X-ray Free Electron Lasers*, Phys. Rev. Special Topics - Accel. and Beams, **9**, 120701 (2006).

P. Craievich, S. Di Mitri and A. A. Zholents, *Single-bunch emittance preservation in the presence of trajectory jitter for FERMI@elettra-seeded FEL*, Nucl. Instr. and Methods in Phys. Res. A **604** (2009) 457–465.

S. Di Mitri et al., *Design and simulation challenges for FERMI@elettra*, Nucl. Instr. and Methods in Phys. Res. A **608** (2009) 19–27.

S. Di Mitri, M. Cornacchia, S. Spampinati and S. V. Milton, *Suppression of microbunching instability with magnetic bunch length compression in a linac-based fel*, Phys. Rev. Special Topics - Accel. and Beams, **13**, 010702 (2010).

S. Di Mitri, *Geometric efficiency of a two-stage fully absorbing collimation system in single-pass linacs*, Phys. Rev. Special Topics – Accel. and Beams, **13**, 052801 (2010).

S. Di Mitri and M. Cornacchia, *Compact Multi-Purpose Optics Insertion in the FERMI@Elettra Linac Bunch Compressor Area*, WEPB42 in Proc. of Free Electron Laser Conf. 2010, Malmo, Sweden (2010).

S. Di Mitri, M. Cornacchia, P. Craievich, G. Penco, S. Spampinati, M. Venturini and A.A. Zholents, *Comparative Study of the FERMI@Elettra Linac, with One and Two-Stage Electron Bunch Length Compression*, THPB03 in Proc. of Free Electron Laser Conf. 2010, Malmo, Sweden (2010).



University of Groningen
Zernike Institute
for Advanced Materials

Zernike Institute PhD thesis series 2011–22
ISSN 1570–1530
ISBN printed version: 978-90-367-5175-9
ISBN electronic version: 978-90-367-5176-6